



Pulse-Shape Analysis and Position Resolution in highly segmented HPGe Detectors

Inaugural-Dissertation

zur
Erlangung des Doktorgrades
der Mathematisch-Naturwissenschaftlichen Fakultät
der Universität zu Köln

vorgelegt von

Lars Lewandowski
aus Langenfeld

Köln 2020

Berichtersteller:

Prof. Dr. Peter Reiter
Prof. Dr. Jan Jolie

Tag der letzten mündlichen Prüfung:

13.05.2020

Abstract

The Advanced GAMMA Tracking Array (AGATA) is a position sensitive γ -ray spectrometer, consisting of highly segmented High Purity Germanium (HPGe) detectors. It relies on the Gamma-Ray Tracking (GRT), which reconstructs the path of the individual γ rays through the array. The GRT enables the detection of γ rays with highest efficiency and provides γ -ray spectra with a Peak-to-Total ratio P/T which is comparable to Compton suppressed spectra. The tracking requires information on the deposited energies and interaction positions of the γ rays. The interaction positions are derived via Pulse-Shape Analysis (PSA).

The PSA utilizes the measured pre-amplified signals of the 36 segments and of the core electrode. These signals are characteristic for each interaction position. The comparison of the measured pulse shapes with reference signals provides the interaction positions of the γ rays. The reference signals are simulated with the AGATA Detector Library (ADL) and the measured and simulated signals are compared with the AGATA adaptive grid search.

In this thesis the distributions of hits, which are obtained by employing ADL and the adaptive grid search, were investigated. An unexpected clustering of hits and a surplus of hits at certain single interaction positions, which can not be explained by statistical fluctuation, were observed. In the frame of this work quantities were introduced which describe the homogeneity of the hit distributions as well as the correlation of the number of hits of neighboring grid points. The obtained results confirm that the hit distributions are less homogeneous than expected and that the number of hits in neighboring grid points are correlated. These observations motivated an in-depth study of the PSA and its results.

The pulse shapes simulated with ADL were analyzed in detail and compared with the corresponding measured signals. Systematic deviations of measured and simulated signals were determined and possible solutions are discussed. In particular, the T_{10-90} rise times of the pulse shapes and the evolution of the difference of measured and simulated signals during the process of charge collection were inspected.

The adaptive grid search determines the best fitting reference signal by minimizing a figure of merit. The working principle of the adaptive grid search and its results were investigated in detail. The impact of employing different figures of merit on the PSA is discussed. Results regarding the position sensitivity, which were extracted from an inspection of the figure of merit landscape, are presented. The strong position dependence of the pulse shapes affects the determination of the starting time T_0 , when using leading edge or Constant-Fraction Discriminator (CFD) algorithms. An energy and position independent T_0 -determination method is discussed and compared to the CFD timing.

In the second part of this thesis the β^+ decay of ^{22}Na was utilized to determine the PSA performance. The emitted positron annihilates with an electron at the source position and the two created 511 keV γ rays were detected with the AGATA spectrometer. The agreement of the measured interaction positions with the expected 180° correlation was used to assess the PSA performance and to estimate the position resolution.

Parameters which are relevant for the shape of the reference signals or the working principle of the grid-search algorithm were investigated and optimized in a systematic study. These parameters were optimized by maximizing the agreement of the determined interaction positions of the 511 keV γ rays with the expectation. In particular the distance of the lines, which connect the 511 keV coincidences,

to the source position was minimized.

The important input quantities for the pulse shapes are the transfer function of the preamplifiers, the hole mobility and the electron mobility. The working principle of the grid search was improved by determining the optimal distance metric and introducing weighting coefficients which increase the contribution of the transient signals in the figure of merit calculation.

Zusammenfassung

Das Advanced GAMMA Tracking Array (AGATA) ist ein ortsauflösendes Spektrometer für Gammaquanten, welches aus hochsegmentierten, hochreinen Germaniumdetektoren besteht. Es basiert auf dem Gamma-Ray-Tracking (GRT), welches den Pfad der einzelnen Gammaquanten durch das Array rekonstruiert. Das GRT ermöglicht die Detektion von Gammaquanten mit höchster Effizienz und bietet Gammaspektren mit einem Peak-to-Total-Verhältnis P/T , welches vergleichbar mit Compton unterdrückten Spektren ist. Das Tracking benötigt Informationen über die Wechselwirkungsorte der Gammaquanten und die Höhe der dort deponierten Energien. Die Wechselwirkungsorte werden mit Hilfe von Pulse-Shape-Analyse (PSA) bestimmt.

Die PSA verwendet die gemessenen Vorverstärker-Signale der 36 Segmente und der Core-Elektrode. Diese Signale sind charakteristisch für jeden Wechselwirkungsort. Der Vergleich der gemessenen Impulsformen mit Referenzsignalen liefert die Wechselwirkungsorte der Gammaquanten. Die Referenzsignale werden mit der AGATA-Detector-Library simuliert und die gemessenen und simulierten Signale werden mit dem AGATA Adaptive-Grid-Search verglichen.

In dieser Dissertation wurden die Verteilungen der Wechselwirkungsorte, welche mit ADL und dem Adaptive-Grid-Search erzeugt wurden, untersucht. Eine nicht erwartete Anhäufung von Wechselwirkungen und ein Überschuss an Treffern an bestimmten einzelnen Wechselwirkungsorten, welcher nicht durch statistische Fluktuation erklärt werden kann, wurden beobachtet. Im Rahmen dieser Arbeit wurden Größen eingeführt, welche sowohl die Homogenität der Verteilungen der Wechselwirkungsorte als auch die Korrelation der Anzahl der Treffer von benachbarten Wechselwirkungsorten beschreiben. Die Ergebnisse bestätigen, dass die Verteilungen der Wechselwirkungsorte weniger homogen sind als erwartet und dass eine Korrelation zwischen der Anzahl der Wechselwirkungen von benachbarten Wechselwirkungsorten besteht. Diese Beobachtungen motivierten eine detaillierte Studie der PSA und ihrer Ergebnisse.

Die mit ADL simulierten Impulsformen wurden im Detail analysiert und mit den entsprechenden gemessenen Signalen verglichen. Systematische Abweichungen zwischen gemessenen und simulierten Signalen wurden bestimmt und mögliche Lösungen werden diskutiert. Insbesondere wurden die T_{10-90} Anstiegszeiten der Impulsformen und die Evolution der Differenz zwischen gemessenen und simulierten Signalen während der Ladungssammlung untersucht.

Der Adaptive-Grid-Search bestimmt die beste Übereinstimmung zwischen Referenz- und Messsignal, indem für jeden Wechselwirkungsort eine Gütezahl berechnet und diese dann minimiert wird. Die Funktionsweise des Adaptive-Grid-Search und seine Ergebnisse wurden im Detail untersucht. Die Auswirkung der Verwendung von verschiedenen Methoden zur Berechnung der Gütezahl wird diskutiert. Ergebnisse bezüglich der Ortssensitivität, welche anhand einer Untersuchung der Gütezahlen für verschiedene Wechselwirkungsorte bestimmt wurde, werden präsentiert. Die starke Ortsabhängigkeit der Impulsformen beeinflusst die Bestimmung der Startzeit T_0 eines Signals, wenn Leading-Edge- oder Constant-Fraction-Discriminator-Algorithmen (CFD) verwendet werden. Ein energie- und positionsunabhängiges Verfahren zur T_0 -Bestimmung wird diskutiert und mit einem CFD-Timing verglichen.

Im zweiten Teil dieser Dissertation wurde der β^+ -Zerfall von ^{22}Na genutzt, um die Leistungsfähigkeit der PSA zu bestimmen. Das emittierte Positron annihiliert mit einem Elektron nahe der Quellposition und die erzeugten 511 keV Gammaquanten wurden mit dem AGATA Spektrometer detektiert. Die

Übereinstimmung der gemessenen Interaktionspunkte mit der erwarteten 180° -Korrelation wurde genutzt, um die Leistungsfähigkeit der PSA zu evaluieren und die Ortsauflösung zu bestimmen. Parameter, welche relevant für die Form der Referenzsignale oder für die Funktionsweise des Adaptive-Grid-Search sind, wurden in einer systematischen Studie untersucht und optimiert. Diese Parameter wurden optimiert, indem die Übereinstimmung der Wechselwirkungsorte der 511 keV Gammaquanten mit der Erwartung maximiert wurde. Im Speziellen wurde der Abstand der Linien, welche die 511 keV Koinzidenzen verbinden, zur Quellposition minimiert.

Die wichtigen Größen, welche in die Impulsformen eingehen, sind die Transferfunktion der Vorverstärker, die Löchermobilität und die Elektronenmobilität. Die Funktionsweise des Adaptive-Grid-Search wurde verbessert, indem die optimale Abstandsmetrik bestimmt und Gewichtungskoeffizienten eingeführt wurden, welche den Beitrag der transienten Signale in der Berechnung der Gütezahl erhöhen.

Contents

1	Introduction	7
1.1	Motivation	7
1.2	AGATA	8
2	Pulse-Shape Analysis	9
2.1	Working principle of the PSA	9
2.1.1	Reference data bases	9
2.1.1.1	The AGATA detector library	10
2.1.2	Search algorithms	14
2.1.2.1	The adaptive grid search	15
2.2	Data acquisition with AGATA	17
2.3	Results of the Pulse-Shape Analysis	18
2.3.1	Hit distributions	19
2.3.2	Position resolution	27
3	Comparison of Measured and Simulated Pulses	29
3.1	Super trace, residuals and figure of merit	29
3.2	Figure of merit landscape	31
3.3	Time dependent difference of measurement and simulation	37
3.4	T_{10-90} Rise times of measured and simulated pulses	43
3.5	T_0 Determination	48
4	Determination and Improvement of PSA performance	53
4.1	^{22}Na -coincidence method	53
4.1.1	Experimental setup	53
4.1.2	Reconstruction of coincident γ rays after e^+/e^- annihilation	56
4.1.3	Determination of the source position	60
4.1.4	Reconstruction of Compton scattered events	62
4.1.5	Estimation of position resolution	67
4.2	Estimation of PSA performance via comparison of determined and expected hit distributions	72
4.2.1	Correlation of neighboring grid points	72
4.2.2	Deviation from the expectation	74
4.2.3	High statistics grid points	76
4.3	Improvement of PSA performance employing a variation procedure	77
4.3.1	Weighting of transient signals	77
4.3.2	Distance metric	82
4.3.3	Weighting of individual segments based on the fluctuation of the baseline	87
4.3.4	Smearing of interaction positions	90

4.3.5	Transfer function	90
4.3.5.1	Transfer function with homogeneity criteria	93
4.3.6	Hole mobility	98
4.3.7	Electron mobility	102
4.4	Comparison of results before and after optimization	104
4.4.1	Comparison of ^{22}Na results	104
4.4.2	Comparison of hit distributions	108
4.4.3	Comparison of homogeneity criteria	112
4.4.4	Summary of results before and after optimization	113
5	Summary and Outlook	115
5.1	Summary	115
5.2	Outlook	119
5.2.1	Further developments and improvements with ADL	120
5.2.1.1	Point-like charges	120
5.2.1.2	Hole mobility	121
5.2.1.3	Geometry of the crystals and dead layers	121
5.2.2	Future developments of the search algorithm	121
5.2.2.1	Improvements to the weighting of transient signals	121
5.2.2.2	Two hits within a single segment	123
5.2.2.3	New search algorithms	124
5.2.3	New developments for position-sensitive HPGe-detectors	125
	Bibliography	125
	Acknowledgments	143
	Curriculum vitae	145
	Erklärung zur Dissertation	146

1 Introduction

1.1 Motivation

Current nuclear physics research is concerned with understanding the structure and dynamics of nuclei. For this, the nuclear many-body system is investigated, especially the underlying fundamental forces, symmetries and effective interactions. For the understanding of these properties, the study of nuclei under extreme conditions is needed. These investigations concern nuclei far from stability, at highest spins and temperatures.

Currently, a new generation of radioactive ion beam (RIB) facilities is being build, which will provide a wide range of exotic nuclei. Among others, these are FAIR [1], HIE-ISOLDE [2], SPES [3] and SPIRAL2 [4]. The γ -ray spectroscopy of the produced exotic nuclei is key for understanding their underlying fundamental properties. The experimental conditions for γ -ray spectroscopy at these facilities are very challenging. The demands for a γ -ray spectrometer are highest efficiency, best peak-to-total ratio (P/T), high count-rate capabilities, a wide energy range and excellent energy resolution. Different detector systems excel at certain aspects of these specifications, e.g. NaI scintillators provide high efficiency but lack a good energy resolution. When combining the different experimental requirements High-Purity Germanium (HPGe) detectors emerge as the most promising solution.

In the past, the powerful and outstanding HPGe-detector arrays were GAMMASPHERE [5] and EUROBALL [6], which are 4π Compton-suppressed spectrometers. The usage of germanium causes a very good energy resolution, while the Compton suppression ensures a good P/T ratio. The 4π design leads to a decent overall efficiency, although the actual solid angle coverage is limited by the Compton-suppression detectors (BGO scintillators). The angular resolution, given by the size of the crystals, allows for a Doppler correction, limited by the detector opening angle. Since future experiments at the newly constructed facilities will typically provide nuclei with a high recoil velocity β , an excellent angular resolution is needed to overcome Doppler effects and to maintain the good energy resolution of the system.

The next step in the evolution of γ -ray spectrometers was the introduction of electronically segmented HPGe detectors, first MINIBALL [7] and EXOGAM [8] and then the current state-of-the-art 4π tracking arrays GRETINA [9] and AGATA [10]. The electronic segmentation of HPGe detectors allows to determine the interaction position of γ rays by measuring the signals induced on the electrodes of the segments. This method, called Pulse-Shape Analysis (PSA), enables the Gamma-Ray Tracking (GRT) which reconstructs the path of a γ ray through the array.

The reconstruction is based on the determined interaction positions and the deposited energies. In combination with the scattering angles calculated from the Compton-scattering formula the most

probable γ -ray path is assessed. The tracking also takes the energy dependent interaction cross sections and the penetration depth into account. This method allows to reject γ rays which did not deposit their full energy in the array, which would otherwise cause background in the γ -ray spectra. In addition, γ rays which interact in different crystals of the array can be reconstructed, increasing the efficiency of the system ("add back"). The first interaction position of the γ ray is determined by the tracking, which enables a precise Doppler correction. The knowledge of the interaction positions also allows for a correction of neutron damage by calculating drift path and drift velocity of charge carriers for a given interaction position and estimating the loss due to trapping of charge carriers and thereby retaining the good energy resolution of the HPGe detector [11]. Neutron damage affects the measured pulse shapes, but simulations suggest that the impact on the position resolution is negligible [12]. This work is concerned with the position determination of γ -ray interactions with the γ -ray spectrometer AGATA, which will be introduced briefly in the next section.

1.2 AGATA

The Advanced GAMMA Tracking Array (AGATA) is designed as 4π γ -ray spectrometer. In its final configuration the array consists of 180 individual highly segmented HPGe detectors. Three different types of asymmetric, hexagonal crystals (A, B and C type) are mounted into triple cryostats [13], forming nearly a full shell with an inner radius of 22.5 cm. The n-type HPGe crystals are encapsulated and the central electrode (core) extends from 13 mm to the back of the crystal. More details on the shape of the crystal and the tapering can be taken from Ref. [10] Fig. 4 and 5. Each crystal is 36 fold electrically segmented and the charges induced on the individual electrodes are pre-amplified and digitized with a 100 MHz sampling rate. More details on the data acquisition are given in section 2.2. Simulations for the full 4π array predict a photopeak efficiency of 43% and a P/T ratio of 59% for single 1 MeV interactions, as well as 28% photopeak efficiency and a 43% P/T ratio at a multiplicity of 30 [14].

The measurement of the 37 preamplifier signals enables the determination of the individual interaction positions of the γ ray. The working principle of the most commonly used PSA algorithms is discussed in detail in section 2.1. Several tracking algorithms have been developed, the most commonly used algorithms, the Orsay Forward Tracking (OFT) [15] and the Mars Gamma-Ray Tracking (MGT) [16], are so called forward-tracking algorithms. Here, the individual interactions are grouped into clusters by setting multiplicity dependent gates on the ϕ and θ angles (spherical coordinates). Within these clusters different hypotheses regarding the number of γ rays and the interaction sequence are tested, taking deposited energies, scattering angles and cross sections into account. For the testing and validation of these hypotheses (synonymous to the rejection of some measured γ -ray interactions) an optimum between achieved efficiency and desired P/T has to be found.

2 Pulse-Shape Analysis

2.1 Working principle of the PSA

The Pulse-Shape Analysis relies on the fact that the shape of the signals, which are induced on the segment and core electrodes, depends strongly on the interaction position of the γ ray. The measured signals therefore constitute a characteristic signature which can be used to determine the interaction position. For this, a link between measured pulse shapes and interaction position is needed. The most common approach is to simulate the electrical fields and the movement of the charges within the crystal. The obtained pulse shapes are stored in reference bases. Within this section an overview of different reference bases and different search algorithms, which compare measured and simulated pulses, are presented. The ones used in this work (the AGATA Detector Library ADL [17] and the adaptive grid search [18]) are introduced in more detail. Other approaches, e.g. creating reference bases with scanning tables, are also discussed.

2.1.1 Reference data bases

For a precise reconstruction of the interaction position of a γ ray, the measured preamplifier signals have to be compared to reference signals, which are related to the position where charges are created by the γ -ray interaction. Several different approaches were made to create position dependent reference signals, for example characterizing the crystals via simulations with the Multi-Geometry Simulation (MGS) [19] code or with the Java AGATA Signal Simulation (JASS) [20]. There, the weighting potentials and the electrical field are obtained by solving the Poisson equation numerically. Within the GRETINA collaboration the software packages "*fieldgen*" and "*siggen*" for the calculation of the fields and of the pulse shapes were developed [21] [22]. The general approach for all these simulations is similar. A detailed explanation of the simulations, based on the example of the AGATA Detector Library [17] is given in section 2.1.1.1.

Within the AGATA collaboration several scanning tables, which can provide measured signals with a known interaction position, were constructed and are operating. Some of the scanning tables rely on collimated γ -ray sources and the coincident detection of Compton scattered γ rays with an ancillary detector to fix the interaction position [23] [24]. The precise knowledge of the interaction position comes with the cost of very long measurement times. Therefore, a full characterization of a crystal with these scanning tables is not realistically possible. The Salamanca Lyso-based Scanning Array (SALSA) is in development and will provide information on the interaction position by using a source

which decays by β^+ emission and a position sensitive pixel detector [25]. Another approach is the so called Pulse Shape Comparison Scan (PSCS) [26]. When employing this technique, the crystal is scanned with simple collimated γ -ray sources from two perpendicular sides. The interaction position is then restricted to a single point by comparing the pulse shapes of two crossing collimated beams via χ^2 minimization. The advantage of this procedure is the strongly reduced measurement duration. In contrast to the scanning methods, which are based on collimated sources and the coincident detection of 90° Compton scattered γ rays, a full characterization of single crystals is feasible.

An additional approach, complementing the simulation and measurement of the pulse shapes, is the so called in-situ method [27]. This method is based on determining estimators for the coordinates (for example for the depth z of the interaction) using simple properties of the pulse shapes (for example the amplitude of the signals in the neighboring segments). These estimators are combined with the expected distribution of interactions from a source measurement, obtained from simulations. In this way a relationship between estimator and most likely coordinate is available. The relationship is used to assign interaction positions to measured pulse shapes. The pulse shapes for a given interaction position are averaged, resulting in a set of reference signals to be used for PSA. The advantage of this technique is the full characterization of all crystals mounted in the frame via a single source measurement. The obtained pulse shapes combine all relevant individual properties of the crystal and the electronics, like the transfer function, impurity concentration and so on. The drawback of this technique is that it has (apart from the simulated hit distribution) no physics input, it is a purely mathematical approach. Certain characteristics of the obtained pulse shapes cannot be traced back to individual physical properties of the crystal or the electronics. In addition, the obtained pulse shapes may have contributions from multiple interactions per segment, as these cannot be resolved by the simple estimators [28].

Since the scanning of all crystals is impracticable and the in-situ bases have not proven to be superior [28], simulated reference bases are up to now the solution of choice. Within the AGATA collaboration the AGATA Detector Library is the most commonly used one and will be introduced in the next section.

2.1.1.1 The AGATA detector library

Within this work the AGATA Data Library was employed. It is described in detail in reference [17]. The basic concepts and the inputs of the simulation will be treated here, as some of these aspects will be investigated later in this thesis. Limitations and applied approximations will also be discussed in this section.

The procedure to obtain simulated pulse shapes, which are suited to be compared to measured traces (pulse shapes), can be divided in the following steps (which are subsequently treated in detail):

1. Calculation of the electrical field by solving the Poisson equation
2. Calculation of the charge-carrier trajectories
3. Calculation of the weighting potentials
4. Calculation of the induced charges on each electrode caused by the charge carriers in the crystal

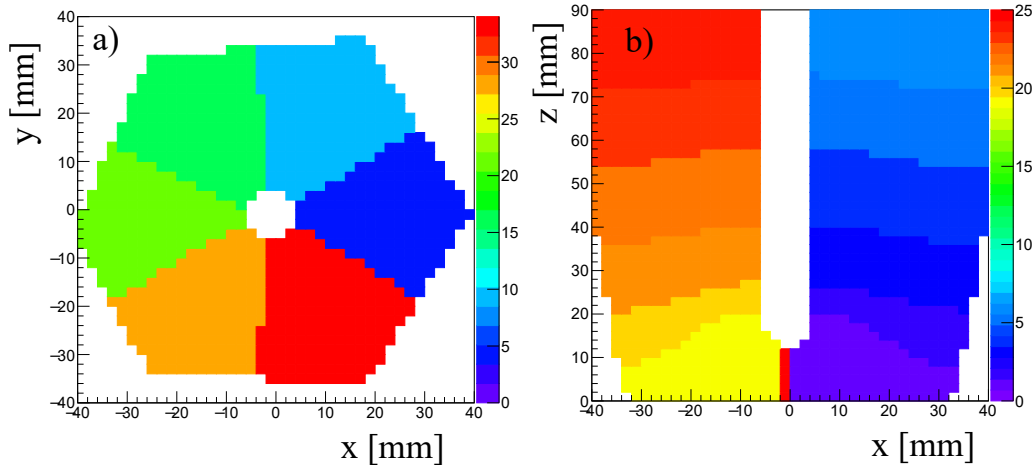


Figure 1: The segmentation simulated with ADL of crystal A001 is shown for a) a fixed z of 40 mm to 42 mm and b) a fixed y of -2 mm to 0 mm. The color code represents the respective segment id (1-36, not all segments visible). Especially in the xz depiction the bending of the segments at small radii becomes apparent. This is caused by the position of the central contact which ends at $z \approx 13$ mm. At the back of the crystal the approximation of a true coaxial detector is applicable.

5. Convolution of the obtained pulses with an electronic response function

1.) The electrical field E is obtained by solving the Poisson equation:

$$\Delta\phi = -\frac{\rho}{\epsilon} \quad (2.1)$$

With ρ being the charge density originating from the space charges, which come from the impurities in the high-purity germanium (HPGe). The density of impurities is in the order of $\frac{10^{10}}{\text{cm}^3}$. The equation is solved with the boundary condition that the difference of the potential at the inner electrode (core) and the segment electrode corresponds to the applied high voltage V .

The actual impurity distribution in the detection material is not known, only two values for the front- and for the backside of the crystal are provided by the manufacturer. The impurity profile in the crystal is modeled by a linear gradient between the front and back of the crystal, assuming a radial independence of the profile. Results of capacitance-voltage measurements indicate that these assumptions are valid [29] [30]. The form of the electrical field lines also determine the hit segment for a given interaction position. The shape of the segments is illustrated in Fig. 1. Note that all distributions referring to single crystals are plotted in the coordinate system of the individual crystal. Here the origin is centered at the front of the crystal and the z coordinate is in parallel to the central contact, see Fig. 2.

2.) The charge carriers move along the electrical field lines. The full time dependent trajectory $\vec{r}(t)$ is crucial for the shape of the pulses. For this, the drift velocity v_D , which depends on the charge-carrier mobility and the electrical field strength, is needed. The mobility depends on the charge carrier type (electrons or holes), direction of the drift, temperature and impurity concentration of the crystal. The

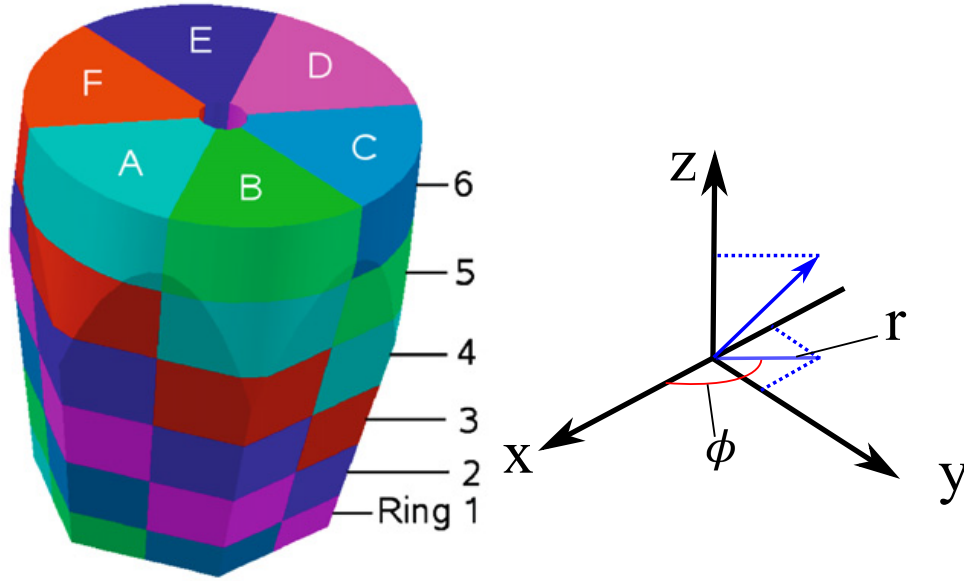


Figure 2: A sketch of an AGATA crystal is shown. The electronic segmentation divides the crystal in 36 segments, consisting of 6 rings and 6 slices. The segments are labeled by the corresponding slice A-F and by the ring number 1-6. The coordinate system of the crystal is chosen such that the origin is centered at the front of the crystal (ring 1). The z axis is in parallel to the core. The y axis goes along the segmentation border of slices B and C and slices E and F. Cylindrical coordinates in terms of r , ϕ and z are useful to describe the (approximate) cylindrical symmetry of the crystal. Depiction of the crystal adapted from [10].

mobility of holes and electrons is not isotropic due to the non-negligible electrical field of the lattice. The drift velocity in the $\langle 100 \rangle$ direction is up to 30% faster than in the $\langle 111 \rangle$ direction. The models for the drift velocity and the mobility are discussed and investigated in more detail in section 4.3.6 and 4.3.7. For the simulations a constant temperature and a constant mobility in all parts of the crystal is assumed.

3.) The weighting potentials φ_i contain the information on the charge Q_i which is induced on the electrode i by a charge q which is located at a position \vec{r} . The induced charge is given by:

$$Q_i(\vec{r}) = q\varphi_i(\vec{r}) \quad (2.2)$$

The weighting potentials are obtained under application of the Shockley-Ramo theorem [31] by solving the Poisson equation in the absence of any charge (i.e. $\rho = 0$) and by setting the considered electrode to 1 V, while all other electrodes are grounded. The equation is solved with the boundary condition $\varphi_i(S_j) = \delta_{i,j}$ which ensures that a charge q located at the surface S_j of electrode j will either induce the full charge $Q_i = q$ if $i = j$ or $Q_i = 0$ if $i \neq j$. An example for the weighting potential of the core and of a segment are given in Fig. 3.

For simplification purposes it is assumed that a single point-like charge is created for both electrons and holes when a γ ray interacts in the germanium. This is a valid approximation for low-energy interactions of a few hundred keV, which are the most likely ones to occur. For example a photo or

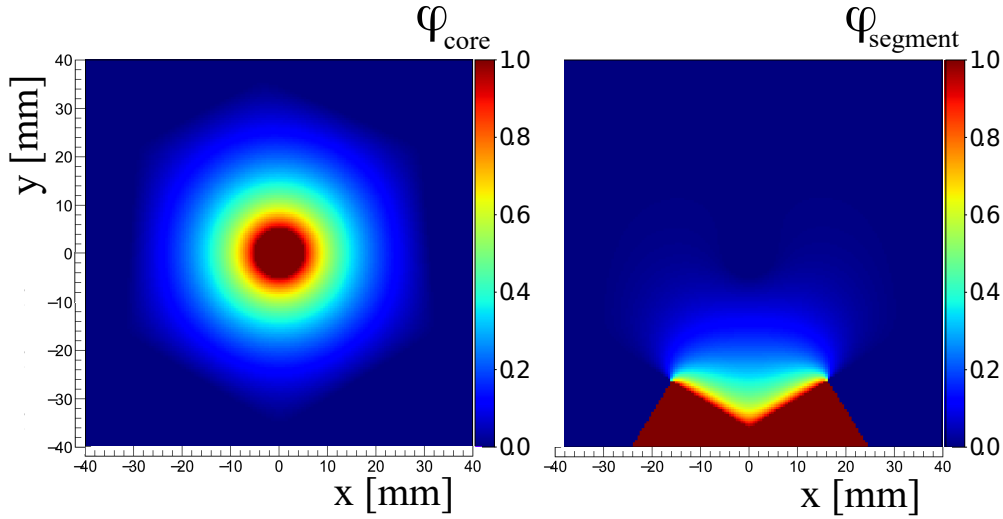


Figure 3: The ADL weighting potential for the core (left) and for segment A3 of an A-type crystal is shown at a detector depth z of 23.5 mm. For a given trajectory the charge induced on the respective electrode is given by the weighting potential. Both the charge of the electrons and of the holes contribute to the induced charge Q_i , but with their respective opposite signs.

Compton electron with an energy of 100 keV has a range of $44\ \mu\text{m}$ [32]. A 1 MeV electron has a range of 1.2 mm, which is not insignificant, but still smaller than the expected achievable position resolution. Single 1 MeV interactions are rather unlikely due to the relative larger cross section for Compton scattering compared to a photo effect. In addition, for high energy γ rays forward scattering is more probable, leading to typical energy depositions of a few hundred keV. The diffusion of the charge cloud during the movement to the electrodes is neglected.

4.) The combination of the weighting potentials φ_i and the time dependent trajectories of the charges $\vec{r}(t)$ (using the electrical field E and the drift velocity v_D) enables the calculation of the induced charges $Q_i(t)$ on all electrodes i via eq. 2.2 and therefore the calculation of the complete time dependent pulse shapes.

5.) In order to compare the calculated pulses to the measured signals, the influence of the acquisition electronics has to be taken into account. Here, two aspects have to be accounted for: the measured signals are shaped by the preamplifiers. Therefore, the simulated signals have to be convoluted with the transfer function of the preamplifiers. The transfer function is measured by injecting a fast rectangular pulser signal into the preamplifier. Due to the high number of channels, the direct measurement of the transfer function of all channels is not feasible. Instead, the transfer function is described by an exponential decrease, with a time constant τ as parameter. The transfer function and the impact of different τ values on the results of the PSA was investigated within this work, more details are presented in section 4.3.5.

The second aspect is the crosstalk of segments and core. This is caused by the fact that - in contrast to the assumptions of the Shockley-Ramo theorem - the electrodes are not grounded. The electrodes are connected to preamplifiers. An adjustment of the Ramo theorem is given in [33]. The capacitive

coupling of segments and core causes a reduction of the measured energy in segment i if segment j is hit, depending on the energy of the interaction. This proportional crosstalk is well understood and described by a linear electronic model in refs. [34] and [35]. Additionally, in segments adjacent to the hit segment a crosstalk is observed, which is proportional to the derivative of the signal of the hit segment. It is therefore important for the PSA as the so called "derivative crosstalk" appears during the charge collection and has to be distinguished from the transient signals, which contain the information on the interaction position. A model was developed to correct for the derivative crosstalk based on the measured proportional crosstalk [36] [37]. Also a method was invented to distinguish derivative crosstalk and transient signals for measurements with a collimated source (see Ref. [38] section 2.3.2).

After including the complete electronic response, the simulated signals can be compared to the measurement to extract the interaction positions. The final results depend on the algorithm which is used for this comparison. An overview of different search algorithms and a discussion of their respective advantages and limitations is given in the next section. The adaptive grid search, which is used by the AGATA collaboration and which was also employed in this work, is introduced in more detail.

2.1.2 Search algorithms

PSA algorithms have to fulfill two main requirements: 1.) A position resolution within the specifications of ~ 5 mm Full Width at Half Maximum FWHM. 2.) A fast computing time (less than 1 ms for one event on a single CPU). Due to the high counting rate, the algorithm has to process events in a very efficient way while remaining stable and robust. The computing time of the algorithm becomes especially important in the case of multiple interactions in different segments of the detector and/or multiple interactions within a segment. For multiple interactions the number of degrees of freedom grows exponentially.

The position resolution is commonly specified as FWHM of a Gaussian distribution, assuming an identical resolution in each direction x, y, z . In fact, most PSA algorithms tend to allocate hits in a non-Gaussian distribution around the physical interaction [39] [20]. In reality the distributions have left and right tails, distorting the relation between standard deviation and FWHM. Other quantities to describe the position resolution, such as the median of the distribution, have been suggested [40]. This should be taken into account when comparing different quantities for the position resolution, e.g. the standard deviation σ and the FWHM, since the relation $\text{FWHM} \approx 2.35\sigma$ applies only for Gaussian distributions.

To achieve the needed position resolution, a precise T_0 determination is needed (around $\Delta T_0 < 10$ ns). Therefore, T_0 is typically included in most search algorithms by introducing a variable time shift, which is determined along with the interaction position. Especially for low-energy interactions the small signal-to-noise ratio makes a precise T_0 determination very challenging.

PSA algorithms can be divided into two groups. The first group compares the measured signals with a set of reference signals, while the second group extracts the interaction position from properties of the

pulse shape. An example for the latter one is a simple approach, which was developed and applied for MINIBALL, where the amplitude of the transient signals of neighboring segments is considered [41]. More elaborate approaches, like the in-situ method discussed in section 2.1.1, extract the interaction positions using estimators which are calculated from the pulse shape. The achieved position resolution was below the methods using reference signals [28].

The most commonly used algorithms compare the measured signals with a previously calculated set of reference signals. For the determination of interaction positions in the γ -ray spectrometer GRETINA, which has very similar properties as AGATA, a signal decomposition is used on an irregular grid. Here the density of grid points depends on the relative change of the reference signals. The density is especially large at positions in the detector where the sensitivity is highest (see reference [42] on the sensitivity of different interaction positions). This leads to a high density of grid points for example at segment boundaries. Measured and simulated signals are first compared on a coarse grid, then on a fine grid. The GRETINA signal decomposition also looks for multiple interactions in single segments (see reference [43]).

Another approach is the so called Fully-Informed Particle-Swarm (FIPS) algorithm [40]. Here, the comparison of measurement and simulation is not performed on a fixed grid. Instead, the search is divided in different iterations. At each iteration certain hypotheses regarding the final result (i.e. interaction positions, but also number of interactions per segment, energy ratio between those interactions) are tested. Each hypothesis corresponds to the position of the respective member of the "swarm". At the next iteration step the new hypotheses to be tested are derived from the previous iteration by considering the agreement of the different hypotheses with the measurement. In this way a fast convergence of the algorithm is ensured, which allows to test for more "complex" results, especially multiple interactions per segment.

2.1.2.1 The adaptive grid search

Within the AGATA collaboration the adaptive grid search is used for the comparison of the ADL reference signals and the measurement. The comparison is done by minimizing the following figure of merit:

$$\text{Figure of Merit} = \sum_i \sum_{t_j} |A_{i,s}(t_j) - A_{i,m}(t_j)|^p \quad (2.3)$$

Here $A_{i,s}(t_j)$ and $A_{i,m}(t_j)$ are simulated s and measured m pulse heights of segment i at time index t_j . For the calculation the first 40 samples after the determined T_0 are considered. This corresponds to 400 ns, which is long enough to ensure that the charge collection is completed.

This search is done on an "adaptive" grid which means that first an interaction position is determined on a coarse grid of 6 mm and then on a fine grid of 2 mm around the determined interaction position. This is necessary to reduce the number of operations which have to be computed. Depending on segment size a segment typically has around 10^3 grid points using the fine grid.

A precise alignment of simulation and measurement is crucial for achieving a good position resolution. For the T_0 determination the strong dependence of the pulse shapes on the interaction position

has to be taken into account. Therefore, a T_0 determination via leading edge or via a (digital) Constant-Fraction Discriminator CFD is not sufficient. For a position independent timing the following characteristics of core and segment signals is exploited: The sum of all segment signals and of the core signal is in good approximation a linear pulse with a constant slope. This linear pulse is fitted with a first order polynomial to determine the starting time of the pulse. The differences of T_0 determined via CFD and this method is investigated in more detail in section 3.5.

In addition to the initial T_0 determination, the starting time is also included as a variable in the grid search. This is done by first determining an interaction position with the initial T_0 and then shifting the measured signals by a fixed time t_s with respect to the found best fitting simulated signals. The time shift t_s is chosen such that the agreement of measurement and simulation is maximized, by minimizing this adjusted figure of merit:

$$\text{FOM}_{T_0} = \sum_i \sum_{t_j=0}^{25} |A_{i,s}(t_j) - A_{i,m}(t_j + t_s)|^2 \quad (2.4)$$

In contrast to the figure of merit in eq. 2.3 only the first 25 samples are used and the exponent is set to two (while $p \approx 0.3$ in eq. 2.3). With the such determined time shift the grid search is performed again, leading to (possibly) different interaction positions. This procedure is repeated until the algorithms converges or a maximum number of iterations is reached (typically four due to time constraints).

If multiple interactions occur in different segments of the detector it is a priori not clear, which part of the measured pulse shapes is caused by each individual interaction, because transient signals from one interaction can overlap with transient signals or the net charge signal from another interaction. It is not trivial to disentangle the individual contributions to the final measured signals. To reduce the needed computing time the following simplifying approach is used: The interaction position of the interaction with the highest energy deposition is determined by treating it as a single interaction. The signals from the other hit segments are excluded from the figure of merit calculation. The obtained best fitting simulation for this single interaction is then subtracted from the initially measured signals. The procedure is repeated with the 2nd highest energy deposition and so on. This approach simplifies the handling of multiple interactions drastically, although a systematic error is introduced which especially takes effect in the case of directly or diagonally neighboring hit segments.

It should be noted that, depending on the number of possible solutions, the problem of assigning an interaction position is mathematically underdetermined. This means that the parameter space is very large compared to the available information: A segment has about 1k grid points on a 2 mm grid, the number of possible combinations of interaction positions for two hits in one segment therefore is in the order of 10^6 , not taking the unknown ratio of energies into account. The variable T_0 (typically ± 5 ticks of 10 ns length) and multiple interactions in different segments increase the number of possible solutions even more. On the other hand there are only $6 \cdot 40 = 240$ non-trivial numbers, coming from the measured 40 samples (corresponding to 400 ns) of the hit segment, the core and the nearest neighbors. The number of measured samples with usable information is even smaller: Depending on interaction position the charge collection is finished within 150-350 ns and for interactions in the

front or back segments the transient signals of only three neighbors can be utilized.

Furthermore it was shown that, at sufficient high sampling rates, the PSA performance does not depend significantly on the rate of digitization. A down-sampling of 100 MHz to 50 MHz did not change the position resolution noticeably [44]. This means that the effective number of samples for fitting is even smaller.

Therefore it is necessary to reduce the complexity of the search algorithm by decreasing the number of possible solutions. One step in reducing the complexity of the problem is the already mentioned simplifications in the treatment of multiple interactions in different segments of a detector. A further simplification is achieved by assuming only single interactions within a segment. This assumption introduces a systematic error into the final PSA results. Two interactions inside a single segment are expected to be allocated as single interaction in between the two interactions. Therefore, an accumulation of hits in the center of the segment is qualitatively expected. Other algorithms, like the GRETINA signal decomposition and the "swarm search" do not use the assumption of single interactions within a segment, but have to cope with the large number of possible solutions. In the GRETINA signal decomposition so-called "penalty factors" had to be introduced which allow two-hit solutions only if a certain improvement in the figure of merit is achieved. Algorithms including multiple interactions per segment still have to prove their superiority compared with the adaptive grid search. Nevertheless, the assumption of single interactions per segment has to be kept in mind and future versions of the grid search should address this problem.

2.2 Data acquisition with AGATA

The process of data taking, starting from a certain number of interactions in one or more crystals and ending up with tracked γ rays including their respective energies and interaction positions, is best described via a flowchart, which is depicted in Fig. 4.

The measured signals are amplified by charge sensitive preamplifiers [45] [46] and sent to the front-end electronics where they are digitized at a rate of 100 MHz using 14 bit ADCs (analog-to-digital converter). A global clock running at 100 MHz generates a time stamp and distributes it to all digitizer modules. The pre-processing electronics identify which segments comprise an interaction and determine the deposited energies using a moving-window-deconvolution (MWD) algorithm [47] [48]. For more details on the electronics, see reference [10]. The data from the core and from the hit segments are sent to the "PSA farm", which consists of high-performance computers, where the interaction positions are determined. Optionally the traces are stored for later use. The events from individual detectors are connected via their time stamps in the event building using a $\pm 2.5\mu\text{s}$ (variable) time window. The linked events, consisting of interactions in the complete array, are then tracked and the information is stored in a ROOT tree for further analysis.

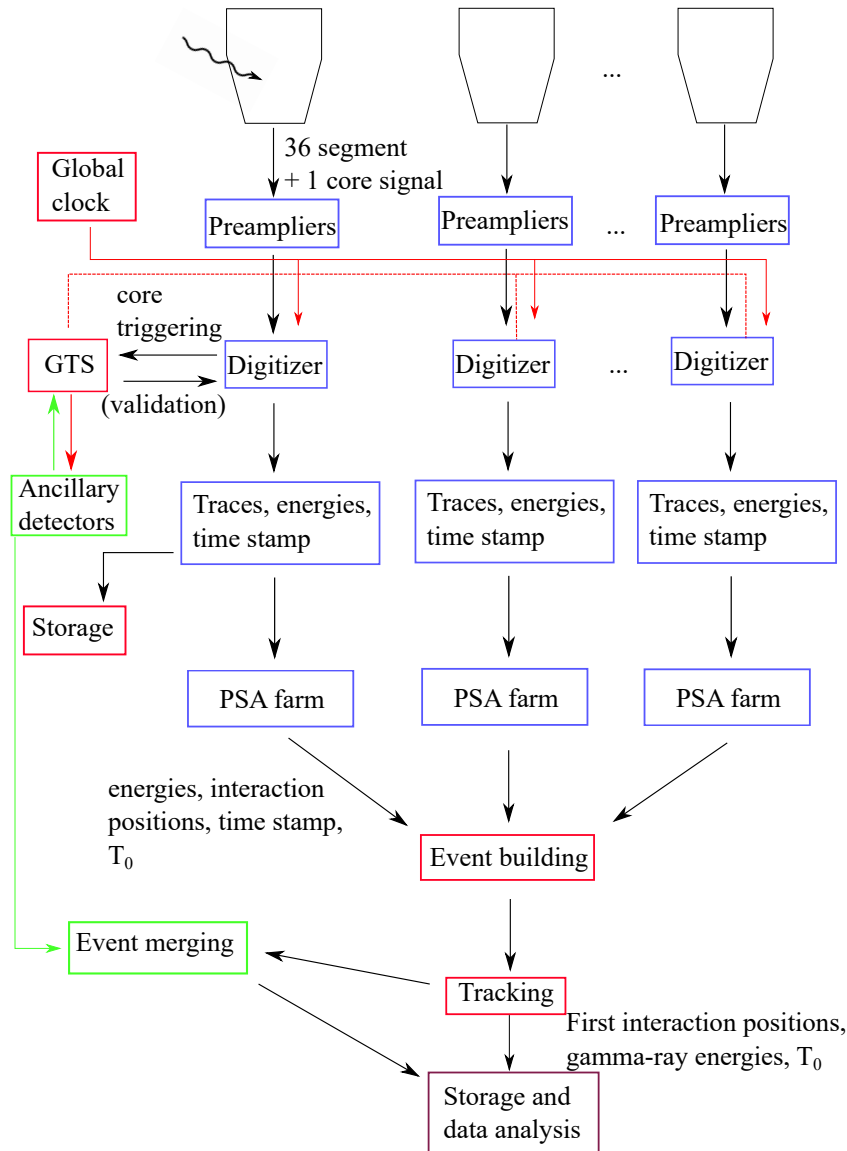


Figure 4: Flow chart of the AGATA data acquisition. The pre-amplified segment and core signals are digitized. The digitizer modules trigger on the core signal and determine the segment and core energies. The event is marked with a time stamp, which is distributed by a global clock. The digitizers also communicate with the Global-Triggering System (GTS), which can trigger the data taking of ancillary detectors. The trace data is sent to the PSA farm, where interaction positions and a more accurate T_0 are determined. Using the assigned time stamps, events including multiple crystals are built. The energies and positions of simultaneous interactions are used to track the γ rays. If ancillary detectors are present, their data is merged with the information of the tracked γ rays.

2.3 Results of the Pulse-Shape Analysis

The results of the PSA can be studied in several ways. The most obvious and most qualitative way is the inspection of the distribution of determined interaction positions. For simple geometries - e.g. when γ rays are emitted from the center of the sphere which is formed by the AGATA crystals

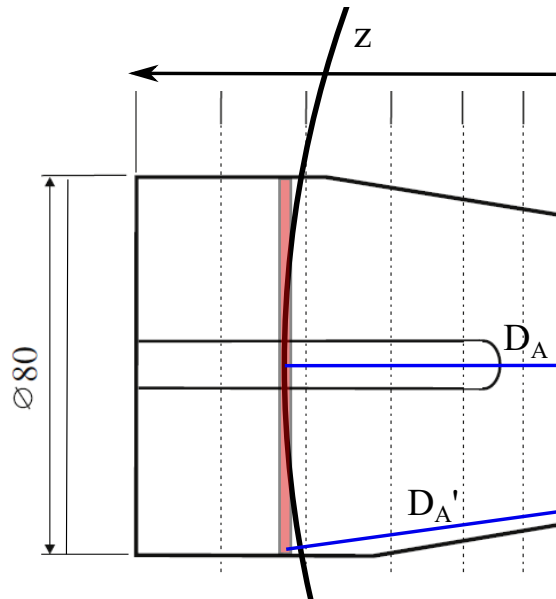


Figure 5: A schematic drawing of an AGATA crystal is shown. The section of the black circle marks the points which have the same distance to the source, which is placed at the center of AGATA. In good approximation grid points with a constant detector depth z have the same distance to the source (red marked area). The distances D_A and D_A' - which are relevant for absorption - are also equal in good approximation for γ rays emitted from the source. Therefore, within statistical fluctuations the same number of hits is expected for grid points with identical detector depth z .

- the expected distribution of hits is known. Disagreement of the found hit distributions with the expectation indicates a deviation of the physical interaction positions and the interaction positions found by the PSA. A more quantitative value is the achieved position resolution, which is not easy to extract. Finally, the results of the tracking depend on the PSA results. The quality of the Doppler correction, the tracking efficiency and the peak-to-total ratio give insight to the achieved performance. The results obtained with AGATA using ADL and the adaptive grid search will be discussed in the next sections.

2.3.1 Hit distributions

A source measurement was performed with AGATA at the Grand Accélérateur National d'Ions Lourds (GANIL) employing 29 AGATA crystals, set up in nine triple cluster and one double cluster detectors. A ^{60}Co source was placed in the center of the sphere formed by the AGATA crystals, such that the distance of the source to each crystal is equal and every crystal is facing directly towards the source. In this way the expected number of hits for a given detector depth z is approximately the same, which is illustrated and explained in Fig. 5. In this section the interaction positions obtained with ADL and the adaptive grid search are presented.

Hit distributions of the complete array (lab system) are shown in Fig. 6. Distributions for single crystals (crystal coordinate system, see Fig. 2), gated on different detector depths z , are shown for

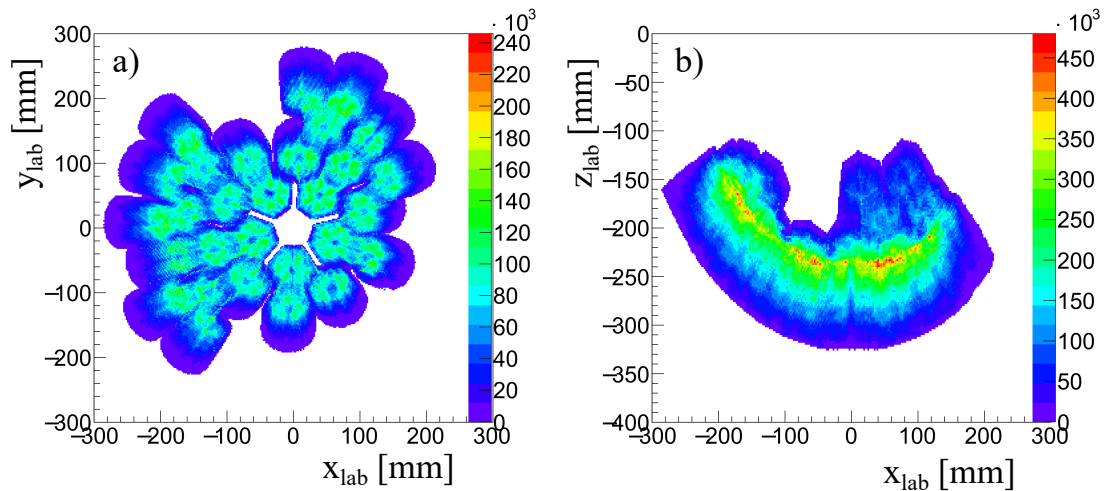


Figure 6: The a) front view (projection on $(x_{\text{lab}}, y_{\text{lab}})$ plane) and b) bottom view (projection on $(x_{\text{lab}}, z_{\text{lab}})$ plane) of the determined interaction positions is shown (no gates). The lab coordinate system is chosen such that the origin is in the center of the sphere formed by the AGATA crystals.

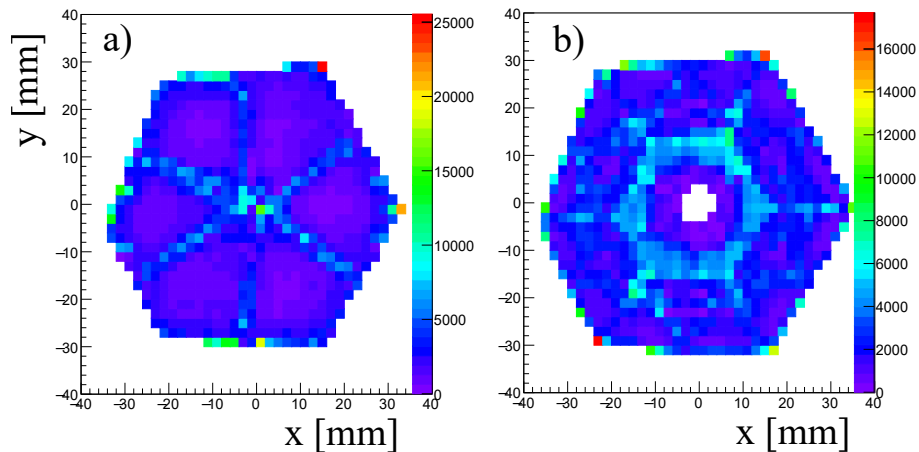


Figure 7: The distribution of hits of the ^{60}Co -source measurement for crystal A001 is shown for a) $z = 2 - 4$ mm and b) $z = 14 - 16$ mm. No further gates were set. A strong accumulation at the edge of the detector is observed. Certain grid points (red color) have up to ten times more statistics than comparable grid points in the center of the segment (see Fig. 1 a) for the segmentation of the crystal), which cannot be caused by statistical fluctuation. The distribution in a) has less hits in the segment centers and more at segment borders, while figure b) shows an accumulation of hits for intermediate radii. Note that there is a segment border in b) at a radius of $r \approx 20$ mm (see also Fig. 1 b) for details).

the front part of a crystal in Fig. 7 and for the back part in Fig. 8. A strong discrepancy between the expected homogeneous distribution with statistical fluctuation and the obtained hit distributions is observed.

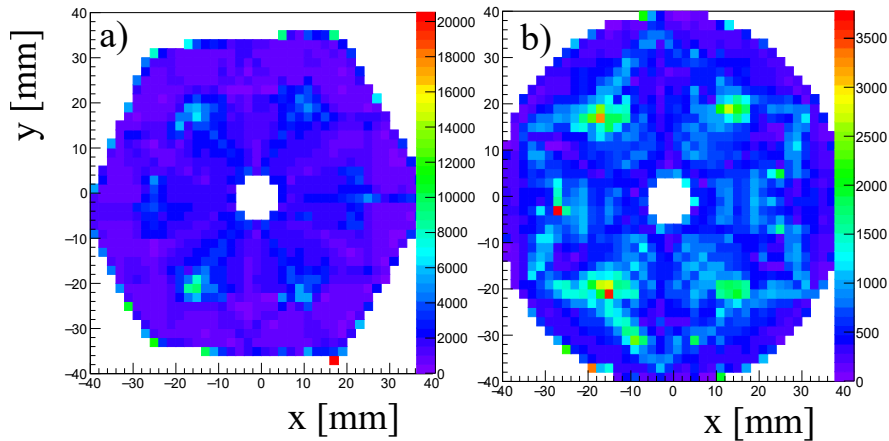


Figure 8: The distribution of hits for crystal A001 is shown for a) $z = 46 - 48$ mm and b) $z = 86 - 88$ mm. The distribution in a) corresponds to a part in the crystal, which can be approximated by a cylindrical geometry. Even with the less complex electrical field a surplus of hits in single grid points at the edge of the detector is observed. In contrast to Fig. 7 a) an accumulation of hits in the segment centers is seen. The plot in b) corresponds to the second last plane of grid points, at the very back of the crystal. The number of hits at the edge of the detector is strongly reduced, but several aggregations in the segment centers are observed.

The 2D histogram from Fig. 8 a) is plotted with additional gates on energy and multiplicity in Fig. 9: In picture a), where a gate on one hit segment in the crystal was set, an accumulation of hits in the lower right corner is observed. In relation to the number of hits in the complete histogram more hits are found in this lower right corner, compared to the histogram without gates in Fig. 8 a). The gates on energy depositions above 400 keV in b) and below 100 keV in c) reveal the strong energy dependence of the PSA performance. In b) still a clustering of hits in the segment centers is observed. However, only a small surplus of hits is seen in the lower right corner. The opposite is the case for low energy interactions in c).

The deviation of the obtained distributions from a flat distribution with statistical fluctuations becomes especially apparent when transforming the found hit distribution into a surface plot, which is shown in Fig. 10.

An overview of slices with identical z for all crystals reveals a very similar behavior, especially for identical crystal types A, B and C, see Fig. 11 and 12. The observed distribution of hits and the deviation from the expectation are generally very similar for all crystals. Most of the plots shown in this section depict crystal A001 for the easier comparison with the segmentation shown in Fig. 1.

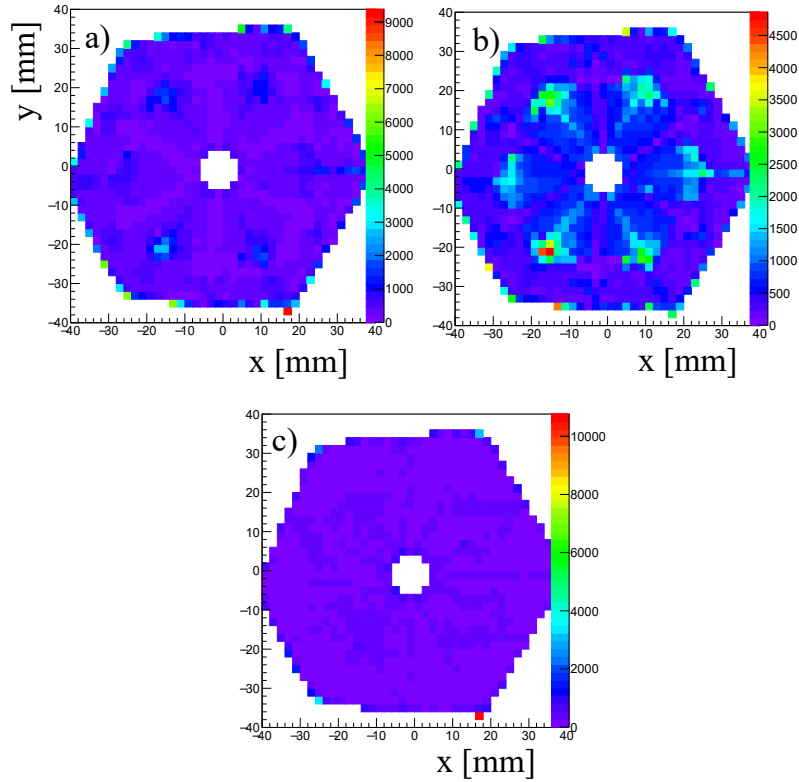


Figure 9: The distribution of hits for crystal A001 is shown for $z = 46 - 48$ mm (corresponding to picture a) in Fig. 8). It is plotted with an additional gate on either a) exactly one triggered segment, b) $E_\gamma > 400$ keV and c) $E_\gamma < 100$ keV. The original plot consists of $1.87 \cdot 10^6$ individual interactions, the gated spectra comprise of a) 28.7% b) 36.4 % and c) 15.2% of the statistics. For more details see text.

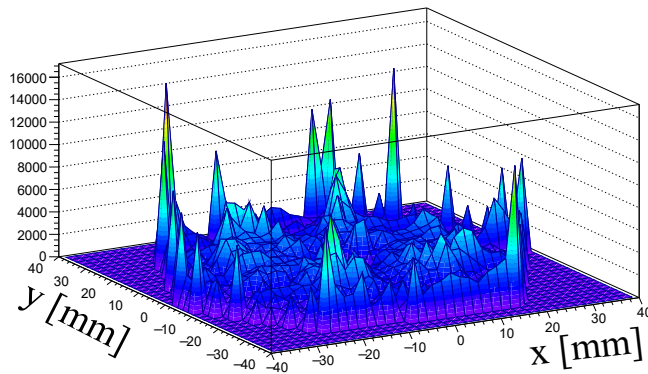


Figure 10: A surface plot of crystal A001 at $z = 26 - 28$ mm is shown (no additional gates). The height corresponds to the number of hits per grid point. The different heights of single peaks and the rest of the surface illustrates the large deviation of the number of hits allocated to the individual interaction positions, which differ by up to a factor of 10. The average number of counts per grid point is 2350 and the standard deviation is 1545 counts.

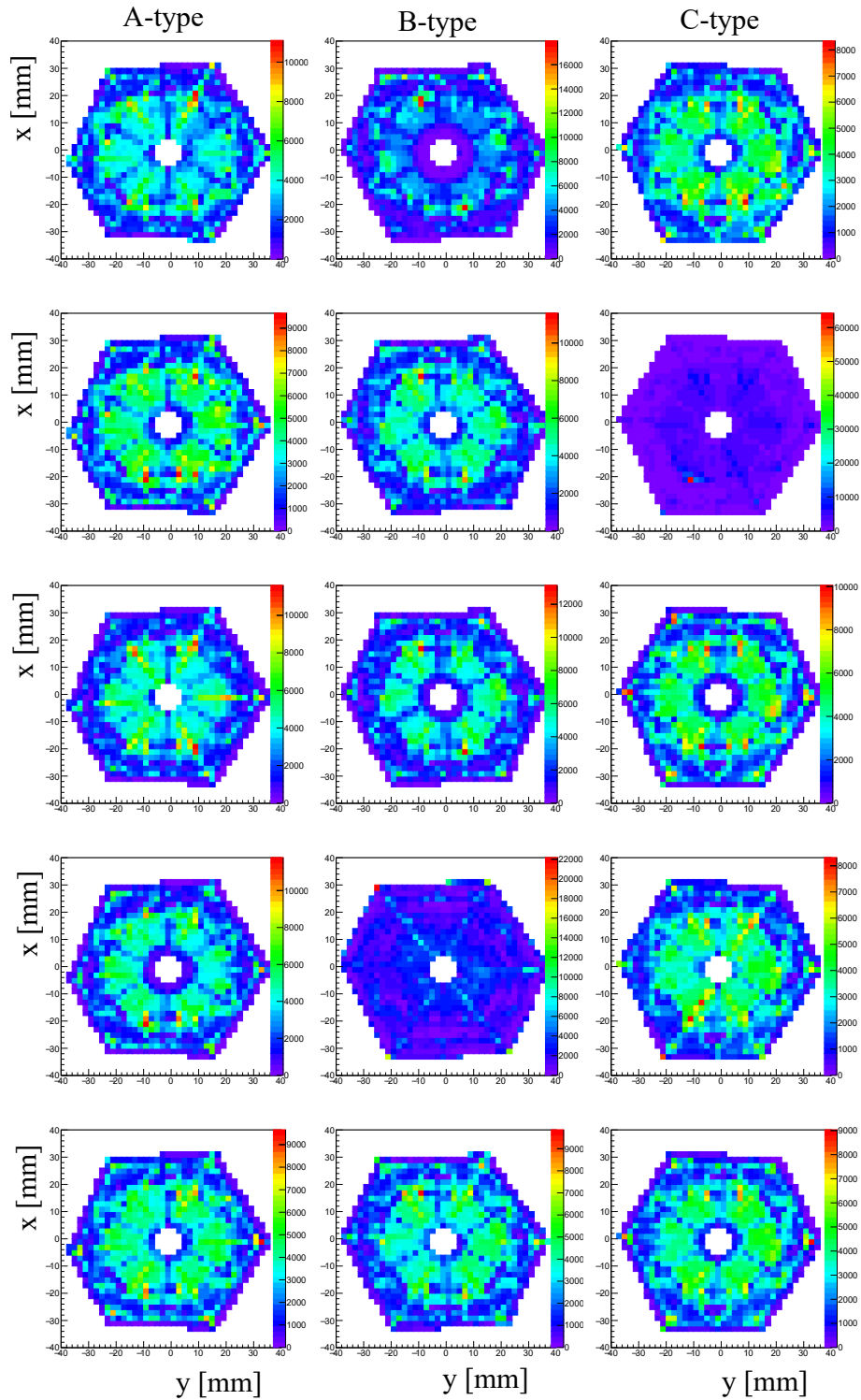


Figure 11: An overview of the first 15 crystals is shown. All hits at detector depth $z = 20 - 22$ mm are plotted. The distributions are sorted by their corresponding crystal type (A, B, C). A very similar behavior in all distributions is observed, which indicates that potential problems with the PSA are not related to single crystals. One exception is the C type-crystal in the second row (C012). Here the number of hits in the grid point with highest statistics is a factor ~ 7 larger than in the other C type-plots. This crystal had a missing segment, which might explain the poor performance.

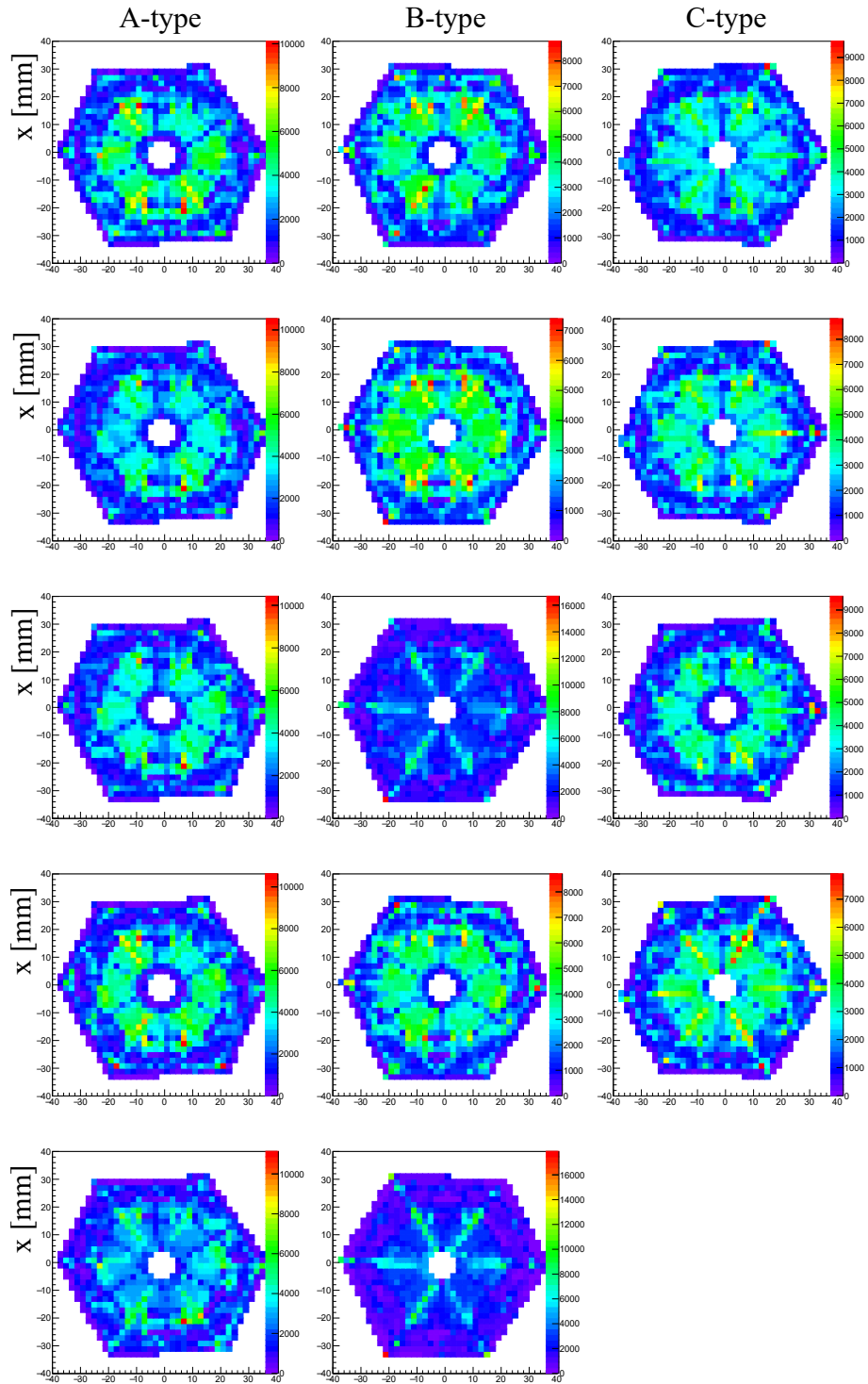


Figure 12: An overview of crystals 16-29 is shown at a detector depth $z = 20 - 22$ mm (same gate as Fig. 11). With some fluctuation a similar pattern is observed for all crystals.

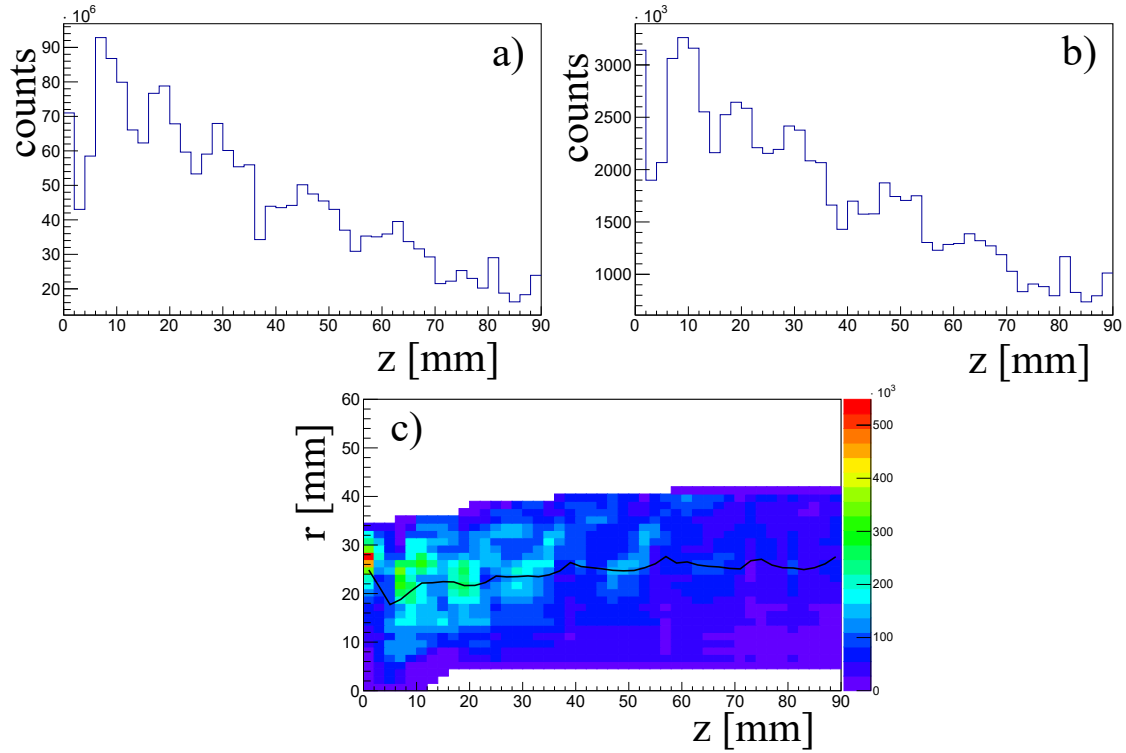


Figure 13: The number of hits in dependence of the detector depth z is shown for a) all hits and b) for crystal A001. In first approximation an exponential decrease due to absorption and a $\propto \frac{1}{z^2}$ dependence (solid angle coverage) is expected. A significant deviation from this expectation is observed, especially in the first few millimeters of the crystal. The correlation of the detector depth z and the radius $r = \sqrt{x^2 + y^2}$ is shown in c). The black line marks the mean determined radius at the given detector depth. At the front of the crystal and near segment boundaries an unexpected variation of the mean radius is observed.

The number of hits in dependence of the detector depth z is depicted for a single detector and for all detectors in Fig. 13. The cylindrical radius $r = \sqrt{x^2 + y^2}$ in dependence of the detector depth z reveals an unexpected allocation of hits, see also Fig. 13.

It should be noted that the perceived distribution of hits depends on the choice of the depiction. The color code assigns a color to a given number of hits of a grid point. This is demonstrated in Fig. 14 and 15. It is necessary to choose an identical color code when comparing hit distributions before and after a change to the PSA.

An inspection of the distribution of hits yields only a qualitative impression of the PSA performance. A quantitative analysis of the hit distributions is given in section 4.2. Other quantities which are suited to describe the PSA performance are discussed in the next sections and in the later parts of this thesis.

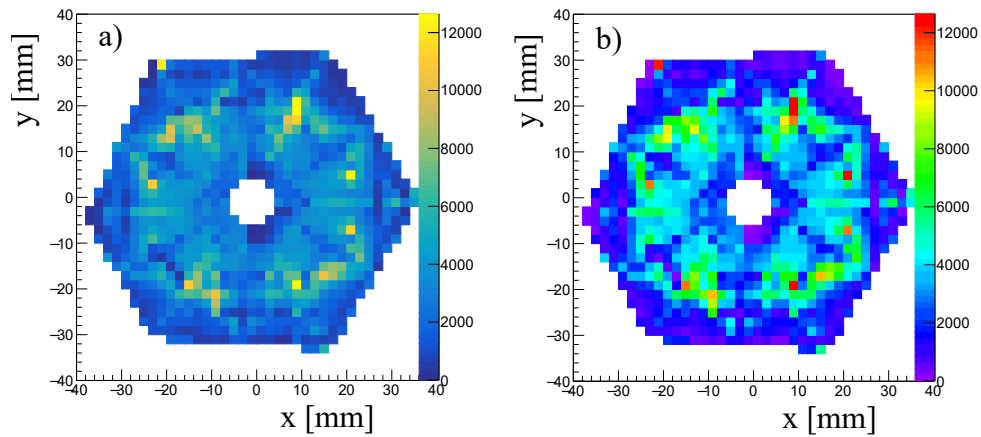


Figure 14: The distribution of hits is shown for $z = 18 - 20$ mm. The identical distributions in a) and b) use different color codes. The two depictions highlight different aspects of the distributions. For example, the distribution in b) is seemingly more clustered, while the distribution in a) seems to be more homogeneous. However, both figures depict the same measured data set.

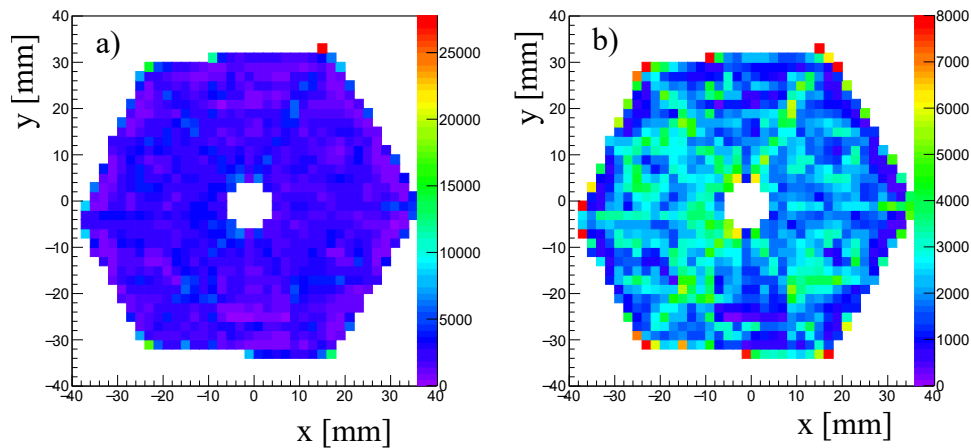


Figure 15: The distribution of hits is shown for $z = 24 - 26$ mm in both distributions a) and b). An allocation of hits in the upper right corner is observed in a). In b) the same distribution is shown, but the data was cut off at 8000 hits. This means, the red color in the depiction corresponds to 8000 or more hits in the respective grid point. A clustering of hits and the segment structure is visible in b), which is not observed in a). This is caused by the different color code in a) which includes the outliers and blurs the rest of the image, which is seemingly homogeneous. This effect has to be accounted for when comparing distributions with and without outliers.

2.3.2 Position resolution

The PSA performance and the achieved position resolution was investigated in several works [49] [50] [51]: One approach is the use of in-beam data, where the energy resolution of a Doppler corrected peak is considered. Here the γ ray is emitted from a nucleus which is moving at a given velocity. Depending on the angle between velocity of the nucleus and direction of the emitted γ ray, the energy of the γ ray is Doppler shifted. The correction of this Doppler shift depends on the correct measurement of this angle and therefore on the determined interaction positions. GEANT 4 simulations of the in-beam data including an uncertainty of the determined interaction positions could reproduce the measured Doppler corrected peaks. The position uncertainty was assumed to be Gaussian. A FWHM of 5.1 mm at 1382 keV (all multiplicities) and 3.8 mm for single interactions was obtained by Recchia et al. [49]. Another work by Söderström et al. determined the energy dependence of the position resolution, which ranges from 8.5 mm at 250 keV up to 4 mm at 1.5 MeV [50].

A different approach by Klupp et. al utilized the 180° coincidences from e^+e^- annihilation of ^{22}Na [51]. The found coincidences were compared with simulations including a position uncertainty. A position resolution of 5.4 mm FWHM ($\sigma = 2.3$ mm) was obtained. The results of Klupp et al. also showed that a better fit of measurement and simulation is achieved by assuming a non-Gaussian smearing of the interaction positions. A Laplace distribution (which has a sharper peak and longer tails than a Gaussian) with $\sigma = 1.8$ mm yielded best agreement of simulation and measurement.

Within this thesis a ^{22}Na measurement was utilized to estimate the position resolution, which is described in section 4.1.2.

3 Comparison of Measured and Simulated Pulses

In this chapter a detailed comparison of measured and simulated detector signals will be presented. In particular, systematic deviations of measurement and best fitting simulation are of interest because they indicate underlying problems of the PSA and may give hints to a solution. To find the best fit of measurement and simulation a figure of merit is used. Its impact on the PSA results is investigated. The charge collection times of measured pulse shapes and best fitting simulations are determined and compared. Finally, the dependence of the starting time T_0 on the interaction position is discussed. Some of the systematic deviations of measurement and simulation motivated an inspection of specific input parameters. These investigations are presented in chapter 4.3.

3.1 Super trace, residuals and figure of merit

In this section a comparison of simulated and measured pulse shapes is presented. For a quick overview of all signals that belong to one event a so called super trace is plotted. In a super trace the signals of all preamplifiers are plotted consecutively starting with segment A1 up to segment F6. The last pulse shape belongs to the core. Each of the 37 signals depicts the measured pulse shape in the first 600 ns after the interaction. Such a super trace is shown in Fig. 16. The corresponding best fitting simulated super trace and the residuum are plotted as well. The pulse height is proportional to the energy of the interaction. With a proper energy calibration, the maximum pulse height corresponds to the energy deposited by the γ ray. Therefore, the pulse height is typically given in keV. The best fit of simulation and measurement is determined by minimizing the following figure of merit:

$$\text{Figure of Merit} = \sum_i \sum_{t_j} |A_{i,s}(t_j) - A_{i,m}(t_j)|^p \quad (3.1)$$

With $A_{i,s/m}(t_j)$ being the simulated (s) or measured (m) pulse height of segment i at time index t_j . The different residuals of the squared difference and the figure of merit depicted in Fig. 16 demonstrate how the chosen exponent p in eq. 3.1 affects the result of the fitting procedure. Very small values of p are not expedient because the difference of measurement and simulation converges to 1 and the figure of merit becomes constant. Large values of p cause the final figure of merit to be largely dominated by single large deviations of measurement and simulation. Several investigations [52] [53] showed that a relative small value of $p \approx 0.3$ to 0.4 yields the best PSA performance. The influence of different exponents p in the figure of merit calculation on the PSA results was investigated and more details are given in section 4.3.2.

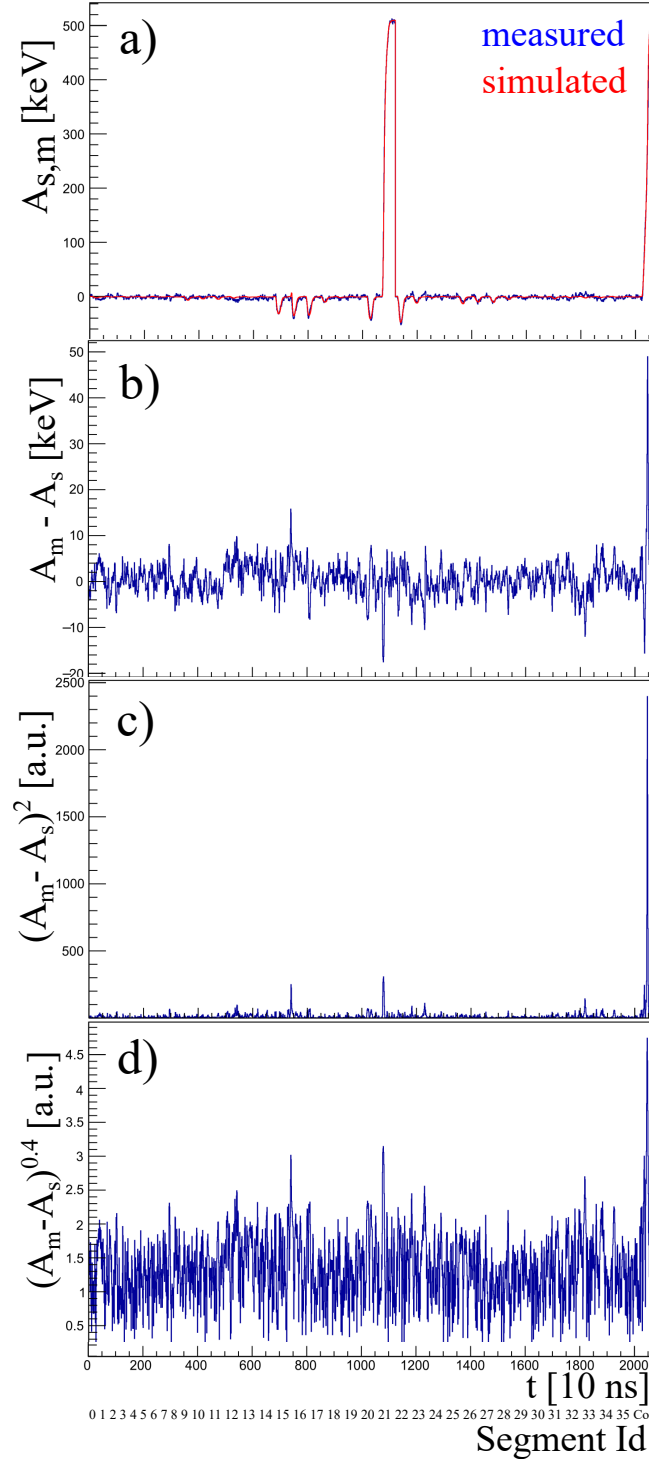


Figure 16: The super trace (see text) is plotted for one exemplary event. Figure a) shows the measured preamplifier signals A_m and the corresponding best fitting simulation A_s (using $p = 0.4$). The net charge signal in segment 21 (D3), the transient signals of the neighboring segments and the core signal is used for the comparison. The residual in b) depicts the differences of measurement and simulation. Figures c) and d) illustrate how the exponent p in the term $|A_{i,s}(t_j) - A_{i,m}(t_j)|^p$ has an impact on the figure of merit calculation. In general, different simulated pulse shapes minimize the figure of merit when using different values of p .

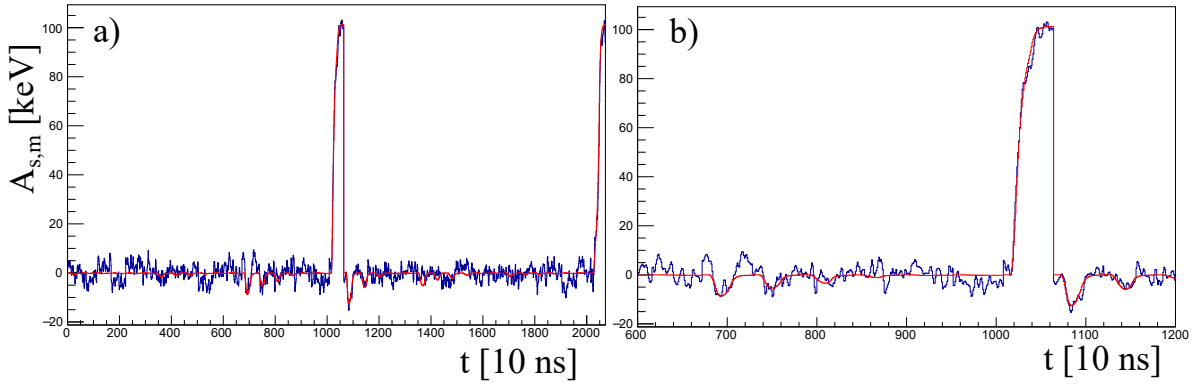


Figure 17: The super trace for a low-energy interaction is shown in a). Even though the signal-to-noise ratio is small the matching of the simulation is convincing. The zoom in b) shows how the small transient signals, which have a size in the order of the noise level, are identified.

The super trace for an interaction with relatively low energy is shown in Fig. 17. The small signal-to-noise ratio decreases the reliability of the PSA results. Certain details of the pulse shape, which are characteristic for the interaction position, can not be distinguished from noise. In particular, it is challenging to identify the small transient signals properly. It was shown that the position resolution decreases for lower energies [50].

3.2 Figure of merit landscape

A detailed investigation of the results of the grid search was performed on an event-by-event basis (see section 2.1.2.1 for more details on the working principle of the grid-search algorithm). The figure of merit was extracted for all interaction positions which were tested by the grid search and visualized for single events. The extraction of the different figure of merit values is not foreseen in the adaptive grid search for computational reasons. The code was adapted accordingly: The relevant information, such as the position of the grid point and the corresponding figure of merit value, were written to an ASCII file. A C++ sorting tool was written to analyze the produced data.

To get a full picture of the figure of merit landscape the grid search was performed as a full search on the fine grid, instead of the adaptive version. The results for one exemplary event are shown in Fig. 18. The hit segment was C6, the energy of the interaction was 744 keV and no other segments were hit. A strong change of the figure of merit in radial direction is observed. This shows that the PSA can determine the radial position with high precision. In contrast to that the figure of merit changes only slightly when moving in angular direction (the terms angle and radius are used as in a cylindrical coordinate system, see Fig. 2). The change of the figure of merit is also relatively small along the z axis. For better comparability all plots use the same color code.

The large amplitude pulses of the hit segment and of the core provide a characteristic signal depending on the radius of the interaction, caused by the different charge collection times of electrons and holes.

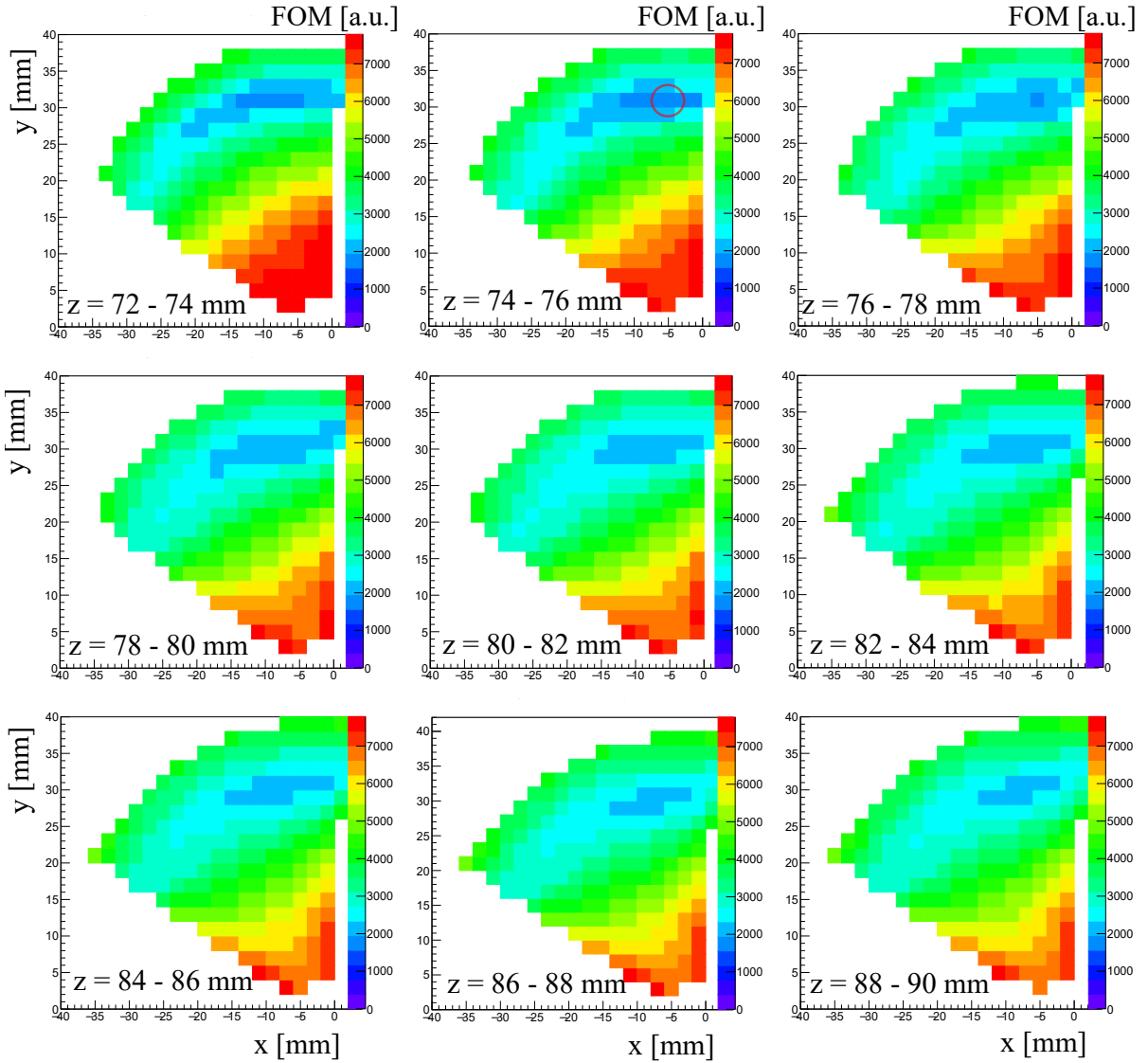


Figure 18: The figure of merit evaluated by the grid search for all possible interaction positions is shown for **one** exemplary event (the color code depicts the figure of merit value). The determined interaction position with the smallest figure of merit at $z = 74 - 76$ mm is marked with a circle. The change of the figure of merit in radial direction is larger compared to the change along the angular position as well as along the z axis.

On the other hand the angular and z position of the interaction is (mostly) determined by the small amplitude pulses of the neighboring segments. Therefore, the grid search algorithm was adjusted by implementing a weighting coefficient in the figure of merit calculation to amplify the proportion of the transient signals compared to the relatively large signals of hit segment and core. The adjusted figure of merit is:

$$\text{Figure of Merit} = \sum_i w_i \sum_{t_j} |A_{i,s}(t_j) - A_{i,m}(t_j)|^p \quad (3.2)$$

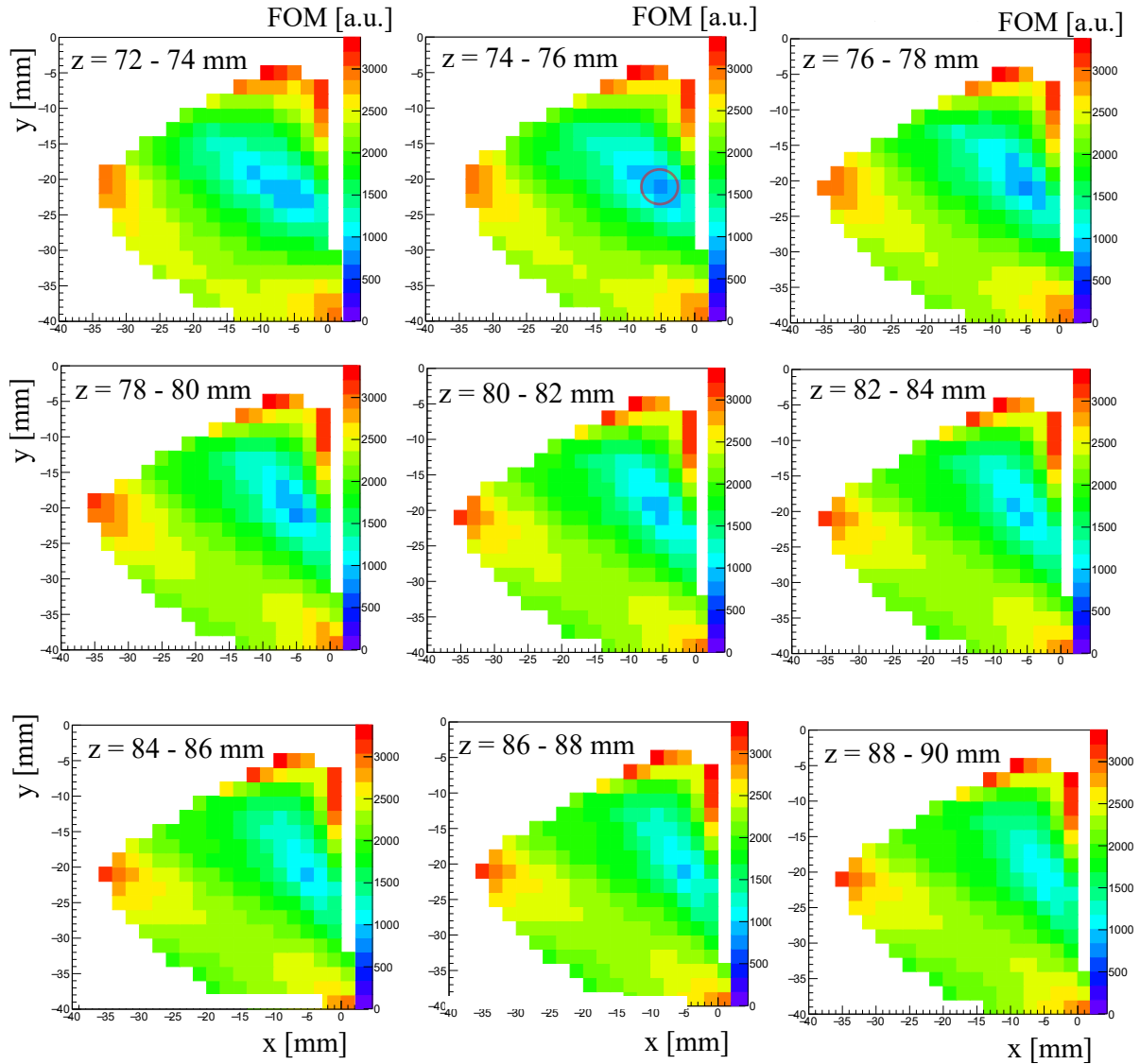


Figure 19: The figure of merit landscape is shown after a weighting of the transient signals was introduced in the grid search. The figure of merit minimum is more distinct, which indicates a better position resolution.

In contrast to the typically used figure of merit (see eq. 3.1) a weighting coefficient w_i was included. It was set to one if the index i corresponded to the hit segment or the core and to five for the nearest neighbors. Next nearest neighbors were not considered.

The impact on the grid search is visualized in Fig. 19. The energy of the interaction was 550 keV and the hit segment was E6. For technical reasons a different event was used. A more distinct minimum around the interaction position can be found, not only in radial direction but also concerning the angular position. This implies (in a very qualitative way) that the angular resolution can be improved by employing a weighted figure of merit. This is partly also true for the z position of the interaction. The impact of the transient weighting on the PSA performance was investigated in a more quantitative

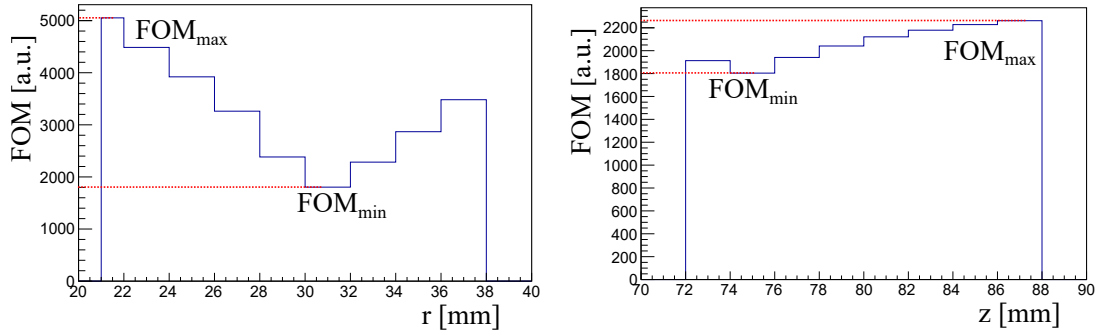


Figure 20: The figure of merit is shown for different radii and z positions, corresponding to the event depicted in Fig. 18. A distinct minimum along the radial direction is observed whereas the minimum along the z axis is rather shallow. The minimal and maximal figure of merit values FOM_{\min} and FOM_{\max} along the respective axes are marked. The ratio of minimal and maximal figure of merit is a quantity which indicates the reliability of the determined interaction position.

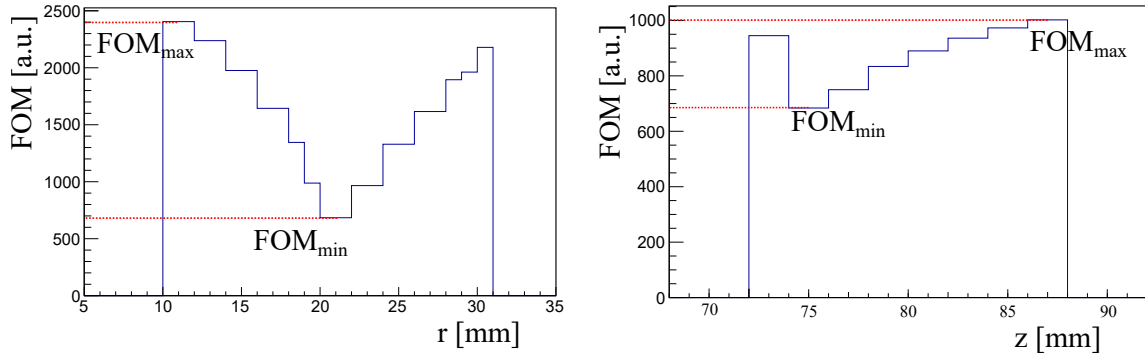


Figure 21: The z and r dependence of the figure of merit is shown. The figure of merit values correspond to the event shown in Fig. 19, for which the weighting was applied. The minima along the r and z -axes are more pronounced which most likely corresponds to a better PSA result. The minimal and maximal figure of merit values along the respective axes are marked.

way and an optimal weighting coefficient was extracted. These results are presented later on in section 4.3.1.

For a better overview and comparison, the figure of merit values along the r - and z -axis were plotted for both events in Fig. 20 and 21. For both events a distinct minimum with respect to the radius can be found. The minimum with respect to the z axis is less pronounced in comparison.

The ratio of the minimal and maximal figure of merit FOM_{\min}/FOM_{\max} along a certain axis can be used to assess the reliability of the determined interaction position. A large ratio corresponds to a shallow minimum and a presumably imprecise PSA result and vice versa. This ratio was extracted on an event-by-event basis for the r and z axis and is plotted for about 10 k events in Fig. 22.

The average ratio FOM_{\min}/FOM_{\max} for the radial direction (Fig. 22 a)) is 0.56. Events with a very similar minimal and maximal figure of merit (with a ratio near 1) occur only rarely, which shows the high sensitivity with respect to the radial position of the interaction. The same distribution for the z axis is

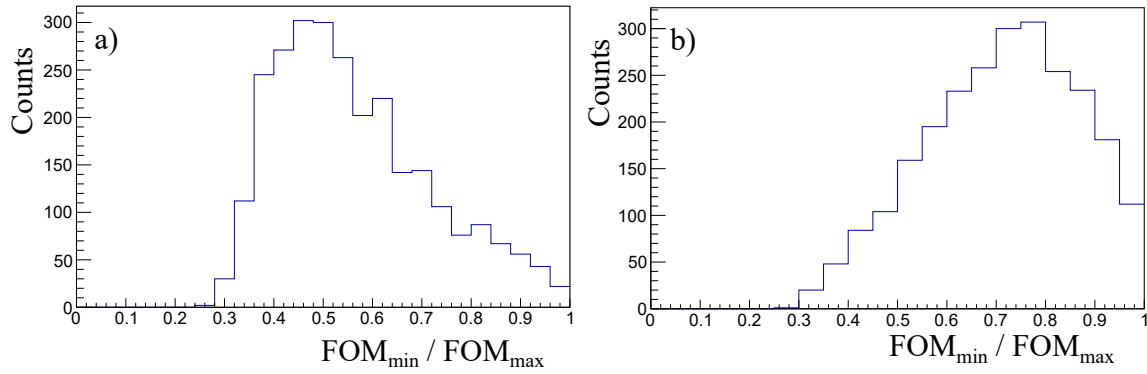


Figure 22: The ratio of minimal and maximal figure of merit is shown either along a) the radial direction or b) the z axis. Values close to 1 correspond to a very shallow minimum and a less precise PSA result. The radial position is better resolved than the z coordinate.

shown in the second plot marked as b). The higher mean of 0.71 and the large number of events with a ratio close to 1 illustrate, that it is more difficult to resolve the z position. The higher ratios of minimal and maximal figure of merit along the z axis is also caused by the fact that the length of the segments of 30 to 40 mm is much larger than the depth of the segments of 8, 13, 15 and 3×18 mm (from front to back).

The investigation of the position dependency of the figure of merit shows that no local minima are present and that there is only one global minimum when employing the standard FOM. This finding excludes choosing the "wrong" minimum as a cause of error.

The ratio of minimal and maximal figure of merit is also correlated with the energy of the interaction. This is caused by the lower signal-to-noise ratio at small energies and is depicted in Fig. 23 a). The ratio (which is also an inverse measure for the performance of the PSA) drops with increasing energy. In a first approximation this can be described by an exponential function of the form $a_0 + a_1 \cdot e^{a_2 E}$. Fig. 23 b) shows the the mean ratio and its error for a given energy in steps of 1 keV. The fit (red line) provides the following results:

$$a_0 = 0.437 \pm 0.003, \quad a_1 = 0.496 \pm 0.011, \quad a_2 = -0.0094 \pm 0.0004 \cdot \frac{1}{\text{keV}} \quad (3.3)$$

The decisive information lies within the parameter a_2 or the inverse of this parameter: $1/a_2 \approx -107$ keV. This means that the PSA performance increases for higher energies but after a few hundred keV the effect saturates. These results coincide with findings from previous investigations, where the final figure of merit of each event was normalized to the energy and used as a measure for the PSA performance. It was plotted versus the energy of the interaction as shown in Fig. 24 [53].

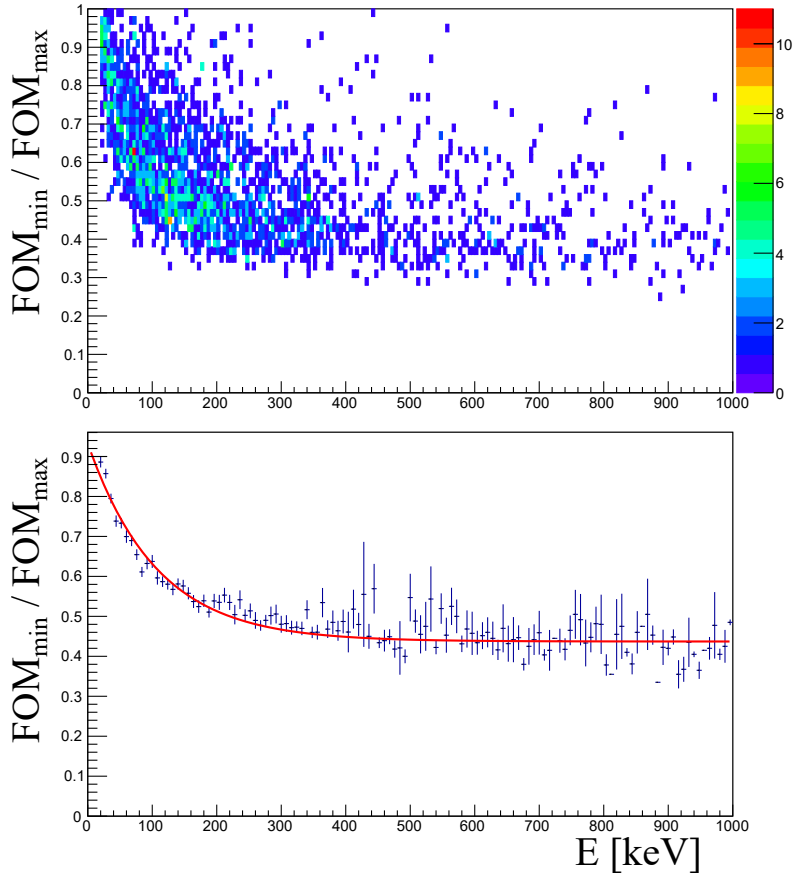


Figure 23: The correlation of the ratio of minimal and maximal figure of merit (with respect to the radius) with the energy of the interaction is shown. Large ratios close to 1 mostly correspond to low energy interactions which are more difficult to resolve for the PSA. The bottom picture shows that this dependence follows an exponential behavior.

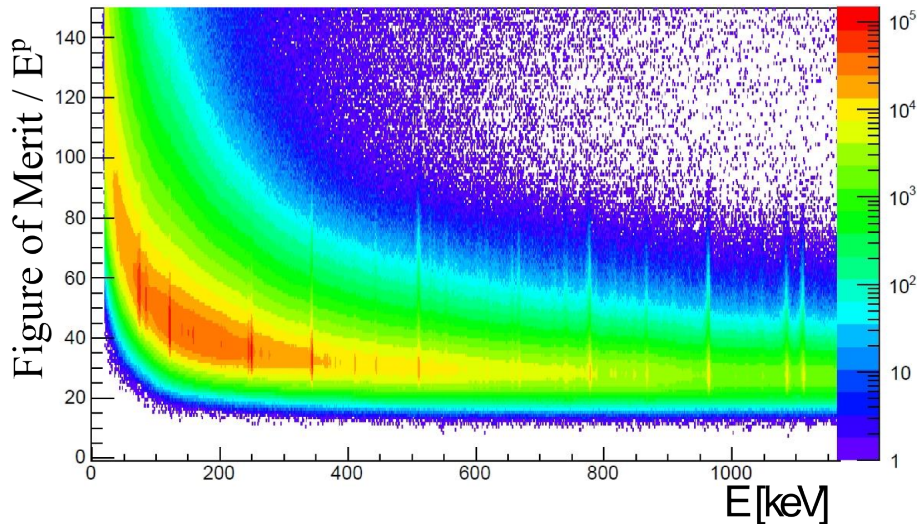


Figure 24: The final (minimal) figure of merit of each event was normalized to E^p with $p = 0.6$ being the exponent from eq. 3.1. This value describes the matching of measurement and best fitting simulation and can therefore be used as a measure for the PSA performance. The result is very similar to the one shown in Fig. 23. Adapted from [53].

3.3 Time dependent difference of measurement and simulation

In a complementary step the difference of measurement and simulation was investigated in the time frame. For this, the difference $(A_s(t) - A_m(t))/E$ for $t = 0 - 400$ ns was inspected. The core, the hit segment and the transient signals were treated separately. Events with only one triggered segment per crystal were selected and all interactions were restricted to ring three of the detector. In this part of the germanium crystal the electric field can be assumed to be radial in a first approximation. In this case the radius r (minus the radius of the core drilling) corresponds to the drift length of the electrons to the central electrode.

The results are given for seven different radii, starting at $5 \text{ mm} < r < 10 \text{ mm}$ up to $35 \text{ mm} < r < 40 \text{ mm}$. Events were sorted according to the interaction positions determined by the PSA. The results are shown for the core in Fig. 25, for the hit segment in Fig. 26 and for the transient signals in Fig. 27. For the measured and simulated signals of the core and the hit segment systematic deviations are observed at specific times during the charge collection.

In the first few ticks at $t < 50$ ns, marked as i), the simulation systematically overestimates the measurement for interactions at small (core) and large (hit segment) radii. In a subsequent analysis the time alignment, that is performed by the grid search algorithm, was scrutinized. The mean value of $A_s(t) - A_m(t)$ for the first 50 ns was plotted versus the time shift that minimized the figure of merit in Fig. 28 (during the grid search the figure of merit is not only minimized with respect to the interaction position, but also with respect to a time shift. For more details on T_0 determination during the grid search, see section 2.1.2.1). A small systematic correlation is observed. Negative time shifts, corresponding to shifting the measured signal to the left, correlate with a small overestimation of the measurement by the simulation. The systematic deviations observed in region i) therefore might be caused by the T_0 determination.

A second region of interest, marked as ii), shows a systematic deviation of measurement and simulation at specific times. The time interval at which these deviations appear is clearly correlated with the radius of the interaction. In Fig. 26 the simulated signals of the hit segment at small radii and large times, marked as ii a), underestimate the measurement. The overall disagreement of simulation and measurement in this region is also increased. Subsequently this region of increased disagreement moves back in time when going to higher radii (ii b-e)). At $r < 30$ mm it is no longer observed.

This behavior suggests that the observed deviations correlate with the finished charge collection of the holes and that this point in time is not well reproduced by the simulation. At large radii the holes, which move to the outer electrode, are collected nearly instantly. There these deviations are not observed.

A similar observation can be made for the pulse shapes of the core in Fig. 25. Here the opposite behavior is seen as the simulation overestimates the measurement for large radii and large times (ii d)). For smaller radii the increased deviation of measurement and simulation is observed at earlier times (ii a-c)). This suggests that the discrepancy of measurement and simulation is correlated with the finished charge collection of the electrons.

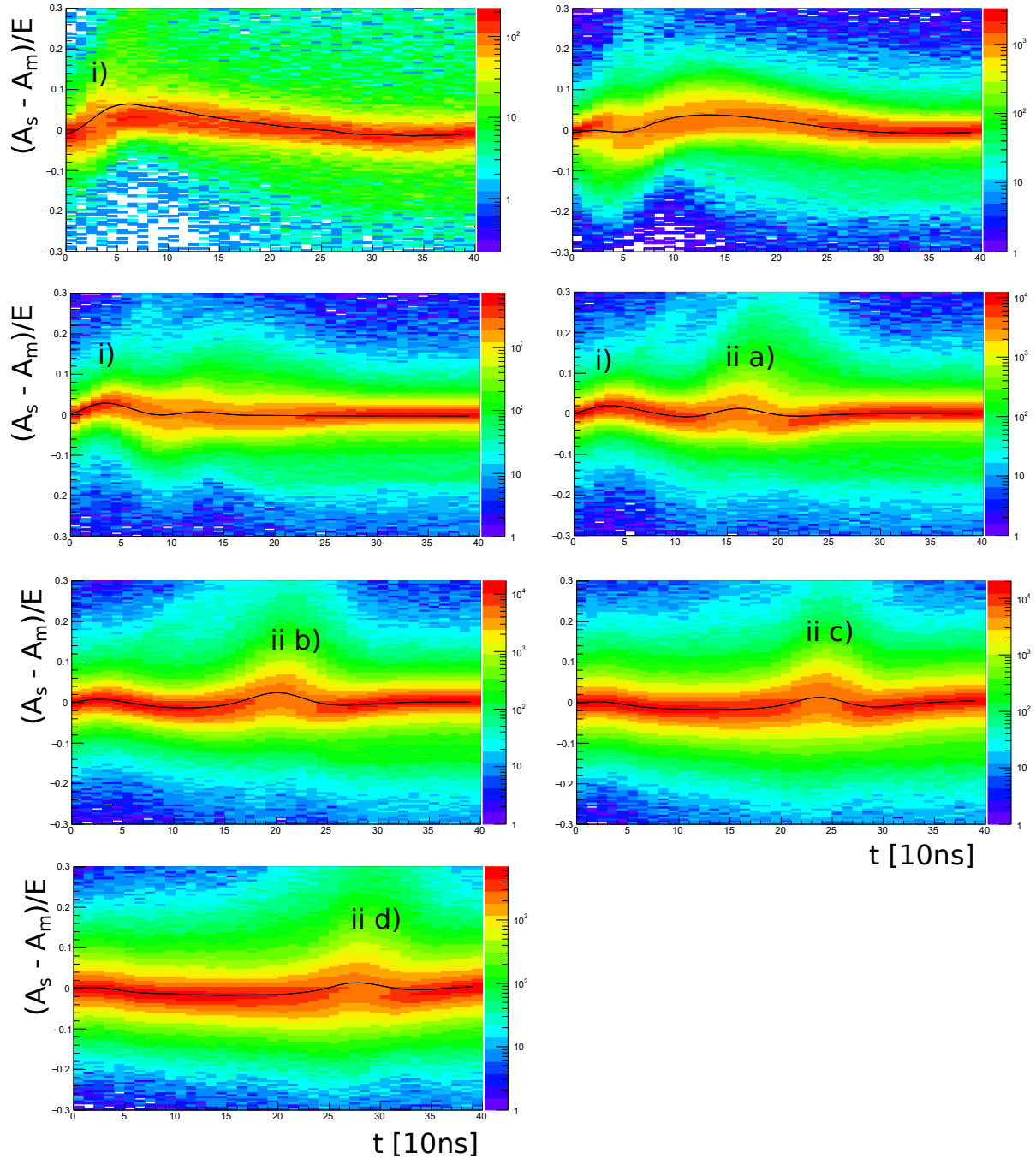


Figure 25: The difference of measured $A_m(t)$ and simulated $A_s(t)$ pulses, normalized to the energy of the interaction, is shown for the core signal for the first 400 ns. The traces are sorted by the radius of the interaction determined by the PSA, starting at $r = 5 - 10$ mm in the top left up to $r = 35 - 40$ mm in the last picture. To guide the eye a black line marks the mean value of $(A_s(t) - A_m(t))/E$ at the given time t . Several regions of interest are marked i), ii a-d), iii). For more details see text.

Another radius/time dependent systematic deviation of measurement and simulation, marked as region iii), is observed. In contrast to to region i) and ii) the relative difference of measurement and simulation is rather large but only a small subset of events seems to be affected. Note that the scale

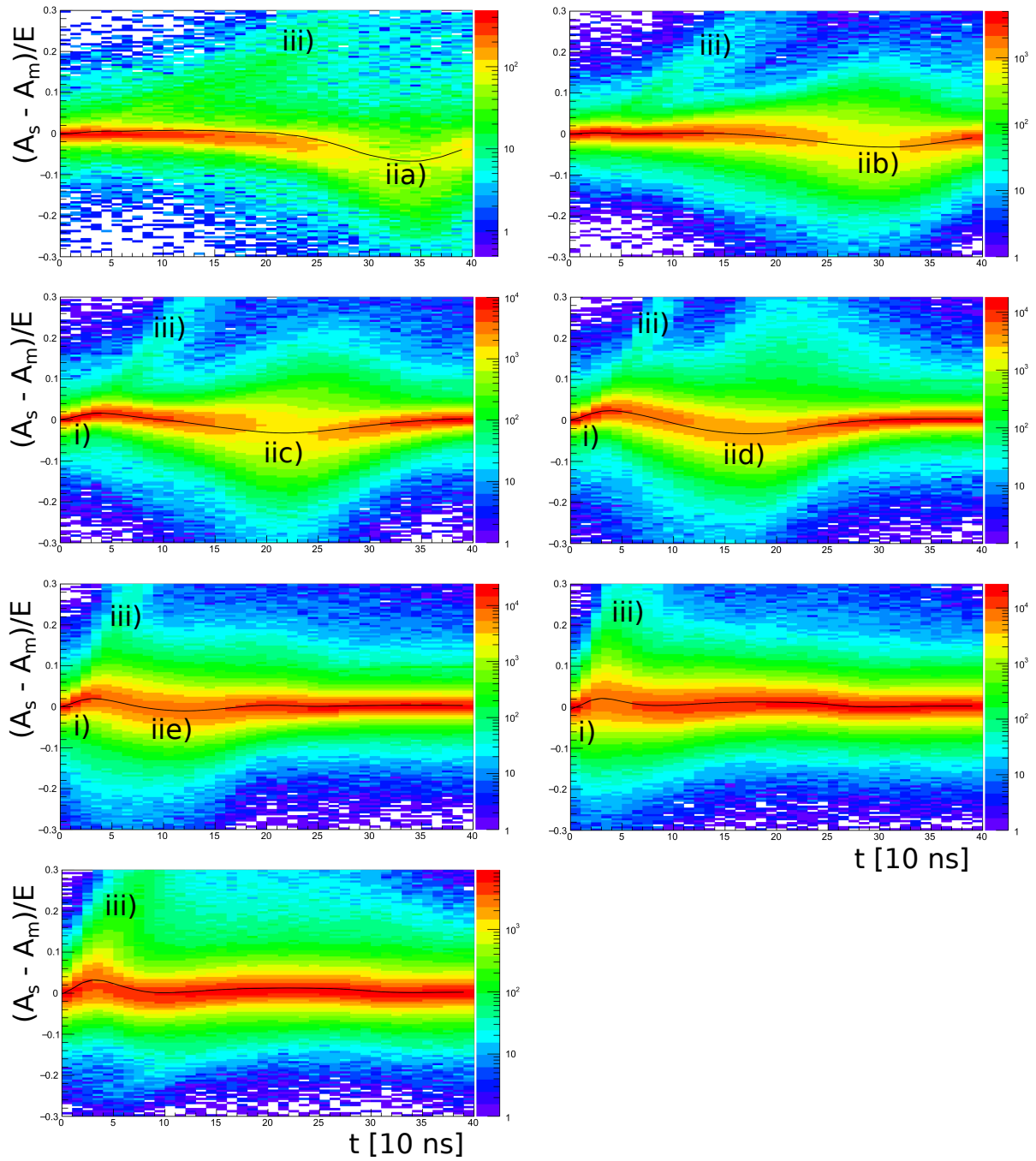


Figure 26: The difference $(A_s(t) - A_m(t))/E$ (as in Fig. 25) is shown for the hit segment. A mirrored behavior compared to the core signals is observed. The overestimation of the measurement by the simulation in the first few ticks i) is observed for large radii. This behavior is seen for small radii for the core signals from Fig. 25. A similar mirrored behavior is observed for the region marked as iia-e).

is logarithmic and the bin content is reduced by two to three orders of magnitude compared to the majority of points around zero.

The 2D histograms shown in Fig. 25, 26, and 27 were projected onto the y axis. From these 1D

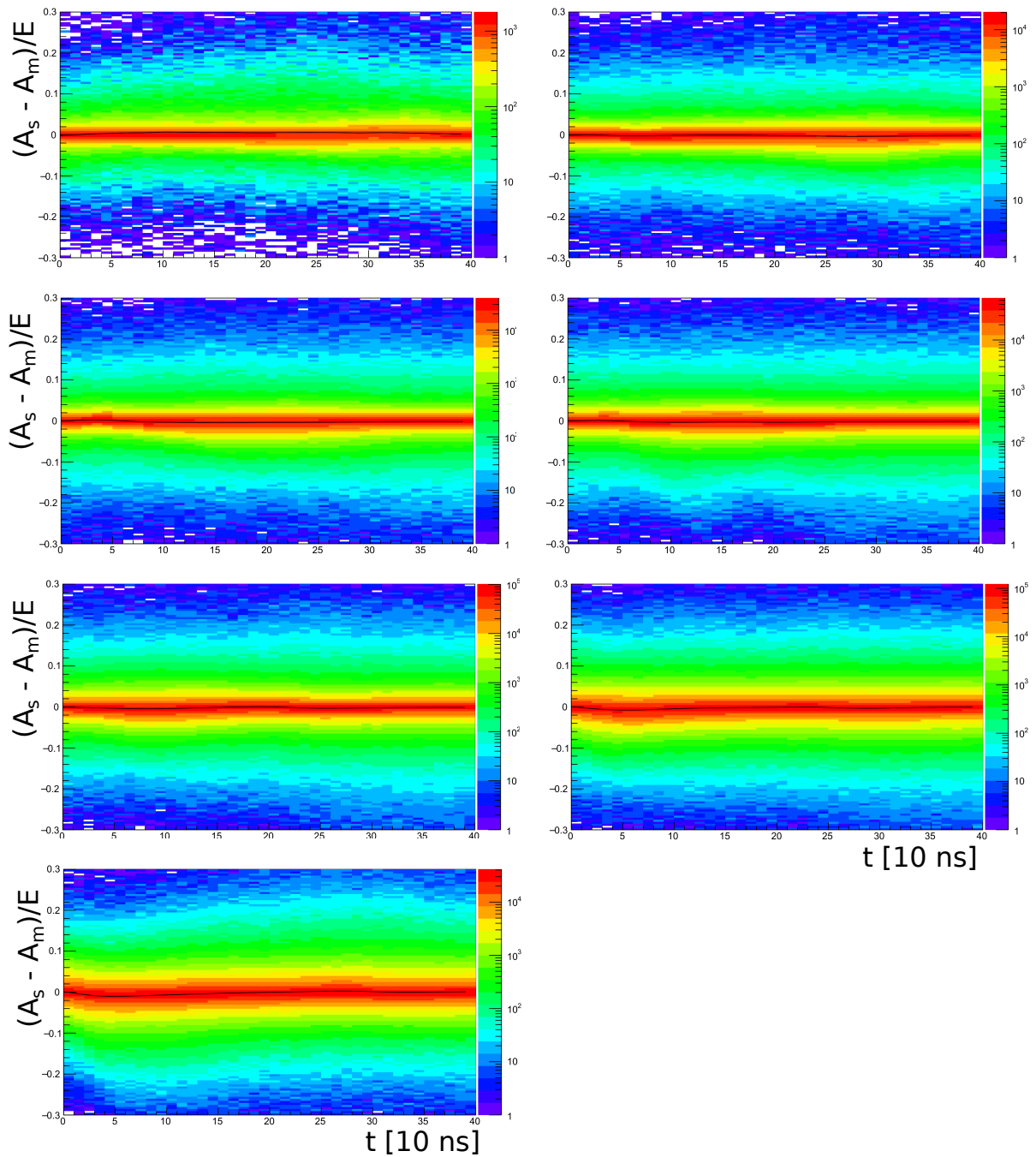


Figure 27: The difference $(A_s(t) - A_m(t))/E$ (as in as in Fig. 25) is shown for the transient signals. In contrast to the simulated and measured signals of core and hit segment a systematic deviation in time is not observed. The agreement of measurement and simulation shows that the transient signals are well described by the simulation.

histograms the mean value and the standard deviation σ were extracted. The results for the different radii are depicted in Fig. 29. In all cases the mean difference of measurement and simulation is very close to zero. The standard deviation, which can be used as a measure for the overall matching of

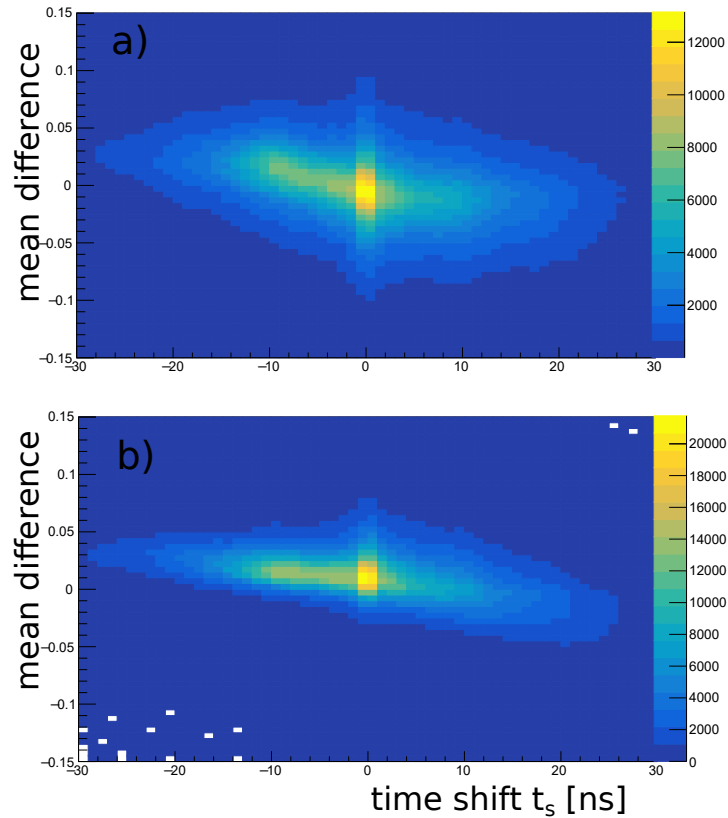


Figure 28: The time shift, which is applied to the measured trace and determined by the grid search algorithm, is plotted against the mean difference of measurement and simulation extracted from the first 50 ns. In an ideal scenario no correlation is expected. Albeit for negative shifts the simulated signal is slightly larger than the measurement.

measurement and simulation is increased close to the electrodes for very small and very large radii. The increase is especially large near the core.

One possible explanation for the difficulties to reproduce the measured signals near the core is the assumption of a point like charge. The simulation assume that charges are point like. However, a charge cloud of finite size is created by an interaction. For example, the photo electron from a 1 MeV photo absorption has a range of 1.2 mm [17]. Due to the radial electrical field the effective size of the hole charge cloud increases during the charge collection, which is discussed later on in section 5.2.1. For interactions close to the central electrode the difference of initial and final charge cloud size is largest.

As the disagreement of measurement and simulation is also increased (to a lesser extend) at large radii another explanation is also possible. The time of full charge collection is longest for interactions close to the electrodes. This is especially true for interactions close to the core because the holes, that are slower than the electrons, drift through the whole segment. In case the drift velocities are not correctly reproduced by the simulations, the longer drift times increase the overall deviation of measured and simulated pulse shapes.

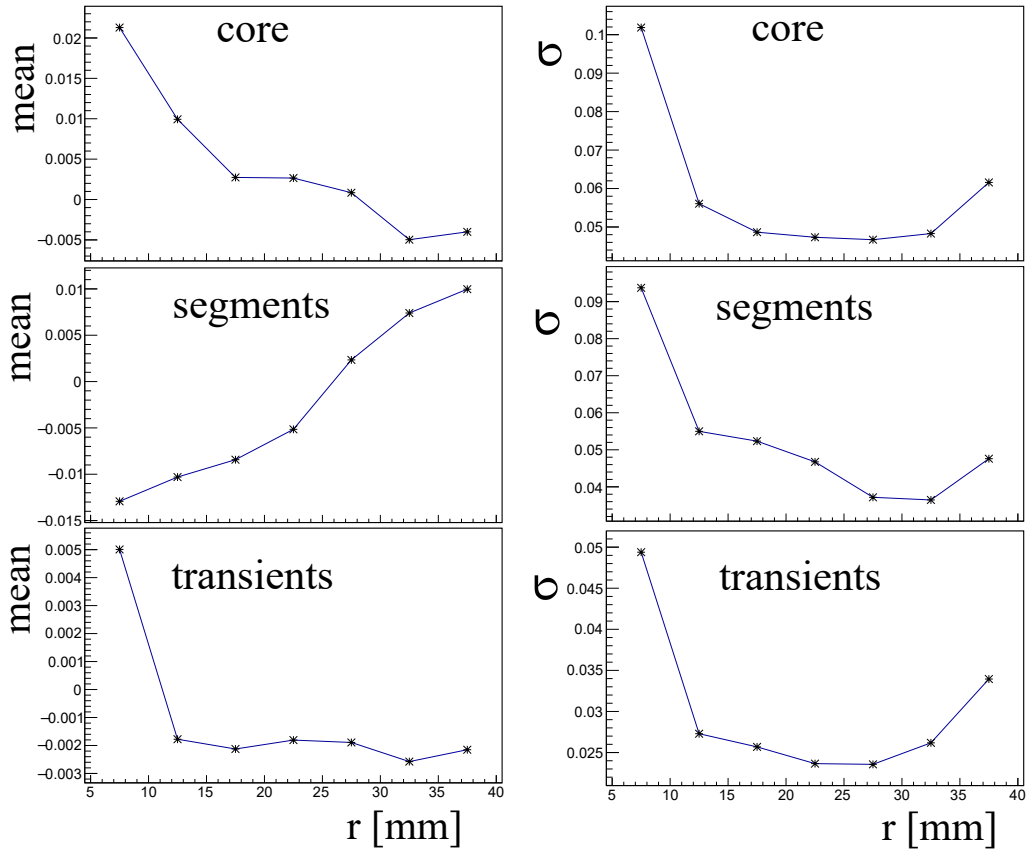


Figure 29: The mean difference of simulation and measurement (normalized by the energy of the interaction) and the standard deviation is plotted in dependence of the radius of the interaction. This was done for the core, the hit segments and the transient signals independently. For all cases the mean is very close to zero as expected. The mean values for the core and the hit segments show a mirrored behavior. The difference of measurement and simulation, summarized by the standard deviation σ is larger close to the electrodes.

Related to this the $T_{10\%–90\%}$ rise times were inspected. The results are presented in section 3.4. The hole mobility and the electron mobility, which are crucial parameters for correct drift velocities, were also investigated and optimized in sections 4.3.6 and 4.3.7.

For all investigations presented in this section, the interaction positions were determined by the PSA. Therefore, differences of measurement and simulation originate from two sources: First, simulated pulses at a given interaction position differ from the measured pulses at this position due to the imperfect data base. Second, the interaction position determined by the PSA differs from the physical interaction position, leading to systematic deviations.

Overall the agreement of simulation and measurement is quite good and deviations are relatively small. Note the logarithmic scale of all shown distributions and that deviations above 10% arise primarily from low energy interactions as shown in Fig. 30. This is caused by the energy independent baseline fluctuation and the normalization of the differences $A_s(t) - A_m(t)$ to the energy of the interaction.

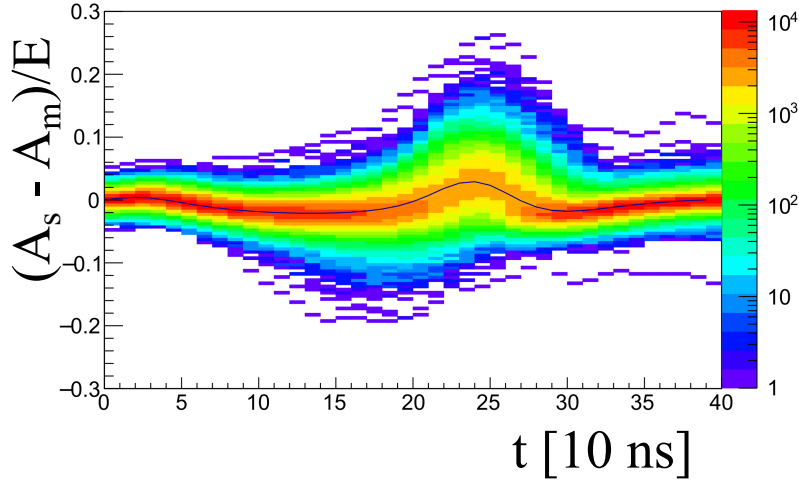


Figure 30: The difference $(A_s(t) - A_m(t))/E$ is shown for the core signal at a radius of $r = 30 - 35$ mm (corresponding to Fig. 25 bottom right). An additional gate on interaction energies above 300 keV was applied. Systematic deviations at $t = 200 - 250$ ns are still present, but outside of this region deviations above 10% are no longer observed.

3.4 T_{10-90} Rise times of measured and simulated pulses

The process of charge collection takes about 100-350 ns, depending on the interaction position. A criterion to describe the duration of this process is the T_{10-90} rise time of the pulses. The T_{10-90} rise time is derived by subtraction of the points in time at which the pulse reaches 90% and 10% of the maximum pulse height. The rise time in large volume HPGe detectors has a strong dependency on the interaction position. It is either determined by the completed charge collection of the electrons or of the holes. In this section T_{10-90} rise times, which were derived from segment signals of events with only one triggered segment, are shown. Crystal A001 was divided into 45456 individual $2\text{ mm} \times 2\text{ mm} \times 2\text{ mm}$ grid points. The T_{10-90} rise times were evaluated for all of these grid points. This was done for both measured and simulated pulse shapes, see Fig. 31. The time at which the pulse reaches either 10% or 90% was extrapolated between the two time ticks at which the threshold was reached. This way, a timing resolution below the tick length of 10 ns was achieved.

Since the drift velocity of holes is slower than the drift velocity of electrons, the charge collection of the electrons is finished before the full collection of the holes for most interaction positions. Only interaction points with a large radius have a rise time that is determined by the charge collection time of the electrons, because the holes drift towards the segment electrode and the electrons towards the central contact.

In the following, only interactions from ring three were considered because of the near radial electrical field. The rise times depend mainly on the radius of the interaction. This radius dependence is shown in Fig. 32a.

As the drift velocity of the holes is smaller than that of the electrons the largest rise times are observed for very small radii. In this case electrons are collected almost instantly and the holes drift through

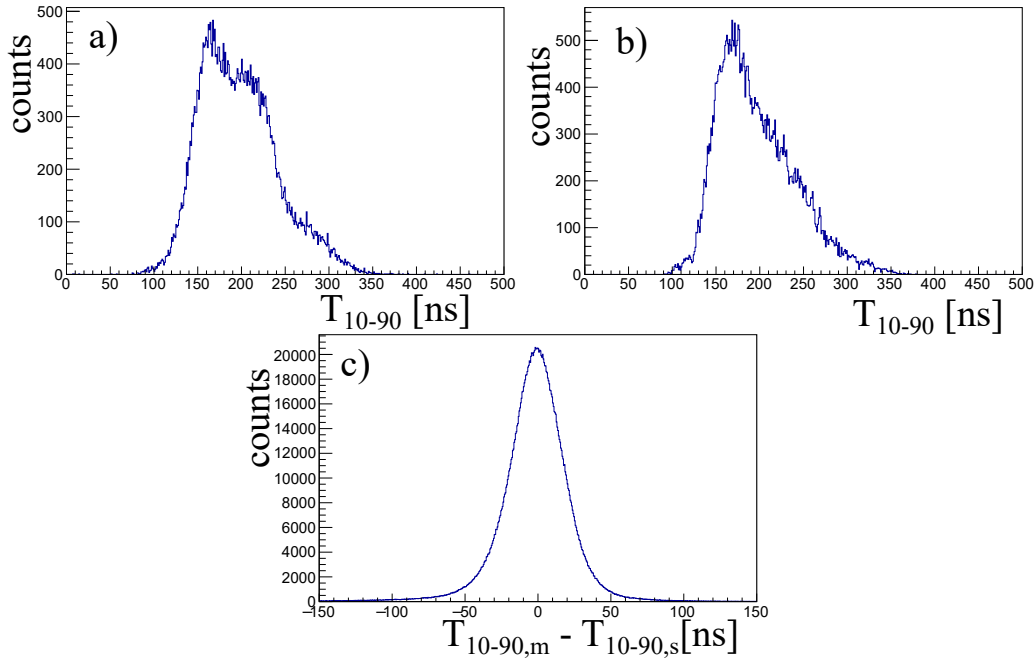
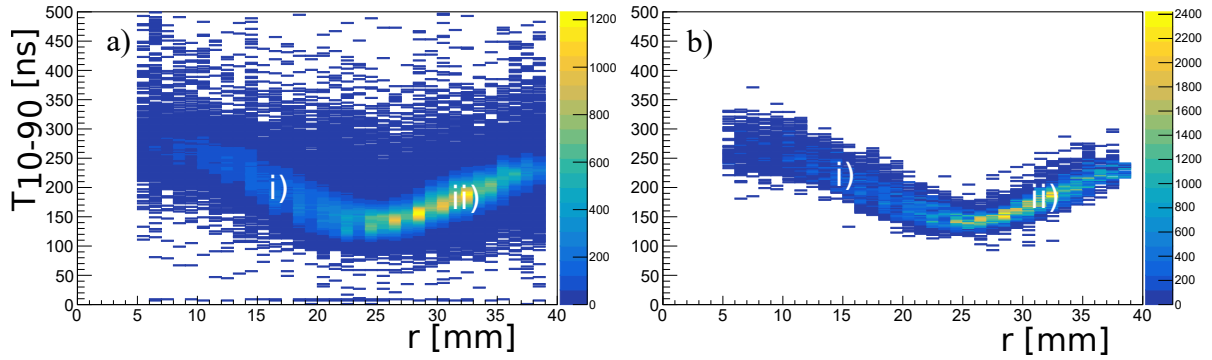


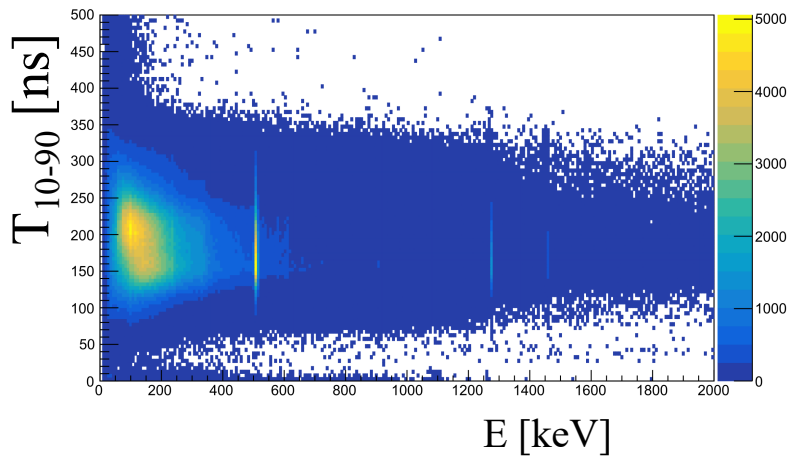
Figure 31: The a) measured and b) simulated T_{10-90} rise times are plotted. Crystal A001 is divided by the adaptive grid search into 45456 grid points and for each grid point the T_{10-90} rise time was evaluated. For the measured values the average rise time at the corresponding grid point was used. The difference of simulated and measured rise times, which was derived on an event-by-event basis for about $1.9 \cdot 10^6$ events, is shown in c). It has a near Gaussian shape with some tails (FWHM \approx 39 ns, FWTM/FWHM \approx 2.09, mean= -2.3 ns).

the full length of the segment. These rise times are in the range of 300-350 ns. This shows that the time window of 400 ns, as it is used by the grid search algorithm, is sufficient. The small spread of the simulated rise times for a given radius is caused by the angle dependence of the T_{10-90} rise times. The drift length differs slightly for different angles and a fixed radius. The vast majority of measured rise times is within the region expected by the simulation.

Deviations of measured and simulated rise times are caused by either a) wrong radius determination of the PSA, b) baseline fluctuations of the measured pulse or c) an imperfect simulated data base. For the rise time calculation a simple algorithm was used, that employs a threshold to determine the points in time when the pulse reaches 10% or 90% of the maximum amplitude. Such an algorithm is prone to trigger on noise, especially for low energies. This early triggering leads to larger than expected rise times for some low energy events, which is shown in Fig. 32b.



(a) The T_{10-90} rise times of the a) measured and b) corresponding best fitting simulated pulses are plotted versus the radius of the interaction, which was determined by the PSA. Only segment pulses were considered. For small radii, marked as region i), the rise time is given by the charge collection time of the holes. For large radii, marked as ii), it is determined by the collection time of the electrons. The point with the smallest rise time at $r \approx 25$ mm is defined by identical drift times of both charge carrier types.



(b) The T_{10-90} rise times of the measured signals is plotted in dependence of the energy of the interaction. As expected, the mean rise time of the pulses does not change with respect to the energy of the interaction. Only for very small energies a tendency to large rise times is observed. This is most likely caused by the small signal-to-noise ratio. For low energy interactions it is more likely to trigger on noise, when determining the times at which the pulse reaches the 10% and the 90% level. This effect is also the reason for the T_{10-90} rise times close to 0 ns.

Figure 32: The a) radius and b) energy dependence of the T_{10-90} rise times is shown.

For a visual comparison of measured and simulated rise times at different interaction positions, the mean measured rise times were compared to the simulation in the xz plane in Fig. 33. A good agreement is observed. Nevertheless, positive and negative differences are not spread randomly, which would be expected if deviations were only caused by noise. Close to the electrodes the simulated rise times are larger than the measured ones. There is also a region in the middle between the electrodes where the opposite is the case (visible in Fig. 33 d)). Due to computational restraints of the trace analysis only a subset of about $1.9 \cdot 10^6$ events were used. Therefore, some of the grid points are empty and the calculated mean rise times are subject to statistical fluctuations.

In the back of the detector, close to the core, the simulated rise times show a drop off which is not

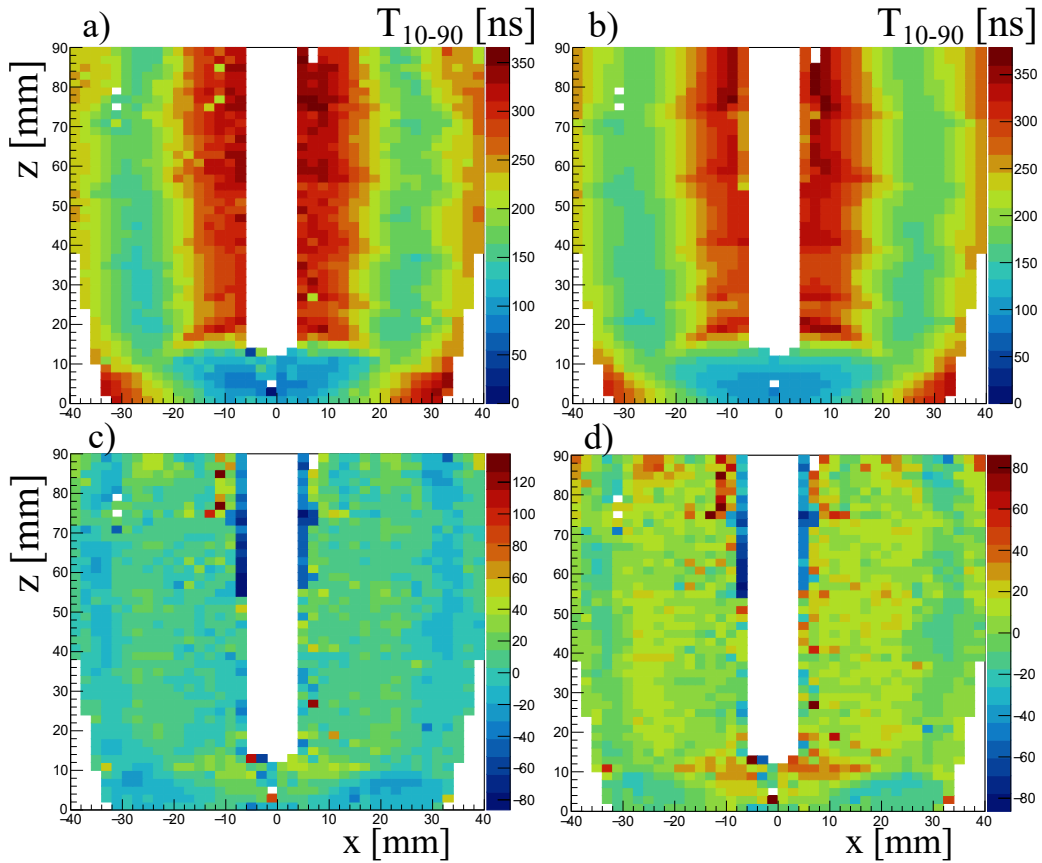


Figure 33: The a) measured average T_{10-90} rise times and the b) simulated T_{10-90} rise times are plotted for different x and z values and a fixed y coordinate of -2 to 0 mm of crystal A001. The T_{10-90} rise time is given by the color scale. The difference of simulation and measurement is shown in c). The last histogram d) also shows the difference but the color scale was adjusted to be symmetric for increased clarity by omitting some of the large statistical fluctuations present in the measurement.

observed in the measured pulses. The deviations in the order of 40 to 80 ns are rather large and can not be explained by statistical fluctuation.

The same comparison was done for the xy plane in Fig. 34. Here, the segment structure is clearly visible. The measured rise times of segment F1 are systematically larger than in the rest of the detector. This is not reproduced because no segment specific influence is assumed in the simulations. The same transfer function is used for all segments. The simulated signals are convoluted with an exponential decrease to account for the electronic response of the system. The exponent of this exponential function was set to 40 ns. This exponent was then set to 55 ns for segment F1 and the corresponding transfer function was convoluted with the simulation. The impact on the simulated T_{10-90} rise times is shown in Fig. 35. The new simulations reproduce the measurement much better and the systematic deviation for this segment is no longer observed.

Similar segment specific deviations in the T_{10-90} rise times are observed in other segments as well. These observations show that the transfer function is crucial for a working Pulse-Shape Analysis.

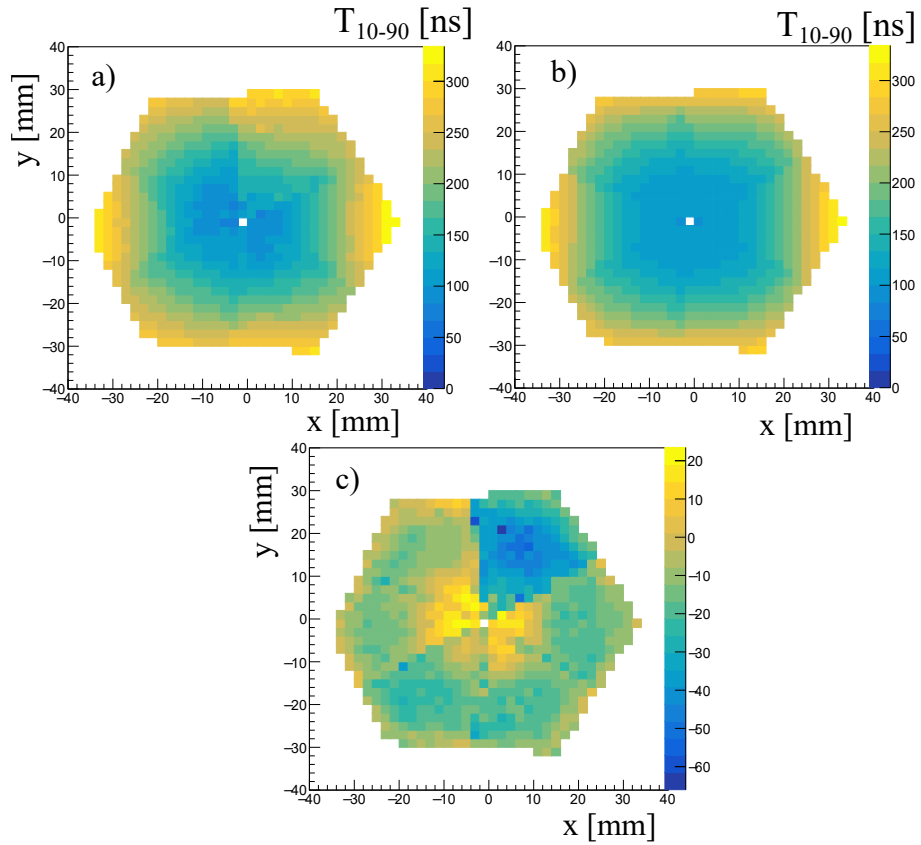


Figure 34: Measured a) and simulated b) T_{10-90} rise times are plotted for $z=4-6$ mm for crystal A001. A significant increase in the rise time is observed for segment F1 which can not be reproduced by the simulations. The difference of simulated and measured rise times is plotted in c). The same transfer function was used for all segments in the simulations.

Therefore, it was investigated and adjusted on a general level in section 4.3.5 and on a segment by segment level in section 4.3.5.1.

The observed deviations of measured and simulated T_{10-90} rise times, which are not segment specific, can be caused by the drift velocity of electrons and holes which are used in the simulations. Results are described in sections 4.3.6 and 4.3.7.

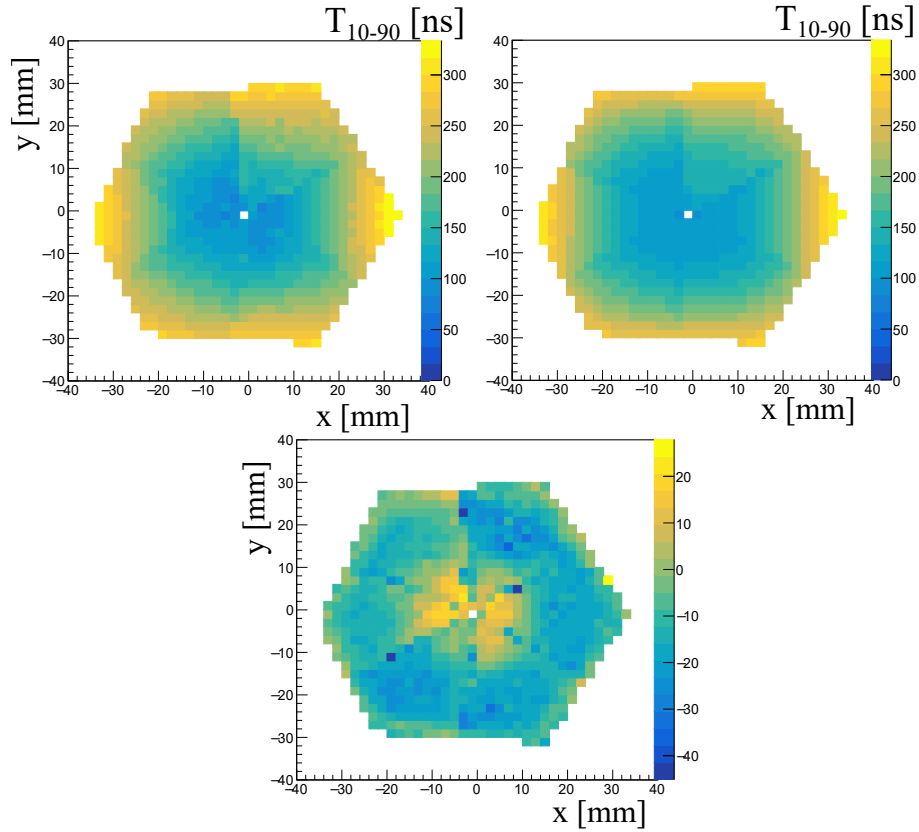


Figure 35: Measured a) and simulated b) T_{10-90} rise times are plotted for $z=4-6$ mm for crystal A001. The decay constant of the transfer function of segment F1 (upper right) was adjusted to 55 ns. The agreement of measurement and simulation is increased for this segment.

3.5 T_0 Determination

A correct T_0 determination is crucial for a proper alignment of the simulated traces with the measured signals. The T_0 determination via a leading-edge algorithm, has the disadvantage to be energy dependent. Low energy events are shifted to later starting times. The established solution is the usage of a constant fraction discriminator (CFD) which identifies T_0 independent of energy.

However, the CFD timing still depends on the interaction position in large volume HPGe detectors because of the position dependent pulse shape of the signals. Therefore, a position and energy independent T_0 determination is needed. This is achieved by adding the pulses of the hit segments and of the core. The result is a straight line, independent of interaction position. Such a trace is depicted in Fig. 36.

A fit of the pulse yields an energy and position independent T_0 value. Threshold values of 10% and 90% of the maximal pulse height were used to determine the fitting region. The fitting region should be as large as possible to reduce the statistical errors. However, thresholds which are too small may result in triggering on noise and therefore inaccurate results. In addition, the last part of the signal is no longer a straight line, which is caused by the impact of the measurement electronics.

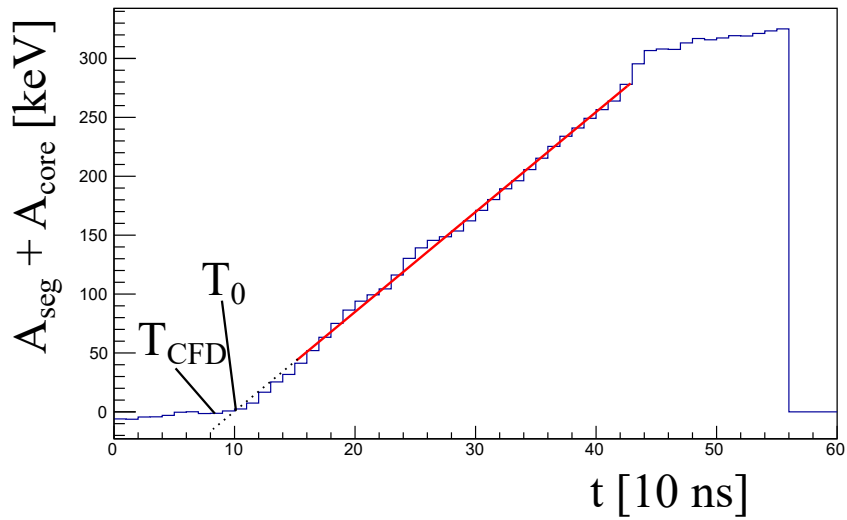


Figure 36: The summed signals of hit segment A_{seg} and core A_{core} are plotted for a measured trace for a single event. Due to the complementary shape of the core and segment signals the sum is a straight line. The obtained summed trace was fitted by a first order polynomial (red line). The crossing with the baseline (dotted line) corresponds to the T_0 value. The front-end electronics provide a different timing via a digital CFD T_{CFD} , which is marked in the plot. The stored trace comprises 8 samples before T_{CFD} , as well as the trace signal.

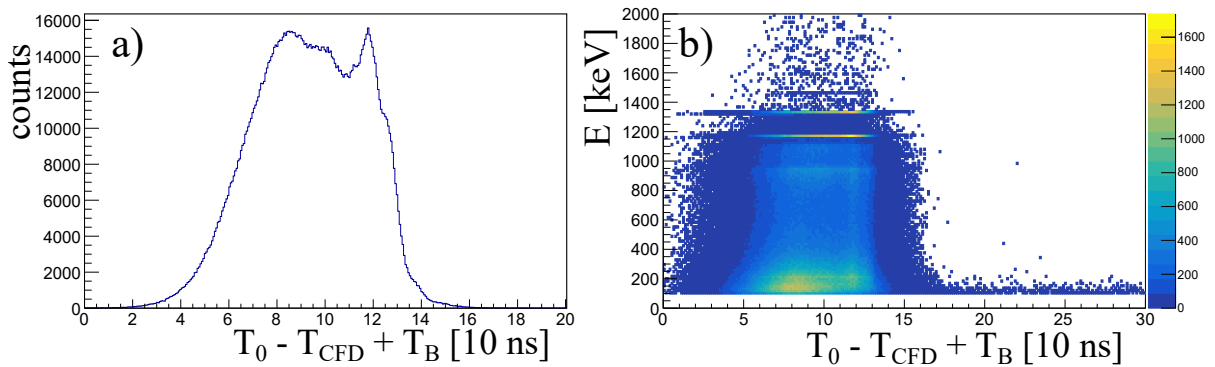


Figure 37: The determined T_0 values are plotted with respect to T_{CFD} . $T_B = 80$ ns is a constant offset which corresponds to eight pre-trigger samples, which are used to calculate the baseline. The second picture b) shows that there is mainly no energy dependence of the timing. At energies below 150 keV some outliers are observed. These are most likely caused by a poor choice of the fitting region, due to the lower signal-to-noise ratio.

The error of the baseline crossing in terms of the fitting error is negligible; systematic errors are dominant. Possible causes for systematic errors are the choice of the fitting region and the approximation of a linear pulse shape.

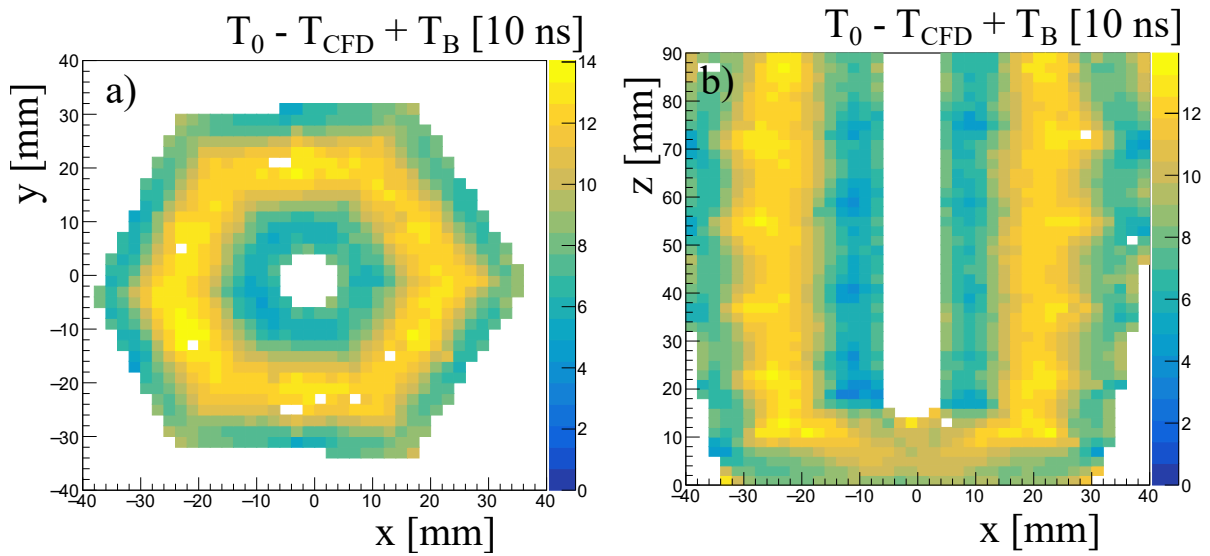


Figure 38: The average found T_0 values with respect to T_{CFD} are plotted for a) a fixed depth z of 22-24 mm and b) for a fixed y coordinate of 36-38 mm. A distinct dependency on the interaction position is observed, which is caused by the reference timing T_{CFD} . Largest values are seen in the middle of the segments where the T_{10-90} rise times are the smallest.

Events with one hit segment were considered and the added traces of hit segment and core were fitted as described above. Low energy interactions below 50 keV were excluded. For a T_0 value to be meaningful, it has to be given with respect to a reference timing. The front end electronics provide a timing via a digital CFD T_{CFD} . The obtained T_0 values are given with respect to this timing.

The resulting timing distribution is shown in Fig. 37 a). The peculiar shape is explained by the fact that the timing provided by the CFD algorithm is position dependent. Fig. 37 b) shows that this timing is mainly not dependent on energy, except for a very small amount of events below 150 keV which seem to have arbitrary T_0 values.

For each interaction position the found T_0 values were averaged. The dependency of the determined T_{CFD} values on the interaction position is depicted in Fig. 38 for two exemplary slices of the detector. This figure demonstrates that a CFD timing is not sufficient to determine T_0 in large volume HPGe detectors with the required accuracy.

The same fitting procedure was performed for the simulated signals. The difference of the starting times of measured $T_{0,m}$ and corresponding simulated $T_{0,s}$ pulse shapes is shown in Fig. 39. The PSA uses a very similar technique of fitting the added traces of segment and core to determine T_0 and to align the simulation to the measurement. Therefore, the difference should be zero or very close to zero by default. Deviations arise from a different choice of the fitting region and different fitting algorithms. For the purpose of this work the well established MIGRAD algorithm, which is implemented in the ROOT framework, was used [54]. The fact that the difference $T_{0,m} - T_{0,s}$ deviates from zero with a standard deviation of $\sigma = 10$ ns demonstrates the difficulty and ambiguity of the T_0 determination.

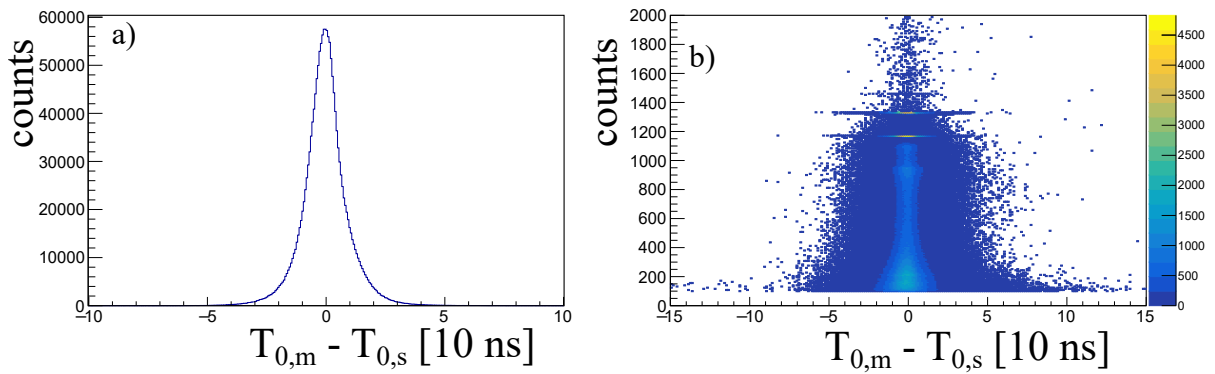


Figure 39: The difference of the found T_0 values is plotted for the measured $T_{0,m}$ and the simulated $T_{0,s}$ traces in a), as well as the correlation with the interaction energy in b). Most differences are close to zero as expected. The distribution has a standard deviation of $\sigma \approx 10$ ns. For very few events at low energy the difference is significantly larger which indicates a failed T_0 determination for these events.

Note that the distribution in Fig. 39 does not show the timing resolution of the detectors. In the future an external trigger, e.g. from a scintillator, may be utilized to determine the timing resolution of the HPGe detectors and to further improve the T_0 determination.

4 Determination and Improvement of PSA performance

4.1 ^{22}Na -coincidence method

To improve the results of the PSA, a reliable way to assess the PSA performance is needed. A ^{22}Na source measurement was utilized to achieve this. ^{22}Na decays via β^+ emission. The positron annihilates with an electron close to the source position and two 511 keV γ rays are emitted at an angle of 180° . The reconstruction of these two coincident γ rays allows for a direct assessment of the accuracy of the two interaction positions. In the following the experimental setup and the reconstruction of the 180° coincidences will be presented. These results are used to assess the PSA performance and to determine optimal input parameters via variation. The input parameters comprise crystal properties, characteristics of the electronics as well as features of the grid search algorithm.

4.1.1 Experimental setup

The source measurement was performed at GANIL in April 2016 with the AGATA spectrometer which consisted of 29 individual HPGe detectors based on nine triple and one double cryostat. To achieve high solid-angle coverage for the 180° coincidences the source was placed in one of the pentagonal holes left open in the germanium shell of AGATA (in the full 4π configuration twelve of these pentagons will remain). Two measurements with slightly different source positions were conducted (see Fig. 40 and table 4.1 in section 4.1.3). The first measurement allows the assessment of the first two rings of the complete array, whereas the second one also copes for the back segments but mainly for the inner detectors. Fig. 41 and 42 depict which segments and which detectors were hit by coincident 180° 511 keV γ rays using the two different setups for the source position. For the determination of the source positions (in terms of x, y, z) see section 4.1.3.

The energy calibration was extracted from a ^{60}Co source measurement which was recorded directly before the ^{22}Na data. The first measurement corresponding to the setup depicted in Fig. 40 a) consists of $7.22 \cdot 10^8$ individual interactions and the second one - Fig. 40 b) - consists of $6.23 \cdot 10^8$ interactions. Since the latter one provides a better overview of the PSA performance in the different segments it was used for the further analysis and all plots refer to this measurement if not mentioned otherwise.

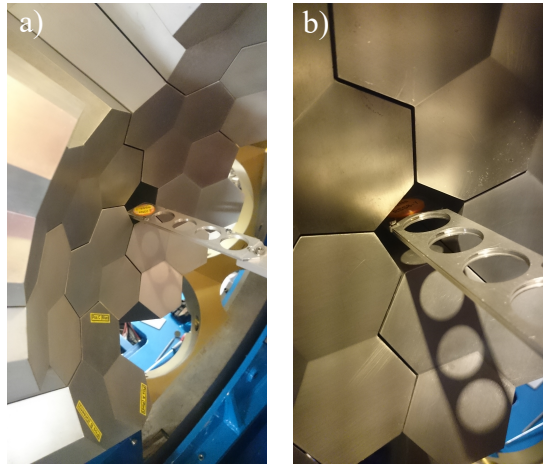


Figure 40: The two source positions for the individual measurements are shown. The first position in a) allows for coincidences between all detectors, though these are only possible in the front part of the detector due to the solid angle coverage. For the second source position in b) the source was moved 2.5 cm into the array and coincidences mainly happen in the five inner detectors. Coincidences between other crystals are possible but are reduced due to absorption. The setup in b) has the advantage that coincidences are possible for all segments of the involved crystals (in contrast to only the first 1-2 rings for the other setup).

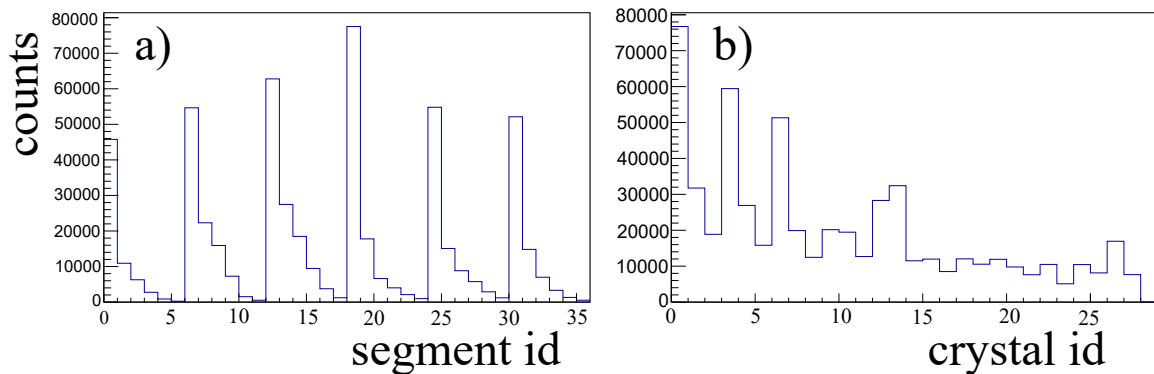


Figure 41: The a) hit segments and b) hit detectors corresponding to the source position depicted in Fig. 40 a) is shown. Only events in which both 511 keV γ rays were detected are considered (the gating procedure is explained in detail in section 4.1.2). In this setup coincidences are found in all of the 29 detectors. However, the geometry of the setup allows mainly for coincidences in the front of the crystals (segment ids 0, 1, 6 correspond to segments A1, A2, B1 and so on. See reference [10] page 6.)

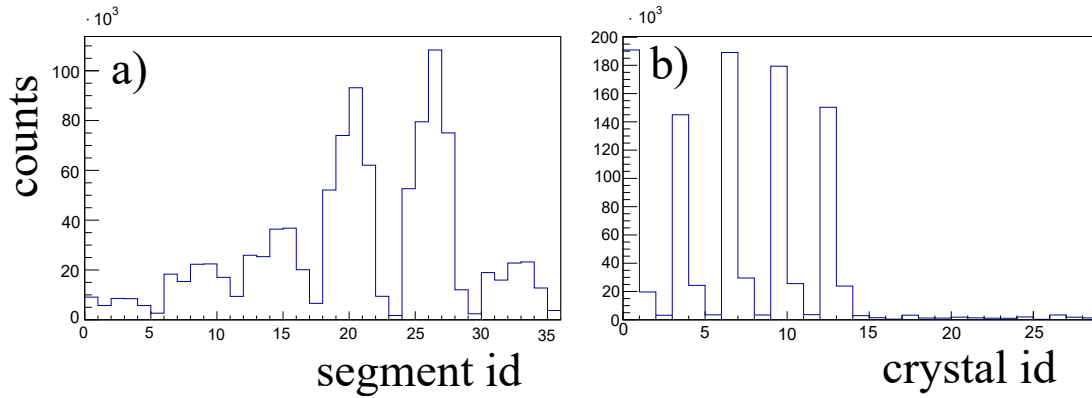


Figure 42: The a) hit segments and b) hit detectors corresponding to the source position depicted in Fig. 40 b) is shown. In contrast to the distribution shown in Fig. 41, coincidences are detected primarily in the five detectors which are closest to the source. In return, coincidences are found in all segments of these detectors.

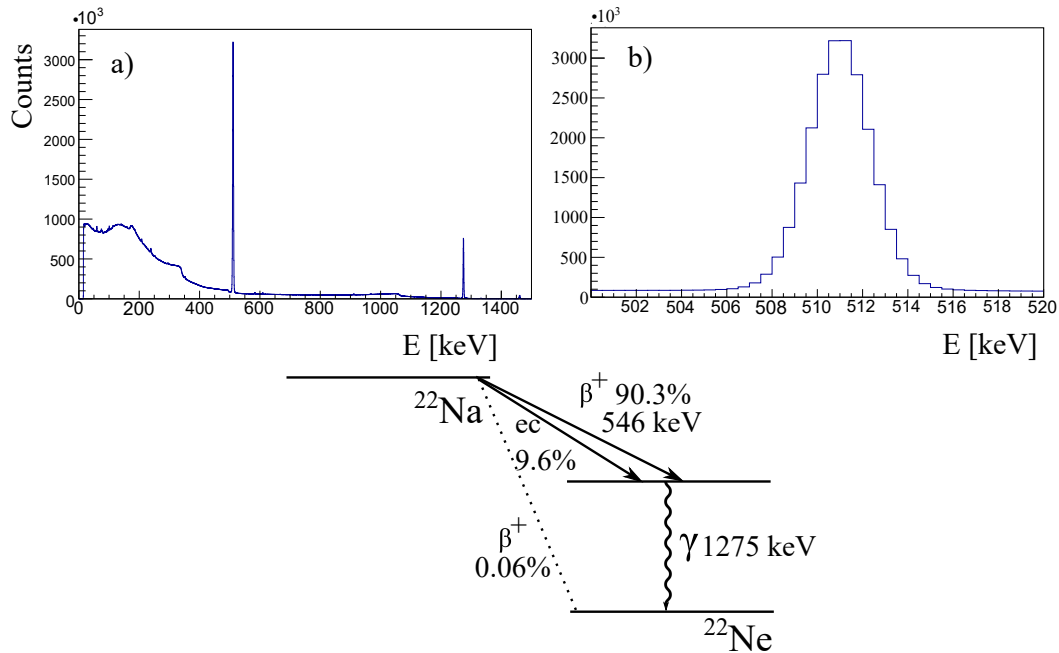


Figure 43: The non tracked γ -ray spectrum is shown in a). In addition to the prominent 1275 keV line of ^{22}Na and the annihilation line at 511 keV some natural background is observed. Figure b) shows a zoom on the 511 keV line which was used to reconstruct the coincident γ rays using a window of 511 ± 3 keV. The figure at the bottom depicts a simplified decay scheme of ^{22}Na .

The non tracked γ -ray spectrum which comprises the individual interaction energies measured in the segments is depicted in Fig. 43 and was used to gate on the interaction energy of 511 keV. The highest observed counting rate was ~ 1 k cps for the inner detectors in the second measurement. The low rate as well as further investigations regarding the timing and the measured angle between the γ rays, which are shown in the next section, indicate that random coincidences coming from background

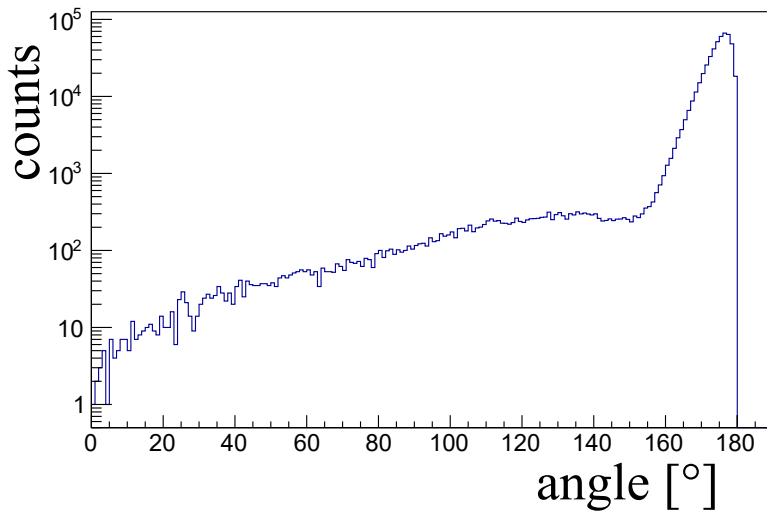


Figure 44: The measured angle between source position and the two interaction points is shown after multiplicity and energy conditions are applied. Only events with interactions in different detectors were considered. Most events have an angle which is close to 180° .

events can be neglected. Dead time effects can be disregarded in good approximation due to the low counting rate.

4.1.2 Reconstruction of coincident γ rays after e^+/e^- annihilation

For the reconstruction of the $\gamma\gamma$ coincidences associated with an annihilation of a positron several analysis conditions are applied. First a gate on number of hit segments = 2 (complete array) is set and an energy of $E=511\pm 3$ keV for both interactions is required. For matching events the angle between source position and the two interaction points is calculated. The distribution of these angles is depicted in Fig. 44 for the second setup (using the source position derived later on in section 4.1.3). Only events with an angle of 150° or more are considered for the further analysis. The distribution also shows that the background of false coincidences, coming from either a background 511 keV interaction or from two independent annihilations, is two to three orders of magnitude smaller than the number of real coincidences.

To study the background of random coincidences the differences of the time stamps for the individual detectors were considered. This difference shows a distinct peak around zero and a small background within the used event building window of ± 250 samples ($2.5\mu s$), see Fig. 45. After applying the conditions to multiplicity, energy, angle and distance the background of random coincidences is no longer observed. This demonstrates that a very clean selection of valid 180° coincidences is possible with the chosen gates. The measured data consists of $6.23 \cdot 10^8$ individual interactions. Out of those 936 k interactions were found to be coincidences from e^+e^- annihilation, which are 0.15% of all interactions. The small percentage of reconstructed coincidences arises from the very strict gates that are applied. Events in which the coincident 1275 keV γ ray interacted in any detector are rejected, due to the requirement of only two hit segments in the complete array. In addition, it is unlikely

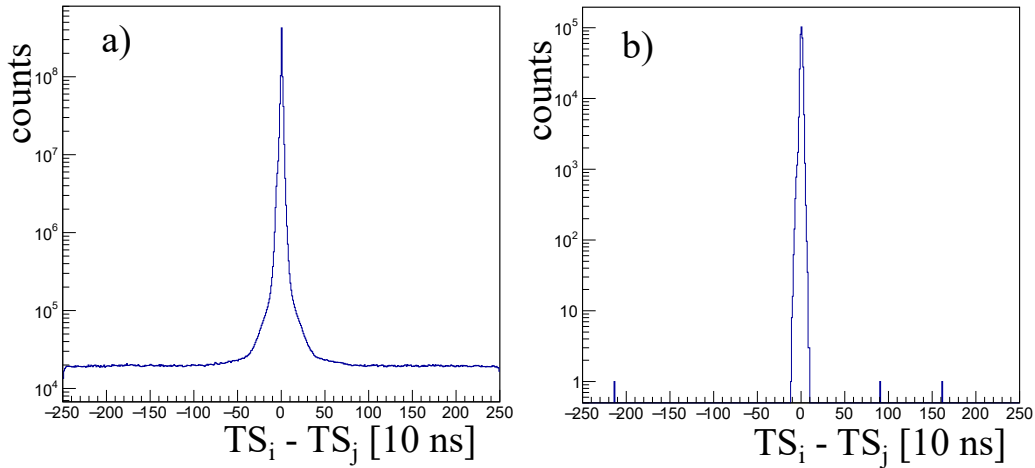


Figure 45: The difference of the time stamps $TS_i - TS_j$ for all possible detector combinations i, j is plotted a) for all events and b) for all reconstructed coincidences. The time stamps are attributed to each detector via triggering of the core.

that both 511 keV γ rays interact via photo effect because of the higher cross section for Compton scattering. Nevertheless, it was decided to use these strict gates to achieve a very clean selection of the 511 keV coincidences.

The interaction positions of the coincidences are shown in Fig. 46. Note that in contrast to the previous chapters the lab system is used and not the coordinate system of the individual crystals. For the first 100 coincidences these are visualized by drawing a line between the two corresponding interaction positions which intersect at the source position. This demonstrates the high but finite precision of the PSA as the intersections accumulate in a small region around the source position. To quantify this, the smallest distance of the line connecting the interaction positions to the source was derived for each event (see Fig. 47 for more details).

The determined distance to the source depends on the position resolution of the PSA and can be used to assess the PSA performance. The distribution of these distances is depicted in Fig. 48. Distances above 14 mm were omitted. The mean of the distribution is $d_{\text{mean}} = 2.73$ mm. The "standard" PSA configuration, that is used to analyze all experiments, was applied. The reduced number of counts close to 0 mm originates from the volume associated with a distance d : The probability for a line to cross the source position at a distance d is proportional to the volume of a spherical shell with inner and outer radii of d and $d + B$, with the binning factor B . Due to the r^3 dependence of the volume, it is unlikely to obtain very small distances close to $d = 0$ mm. A distribution, which is corrected for this geometrical effect, is depicted in Fig. 49.

The point of emission of the two 511 keV γ rays is not point like. This comes from the dispersion of the radioactive material inside the source on the one hand and the finite range of the positron before annihilation on the other hand.

The mean energy of the positron from the β^+ decay of ^{22}Na is 180 keV while the maximum energy is 540 keV. The range of the positron for a given energy can be derived from the stopping power. For a

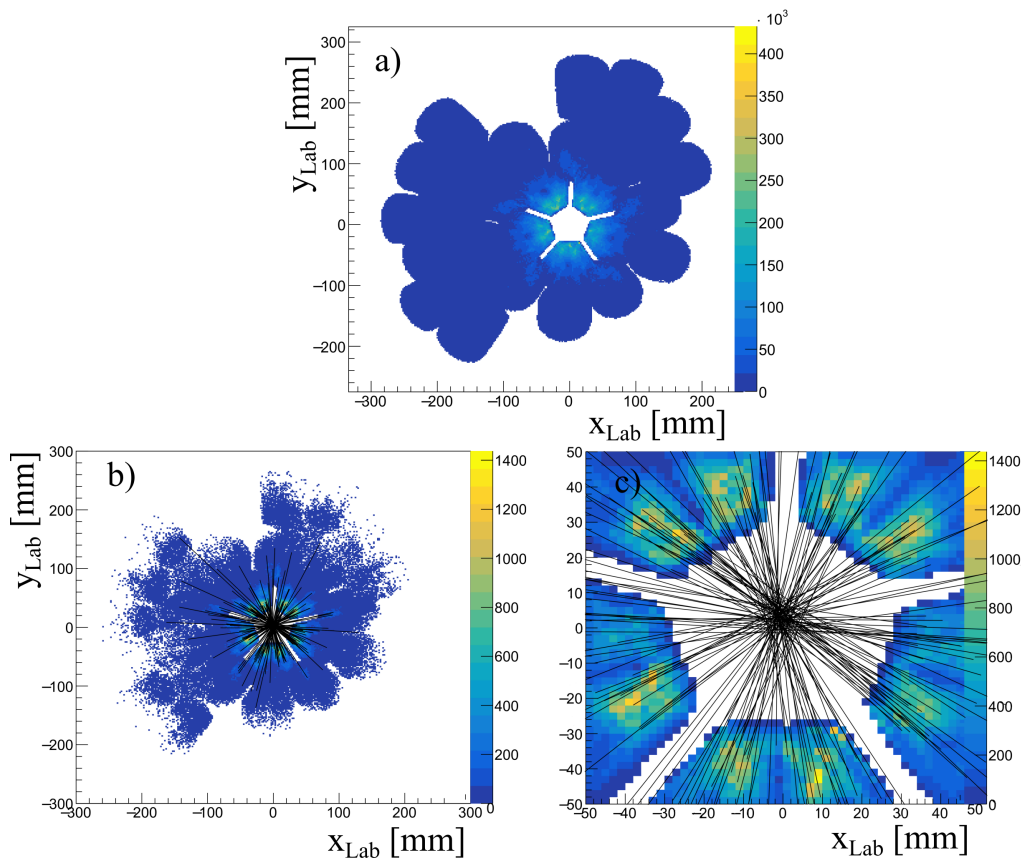


Figure 46: The interaction positions are plotted for a) all individual interactions and b) for all reconstructed 180° coincidences. Figure c) shows a zoom on the source position from b). In addition, in b) and c) a line was drawn between the interaction positions for the first 100 coincidences.

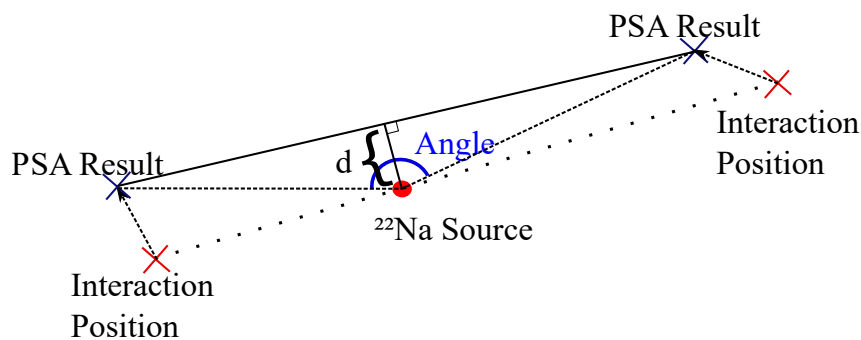


Figure 47: A schematic view for a reconstructed 180° coincidence is shown. The PSA results are very close to the corresponding physical interaction positions but do not match perfectly. The connecting line does therefore not intersect the source position, which is assumed to be point like. The distance of the line to the source position depends on the precision of the two interaction positions allocated by the PSA.

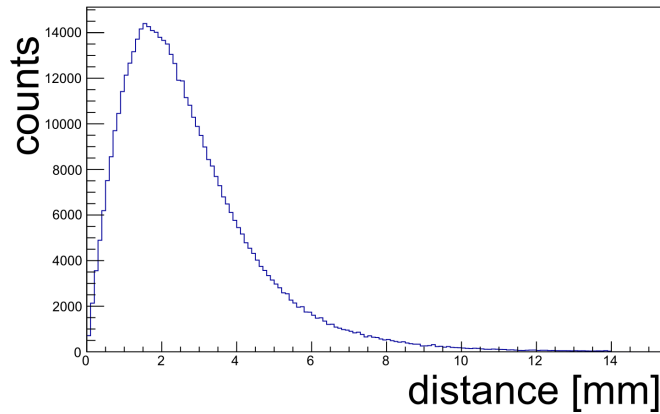


Figure 48: The distance of the lines connecting the reconstructed coincidences to the source position is plotted for all valid events. They intersect the source position mostly within a few millimeters. The mean of the distribution is used later on as a measure for the overall PSA performance.

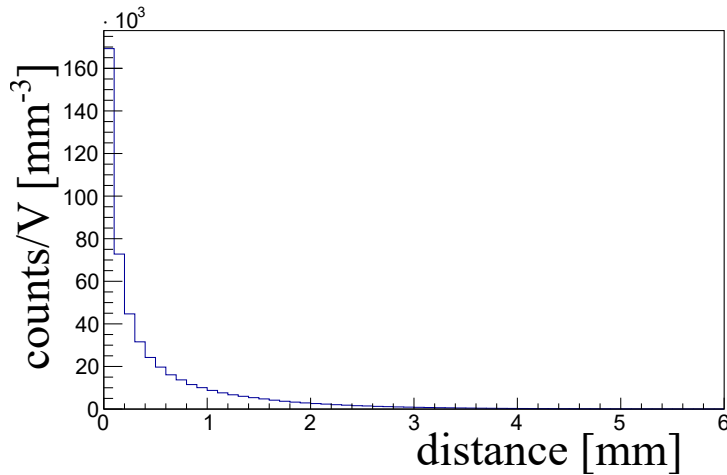


Figure 49: The distance of the lines connecting the reconstructed coincidences to the source position is plotted. The number of counts for each distance d was divided by the volume V of the corresponding shell, with $V = 4/3\pi((d+B)^3 - d^3)$. A binning B of 0.1 mm was used. The plotted value corresponds to the density of lines at distance d .

mean range the possible energies and their probabilities have to be taken into account. The mean range of the positron from ^{22}Na in polyethylene was measured to 0.24 mm by Dryzek et al. [55].

4.1.3 Determination of the source position

The precise knowledge of the source position is crucial for a correct reconstruction of the $180^\circ \gamma\gamma$ coincidences and therefore for the assessment of the PSA performance. For the first setup (with the source being located at the opening of the pentagonal hole) the source position was also measured via laser scanning by an external expert. The result is given in table 4.1. The measurement could provide the source position only with respect to the position of the "honeycomb" frame, which is the holding structure of the individual cryostats. The position of the honeycomb frame is only known with an uncertainty of 1 mm, which is much larger than the precision of the laser scanning measurement. In addition the laser scanning could only measure the position of the structure, on which the source was mounted. The actual source position had to be extrapolated.

For this reason and since for the second setup the position measurement via laser was not available, the average point of emission was determined with a another approach. Different source positions, which are given as input parameter to the analysis, were tested. For each tested interaction position the mean distance to the source (which is the mean of the distribution in Fig. 48) was determined. For the best agreement of tested source position and actual average point of emission of the two 511 keV γ rays, the mean distance is expected to be minimal. The tested interaction positions are located on a three dimensional grid.

For increased precision and reduced calculation time the variation of the assumed source position was done first on a coarse grid of 1 mm grid size and in a second step on a fine grid of 0.1 mm size around the position found on the coarse grid. For the variation in the coarse grid no gate on the angle was set to not reject any real coincidences. In the fine grid only events with an angle of $170-180^\circ$ were considered to increase the precision. The results of the variation are shown in Fig. 50. The variation shows a smooth and symmetric increase of the mean distance to the source for source positions around the global minimum.

Note that systematic errors of the PSA results can bias the result of the variation.

The resolution of 0.1 mm implies a more precise knowledge of the source position than expected as the points of emission are smeared out due to the dispersion of the radioactive material and the range of the positron. The determined source position is therefore only the average point of annihilation and emission of the two 511 keV γ rays. The final results for the determined source positions for the two different setups are summarized in table 4.1.

The agreement of the laser measurement with the variation result is reasonable. For the determined z coordinate, the deviation of 2.9 mm is larger than for the x and y positions. Possible sources for this deviation are the uncertainty of the laser measurement (as the position is only given relative to the holding structure of the cryostats), the finite PSA position resolution, the distribution of the radioactive material and the relative position of the source in the holding structure (the laser measurement assumes the source position to be in the center of the circle in which the source was placed). In general the result of the variation procedure provides reliable results and was therefore used for the second setup for the further analysis.

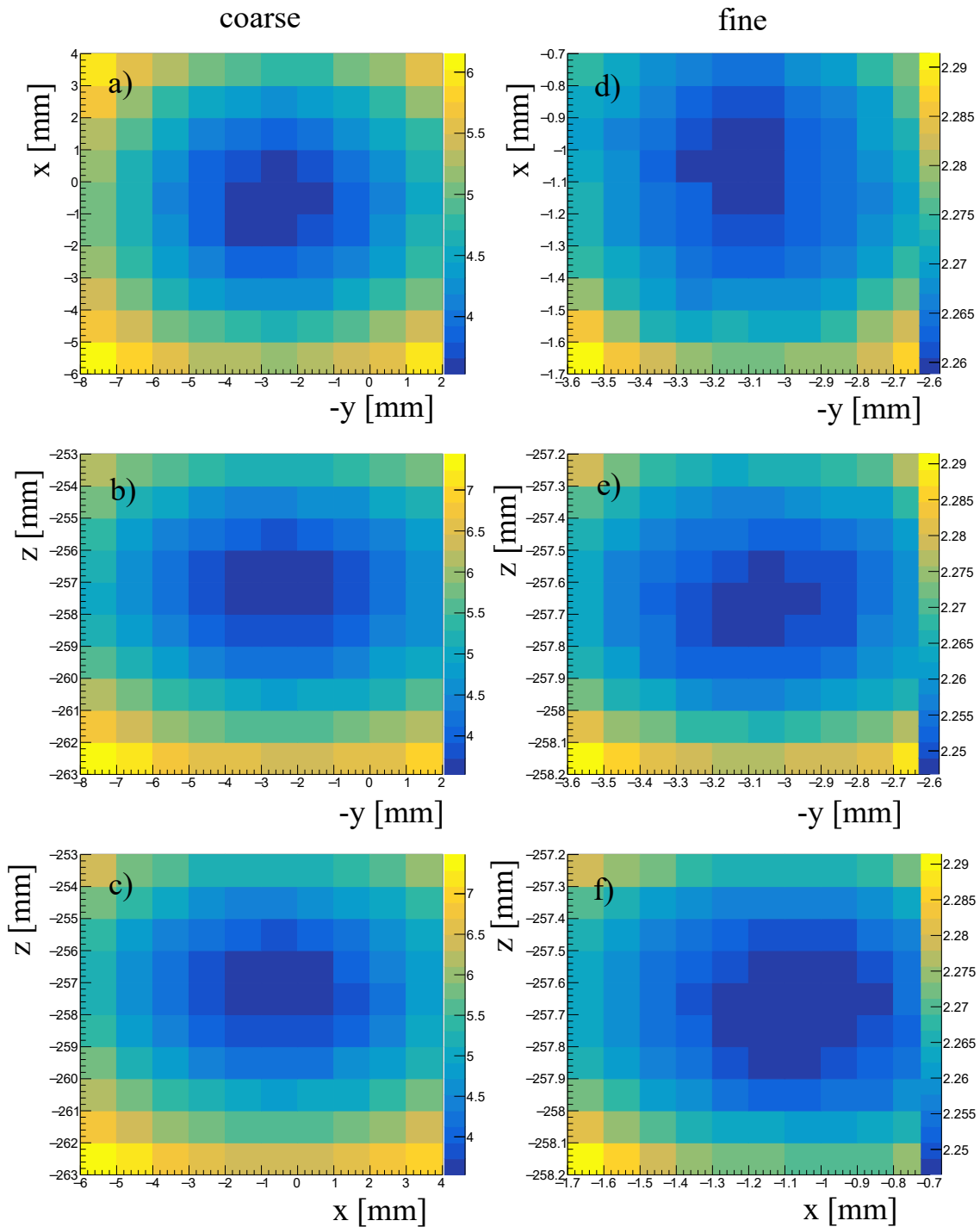


Figure 50: The source position was varied on a 3D grid and the resulting mean distances (given by the color code) were derived. These are shown in a), b) and c) for a coarse grid for the xy, yz, and xz planes that intersect the global minimum. Figures d), e) and f) show the variation in a fine grid around the minimum found previously. Again for the xy, yz and xz planes the corresponding z, x and y coordinate was set to the global minimum. The minima for the source position were used in the analysis.

	first setup laser	first setup variation (deviation)	second setup variation
x [mm]	-8.8	-9.3 (-0.5)	-1.1
y [mm]	1.2	0.3 (-0.9)	3.1
z [mm]	-231.2	-228.3 (+2.9)	-257.8

Table 4.1: The determined source positions for the two individual measurements are shown. For the first setup two independent results are available, coming from a direct measurement via laser scanning and from a variation procedure by minimizing the mean distance of the lines connecting the coincidences to the source. The deviation of these two results is given in the brackets. The x and y coordinates agree quite well whereas the deviation in z is slightly larger.

4.1.4 Reconstruction of Compton scattered events

In the previous section the two 511 keV γ rays were only used if both γ rays deposited their full energy via photo effect. To increase the amount of available coincidences for the analysis the case of Compton scattering followed by a photo effect was also considered. For simplicity only the case of a single photo effect for one of the 511 keV γ rays and a single Compton scattering followed by a photo effect for the other γ ray was considered (see Fig. 51 for a schematic). Note that the PSA cannot resolve the two cases of a γ ray depositing its full energy via a single photo effect or via multiple interactions inside a single segment. For simplicity it is assumed, that a measured energy of 511 keV in a segment originates from a single photo absorption.

Events with three hit segments were selected. Conditions on energy and angle were applied, requiring $E_1 = 511 \pm 3$ keV and $E_2 + E_3 = 511 \pm 3$ keV as well as an angle of $\varphi > 150^\circ$ between the Compton scattering and the 511 keV interaction. Of the two interactions with energy depositions E_2 and E_3 the interaction with the angle φ closest to 180° was assumed to be the Compton scattering.

The scattering angle of the Compton effect given by the energy dependent Compton formula was compared to the measured angle given by the two interaction positions. The difference of these two scattering angles is shown in Fig. 52. In addition, the partition of the 511 keV for the Compton

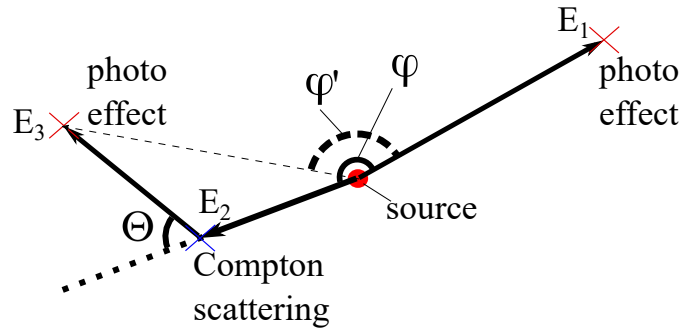


Figure 51: A schematic view of a reconstructed coincidence including a Compton scattering and one photo absorption is shown. A photo effect for one of the 511 keV γ rays and a single Compton scattering followed by a photo effect is assumed. For background reduction a gate on φ , which should be close to 180° , was applied.

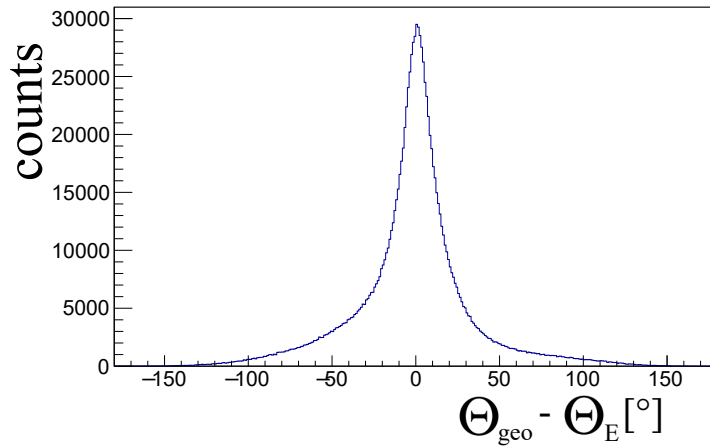


Figure 52: The difference of the measured scattering angle θ_{geo} and the scattering angle given by the Compton formula θ_E is shown. The mean of the distribution is -1.5° and the standard deviation is 34° . The scattering angle θ_E is in average slightly larger than θ_{geo} . This is caused by the energy threshold of 10 keV which does not allow very small scattering angles θ_E . No such restraint exists for the measured scattering angle θ_{geo} .

scattering and the photo effect is limited due to the maximal scattering angle of 180° which corresponds to an energy deposition of 340.7 keV. Therefore, $E_2 < 340.7$ (Compton scattering) and $E_3 > 170.3$ (photo effect) was set as additional condition. The distribution of the energies for the Compton scattering and the following photo effect are depicted in Fig. 53. The correlation of the energy ratio $\frac{E_2}{E_3}$ and the scattering angle θ is plotted in Fig. 54. The angle φ between the Compton scattering and the 511 keV photo effect and the angle φ' are depicted in Fig. 55.

For events with $\varphi \approx \varphi'$ it is not clear which of the two interactions with energy depositions E_2 and E_3 is the Compton scattering. In this case an inversion of the interaction sequence ($E_2 \leftrightarrow E_3$) was tested. The original interaction sequence is defined by the angle φ where the interaction with φ closest to 180° was considered as the Compton scattering. For events with $\varphi - \varphi' < 5^\circ$ the difference $|\theta_{geo} - \theta_E|$ was recalculated for in inverted interaction sequence. For a sufficient increase in the agreement of measured and calculated Compton-scattering angle (5° were used as threshold) the inverted interaction sequence was considered to be the actual physical sequence and used in the further analysis.

The coincidences found including all above mentioned gates are visualized in Fig. 56. The distances of the lines connecting the 511 keV photo effect and the Compton scattering to the source position are depicted for different gates of $|\theta_{geo} - \theta_E|$ in Fig. 57. The mean values and the standard deviations as well as the number of counts for these distributions are summarized in table 4.2. Strict gates decrease the statistics significantly, while including events with a large discrepancy of expected and measured scattering angle increase the mean distance to the source only slightly. A possible explanation for this is that the distance to the source is caused by the uncertainty of the PSA, as well as the smearing of the point of emission of the two 511 keV γ rays. In addition, the uncertainty of the PSA is small compared to the typical distance of the interaction positions to the source.

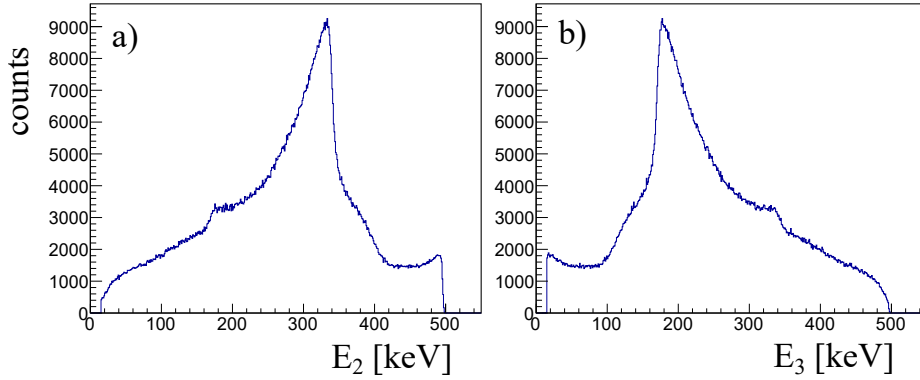


Figure 53: The energy depositions for a) the Compton scattering and b) the photo effect are shown. The maximum energy deposition of a 511 keV γ ray in a single Compton scattering is 340.7 keV ($\theta = 180^\circ$). Events with $E_2 > 340.7$ keV and $E_3 < 170.3$ keV were therefore rejected.

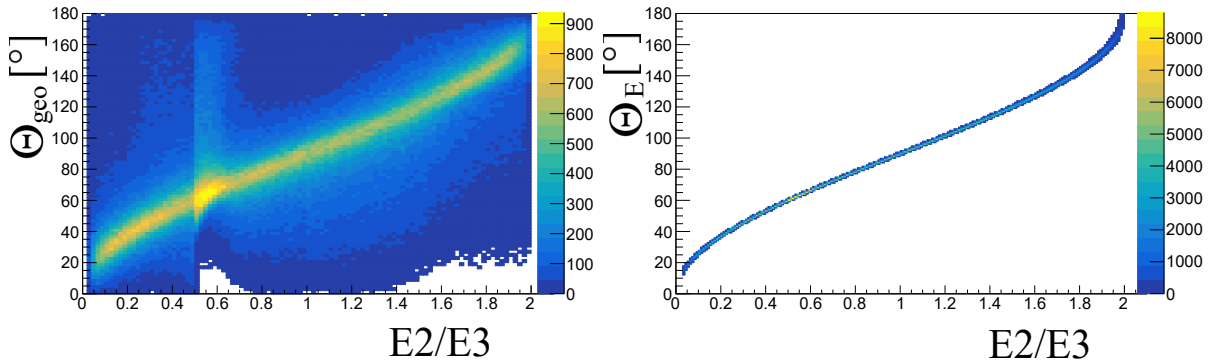


Figure 54: The scattering angles θ_{geo} (measured) and θ_E (Compton formula) are plotted in dependence of the energy ratio E_2/E_3 . A clear correlation is observed. Deviations of $\theta_{geo}(E_2/E_3)$ from the expected shape are caused by the finite position resolution of the PSA and by the ambiguity of the interaction sequence. In comparison, these deviations are very small for $\theta_E(E_2/E_3)$ due to the high energy resolution of the HPGe detectors.

$X [^\circ]$	10	20	30	40	50	no gate	photo
mean d [mm]	2.58	2.66	2.70	2.73	2.74	2.76	2.73
σ [mm]	1.72	1.77	1.80	1.82	1.84	1.89	1.85
counts	$4.95 \cdot 10^5$	$7.50 \cdot 10^5$	$8.89 \cdot 10^5$	$9.72 \cdot 10^5$	$1.03 \cdot 10^6$	$1.13 \cdot 10^6$	$4.89 \cdot 10^5$

Table 4.2: The mean and standard deviation are shown for different limits X with $|\theta_{geo} - \theta_E| < X$. The values correspond to the distributions shown in Fig. 57.

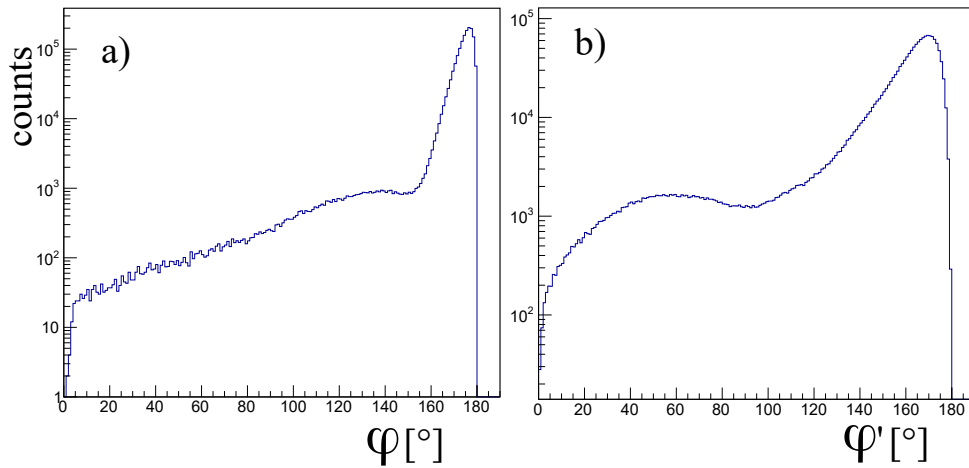


Figure 55: The angles φ (Compton scattering) and φ' (photo effect) are plotted for all events that fulfill the conditions of three hit segments in the array, $E_1 = 511 \pm 3$ keV and $E_2 + E_3 = 511 \pm 3$ keV. The interaction with φ closest to 180° was considered as Compton scattering. For the further analysis a gate on $\varphi > 150^\circ$ was set. Due to the limited range of the γ ray after Compton scattering the angle φ' has a high probability to be close to 180° as well. In this case the sequence of the interactions is ambiguous.

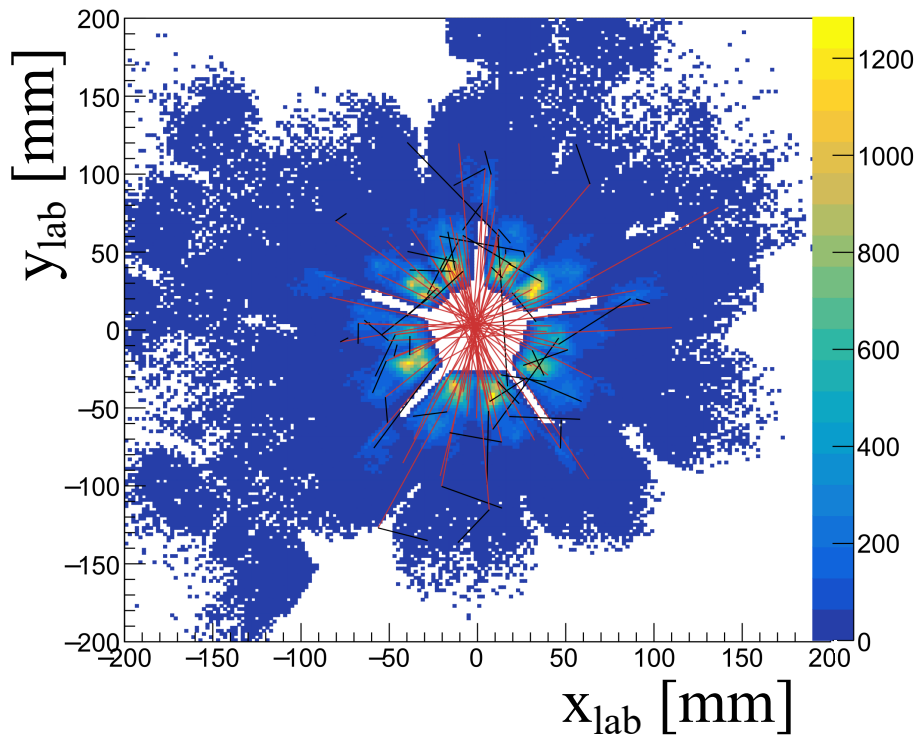


Figure 56: The reconstructed coincidences including a Compton scattering are visualized. For 50 events a red line was plotted, connecting the interaction position of the 511 keV photo effect and the position of the Compton scattering. Black lines connect the interaction position of the Compton scattering and the following absorption of the γ ray via photo effect.

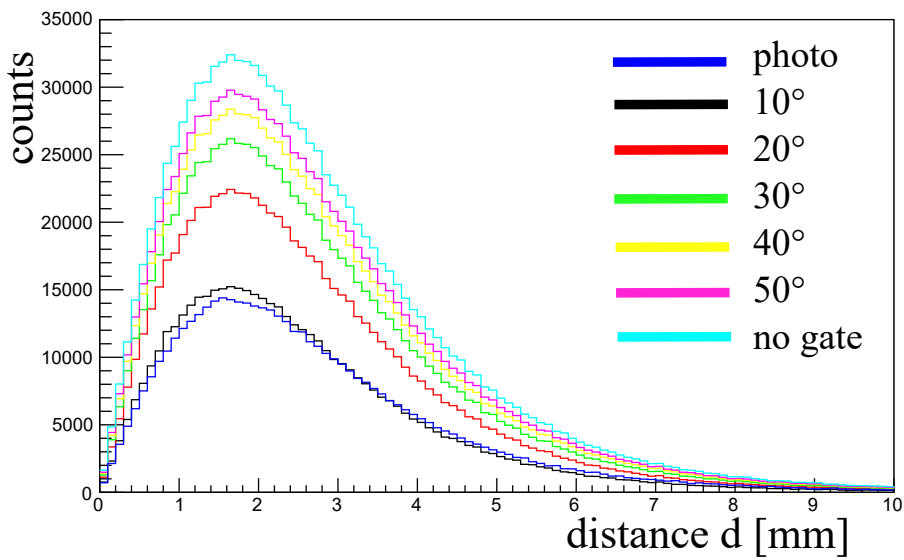


Figure 57: The distance to the source for the reconstructed Compton events is depicted for different gates of $|\theta_{geo} - \theta_E| < X$ where X corresponds to the labels given in the figure. The blue distribution with the label "photo" corresponds to the distribution derived from two single photo effects (without Compton scattering) from the previous section and is given for comparison. For larger values of X the statistics increase significantly whereas the mean values of the distributions shift only slightly.

4.1.5 Estimation of position resolution

In the previous sections a measure for the PSA performance was described by the distance of the connecting line to the source position. This distance depends mainly on the position resolution of both interactions (and on the finite range of the positron before annihilation). Since two interactions and their PSA results have an impact on the final measured distance, it is difficult to disentangle both contributions and to derive an actual position resolution.

Therefore, events were selected for which one interaction was close to the source and the other one was far away. In this case the position uncertainty of the interaction that is far away can be neglected. With this approximation a most likely interaction position for the near interaction was determined (see Fig. 58). The differences of PSA result and most likely interaction position $\vec{r}'_1 - \vec{r}_1$ were then used to estimate the actual position resolution. The distances of the interaction points to the source position are plotted for reconstructed coincidences from two photo effects in Fig. 59. For the used setup the condition $B \gg A$ can only be fulfilled to a certain extend. As a compromise between having a good approximation and sufficient statistics, events were selected with $A < 75$ mm and $B > 200$ mm. From the 489 k reconstructed coincidences 10.8 k fulfill these conditions. For a subset of events the most likely interaction positions are visualized and compared to the PSA result in Fig. 60. Note that the depiction corresponds to a projection on the xz plane. This leads to a distortion of the angles between the black and red lines (corresponding to \vec{r}_1 and \vec{r}'_1) which are always 90° . The difference $\vec{r}'_1 - \vec{r}_1$ is depicted in Fig. 61.

While the mean difference is close to zero, it is difficult to observe a systematic deviation with the chosen coordinate system: The used Cartesian coordinate system (referring to the lab system with the origin being at the center of the AGATA sphere) is not related to the cylindrical symmetry of the individual crystals. The x and y axes do not have a distinguished direction and are chosen arbitrarily. Since the individual crystals form a sphere by facing towards a single point, a spherical coordinate system is the better choice. The spherical radius R is parallel to the detector axis along the core $z_{\text{cylindrical}}$ in good approximation. This approximation is valid since the inner radius of the AGATA shell of 23.5 cm is large compared to the radius of the individual crystals of no more than 4 cm. Therefore, this coordinate system is more suitable to search for systematic deviations of most likely interaction position and PSA result. The spherical coordinate system is defined by:

$$R = \sqrt{x_{\text{lab}}^2 + y_{\text{lab}}^2 + z_{\text{lab}}^2}$$

$$\vartheta = \arccos\left(\frac{z_{\text{lab}}}{R}\right)$$

$$\varphi = \arctan2(x_{\text{lab}}, y_{\text{lab}}) + \pi$$

Where $\arctan2(x_{\text{lab}}, y_{\text{lab}})$ is an abbreviation for the case differentiation for the three cases i) $x_{\text{lab}} > 0$, ii) $x_{\text{lab}} < 0 \wedge y_{\text{lab}} > 0$ and iii) $x_{\text{lab}} < 0 \wedge y_{\text{lab}} < 0$. A simple sketch which depicts the different coordinate systems with respect to AGATA is given in Fig. 62. The results for $\vec{r}'_1 - \vec{r}_1$ in this coordinate system are depicted in Fig. 63. Note that the correlation of ΔR and $\Delta \vartheta$ can be explained by the

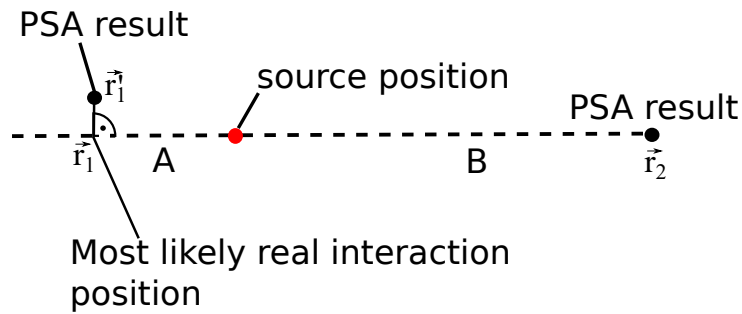


Figure 58: For interactions for which the distance B to the source is large compared to the distance A to the source ($B \gg A$) the position uncertainty of the far away interactions can be neglected. Using this approximation the close interaction position is restricted to a line given by the PSA result of the far away interaction \vec{r}_2 and the source position. The most likely interaction position \vec{r}_1 is then given by the closest distance to the corresponding PSA result \vec{r}_1 .

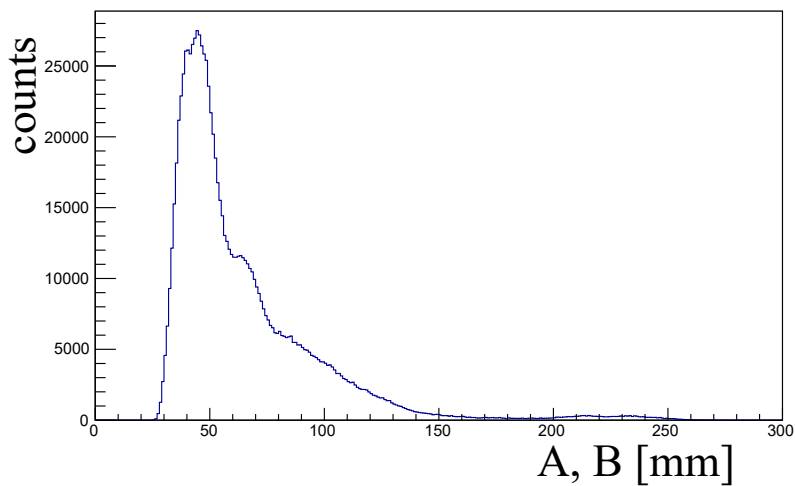


Figure 59: The length of the line segments A and B , which describe the distance from the source position to the interaction positions of the 511 keV γ rays, are plotted (see Fig. 47). Most distances are around 50 mm which corresponds to an interaction in one of the five inner crystals which are closest to the ^{22}Na source.

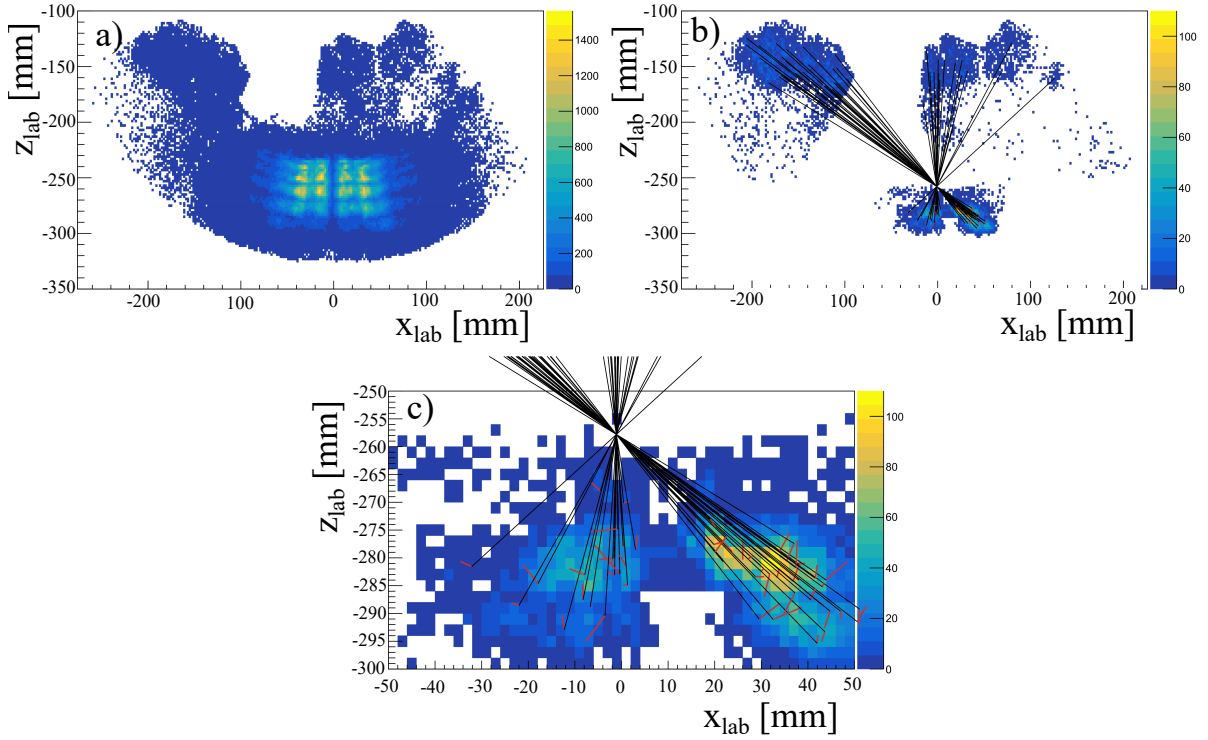


Figure 60: The interaction positions of reconstructed coincidences for two photo effects are shown in the xz plane for all y values in a). Of those events, all coincidences that meet the conditions $A < 75$ mm and $B > 200$ mm are plotted in b). Only for a small amount of detector volume of the far outer and most inner detectors these conditions are fulfilled. In addition, a black line is drawn from the far PSA result to the most likely interaction position. These all intersect at the source position by construction. A red line is drawn from the most likely interaction position to the corresponding PSA result. A zoom is shown in c).

correlation of R and z_{lab} for the interactions that fulfill the condition $A < 75$ mm. These are close to the z_{lab} axis and positioned at around $z_{\text{lab}} = -250$ mm to $z_{\text{lab}} = -300$ mm. For these events $\vec{e}_R \parallel -\vec{e}_z$ is a good approximation (where \vec{e}_R and \vec{e}_z are the radial and the z_{lab} unit vectors). Also ϑ can be rewritten as $\vartheta = \frac{\pi}{2} - \arctan\left(\frac{z_{\text{lab}}}{\sqrt{x_{\text{lab}}^2 + y_{\text{lab}}^2}}\right)$. It follows that:

$$R < R' \Rightarrow z_{\text{lab}} > z'_{\text{lab}} \Rightarrow \vartheta < \vartheta'$$

Which explains the observed correlation.

The results show that the interaction positions assigned by the PSA are within a few millimeters of the most likely interaction position. In first order no systematic deviation is observed in both coordinate systems; while the mean values of ΔR , $\Delta\vartheta$ and $\Delta\varphi$ are not zero within their respective errors, the deviation from zero is small compared to grid size of 2 mm. The results are summarized in table 4.3.

Note that the extraction of FWHM and FWTM values for distributions with limited statistics proves difficult. On the one hand a coarse binning is desirable to extract a good value for the maximum

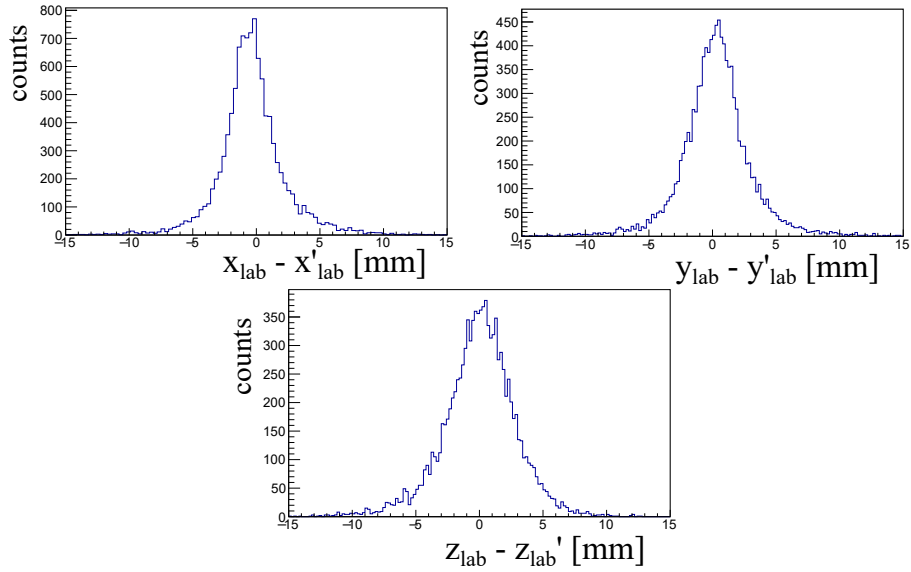


Figure 61: The difference of PSA result and corresponding most likely interaction position is plotted for the coordinates x, y and z of the lab system. The PSA result and the expected interaction position coincide within a few millimeters and are centered around zero. The distributions are not completely Gaussian like as left and right tails are observable. The corresponding values for mean, standard deviation, FWHM and FWTM (full width at tenth maximum) are summarized in table 4.3.

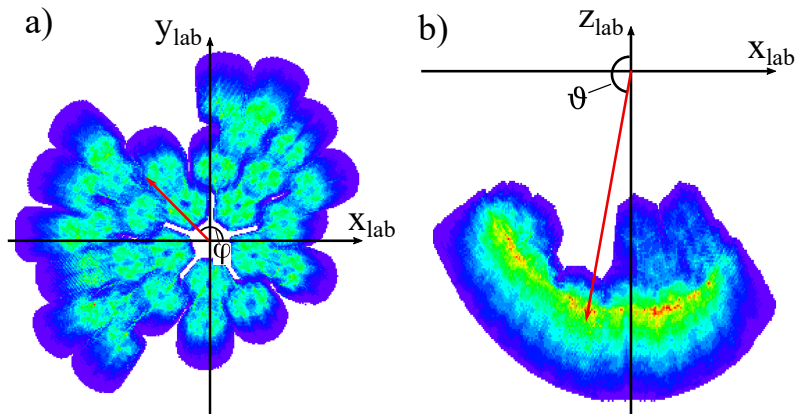


Figure 62: The Cartesian and spherical coordinates are shown in a simple sketch. A projection of all hits on the (x_{lab}, y_{lab}) plane is shown in a) and a projection of all hits on the (x_{lab}, z_{lab}) plane is shown in b). The angles of the spherical coordinate system φ and θ are depicted for exemplary interaction positions.

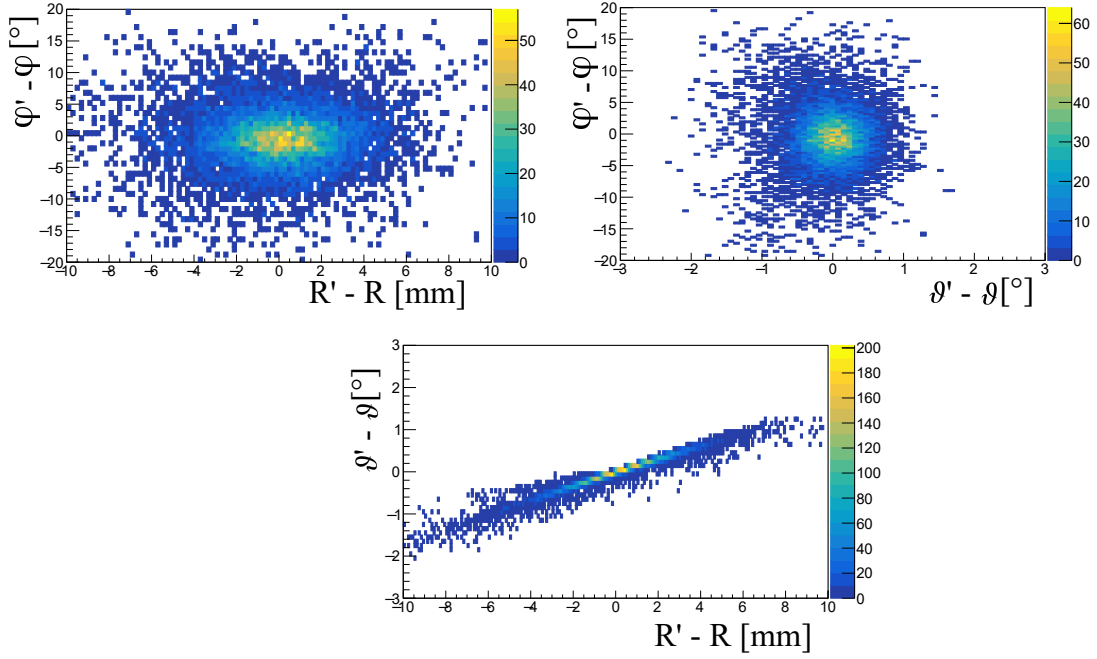


Figure 63: The differences of R , ϑ and φ are plotted and correlated. No correlation is observed between ΔR and $\Delta\varphi$ and $\Delta\vartheta$ and $\Delta\varphi$. The absolute difference $\vartheta' - \vartheta$ is small because the relevant interactions have a large radius of $R \approx 250 - 300$ mm. The correlation of ΔR and $\Delta\vartheta$ is given by the choice of the coordinate system and the position of the relevant interaction positions with respect to the origin (see text).

value. On the other hand a fine binning is needed to achieve a precise result for the width at either the half or the tenth maximum. Due to the limited statistics a binning of 0.3 mm was used as a compromise for $x_{\text{lab}}, y_{\text{lab}}, z_{\text{lab}}$ and R . The binning for ϑ was $0.06^\circ/\text{bin}$ and $0.6^\circ/\text{bin}$ for φ . The FWHM and FWTM values for R , ϑ and φ were extracted from the corresponding projections of Fig. 63. Due to the relatively large binning that was necessary (and the still remaining statistical fluctuation in the distribution) the FWHM and FWTM values and the corresponding ratio should be considered more as a qualitative observation. For a Gaussian distribution the FWHM and FWTM is given by:

$$\text{FWHM} = 2\sqrt{2\ln(2)}\sigma \quad (4.1)$$

$$\text{FWTM} = 2\sqrt{2\ln(10)}\sigma \quad (4.2)$$

$$\Rightarrow \frac{\text{FWHM}}{\text{FWTM}} \approx 1.82 \quad (4.3)$$

The significant deviation of FWHM/FWTM from 1.82 shows the non-Gaussian shape of the distributions.

It should be taken into account that the observed difference $\vec{r}'_1 - \vec{r}_1$ originates not only from the finite position resolution of the PSA result at \vec{r}'_1 . Additional contributions are the finite position resolution for the PSA result at \vec{r}_2 (since the condition $B \gg A$ is only satisfied to a certain extend) and the smeared out point of emission of the two 511 keV γ rays. Therefore, $\vec{r}'_1 - \vec{r}_1$ is only an estimation for the position resolution and its absolute value is in average larger than the difference of the actual

interaction position and the PSA result. In section 4.4 the estimated position resolution of the PSA in standard configuration, that was presented here, will be compared to the resolution achieved with an optimized PSA.

Table 4.3: The mean difference of PSA result and most likely interaction position is shown for a Cartesian and spherical coordinate system. The values correspond to the distributions shown in Figures 61 and 63. The mean values do not coincide with zero within errors, which is an indication for wrongly assigned PSA results. However, $|m|$ is small compared to the grid size of 2 mm. The FWHM, FWTM and their ratio show the left and right tails of the distribution. For a Gaussian distribution a ratio of approximately 1.82 is expected.

	Δx_{lab} [mm]	Δy_{lab} [mm]	Δz_{lab} [mm]	ΔR [mm]	$\Delta \theta$ [°]	$\Delta \varphi$ [°]
mean m	-0.363	0.278	-0.004	0.014	-0.0419	-0.382
Δm	0.026	0.027	0.028	0.025	0.0040	0.040
σ	2.673	2.783	2.888	2.598	0.411	4.198
FWHM	3.3	3.6	4.8	4.2	0.66	6.6
FWTM	8.4	9.3	11.1	10.6	1.56	16.8
FWTM/FWHM	2.5	2.6	2.3	2.5	2.36	2.5

4.2 Estimation of PSA performance via comparison of determined and expected hit distributions

In addition to the ^{22}Na -coincidence method introduced in the previous section, the PSA performance was estimated by comparing the hit distributions determined by the PSA with the expected hit distributions. A ^{60}Co source was placed in the center of the AGATA sphere. This way, all detectors face directly towards the source and the expected number of hits for a given detector depth z is the same. For more details on the setup and the expected hit distribution, see section 2.3.1.

Several quantities were developed to describe the agreement or disagreement of the determined hit distributions with the expectation. These will be introduced in the following sections. A similar approach was utilized previously in ref. [53] to determine and optimize the PSA performance.

4.2.1 Correlation of neighboring grid points

The performed measurements show that the PSA tends to allocate hits in clusters at certain regions of the detector (for example in the center of a segment, see section 2.3.1). In this regions the number of hits per grid point is above the expected number of hits. In the same way there are regions in which the number of hits is below the expectation. The number of hits of neighboring grid points are correlated, which is shown in Fig. 64. In an ideal scenario this is not expected. The observed correlation is a result of a biased PSA result.

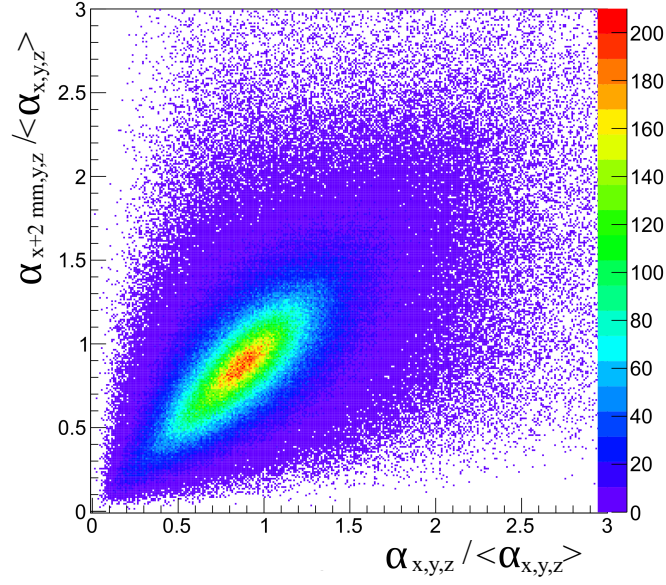


Figure 64: The number of hits for a given position in the detector $\alpha_{x,y,z}$ normalized to the expectation $\langle \alpha_{x,y,z} \rangle$ is compared with the normalized number of hits of the neighboring grid point at $x' = x + 2 \text{ mm}$, $\alpha_{x+2 \text{ mm},y,z}$. A clear correlation is observed: If the number of hits at the position (x, y, z) is above average, there is a high chance that the number of hits in the neighboring grid point $\alpha_{x+2 \text{ mm},y,z}$ is also above average.

The correlation of two neighboring grid points situated at (x, y, z) and $(x + 2 \text{ mm}, y, z)$ (using the coordinate system of the individual crystal, see Fig. 2) is described by the covariance:

$$\text{cov} = \langle (\alpha_{x,y,z} - \langle \alpha_{x,y,z} \rangle) \cdot (\alpha_{x+2 \text{ mm},y,z} - \langle \alpha_{x+2 \text{ mm},y,z} \rangle) \rangle \quad (4.4)$$

Where $\alpha_{x,y,z}$ is the number of hits in the grid point at the position (x, y, z) and the brackets $\langle .. \rangle$ denote the expectation. The expectation is approximated by the mean number of hits for a given detector depth z :

$$\langle \alpha_{x,y,z} \rangle = \langle \alpha_z \rangle = \sum_{x,y \in P} \frac{1}{N} \alpha_{x,y,z} \quad (4.5)$$

With N being the number of grid points in the set P which is given by the grid points in the xy plane for the detector depth z . The correlation term in eq. 4.4 is positive if the number of hits is either above or below average for both grid points.

Multiple grid points are considered to evaluate the expectation of the term given in eq. 4.4: A correlation factor C is introduced, which is the sum of the correlation term in eq. 4.4 for all positions

(x, y, z) . It is given by:

$$\begin{aligned}
 C = \sum_{x,y,z \in D} & (\alpha_{x,y,z} - \langle \alpha_z \rangle) \cdot (\alpha_{x+2\text{mm},y,z} - \langle \alpha_z \rangle) \\
 & + (\alpha_{x,y,z} - \langle \alpha_z \rangle) \cdot (\alpha_{x,y+2\text{mm},z} - \langle \alpha_z \rangle) \\
 & + (\alpha_{x,y,z} - \langle \alpha_z \rangle) \cdot (\alpha_{x,y,z+2\text{mm}} - \langle \alpha_{z+2\text{mm}} \rangle)
 \end{aligned} \tag{4.6}$$

Here D is the set of grid points in which the detector is divided. The correlation in y and z direction is also considered (second and third term). A positive value of the correlation factor C corresponds to a correlation of the number of hits of neighboring grid points. A negative value implies an anti correlation, while zero corresponds to no correlation. The correlation factor C is a good quantity to describe the clustering of hits in a detector. It is useful to compare different hit distributions, which were extracted from the same data set, but using different PSA input parameters. The result is only meaningful in relation to each other ("more" or "less" clustered distribution of hits). The absolute value of the correlation factor is arbitrary.

In an ideal scenario no correlation of the number of hits of neighboring grid points is expected. Therefore, PSA parameters have to be chosen in such a way that the correlation factor is as close to zero as possible to ensure best agreement of measured and expected hit distributions.

4.2.2 Deviation from the expectation

For each grid point at the position (x, y, z) there is an expected number of hits $\langle \alpha_z \rangle$, see eq. 4.5. The number of hits in this grid point $\alpha_{x,y,z}$ deviates by a certain amount, described by the standard

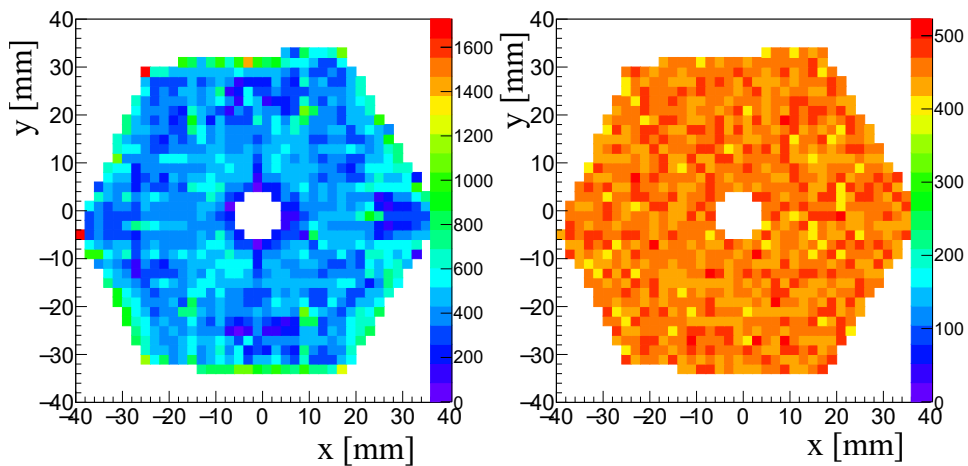


Figure 65: The measured hit distribution for crystal B001 is shown for a detector depth of $z=30-32$ mm in a). A random allocation of the same number of hits is shown in b). In contrast to the measurement, this distribution is more homogeneous and shows only some statistical fluctuation.

deviation $\sigma_{x,y,z}$, which is given by:

$$\sigma_{x,y,z} = \sigma_z = \sqrt{\sum_{x,y \in P} \frac{(\alpha_{x,y,z} - \langle \alpha_z \rangle)^2}{N-1}} \quad (4.7)$$

With P being the set of grid points of the considered crystal with detector depth z and N the number of grid points $\in P$. A certain deviation from the expectation is present even in an ideal scenario, due to statistical fluctuation. The measured hit distribution for grid points with a constant detector depth z is compared to a distribution with random interaction positions (which corresponds to the expectation in a simple approximation) in Fig. 65. The number of hits per grid point α_z of those distributions are depicted in Fig. 66 and show that the measured standard deviation σ_z is much larger than from the expected random distribution.

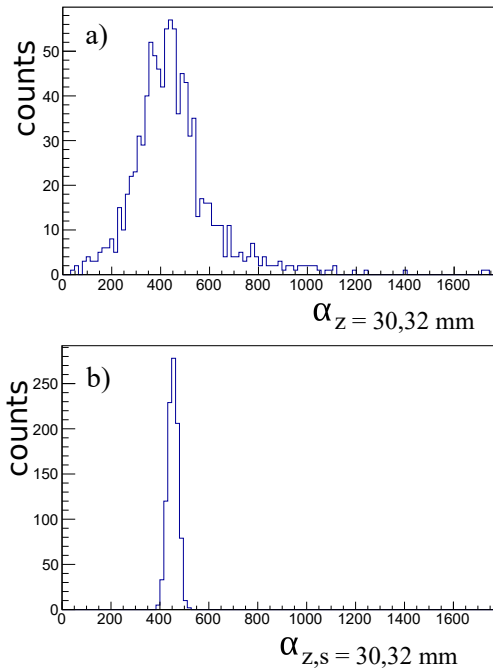


Figure 66: The number of hits per grid point is shown for the measured hit distribution of crystal B001 at $z = 30 - 32$ mm in a) (corresponding to the hit distribution in Fig. 65 a)). In b) the number of hits per grid point for randomly distributed interaction positions is depicted (corresponding to Fig. 65 b)). The histogram in b) is in good approximation a Poisson distribution with a mean of $\langle \alpha_{z,s} \rangle = 452.5$ and a standard deviation of $\sigma_{z,s} = 20.7$ ($\sigma_{z,s} \approx \sqrt{\langle \alpha_{z,s} \rangle}$). The histogram in a) has a standard deviation of $\sigma_z = 176.1$ and a mean value of $\langle \alpha_z \rangle = 452.5$ ($\sigma_{z,s} \gg \sqrt{\langle \alpha_z \rangle}$)

For the random distribution the Poisson relation $\sigma_{z,s} = \sqrt{\langle \alpha_z \rangle}$ applies. The standard deviation of the measured distribution is proportional to the expectation instead: $\sigma_z \propto \langle \alpha_z \rangle$. This is shown in Fig. 67, where the average standard deviation $\bar{\sigma}_z = \frac{1}{N'} \sum_{z,i} \sigma_{z,i}$ is compared to the number of events. Here $\sigma_{z,i}$ is the standard deviation at detector depth z of detector i and N' the product of the number of detectors (29) and the number of different detector depths (45).

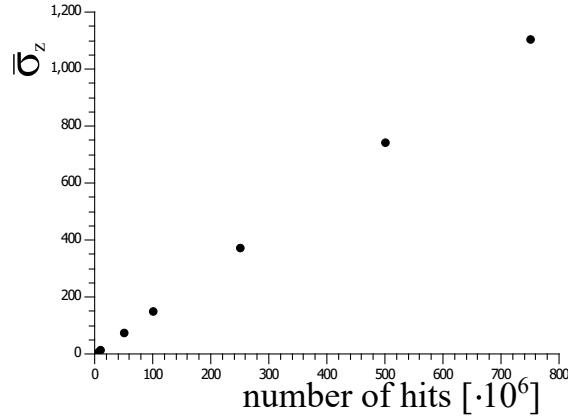


Figure 67: The average standard deviation $\bar{\sigma}_z$ is plotted versus the number of hits which were measured in all detectors. A clear linear correlation is observed. Since the expectation $\langle \alpha_z \rangle$ is proportional to the number of hits, it follows that $\sigma_z \propto \langle \alpha_z \rangle$.

The measured hit distribution is more clustered and less homogeneous than the random distribution. Therefore, to maximize PSA performance, PSA input parameters should be chosen such that the standard deviation σ_z is minimized.

For convenience it is useful to have a quantity to describe the PSA performance of a complete detector. For this, the deviation is introduced:

$$\text{deviation} = \sum_{x,y,z \in D} (\alpha_{x,y,z} - \langle \alpha_z \rangle)^2 \quad (4.8)$$

The deviation describes the homogeneity of the hit distribution. It is useful to compare different hit distributions of the same crystal ("more" or "less" homogeneous), but its absolute value is arbitrary. It is used as a criterion to describe the PSA performance and is minimized in the variation of PSA input parameters.

4.2.3 High statistics grid points

In addition to the described clustering of hits, a significant surplus of hits in single high statistics grid points is observed, see Fig. 7. This is also visible in Fig. 66 where $\alpha_z \approx 4 \cdot \langle \alpha_z \rangle$ is observed for some grid points. The accumulation of that many hits in a single grid point can not be explained by statistical fluctuation and is caused by a wrong assignment of the interaction positions by the PSA. To quantify this, the number of hits in high statistic grid points is compared to the overall number of hits. A grid point is considered to have "high statistics" if $\alpha_{x,y,z} > 2.25 \cdot \langle \alpha_z \rangle$. With this the following ratio is introduced:

$$\text{ratio} = \frac{\sum_{x,y,z \in H} \alpha_{x,y,z}}{\sum_{x,y,z \in D} \alpha_{x,y,z}} \quad (4.9)$$

With H being the set of high statistics grid points. This ratio is used to describe the PSA performance and is minimized in the variation procedure.

It should be noted that all introduced quantities, the correlation factor C , the deviation from the expectation and the ratio of high statistics grid points, are only necessary but not sufficient criteria for a good PSA performance. This becomes clear when considering the extreme scenario, in which the PSA assigns interaction positions at random. The distribution of hits would be very homogeneous in this case, but the position resolution would correspond to the segment size. Therefore, a direct performance criterion, such as the ^{22}Na -coincidence method, is needed as complementary approach to verify the results.

4.3 Improvement of PSA performance employing a variation procedure

In the following sections the ^{22}Na method (and to some extent the quantities introduced in section 4.2) will be employed to determine and optimize the PSA performance. As performance criterion the mean distance of lines connecting reconstructed coincidences to the source position will be used, which corresponds to the mean of the distribution shown in Fig. 48. Other performance criteria, like the standard deviation of this distribution (Fig. 48) or the angle φ between the coincidences, are also viable and will be discussed. The PSA performance will be improved and optimized by varying several parameters that influence the final assigned interaction position. The impact of different approaches for the grid search algorithm on the PSA performance will be investigated.

The variation always follows a similar course of action. First, an input parameter is changed and the complete data set is "replayed". This means that the PSA is performed again using the stored traces. Due to the changed input parameter, different interaction positions are obtained. Finally, the ^{22}Na -coincidence method is applied to the new set of interaction positions, obtaining a new mean distance of coincidence lines to the source. This procedure is repeated for several values of the input parameter and the optimal value is determined.

The replay of the data is very time consuming, which is caused by the large number of calculations performed by the PSA. On 32 CPU cores the replay takes about one day. Therefore, the number of different variation steps is limited. A full scan of the N -dimensional landscape is not feasible (with N being the number of different input parameters). Instead, variations were performed for single parameters. However, input parameters which show a distinct correlation were studied simultaneously. The most relevant results, which are obtained in the following sections, are summarized in ref. [56].

4.3.1 Weighting of transient signals

The results presented in section 3.2 and in Fig. 18 revealed that the figure of merit is more sensitive to a radial change of the interaction position tested by the grid search, than to a change of the angle ϕ or the detector depth z (the terms radius, ϕ and z are used considering the cylindrical coordinate system of the individual crystals, see Fig. 2). The performed analysis indicated that a stronger weighting of the transient signals in the figure of merit calculation might yield improved results.

The importance of the transient signals for a good determination of the interaction position becomes apparent by considering the simulated pulse shapes for different radii and different angles (see Fig. 68 and 69). The depicted traces illustrate that the information of both the hit segment and the transient signals are needed for a correct position determination. The transient signals are crucial for extracting the correct angular position inside the segment. The transient signals are relatively small, the pulse height is typically in the range of 5% of the height of the hit segment. Therefore, their impact on the figure of merit is limited. To cope with this, a weighting was implemented in the grid-search algorithm by using the following adjusted figure of merit:

$$\text{Figure of Merit} = \sum_i w_i \sum_{t_j} |A_{i,s}(t_j) - A_{i,m}(t_j)|^p \quad (4.10)$$

With $A_{i,s}(t_j)$ and $A_{i,m}(t_j)$ being the simulated and measured signal height of segment i at time step t_j . The contribution of each segment to the figure of merit is weighted by a coefficient w_i .

The ^{22}Na data was reanalyzed using different values for the weighting coefficient. The coincidences were reconstructed as described in the previous sections for the both cases of only two photo effects and one photo effect in combination with a Compton scattering followed by photo absorption. The standard deviation and the mean of the distributions shown in Fig. 48 and 57 were evaluated. The results are shown in Fig. 70 and 71. The smallest mean distance to the source, corresponding to the best PSA performance, was achieved for a weighting factor of around $w_i = 2$ to $w_i = 2.75$. Note that the analysis was performed with $p = 0.2$ (referring to eq. 3.2). This produces slightly worse results than the standard value of $p = 0.3$ which was used in the previous section. This results in a small offset of the found mean distances. Due to the long time needed for the analysis the variation of the weighting coefficient was performed with this configuration as no (significant) systematic deviation of the final results is expected. The obtained results show that indeed a stronger weighting of the transient signals improves the PSA performance. The signals of hit segment and core are still needed for the best possible position resolution as the mean distance to the source increases for larger weighting coefficients.

In the case of two photo effects, even for very large values of *e.g.* $w_i = 10$ the mean distance to the source is smaller than without any weighting (*i.e.* $w_i = 1$). For the Compton scattered events this is not the case. On the one hand this deviation may arise from the different interaction energies, leading to different signal to noise ratios. On the other hand the reconstructed coincidences including a Compton scattering have a high chance of having two interactions in one detector. The gates which were set for the reconstruction of two photo effects allow only for one interaction per crystal. For hits in directly neighbored segments the transient signal and the net charge signal overlap, which may cause a different effect of the weighting on the PSA result and explain the different behavior at large weighting coefficients.

The variation considering the standard deviation and the deviation of the mean angle $\bar{\varphi}$ from 180° (Fig. 71) shows similar, but not identical results compared to the variation considering the mean distance d (Fig. 70). The smallest standard deviation is found for $w_i = 1.7$ instead of 2.75 for the case of two photo effects. The minima for the other curves are the same as for the mean distance to the

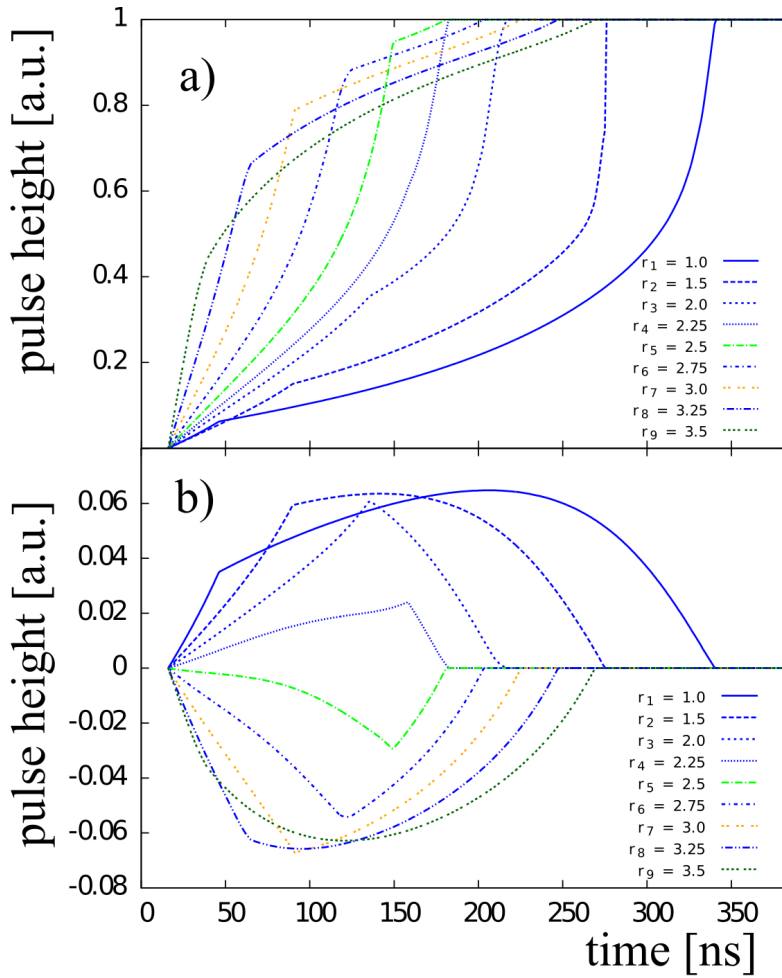


Figure 68: Simulated traces are shown for different interaction positions: The detector depth z and the angle φ were kept constant at $z = 40$ mm and $\varphi = 15^\circ$. The pulse shapes are plotted for different radii from $r = 1.0$ cm to $r = 3.5$ cm. The upper picture a) shows the signals of the hit segment, while b) shows the transient signals of the left neighbor. Very characteristic and distinguishable pulse shapes of both the segment and a transient signal are shown, enabling a precise determination of the interaction radius.

source position. Due to the shallow and not very distinct minimum for the curve of the mean distance to the source in case of two photo effects, the results of $w_i = 2.75$ and $w_i \approx 2$ are still consistent.

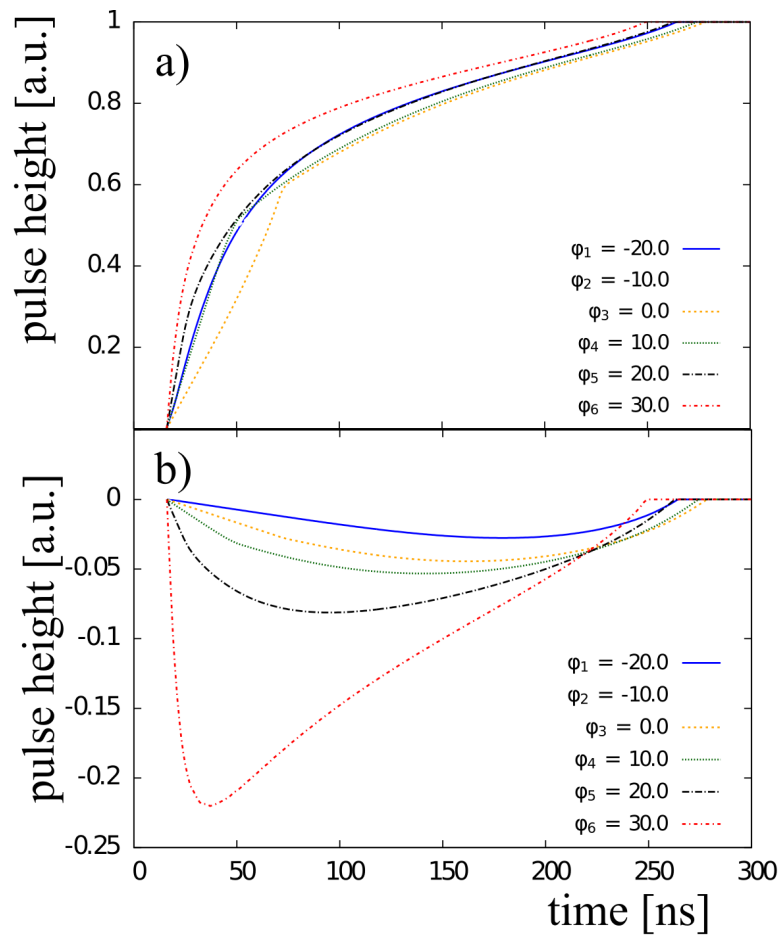


Figure 69: Simulated traces are shown for a fixed radius of $r = 35$ mm and a fixed detector depth of $z = 40$ mm, depicting angles from $\varphi = -20^\circ$ to $\varphi = 30^\circ$. The pulse shapes of the hit segment are shown for different angles in a). The pulse shape changes only slightly, making it difficult to disentangle the different interaction positions. A distinct change of the pulse shape of the transient signals is visible.

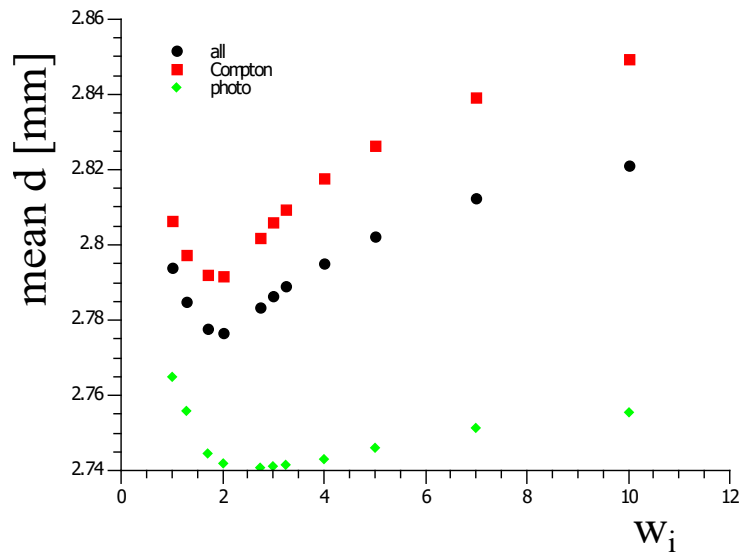


Figure 70: The mean distance to the source d as function of the weighting coefficient w_i is shown. The mean distance d , which is a measure for the PSA performance, was evaluated for reconstructed coincidences including one Compton scattering ("Compton"), two photo effects ("photo") and the combination of both ("all"). The position of the minimum is similar for the three cases, though deviations are observed for large weighting coefficients.

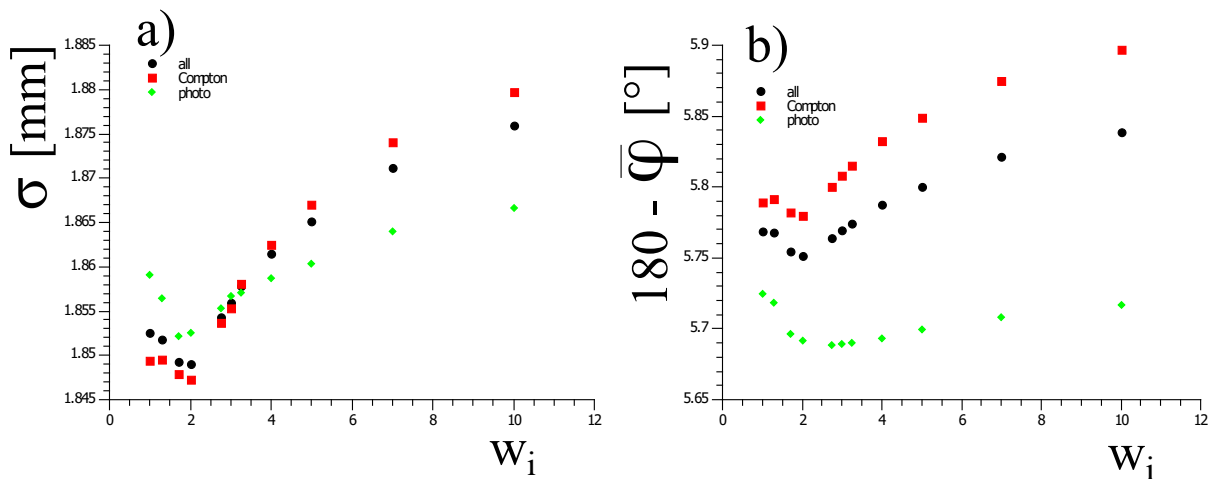


Figure 71: The standard deviation (of the distribution shown in Fig. 48) as function of the weighting coefficient w_i is shown in a). The plot in b) shows the difference of 180° and the mean angle $\bar{\varphi}$ between the two interactions (which should be close to 180°). The minimum, corresponding to best PSA performance, is observed for similar weighting coefficients.

4.3.2 Distance metric

The measured and simulated traces are compared by minimizing the following figure of merit:

$$\text{Figure of Merit} = \sum_i \sum_{t_j} |A_{i,s}(t_j) - A_{i,m}(t_j)|^p \quad (4.11)$$

The exponent p impacts the final assigned interaction position, which becomes apparent when considering Fig. 16 in section 3.1. The exponent p defines the metrics that are used to describe the distance of two super traces in an N -dimensional space, where N is the number of samples in the super trace. For $p = 2$ the metric corresponds to a standard Euclidean metric used in a χ^2 minimization. The super trace consists of all measured preamplifier signals of the detector, which are $37 \cdot 40 = 1480$ samples (36 segments and the core signal times 40 ticks corresponding to 400 ns). In case only the nearest neighbors are considered - which is the standard procedure due to the very small signals induced in the next nearest neighbors - N reduces to $N = 6 \cdot 40 = 240$ for interactions in ring 2-5 and $N = 5 \cdot 40 = 200$ for interactions in ring 1 and 6.

In the case that the difference of measured signal and the simulated signal at the physical interaction position is not Gaussian like, it is possible that best results are obtained using a non Euclidean metric. This is caused by the fact that single large deviations are strongly emphasized by squaring the difference. A Gaussian like difference implies that the deviation between measured and simulated pulses at the interaction position arise solely from the noise of the measured signal. Such distributions are shown in Fig. 72 and 73. The distributions are non-Gaussian like, but have significant left and right tails. This can also be seen by considering the ratio FWTM/FWHM which is summarized in table 4.4. In addition, the energy dependence of this difference was investigated which is shown in Fig. 74 and 75.

The observed deviations from a Gaussian distribution show that there are systematic deviations between measurement and simulation which scale with the energy of the interaction. Possible reasons for these systematic deviations are: an imperfect data base of simulated signals, the T_0 determination,

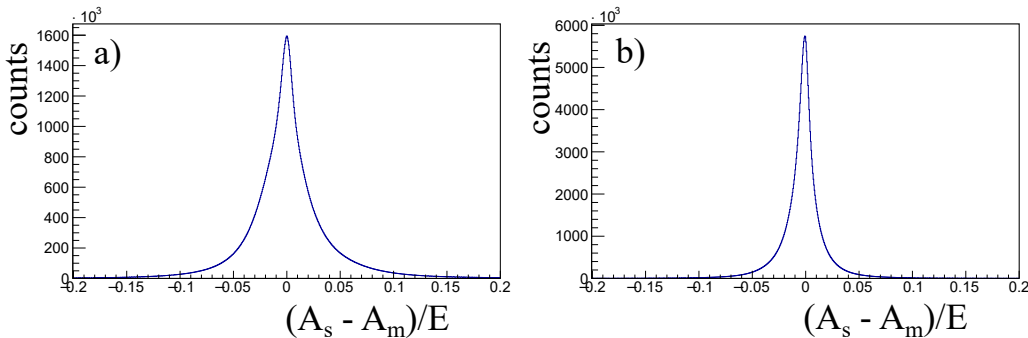


Figure 72: The individual differences $(A_s(t_j) - A_m(t_j))/E$ for the simulated A_s and measured A_m pulse height at time t_j are shown. The traces were normalized to the energy of the interaction E . For each event the first 40 ticks after T_0 (corresponding to 400 ns) were considered. In total about $1.81 \cdot 10^6$ events are depicted.

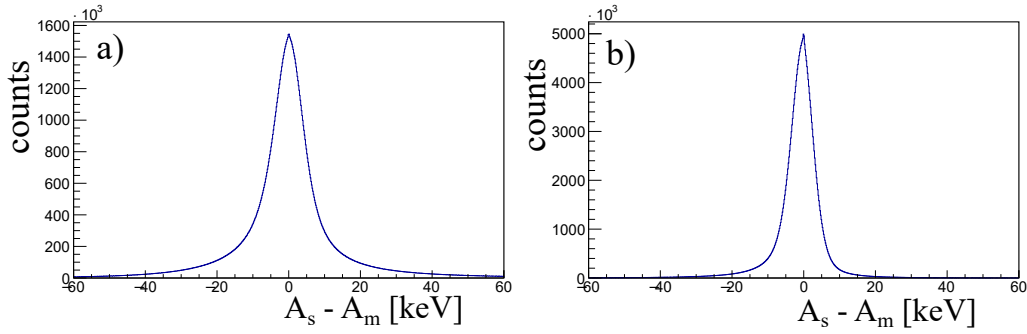


Figure 73: The individual differences ($A_s(t_j) - A_m(t_j)$) for the simulated A_s and measured A_m pulse height at time t_j are shown. In an ideal case the residuum of the measured and simulated traces would be only caused by noise, which is clearly not the case.

Table 4.4: The mean, standard deviation, FWHM and FWTHM of the distributions depicted in Fig. 72 and 73 are shown. In Fig. 72 the traces were normalized to the energy. The deviation of the FWTHM/FWHM ratio from 1.82 is caused by the significant tailing of the distributions.

	mean	σ	FWHM	FWTHM	FWTHM/FWHM
hit segment and core (normalized) transients (normalized)	0.0012	0.043	0.0285	0.1025	3.60
hit segment and core transients	-0.0028	0.024	0.014	0.07	5.0
hit segment and core transients	0.087 keV	15.88 keV	10.50 keV	31.3 keV	2.98
hit segment and core transients	-1.36 keV	7.32 keV	7.0 keV	16.2 keV	2.31

the description of the electronic response of the system, simplified treatment of multiple interactions in different segments and the assumption of only one interaction per segment.

These considerations regarding the distribution of the differences of measurement and simulation motivated an investigation of the optimal distance metric for the figure of merit calculation. The distance metric parameter p was varied in the range from 0.01 to 2 and the mean distance d was determined for each full set of newly obtained interaction positions. The results are depicted in Fig. 76 and Fig. 77. The optimal values for p , corresponding to the minimum positions of the variations, are 0.4 or 0.5. It depends on the considered quantity which is used to determine the PSA performance (mean distance d , σ and $\bar{\varphi}$) and on the type of included coincidences. The different types of coincidences are the same as introduced in the previous sections: Two photo effects, labeled as "photo" in the figures; one photo effect and one Compton scattering followed by a photo effect, labeled as "Compton"; and the combination of both, labeled as "all".

The results presented in section 4.3.1 showed that a weighting of the transient signals yields improved PSA results. Likewise it is not clear that an identical distance metric for hit segment and core on the one hand and transient signals on the other hand gives best results. A different exponent for both can also act as a different form of weighting. In addition, all performance criteria show only a small change in the range from $p = 0.3$ to $p = 0.6$. This might originate from two different optimal distance metrics for hit segment and core and the transient signals. Therefore, a new figure of merit

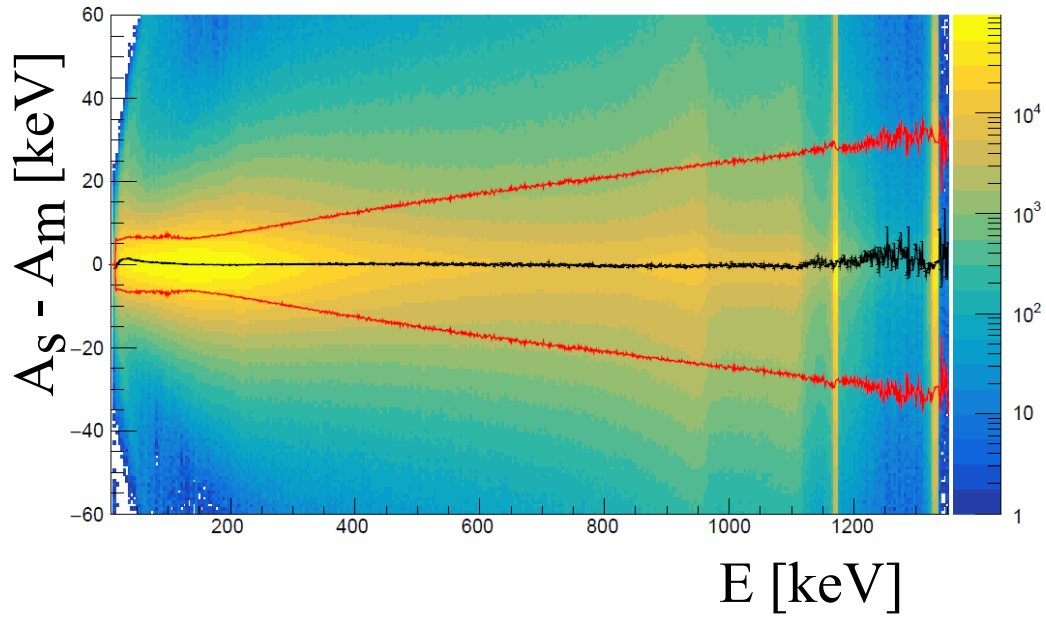


Figure 74: The energy dependence of the difference depicted in Fig. 73 is shown. The black line marks the mean difference of simulation and measurement and is constant at zero (in good approximation), as expected. The red lines mark the 1σ interval, which is constant for low energies and scales nearly linearly for energies above ~ 150 keV. This indicates systematic deviations between measurement and simulation which could not be resolved by the reference basis or the grid search. Fluctuations above the 1.17 MeV line from ^{60}Co arise from the decreased statistic in this energy range.

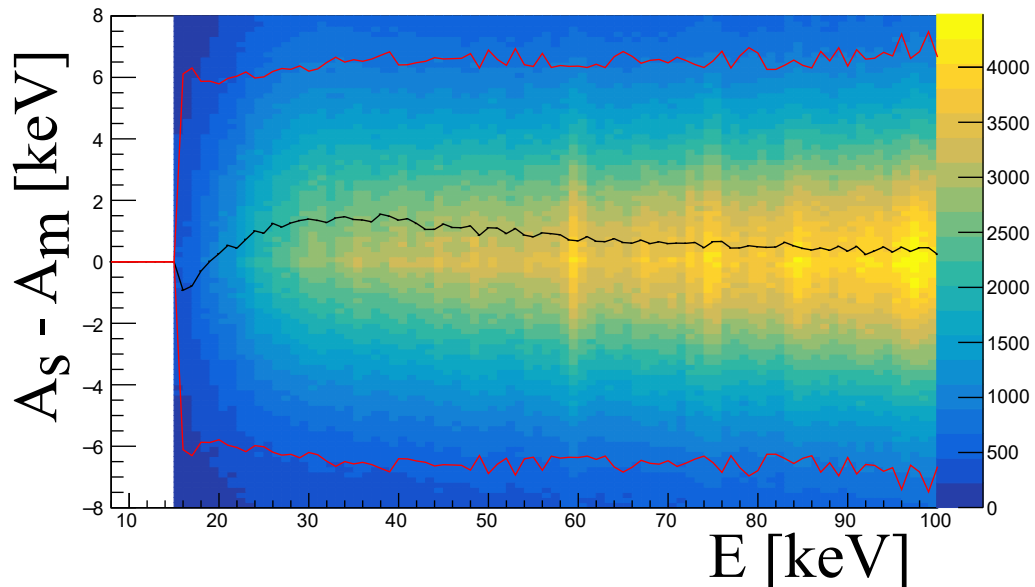


Figure 75: A zoom of Fig. 74 on low energies $E < 100$ keV and small differences is shown. A slight systematic overestimation of the measured pulses by the simulation in the order of 1-2 keV is observed (black line), which is not seen for higher energies. A possible reason for this might be the T_0 determination, which is more difficult for low-energy interactions due to the small signal to noise ratio. However, the observed systematic deviation is too small to have a significant impact on the final PSA result.

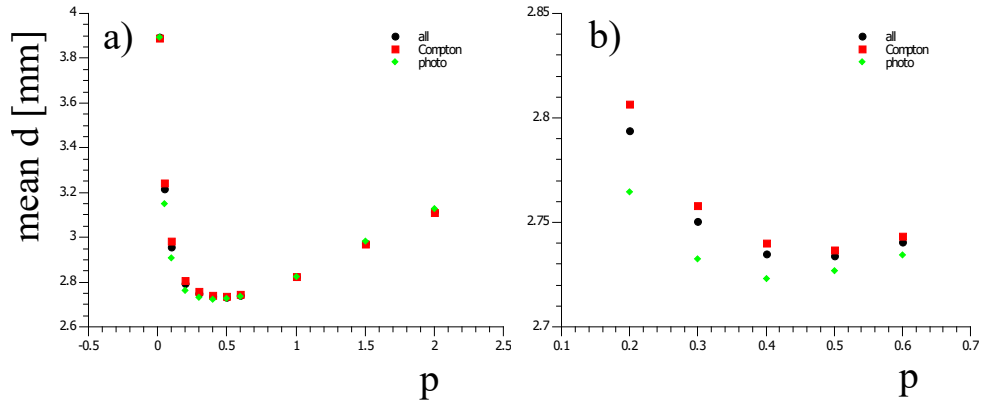


Figure 76: The mean distance d as function of the distance metric parameter p is shown. Best PSA performance is achieved for $p = 0.4$ (photo) or $p = 0.5$ (Compton, all). The change of the mean distance d between both values of p is small, as seen in the zoom in b). The result shows that an Euclidean metric with $p = 2$ is not favorable. For very small values of p the term $|A_m(t_j) - A_s(t_j)|^p$ converges to one and the figure of merit becomes constant. Therefore, very small values are not reasonable, which is also reflected in the significant increase of the mean distance d in that region.

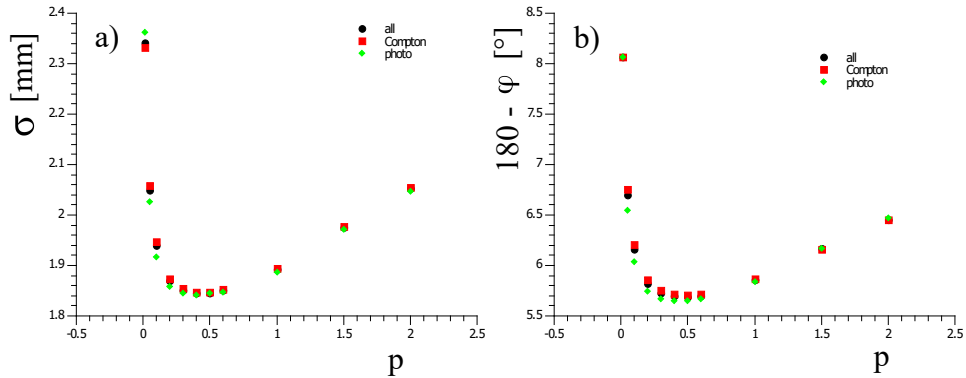


Figure 77: The standard deviation σ and the deviation of the measured mean angle $\bar{\varphi}$ from 180° is shown in dependence of the distance metric parameter p . The obtained positions of the minima at $p = 0.4$ and $p = 0.5$ are consistent with the results of the variation considering the mean distance d .

with different exponents p and q was introduced:

$$\text{FOM} = \underbrace{\sum_{i,t_j} |A_{i,m}(t_j) - A_{i,s}(t_j)|^p}_{\text{hit segment and core}} + \underbrace{\sum_{k,t_j} |A_{k,m}(t_j) - A_{k,s}(t_j)|^q}_{\text{neighboring segments}} \quad (4.12)$$

The exponents p and q were varied in an iterative procedure. Due to the long computing time for each variation step, only a few iterations were performed. The results are shown in Fig. 78. The final optimal configuration was found to be $p = 0.4$ and $q = 0.7$ considering only two photo effects. The weighting coefficient was set to one for this investigation. The exponent q for the transient signals

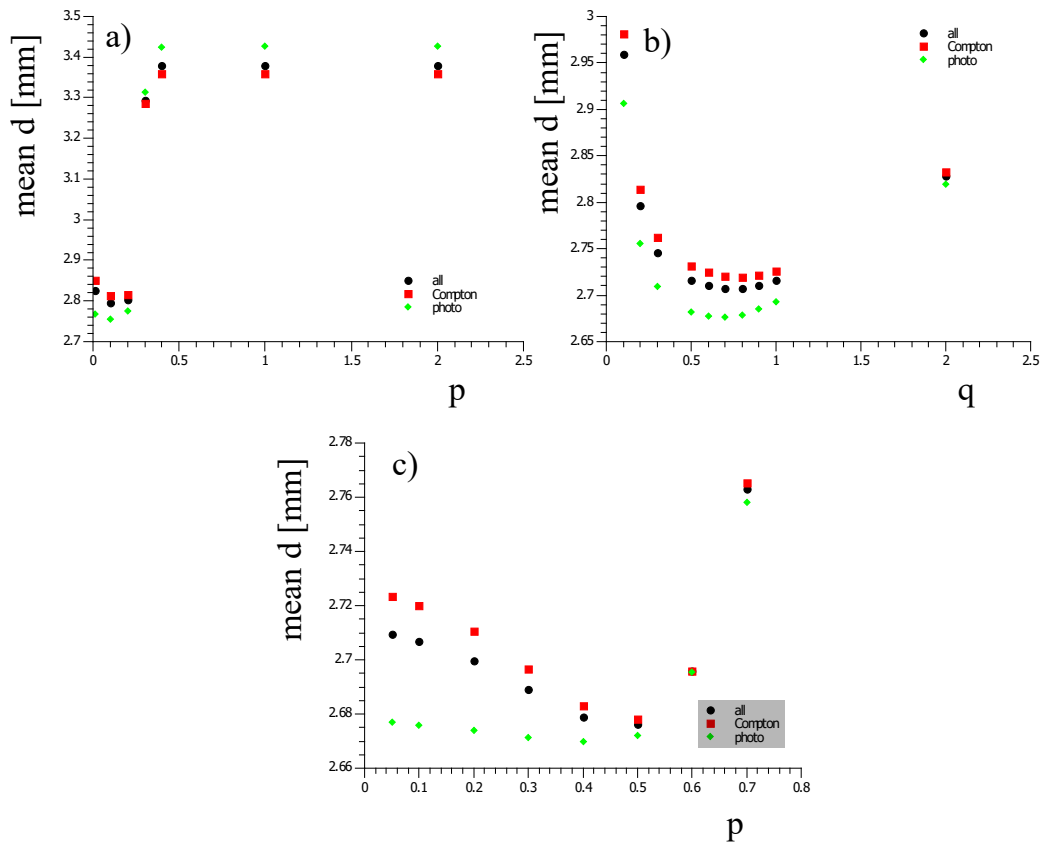


Figure 78: The variation of the newly introduced distance metric parameters p and q is shown. The variation was performed iteratively: Picture a) shows the variation of the distance metric parameter p for the hit segment and core, q was kept constant at $q = 0.2$. A minimum is found at $p = 0.1$ while values above 0.2 are strongly rejected. Picture b) shows the variation of q with $p = 0.1$ and a minimum at $q = 0.7$ is obtained. The depiction in c) shows the last iterative step with $q = 0.7$.

is larger than the exponent for the hit segment and core. This amplifies the impact of the transient signals to the figure of merit, similar to the linear weighting coefficient w_i . The overall decrease of the mean distance is larger than for the linear weighting. The better performance for larger exponents for the transient signals also arises from the smaller signal to noise ratio for these pulses, making single large deviations of measurement and simulation less likely.

Similar to the variation of the weighting coefficient, the optimal values obtained differ slightly using either only photo effects or also considering a Compton scattering. If multiple interactions in a crystal are also included a smaller weighting (here by choosing a smaller exponent q) of the transients seems to give better results. This is also seen by considering the last iterative step in Fig. 78 c) where only a moderate change of the mean distance d is observed for the case of two photo effects while small values of p are clearly disfavored if one Compton scattering is included. This is probably caused by the fact that the individual transient signals or transient signals and signals of the hit segment overlap for multiple interactions in the crystal.

4.3.3 Weighting of individual segments based on the fluctuation of the baseline

The fluctuation of the baseline of all individual segment signals and its impact on PSA performance was investigated. Typically, triggerless data, taken for example with an oscilloscope, is used to determine the baseline fluctuation of a single channel. This is not feasible for the large number of channels (36 segments · 29 crystals = 1044 segment channels in total), a different approach was employed: The collected pulse shapes from a source run were analyzed and sorted into segment traces including an actual signal from an interaction (hit segment, nearest neighbor and possibly next nearest neighbor) and segment traces without a signal. The latter were then used to estimate the baseline fluctuation of the segments. For this, the following conditions were applied: A single hit segment in the crystal, an interaction energy of above 500 keV and an amplitude in the range of ± 10 keV in the considered segment. The ± 10 keV condition is used to distinguish between actual pulse shapes and the fluctuation of the baseline. The >500 keV interaction energy gate is to ensure sufficiently large transient signals to enable a clear discrimination of signal and baseline fluctuation. The distinction between baseline fluctuation and signal is shown for one exemplary 'super trace' (as introduced in section 3.1) in Fig. 79.

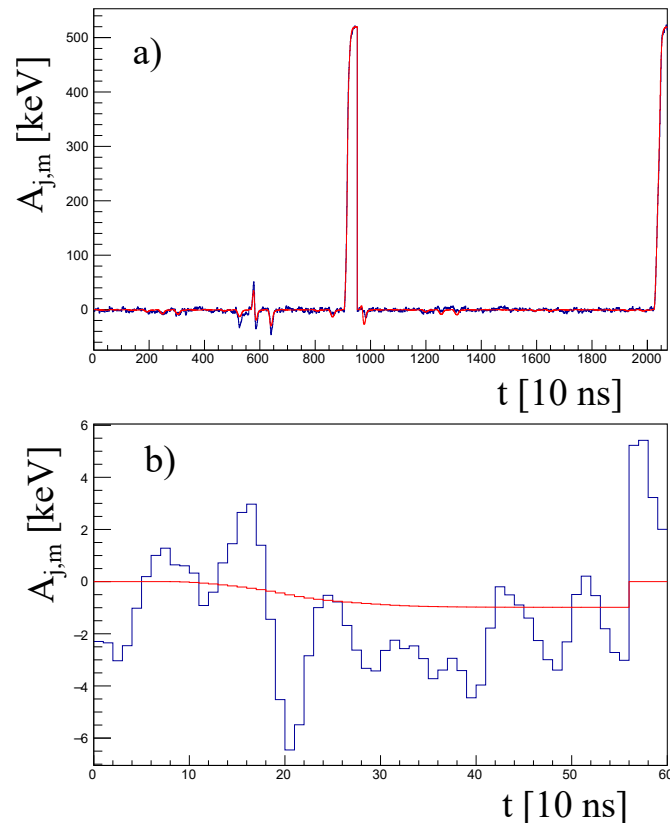


Figure 79: The measured (blue) and simulated (red) super trace for a single interaction in segment C4 is depicted in a). Only the neighboring segments show a signal that is significantly above the baseline fluctuation. Picture b) shows the measured trace of segment A1. No significant signal is expected (red) in this segment and the measured pulse shape consists mainly of baseline fluctuation.

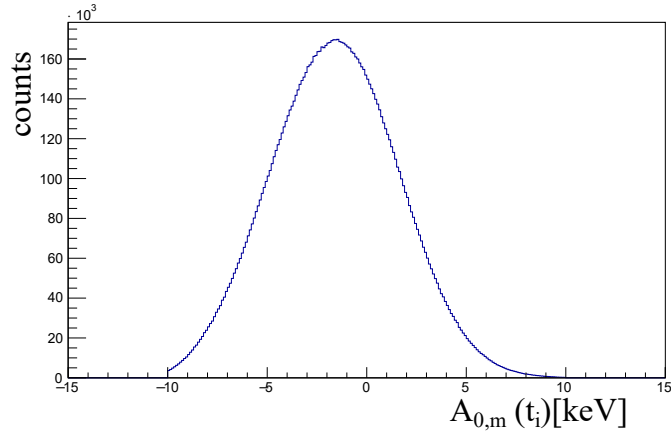


Figure 80: The measured amplitude A_m is plotted for multiple events for segment A1 (segment id 0), corresponding to the first 560 ns in Fig. 79. The measured trace consists mainly of baseline fluctuations. The standard deviation of the distribution $\sigma = 3.155$ keV gives an estimation for the general baseline fluctuation of that segment. The mean of the distribution $m = -1.58$ keV is slightly below zero. This is caused by the fact that only the measured signal A_m is considered. The expected signal A_s is not subtracted to not introduce any bias by wrongly allocated interaction positions. The condition of $|A_m| < 10$ keV causes a cutoff at ± 10 keV.

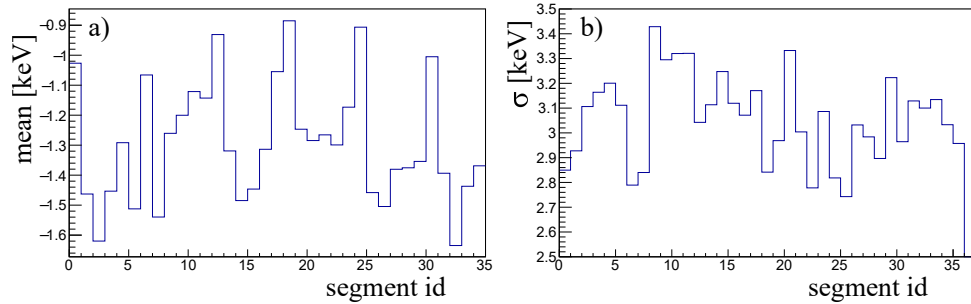


Figure 81: The mean and standard deviation of the baseline for all 36 segments of crystal A001 are drawn. The mean is slightly negative and shows a six fold symmetry, the first row of segments (corresponding to 0,6,12 and so on) has a mean that is about 0.5 keV larger than in average. The standard deviation is around 3 keV and shows no systematic dependency on the segment number.

Fig. 80 shows the obtained baseline fluctuation for a single segment extracted from a large number of events. Note that for the determination of the baseline fluctuation only the measured signal A_m is considered. The expected signal amplitude A_s should be zero and is not subtracted to exclude any possible bias from the allocated interactions position. The remaining offset of about ~ -1.5 keV is small and does not affect the determined standard deviations in a first approximation. The obtained mean values and standard deviations, corresponding to the distribution in Fig. 80 of the respective segment, are shown for a single crystal in Fig. 81 and for all 1044 segment channels in Fig. 82. The observed average baseline fluctuations range mainly from 2.5 to 3.5 keV with the exception of a few single channels at up to 4.5 keV.

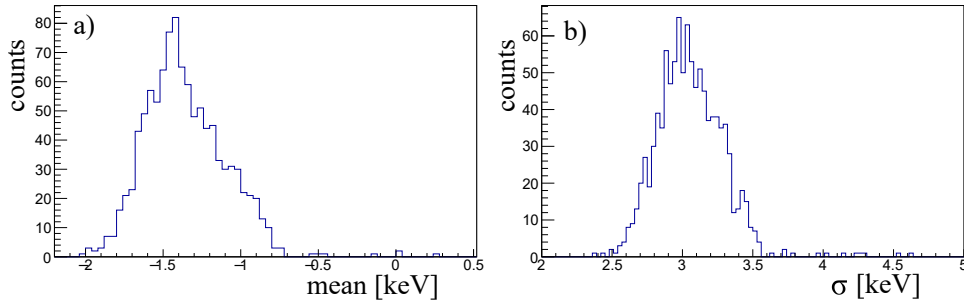


Figure 82: The mean values and standard deviations of the baseline fluctuation are plotted for all 1044 segment channels. The negative mean values of in average -1.36 keV in a) are caused by the finite expected signal amplitude A_s , which is not subtracted. The standard deviation of the distribution in a) is 0.26 keV. The average baseline fluctuation, which is the mean of distribution in b), is 3.06 keV. A few single channels show a larger standard deviation of up to 4.5 keV. The standard deviation of the distribution shown in b) is 0.24 keV.

Subsequently the influence of the baseline fluctuations on the PSA performance was investigated. In a first approach the segment channels with high baseline fluctuation were excluded from the Pulse-Shape Analysis, using a threshold of 3.7 keV. The ^{22}Na data set was analyzed without considering these channels in the determination of the figure of merit. The mean distance to the source d , which is the parameter for the PSA performance, did not change significantly. Excluding these channels does not improve the PSA performance. This is probably caused by the fact that only 11 of 1044 channels are above this threshold. In a second step the baseline fluctuation of all channels was taken into account. A new attenuation/weighting factor, that depends on the baseline fluctuation of the individual segments, was introduced:

$$w_i = \left(\frac{\sigma_{\text{mean}}}{\sigma_i} - 1 \right) \cdot S + 1 \quad (4.13)$$

Here $\sigma_{\text{mean}} = 3.06$ keV is the average standard deviation, σ_i the standard deviation of the considered segment and S a scaling factor. In this way, channels with an average baseline fluctuation are treated the same way as before, with a weighting factor $w_i \approx 1$. Channels with a high baseline fluctuation have their impact on the figure of merit reduced, while channels with low baseline fluctuation are weighted more strongly. The obtained weighting factors and the variation of the scaling factor S is depicted in Fig. 83. The variation shows that the PSA performance does not increase with a baseline fluctuation dependent weighting. This is probably caused by the fact that most of the segments have a very similar baseline fluctuation (within ± 0.5 keV) and that the baseline fluctuation only has a minor impact on the position resolution, which is for example suggested by ref. [57].

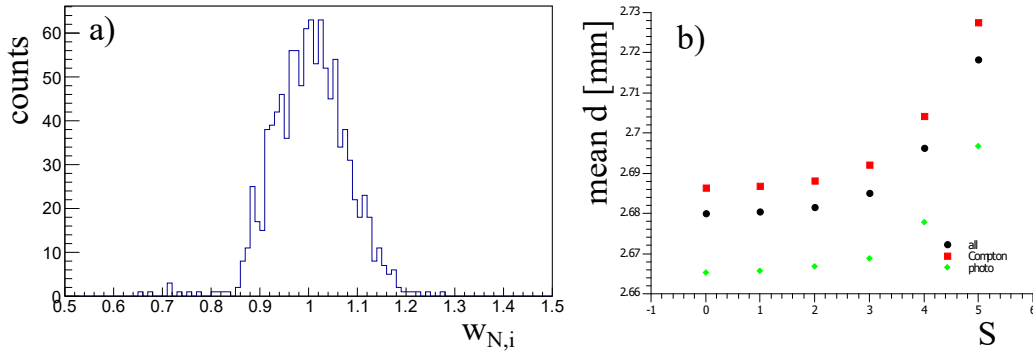


Figure 83: The individual weighting factors for all 1044 segments, which are obtained using eq. 4.13 with $S=1$, are shown in a). The variation of that weighting factor is shown in b). The best PSA performance is achieved for $S=0$, i.e. no weighting based on the baseline fluctuation of the segments.

4.3.4 Smearing of interaction positions

The online and offline analysis software of AGATA provides the possibility to smooth/smear out the found interaction positions within the $2 \times 2 \times 2$ mm voxels of the fine grid search. This is done by randomizing the interaction position within this volume. In the standard configuration the smearing of interaction points is enabled. Otherwise, the interaction position is allocated at the center of the grid point. The impact of this smearing was investigated using the ^{22}Na -coincidence method. The mean distances to the source were extracted for the standard settings and without smearing. The results are summarized in table 4.5. The smearing of interaction positions is clearly not favorable. A randomization of interaction positions obviously reduces the position resolution. A hit in the corner of the grid point is up to $\sqrt{3}$ mm ≈ 1.73 mm away from the center of the grid point. In the future the interaction position within the $2 \times 2 \times 2$ mm grid point should be extrapolated using the figure of merit values of the grid point and its nearest neighbors.

Table 4.5: The mean distance was extracted as a measure for the PSA performance for the standard configuration with smearing enabled and without. The randomization of interaction points is clearly declined.

	mean distance [mm]		
selected coincidences	all	Compton	photo
with smearing (standard)	2.674	2.686	2.648
without smearing	2.619	2.634	2.586

4.3.5 Transfer function

The measured signals are amplified by charge sensitive preamplifiers [45] [46]. The measured signals are shaped by the preamplifier electronics. A finite $T_{10\%-90\%}$ rise time is observed as output when a Heaviside step function from a fast pulser is injected into the preamplifier input. The connection

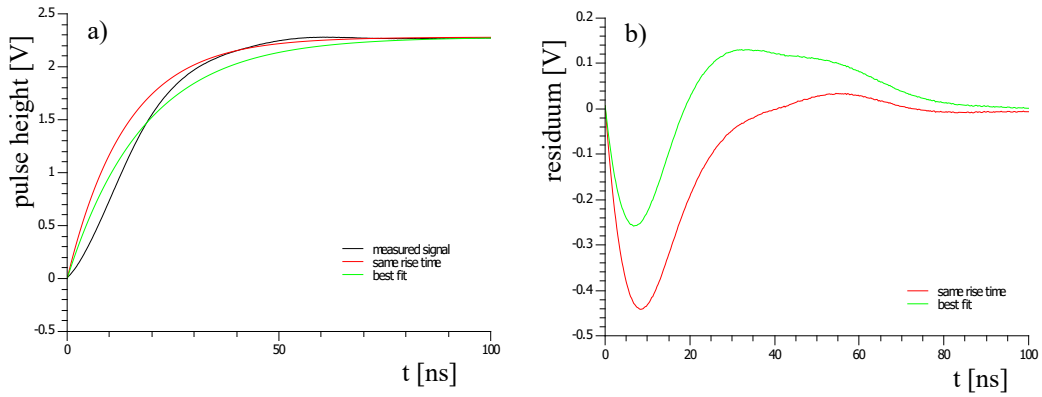


Figure 84: A step function from a fast pulser (3-4 ns rise time) was injected into an AGATA segment preamplifier on a test bench. The resulting pulse was measured with a digital oscilloscope and averaged over 256 pulses, which is depicted in a). It is also compared to the convolution of a step function with the exponential response given in eq. 4.15 with two different τ values. The first one ("same rise time") has the same $T_{10\%-90\%} = 30.5$ ns rise time as the measured signal, by choosing $\tau = \frac{T_{10\%-90\%}}{2.2} \approx 13.7$ ns . The second one ("best fit") is the result of a least squares fit with $\tau \approx 18.2$ ns. The difference of measured signal and exponential response is depicted in b).

between input signal and preamplifier output is given by the transfer function. In order to compare the simulation with the measured signals, the simulated "raw" signals have to be convoluted with the electronic response of the system. The digitizers [58] also contribute to this electronic response due to their bandwidth B , which is about 40 MHz. As a rule of thumb the rise time is related to the bandwidth via [59]:

$$T_{10\%-90\%} \approx \frac{0.35}{B} \quad (4.14)$$

Which gives a rise time of 8.75 ns for the digitizer. Since preamplifier and digitizer are independent, their rise times add quadratically. The $T_{10\%-90\%}$ rise time of the preamplifier is about 35-40 ns. The contribution of the digitizers to the final rise time is therefore only in the range of 1-2 ns and can be neglected in a first approximation. Typically, the electronic response is described as an exponential one. Convoluting a Heaviside step function with such an exponential response yields an exponential saturation.

Fig. 84 depicts the measured pulse after injecting a signal from a pulser into the preamplifier input on a test bench. On the test bench preamplifiers can be investigated outside of the detector system. The detector is modeled by a capacity for more realistic results. The resulting pulse is compared to an exponential response with different time constants τ . The time constant τ of the exponential function can be chosen such that the $T_{10\%-90\%}$ rise time of the exponential saturation matches the one of the measured preamplifier signal. This is true for $\tau \approx \frac{T_{10\%-90\%}}{2.2}$. An overall agreement of the measured pulse and the exponential response is observed. However, some deviations, particularly in the first few ns, can be noticed. When comparing the measured response to the exponential response with the same rise time, a distinct overestimation is observed.

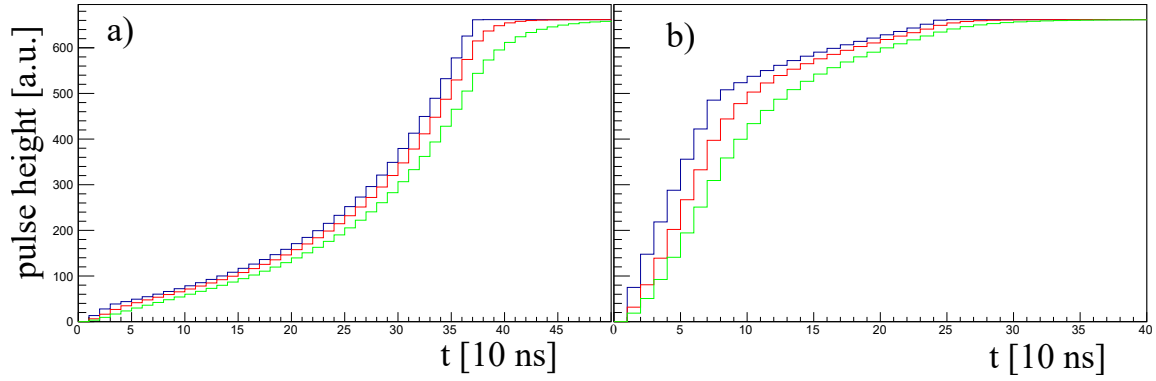


Figure 85: Simulated traces without electronic response (blue) and with an exponential response (eq. 4.15) are shown. The resulting traces for two different τ values are plotted: $\tau = 18$ ns (red) and $\tau = 35$ ns (green). Figure a) depicts the pulse shapes for an interaction position of $r = 10$ mm, $\varphi = 30^\circ$ and $z = 40$ mm. The radius in the second picture b) is $r = 35$ mm.

The convolution of the "raw" simulated signals $A'_{i,s}(t_j)$ with the electronic response is done as follows:

$$A_{i,s}(t_j) = \left(1 - \exp\left(-\frac{\Delta T}{\tau}\right)\right) \sum_{t' < t_j} \exp\left(-\frac{t_j - t'}{\tau}\right) A'_{i,s}(t') \quad (4.15)$$

Here $\Delta T = 10$ ns is the length of a tick, given by the sampling rate of 100 MHz. The impact on simulated signals employing this response function is illustrated in Fig. 85. Depending on the interaction position, the difference between simulated and convoluted traces is largest at different collection times.

In a first approximation the same τ value is used for every core and segment preamplifier. This τ value was varied in the range from 15-65 ns and the ^{22}Na coincidence analysis was performed for each variation step. The results depicted in Fig. 86 show a minimum at $\tau = 45$ ns, which is 10 ns larger than the previously used value of 35 ns.

The typically used value and the newly found optimum correspond to rise times larger than expected from the pulser measurements. The rise time of the preamplifiers, which are put into operation in the cryostats, is artificially increased to prevent an oscillation of the system. This is done on case-by-case basis depending on the performance of the cryostat. However, this can not explain a large optimal τ value of 45 ns. Another explanation might be the approximation of an exponential response, which can lead to larger τ values than expected from $T_{10\%-90\%}$ measurements (as seen in Fig. 84). Additionally, the result is the outcome of a variation procedure. The τ value that maximizes the PSA performance is not necessarily the physically correct one. This is possible if other PSA parameters, which have a similar impact on the pulse shape, are not set to their optimal value. In the case of the transfer function this is for example the drift velocity of the holes. Therefore, the drift velocity of the holes and the hole mobility in particular, was investigated (see section 4.3.6).

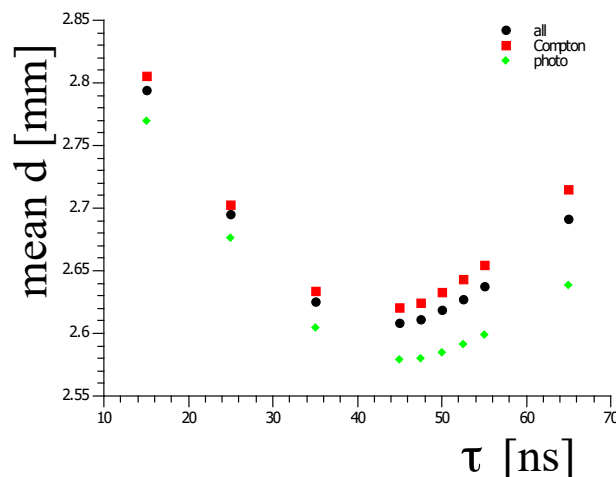


Figure 86: The variation of the preamplifier time constant τ , which is used for the convolution of the simulation with an exponential response, is shown. A minimum at $\tau = 45$ ns is observed, in comparison to the previously used value of 35 ns.

4.3.5.1 Transfer function with homogeneity criteria

The optimal transfer function was also determined with the homogeneity criteria introduced in section 4.2. The time constant τ was varied in the range from 20-80 ns. The correlation factor C (eq. 4.6) and the deviation (eq. 4.8) were summed up for all 29 detectors and plotted vs the time constant τ in Fig. 87. The obtained positions of the minima coincide at $\tau \approx 45$ ns and are consistent with the results determined with the ^{22}Na -coincidence method.

The graph in c), depicting the ratio of hits in high statistics grid points in dependence of the used τ value, is less smooth than the other curves. This is caused by the definition of the considered ratio (see section 4.2.3): A different assignment of interaction positions can cause a grid point to be below the threshold of $\alpha_z > 2.25 \cdot \langle \alpha_z \rangle$ and to be no longer considered to have "high statistics". As a consequence the ratio of hits in high statistics grid points takes a sudden drop.

The three considered PSA-performance criteria were also evaluated for each detector individually. The determined minimum positions are summarized in Fig. 88. The difference of the minimum positions obtained with the three performance criteria is plotted in Fig. 89. The obtained optimal τ values for the correlation factor C and the deviation from the expectation are consistent. The values which are obtained by minimizing the ratio of hits in high statistics grid points disagrees with these optimal τ values for some detectors.

The three PSA-performance criteria were also evaluated on a segment-by-segment level. Each individual preamplifier has a slightly different rise time. Therefore segment specific transfer functions are expected to improve the PSA performance. Grid points, which belong to the considered segment, were used to calculate segment specific values for the correlation factor, the deviation from the expectation and the ratio of hits in high statistics grid points. For example the segment specific

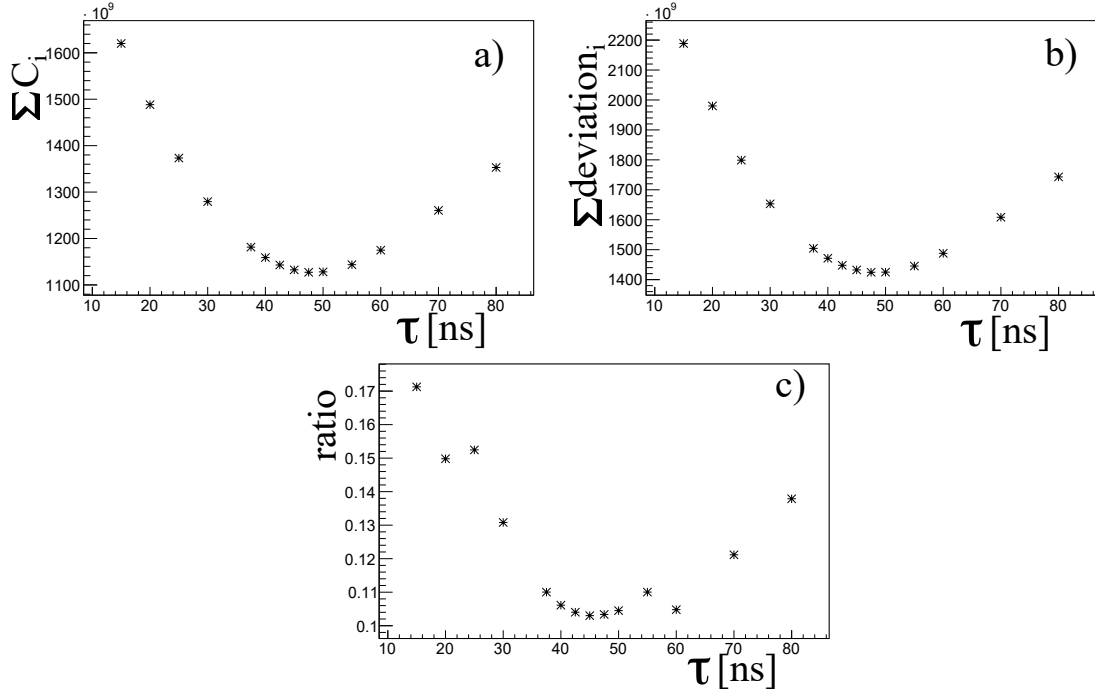


Figure 87: The a) sum of the correlation factor C for all detectors, the b) sum of the deviation from the expectation for all detectors and c) the ratio of hits in high statistics grid points (all detectors) are plotted versus the time constant τ , which is used to describe the transfer function. The minimum positions, corresponding to the best PSA performance, are at 47.5 ns in a) and b) and at 45 ns in c).

correlation factor C_{seg} is given by:

$$\begin{aligned}
 C_{\text{seg}} = \sum_{x,y,z \in S} [& (\alpha_{x,y,z} - \langle \alpha_z \rangle) \cdot (\alpha_{x+2\text{mm},y,z} - \langle \alpha_z \rangle) \\
 & + (\alpha_{x,y,z} - \langle \alpha_z \rangle) \cdot (\alpha_{x,y+2\text{mm},z} - \langle \alpha_z \rangle) \\
 & + (\alpha_{x,y,z} - \langle \alpha_z \rangle) \cdot (\alpha_{x,y,z+2\text{mm}} - \langle \alpha_{z+2\text{mm}} \rangle)]
 \end{aligned} \tag{4.16}$$

Which is the same definition as for the correlation factor C in eq. 4.6, with the exception that only grid points within the segment S are considered.

The segment specific performance criteria were used to determine optimal tau values on a segment-by-segment basis. The results are summarized in Fig. 90. A relatively large spread of optimal τ values is observed. In addition, for a significant number of segment channels the minimum is found at the largest applied time constant of $\tau = 80$ ns. The variation of the time constant τ with respect to the segment specific correlation factor C_{seg} is shown exemplarily for two segment channels in Fig. 91.

The τ values which were obtained as described above on a detector-by-detector and on a segment-by-segment level were applied to the ^{22}Na data, using the average of τ_C and τ_{dev} . As PSA-performance criterion the mean distances d were determined, using the ^{22}Na -coincidence method. The mean distances are summarized and compared to the previously obtained results in table 4.6. The compari-

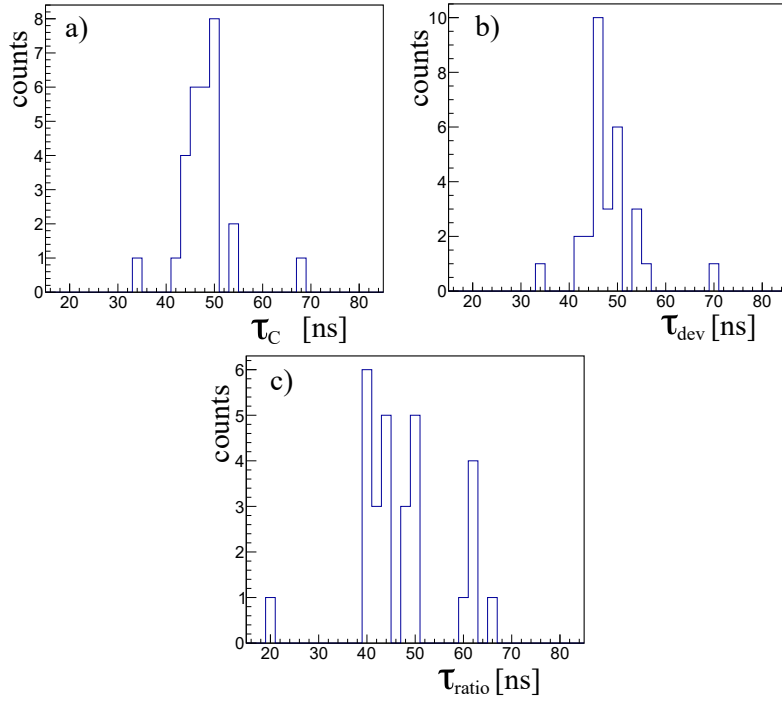


Figure 88: The optimal τ values, which were determined for the 29 individual detectors minimizing a) the correlation factor C , b) the deviation from the expectation and c) the ratio of hits in high statistics grid points, are shown. For a few detectors the obtained values deviate significantly from the previously obtained optimal value of $\tau = 45$ ns.

son shows that the τ values which are obtained on a detector-by-detector level yield similar results. The PSA yields worse results when using the τ values which were determined for each segment individually.

As a conclusion, the utilized performance criteria are suited to determine the optimal time constant τ for the transfer function on a global level, when choosing identical τ values for all channels. The obtained value is consistent with the result from the ^{22}Na -coincidence method. The evaluation of segment specific τ values did not improve the PSA results. The used performance criteria are not suited to be used on a segment-by-segment basis.

Table 4.6: The mean distances d , which were obtained with the ^{22}Na -coincidence method are compared for different applied τ values. The previously determined optimal τ value of $\tau = 45$ ns (all channels) is compared to choosing the τ value individually for each detector ("detector level") or individually for each segment ("segment level"). Events with two single 511 keV interactions ("photo") or one 511 keV interaction and one Compton scattered 511 keV γ ray ("Compton") were considered.

choice of τ	mean d (all) [mm]	mean d (Compton) [mm]	mean d (photo) [mm]
all channels $\tau = 45$ ns	2.609	2.626	2.570
detector level	2.613	2.631	2.571
segment level	2.661	2.684	2.605

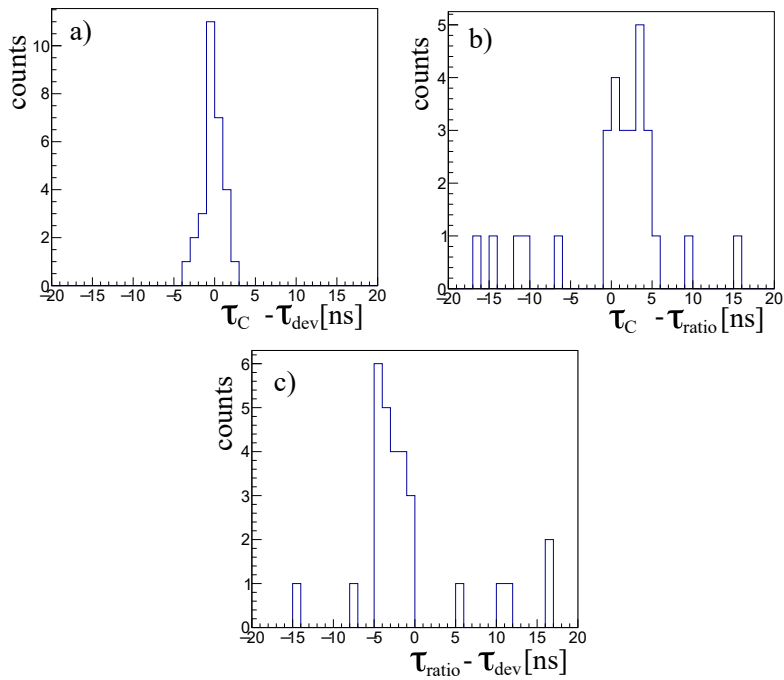


Figure 89: The differences of the optimal τ values obtained with the different PSA-performance criteria are shown. The optimal τ values for the correlation factor C , τ_C , and the deviation from the expectation, τ_{dev} , coincide within a few ns, which is shown in a). The τ values, which minimize the ratio of hits in high statistics grid points, τ_{ratio} , are systematically smaller, which is shown in b) and c). The minimum positions were extrapolated for τ_C and τ_{dev} , but not for τ_{ratio} .

This becomes apparent when considering the large number of segment channels for which an optimal τ value of 80 ns was obtained (see Fig. 90 and 91). Here, the drawback of the used homogeneity criteria becomes apparent: A homogeneous distribution is only a necessary, but not a sufficient criterion for a good PSA result.

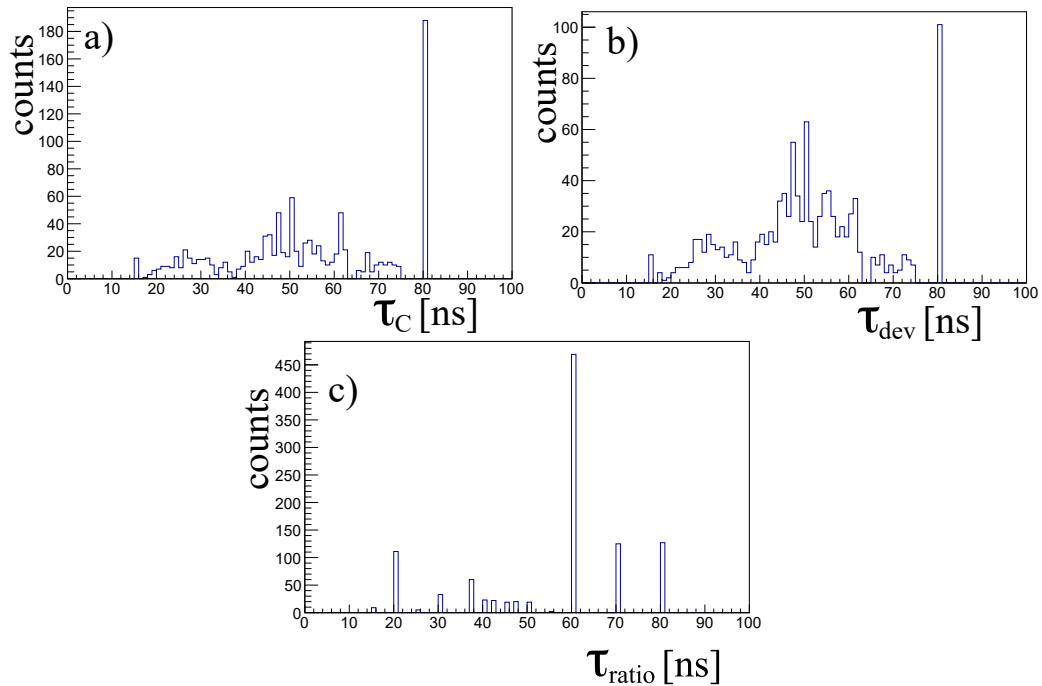


Figure 90: The optimal τ values which were obtained by minimizing a) the segment specific correlation factor C_{seg} , the segment specific deviation from the expectation and c) the segment specific ratio of hits in high statistics grid points is shown. A broad spread of obtained τ values is observed. In a) and b) a significant surplus is observed at $\tau = 80$ ns. In c) only discrete τ values are observed since τ_{ratio} was not extrapolated from the discrete data.

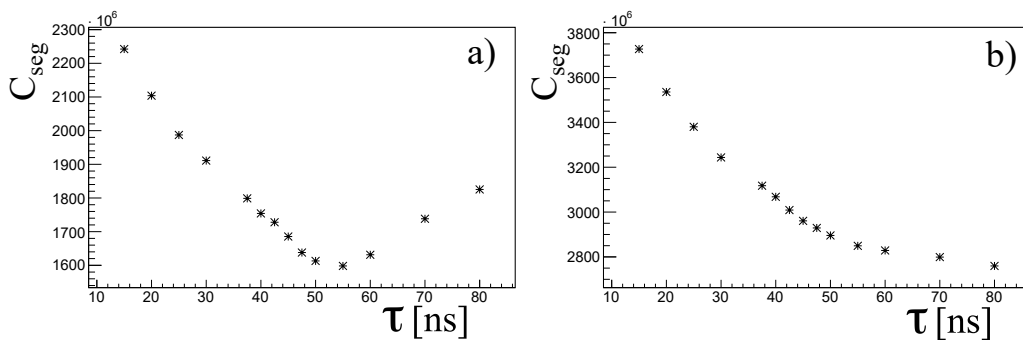


Figure 91: The variation of the time constant τ with respect to the segment specific correlation factor C_{seg} is shown exemplarily for a) segment B3 and b) segment B4. In a) an optimal τ value of about 55 ns is obtained. In b) the smallest correlation factor C_{seg} is observed at the last data point at $\tau = 80$ ns. In this case no global minimum is found and the obtained τ value is most likely not reliable.

4.3.6 Hole mobility

The AGATA Data Library simulates the position dependent pulse shapes employing an empirical model for the drift velocity of holes (see eq. 4.17). A crucial parameter for the description of the drift velocity is the hole mobility. The electron and hole mobilities were measured using a 12-fold segmented MINIBALL detector by Bruyneel et al. in [60] and [38]. Later on, the same method was applied to the symmetric AGATA prototype S001. Results of these studies are used by ADL [17]. The parameters are summarized for the hole drift velocity in table 4.7. Note that different values are given along the different crystallographic axes. The drift velocity is not isotropic, since the electrical field from the lattice cannot be neglected. The collection times differ up to 30% for the different crystallographic directions. The drift velocity v_D for the holes is given by:

$$v_D = \frac{\mu_h E}{(1 + (\frac{E}{E_0})^\beta)^{\frac{1}{\beta}}} \quad (4.17)$$

Where μ_h is the mobility of the holes and E the electrical field strength. E_0 and β are empirically determined parameters. The dependence of the drift velocity on the electrical field strength is depicted in Fig. 92.

One of the crystallographic $\langle 100 \rangle$ axes is fixed along the central axis of the germanium crystal parallel to the core due to the crystal growing process. The orientation of the lattice is given by one of the other $\langle 100 \rangle$ axes. These were measured via rise time measurements along the crystal surface using the following fit function (see for example [61] and [17]):

$$T_{10\%-90\%} = A(1 + R_4 \cos(4(\theta - \theta_4))) \cdot (1 + R_2 \cos(2(\theta - \theta_2))) \quad (4.18)$$

Where $A, R_2, R_4, \theta_2, \theta_4$ are fit parameters. Main contributions come from the four-fold symmetry of the crystal axes (R_4, θ_4), while some contributions come from the asymmetric shape of the crystal (R_2, θ_2).

Due to the cubic structure of germanium two $\langle 100 \rangle$ axes are sufficient to orient the crystal. The third $\langle 100 \rangle$ axis is perpendicular to the other ones. The $\langle 111 \rangle$ axes are then obtained via superposition.

The measurement of the hole mobility in n-type HPGe detectors, using the method of Bruyneel et al.,

Table 4.7: The drift velocity parameterization for the holes is given by the hole mobility μ_h and the empirical parameters E_0 and β , which contain information on both the scaling with the electrical field strength as well as on the anisotropy of the drift velocity.

	$\langle 100 \rangle$	$\langle 111 \rangle$
$\mu_h [\frac{\text{cm}^2}{\text{mVs}}]$	62.934	62.383
$E_0 [\frac{\text{V}}{\text{cm}}]$	181.9	143.9
β	0.7353	0.7488

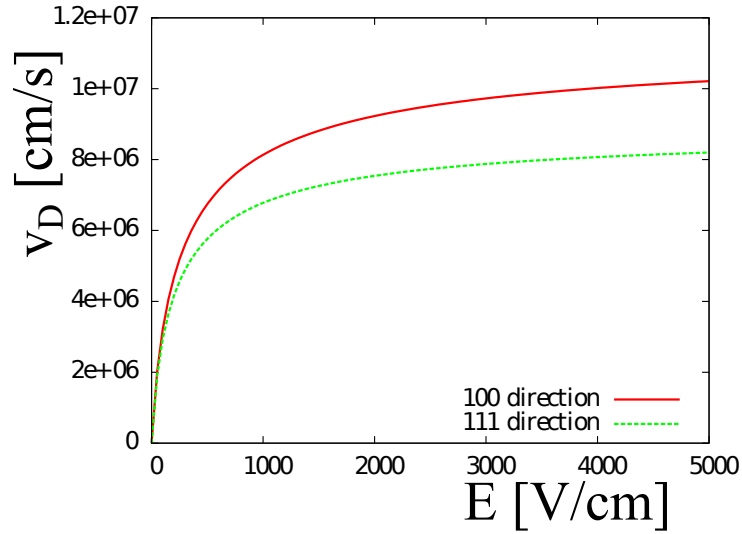


Figure 92: The hole drift velocity in dependence of the electrical field strength E is plotted for the $\langle 100 \rangle$ and $\langle 111 \rangle$ directions using eq. 4.17 and the values given in table 4.7. The drift velocity saturates for large electrical fields and a distinct deviation between both crystallographic directions is visible.

is challenging. This is caused by the fact that the mobility parameters are extracted from detailed rise time measurements. For the holes a γ -ray interaction close to the core is needed. This was achieved by utilizing the 356 keV line of a collimated ^{133}Ba source. In contrast to electron mobility measurements, where a very precise interaction position close to the surface can be ensured with a low-energy γ -ray source, this increases the experimental error. The obtained result [38] and literature [62] [63]) show some deviations. The mobility of the holes was also subject to recent investigations by the GRETINA collaboration [64]. In addition to the entanglement of drift velocity and transfer function regarding simulated pulse shapes (see section 4.3.5), this motivated an investigation of the hole mobility and its impact on the PSA results.

The hole mobility parameter μ_h was varied in a range from 20-70 $\frac{\text{cm}^2}{\text{mVs}}$. For each mobility value new data bases (containing the pulse shapes for all interaction positions) were simulated for all of the 29 crystals. The ^{22}Na data set was analyzed for all different mobilities and the mean distance of the reconstructed coincidences to the source was extracted. Due to the time consuming manner of the variation, the same mobility was used for both the $\langle 100 \rangle$ and the $\langle 111 \rangle$ directions. This approximation is valid because the difference in drift velocity is mainly caused by the empirical parameter E_0 in the parameterization which is used in ADL. The results are depicted in Fig. 93 and show an optimal hole mobility parameter of $\mu_h = 55 \frac{\text{cm}^2}{\text{mVs}}$. For this variation the time constant τ of the transfer function was set to the default value of 35 ns.

Subsequently, the time constant τ of the preamplifier and the hole mobility parameter μ_h were varied simultaneously. Due to long computing time of each variation step, a full 2D-scan is not feasible. Instead τ and μ_h were varied alternately: The time constant τ was varied using the newly obtained value for the hole mobility $\mu_h = 55 \frac{\text{cm}^2}{\text{mVs}}$. This yielded a new minimum at $\tau = 40$ ns, compared to $\tau = 45$ ns using the standard mobility. Finally, the hole mobility was varied again with $\tau = 40$ ns and

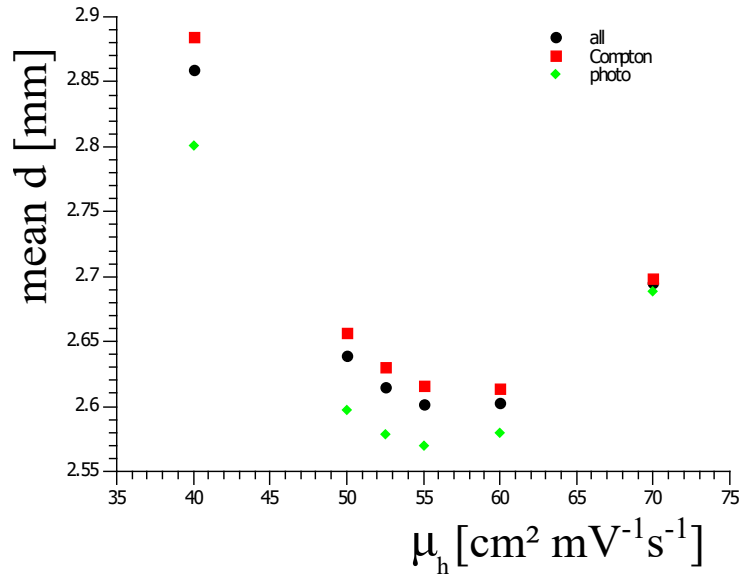


Figure 93: The results of the variation of the hole mobility is shown. A minimum at $55 \frac{\text{cm}^2}{\text{mVs}}$ is obtained, which is slightly smaller than the ADL values given in table 4.7.

an optimal value of $\mu_h = 57.5 \frac{\text{cm}^2}{\text{mVs}}$ was obtained. This iterative variation is depicted in Fig. 94. In comparison to the standard values of $\tau = 35 \text{ ns}$ and $\mu_h \approx 63 \frac{\text{cm}^2}{\text{mVs}}$ the found optimal configuration consists of slightly slower preamplifiers and a reduced hole drift velocity. This shows that the simulated pulse shapes in the standard configuration were too fast. A comparison of simulated pulse shapes for standard and optimized hole mobility is shown in Fig. 95.

One possible explanation for the deviation between the hole mobility measured by Bruyneel et al. (see table 4.7) and the value obtained in this work, is the temperature dependence of the hole mobility. At higher temperatures the mobility decreases (see for example [62]). A temperature dependence of $T^{-2.3}$ or $T^{-2.4}$ is suggested by [65] and [66], respectively. A less effective cooling is observed if the position of the dewar, which holds the liquid nitrogen, is not vertically on top of the crystal. Depending on the position, temperatures differ by up to 10 K. The measurements by Bruyneel et al. were performed in the lab with the dewar on top of crystal, resulting in the best possible cooling and highest mobility. For the ^{22}Na measurement the crystals were located in different positions, but for most of the detectors the dewar was located at the same horizontal level as the crystal, causing a less effective cooling and a decreased mobility. The different positioning of the crystals relative to the dewar might be the reason for the observed deviations.

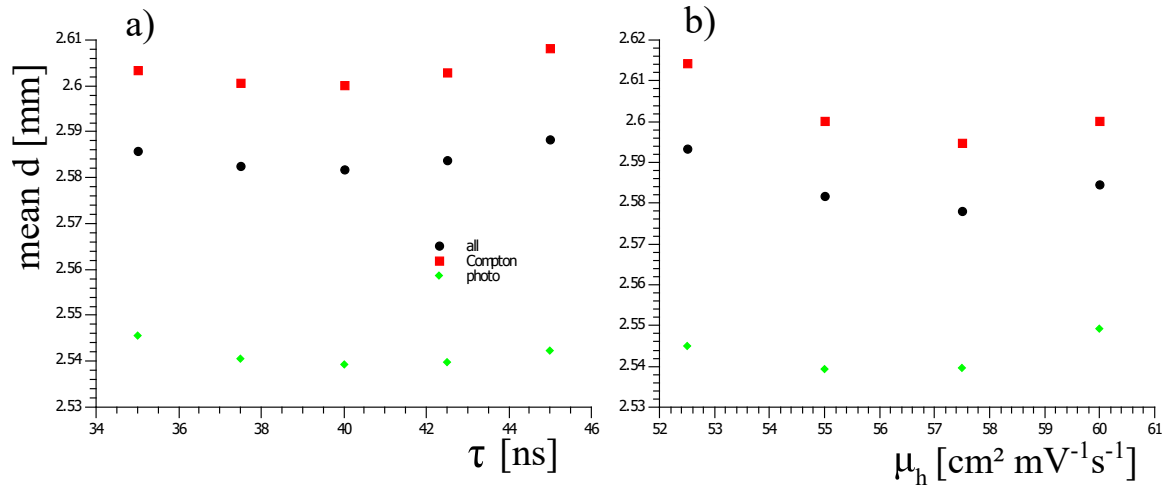


Figure 94: The time constant τ of the preamplifier was varied, while the hole mobility μ_h was set to $55 \frac{\text{cm}^2}{\text{mVs}}$ in picture a). In comparison to the variation in Fig. 86 (with standard ADL configuration) a reduced value of $\tau = 40 \text{ ns}$ is obtained. Using this slightly larger τ value (in comparison to Fig. 93) an optimal hole mobility of either $\mu_h = 55 \frac{\text{cm}^2}{\text{mVs}}$ (photo) or $\mu_h = 57.5 \frac{\text{cm}^2}{\text{mVs}}$ (Compton, all) is determined, see picture b).

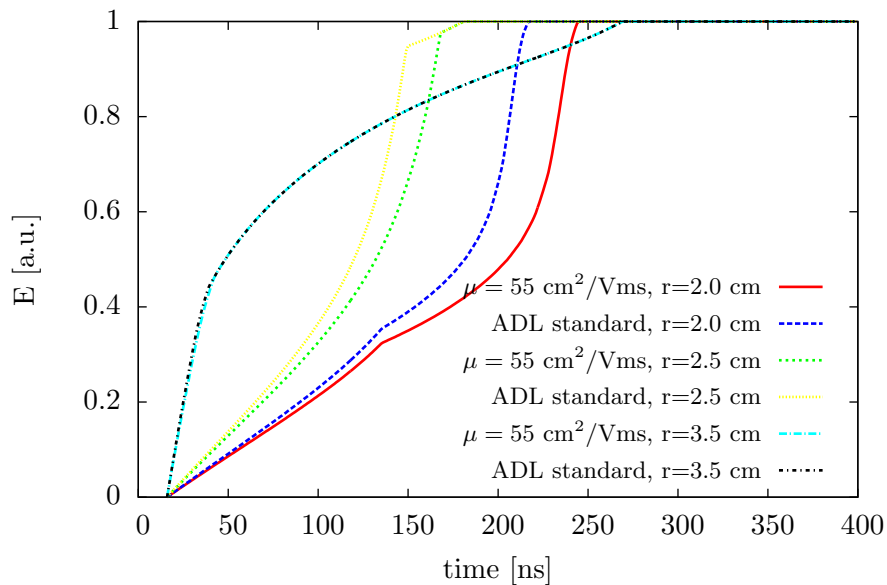


Figure 95: Simulated pulse shapes are compared for different hole mobilities and different radii. Holes drift towards the outer segment electrodes. Therefore, an increased deviation of the pulse shapes is observed for smaller radii.

4.3.7 Electron mobility

The drift velocity of the electrons is calculated using a similar empirical approach as for the holes. An additional term $-\mu_n E$ is added to describe the scattering of electrons with optical phonons (see eq. 4.19). For the given electrical field strength, at typical operating bias voltages of 4000-5000 V, this effect is of minor importance. The drift velocity of the electrons is given by:

$$v_D = \frac{\mu_e E}{(1 + (\frac{E}{E_0})^\beta)^{\frac{1}{\beta}}} - \mu_n E \quad (4.19)$$

The electron mobility parameters of Bruyneel et al. (see Ref. [38]) are summarized in table 4.8.

To investigate the influence of the electron mobility on the PSA performance, data bases with different values for the electron mobility μ_e were simulated. The PSA performance was determined with the ^{22}Na -coincidence method and the results are presented in Fig. 96. An optimal value of $\mu_e = 38 \frac{\text{cm}^2}{\text{mVs}}$ is obtained for the $\langle 100 \rangle$ direction, which is very close to the standard ADL mobility. The change of the mean distance d between both mobility values is negligible small. In contrast to the hole mobility investigations, the approximation of identical mobility values in both the $\langle 100 \rangle$ and $\langle 111 \rangle$ directions is not necessary. Instead, the drift velocity in any direction is calculated from the $\langle 100 \rangle$ values (see [60] and [63]). For electron mobility values far from the minimum at $\mu_e = 38 \frac{\text{cm}^2}{\text{mVs}}$ the mean distance to the source increases rapidly. This is probably caused by the fact that the impact of a changed electron mobility on the pulse shape is more distinct for large radii (see Fig. 97), while the opposite is true for the hole mobility. More interactions take place at large radii, due to the r^2 dependence of the volume of a cylinder.

The very good agreement of measured and optimal mobility obtained via variation can be explained by the more precise measurement of the electron mobility. Here, the interaction position for the rise time measurements is very well known by using a low energy γ -ray source, e.g. the 60 keV line of ^{241}Am . The decreased signal-to-noise ratio is compensated by the ability to create γ -ray interactions directly at the segment electrode in a very localized volume. For all other investigations the electron mobility parameterization measured by Bruyneel et al. was used.

Table 4.8: The empirical parameters for the calculation of the electron drift velocity are depicted. In comparison to the hole mobility parameterization no additional values for the $\langle 111 \rangle$ direction are given. Instead the drift velocity in any given direction is calculated via a scattering model described in [60] eq. 4-8.

	$\langle 100 \rangle$	inter-valley scattering	
$\mu_e [\frac{\text{cm}^2}{\text{mVs}}]$	37.165	$E_0 [\frac{\text{V}}{\text{m}}]$	1200
$E_0 [\frac{\text{V}}{\text{m}}]$	507.7	ν_0	0.459
β	0.804	ν_1	0.0294
$\mu_n [\frac{\text{cm}^2}{\text{mVs}}]$	-145	ν_2	0.000054

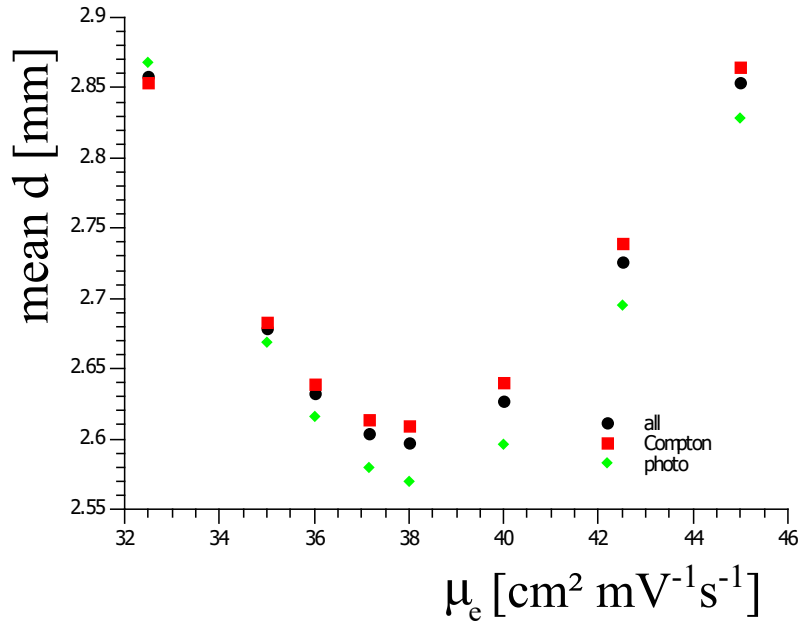


Figure 96: The variation of the electron mobility μ_e is shown. An optimal value is obtained at $\mu_e = 38 \frac{\text{cm}^2}{\text{mVs}}$, close to the ADL standard value of $\mu_e = 37.165 \frac{\text{cm}^2}{\text{mVs}}$. The difference in the mean distance d is only 0.006 mm (two photo effects).

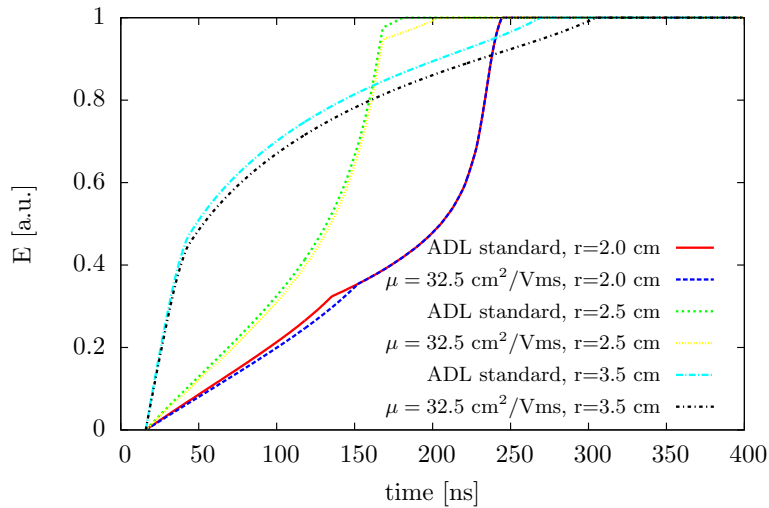


Figure 97: A comparison of simulated segment pulse shapes is shown for different radii and different electron mobilities. To illustrate the impact of the electron mobility on the pulse shape, the ADL standard value is compared to $\mu_e = 32.5 \frac{\text{cm}^2}{\text{mVs}}$. Since electrons drift towards the central electrode, deviations are more notable for large radii, where the holes are collected quickly and the charge collection process is dominated by the drifting of the electrons.

4.4 Comparison of results before and after optimization

In this section the PSA results which were obtained using the standard PSA configuration (which is used in any AGATA experiment) are compared to the results when employing an optimized configuration. The optimized setup consists of an improved transfer function (section 4.3.5), an adjusted hole mobility (section 4.3.6), a new distance metric (section 4.3.2), a disabled smearing of interaction positions (section 4.3.4) and a weighting of transient signals (section 4.3.1). The two configurations are summarized in table 4.9.

Table 4.9: A summary of the initial and final values of the distance metric parameters p and q , the weighting coefficient w_i , the hole mobility μ_h and the preamplifier time constant τ is shown.

parameter	initial value	result after variation
p	0.3	0.4
q	0.3	0.7
w_i	1	2.75
$\mu_{h,(100)}$	$62.934 \frac{\text{cm}^2}{\text{mVs}}$	$55 \frac{\text{cm}^2}{\text{mVs}}$
$\mu_{h,(111)}$	$62.383 \frac{\text{cm}^2}{\text{mVs}}$	$55 \frac{\text{cm}^2}{\text{mVs}}$
τ	35 ns	40 ns

4.4.1 Comparison of ^{22}Na results

The distances d of the lines connecting the 180° coincidences to the source position are shown for the standard and for the optimized configuration in Fig. 98. In the optimized configuration the measured distances are smaller which corresponds to a better reconstruction of the source position and therefore improved PSA results. The corresponding mean values and the standard deviations σ of these distributions are summarized in table 4.10.

Table 4.10: The mean values and standard deviations σ of the distances d to the source are shown for the standard and for the optimized configuration. The values were extracted from the distributions depicted in Fig. 98. The decreased values for the mean and for the standard deviation σ correspond to an improved PSA performance.

	mean d [mm]			σ [mm]		
	photo	Compton	all	photo	Compton	all
standard configuration	2.732	2.758	2.75	1.846	1.854	1.852
optimized configuration	2.544	2.603	2.586	1.801	1.812	1.809

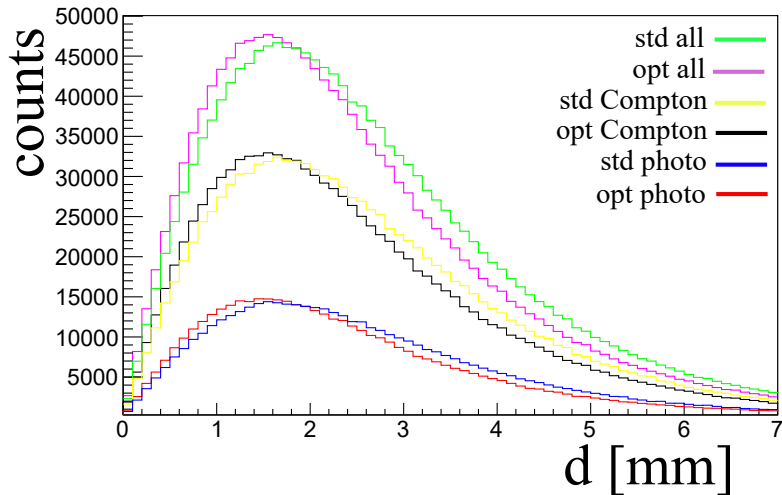


Figure 98: The distances of the coincidence lines to the source position are shown for the standard ("std") and for the optimized ("opt") configuration. The distributions are plotted for two single 511 keV interactions ("photo") and for the case that one 511 keV γ ray did a single Compton scattering ("Compton"). The sum of both distributions ("all") is also shown. In all cases a shift towards smaller distances for the optimized configuration is observed.

The measured distances d are comprised of different parts which contribute to the final measured distance. One of these contributions is the difference of the assumed point-like source-position and the actual point of emission. The point of emission and the assumed source position deviate due to the spread of the radioactive material, the range of the positron (0.24 mm in average) and due to the uncertainty in the determination of the source position. The second contribution is the deviation of interaction positions and corresponding PSA results for the two interactions at 180° . Only the latter changes in the variation process, while the other parts which contribute to the distance d remain constant. Therefore, only small changes to the distances d are expected even for notable improvements of the position resolution.

To estimate the position resolution, events were selected for which one of the coincident interactions was very close to and the other one very far from the source position. The method to estimate the position resolution (which is described in section 4.1.5) was applied to the interaction positions obtained with the optimized PSA configuration. The differences of most likely interaction position and PSA result are compared to the results using the standard configuration in Fig. 99. A zoom on Fig. 99 b) is shown in Fig. 100. Since the number of events in both distributions (standard 10785 and optimized 10909) is not identical, a direct comparison is difficult. The different number of events arises from the different PSA results and the applied gates (see section 4.1.5 for the gates). The results regarding the difference of most likely interaction position and PSA result are summarized in table 4.11 for the optimized configuration and compared to the original, not optimized results from table 4.3 shown in section 4.1.5. The comparison of the results yields an improved PSA performance for the optimized configuration.

As discussed in section 4.1.5, a precise determination of the FWHM and FWTM values is difficult due

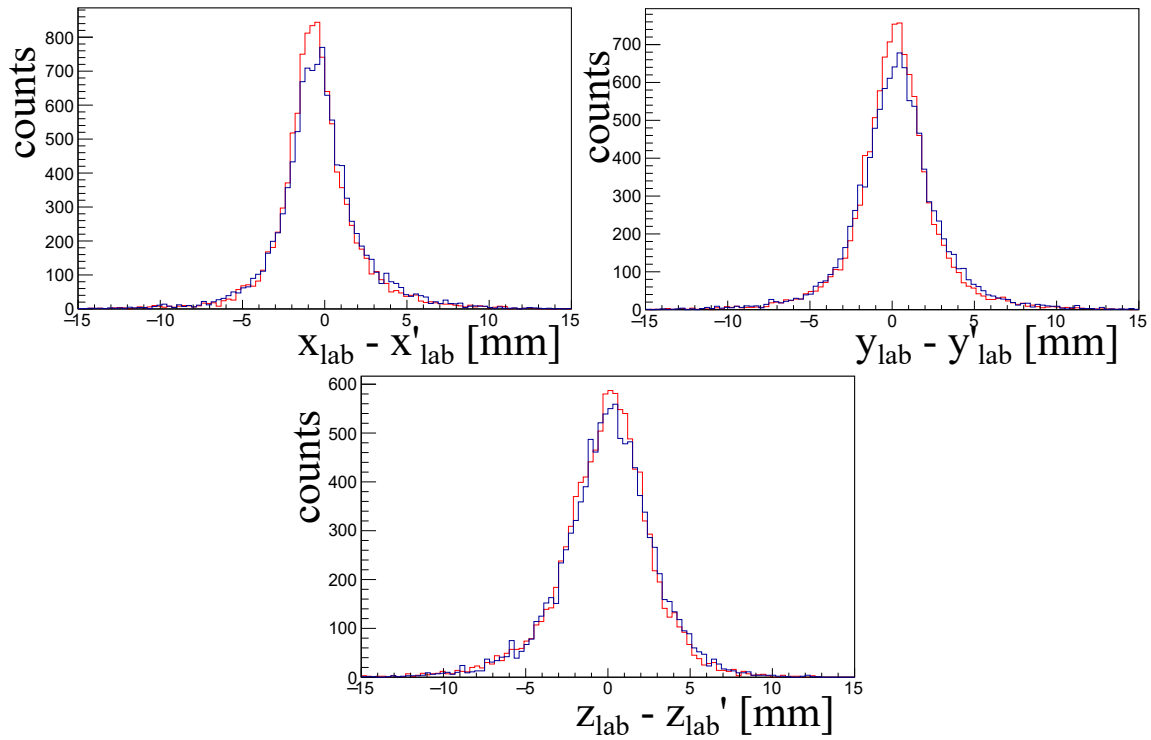


Figure 99: The differences of most likely interaction positions $(x, y, z)_{\text{lab}}$ and PSA results $(x', y', z')_{\text{lab}}$ are shown for the standard (blue) and for the optimized (red) configuration. The positions $(x, y, z)_{\text{lab}}$ and $(x', y', z')_{\text{lab}}$ refer to the lab system. An increased number of events at small differences close to 0 mm is observed.

to the low statistics. The distributions depicting the difference of most likely interaction position and PSA result show a significant tailing. Events in the tails correspond to interaction positions which are not well resolved and they should be reflected in the final result. Therefore, in addition to the FWHM value, the FWTM value and the standard deviation should be considered when comparing the results of standard and optimized configuration. Especially for the FWTM and for the standard deviation improved values are observed in all cases.

The different results which are obtained using the standard or the optimized configuration become also apparent when considering the Distance D of most likely interaction position and PSA result. It is given by $D = \sqrt{(x_{\text{lab}} - x'_{\text{lab}})^2 + (y_{\text{lab}} - y'_{\text{lab}})^2 + (z_{\text{lab}} - z'_{\text{lab}})^2}$ for a most likely interaction position at $(x, y, z)_{\text{lab}}$ and the corresponding PSA result at $(x', y', z')_{\text{lab}}$. The distributions of the distances D for the standard and for the optimized configuration are depicted in Fig. 101 and show an improved PSA performance. This becomes also evident when considering the mean and maximum values of the respective distributions which are summarized in table 4.12.

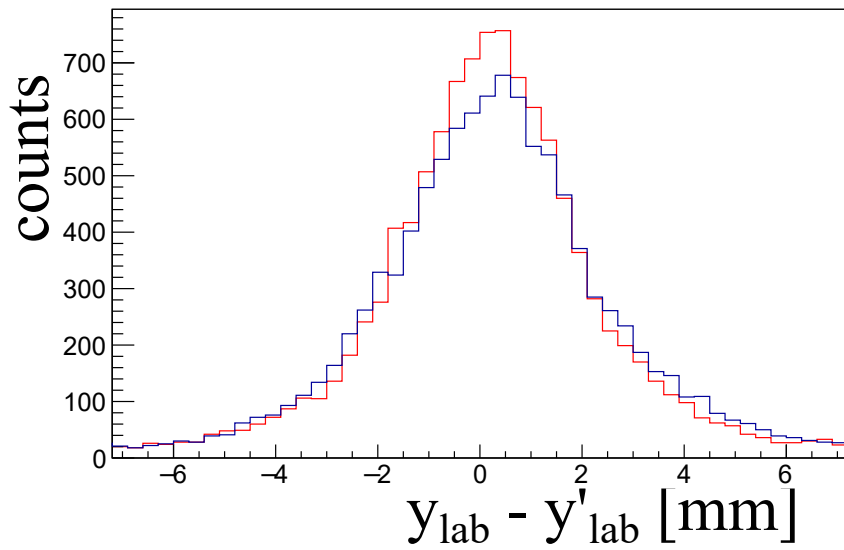


Figure 100: The differences of most likely interaction positions and PSA results are shown in a zoom for the y_{lab} coordinate for the standard (blue) and for the optimized (red) configuration. A shift towards smaller distances is observed.

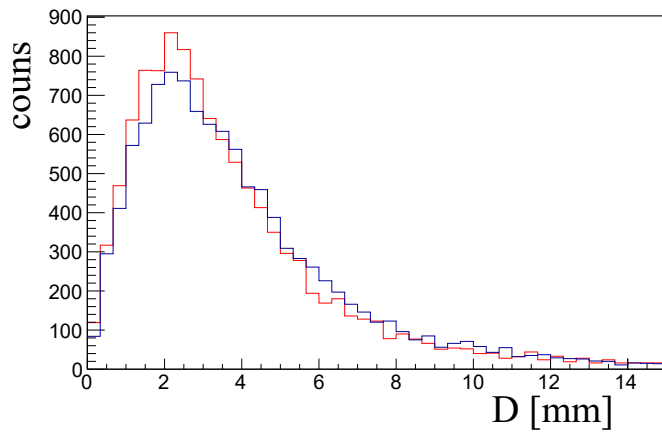


Figure 101: The distances D of most likely interaction positions and PSA results are plotted for the optimized (red) and for the standard (blue) configuration. A shift to smaller distances D is observed for the optimized configuration, which corresponds to a better agreement of PSA result and most likely interaction position. The average, the standard deviation and the maximum value are given in table 4.12.

Table 4.11: The mean m , the standard deviation σ , the FWHM and the FWTM are shown for the difference of most likely interaction position and PSA result for Cartesian and spherical coordinates (lab system). The values for the Cartesian coordinates correspond to the red colored distributions depicted in Fig. 99. The values, which were extracted from PSA results using the optimized configuration, are compared to the values obtained with the standard configuration (see table 4.3) and the difference of both results (Δ FWHM, ...) is stated. Negative differences correspond to an improved PSA performance.

	Δx_{lab} [mm]	Δy_{lab} [mm]	Δz_{lab} [mm]	ΔR [mm]	$\Delta \vartheta$ [°]	$\Delta \varphi$ [°]
mean m	-0.473	0.204	-0.138	-0.110	-0.0434	-0.386
σ	2.503	2.577	2.854	2.562	0.413	4.116
$\Delta \sigma$	-0.170	-0.206	-0.034	-0.036	0.002	-0.082
FWHM	2.7	3.6	4.5	4.4	0.66	5.9
Δ FWHM	-0.6	0	-0.3	0.1	0	-0.7
FWTM	7.5	8.1	10.5	9.2	1.38	17.2
Δ FWTM	-0.9	-1.2	-0.6	-1.4	-0.18	0.4
FWTM/FWHM	2.8	2.3	2.2	2.2	2.09	2.9
Δ (FWTM/FWHM)	0.3	-0.3	-0.1	-0.3	-0.27	0.4

Table 4.12: The mean, the standard deviation σ and the maximum value M are shown for the distributions of distances D of most likely interaction position and PSA result for the standard and for the optimized configuration (corresponding to Fig. 101). The increase of the maximal value of about 11.7% cannot be explained by the different number of events N of the distribution, which is only 1.1% larger. Instead, it is caused by smaller measured distances D , which corresponds to an improved PSA performance.

configuration	mean D [mm]	σ [mm]	maximum M	$\frac{M_{\text{opt}} - M_{\text{std}}}{M_{\text{opt}}}$	number of events N	$\frac{N_{\text{opt}} - N_{\text{std}}}{N_{\text{opt}}}$
standard	4.00	2.87	759	-	10785	-
optimized	3.73	2.79	860	11.7 %	10909	1.1 %

4.4.2 Comparison of hit distributions

In this section the hit distributions are compared using either the standard or the optimized configuration. When employing the setup described in section 2.3.1 the expected number of hits for a constant detector depth z is the same. The length of the detectors of 90 mm is divided into 45 slices of 2 mm length each. Due to the large number of slices of $29 \cdot 45 = 1305$ (29 detectors in use at the time of the measurement and 45 slices per detector) only a selection of hit distributions is shown.

The distribution of hits using the optimized configuration is shown in Fig. 102 for different detector depths of $z = 2 - 4$ mm and $z = 14 - 16$ mm. The corresponding distribution of hits using the standard configuration are given in section 2.3.1 in Fig. 7. In comparison, a reduced number of hits is observed in the grid points, which have more statistics than expected. A comparison of hit distributions at $z = 40 - 42$ mm is shown in Fig. 103 for the standard and for the optimized configuration.

In these figures the color code of the optimized distributions was adjusted such that the maximum

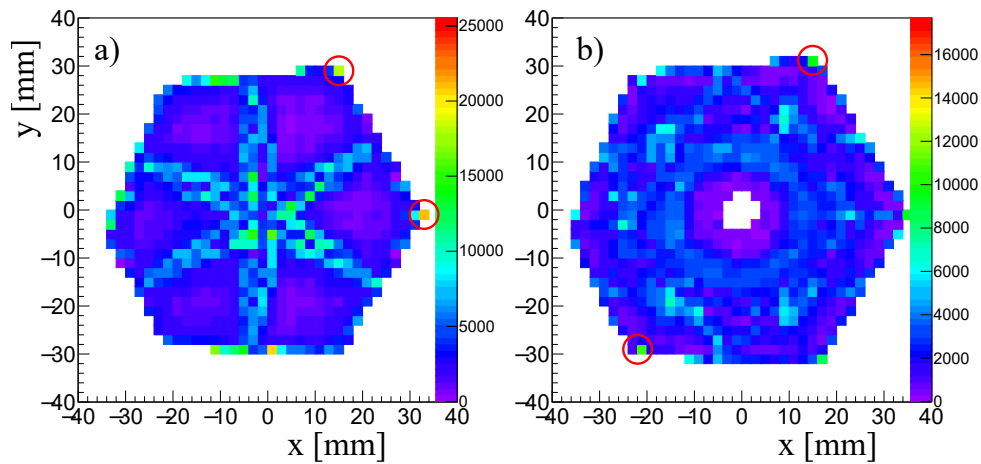


Figure 102: The distribution of hits is shown for a) $z = 2\text{--}4$ mm and b) $z = 14\text{--}16$ mm of crystal A001, using the optimized PSA configuration. No further gates were used. The corresponding distributions using the standard configuration are shown in Fig. 7. The same color code as in Fig. 7 was chosen. In comparison, the number of hits in high statistic grid points (red circles) is reduced for both cases. In a) the surplus of hits at the segment boundaries is more spread out, but a clustering of hits is still observed. In b) the clustering of hits at intermediate radii is significantly reduced.

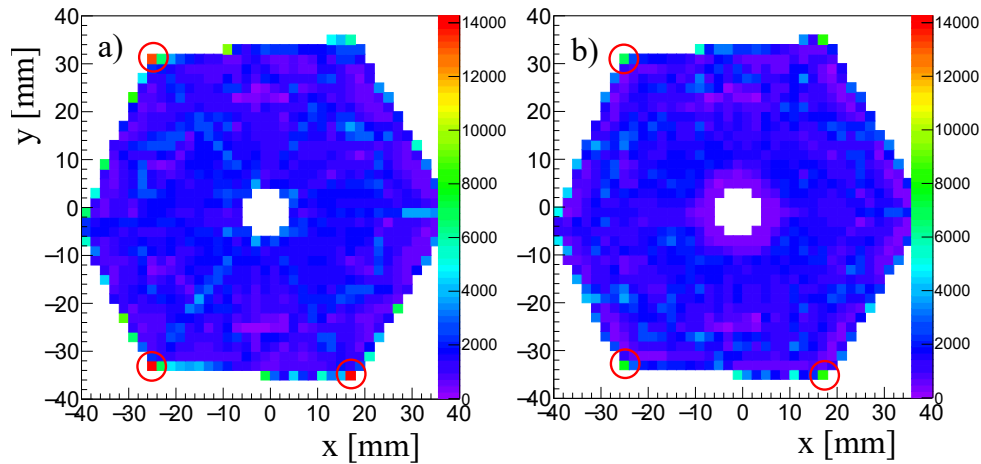


Figure 103: The distribution of hits is shown for $z = 40\text{--}42$ mm of crystal A001 using the a) standard and b) optimized configuration. In b) the same color code as in a) was used. The surplus of hits at certain grid points at the edge of the detector (red circles) is reduced. In this depiction, other details of the hit distribution, such as the clustering of hits in the middle of the segments, are not visible.

value (depicted by the color red) is equal to the maximum value of the distributions obtained with the standard configuration. This adjustment is necessary to enable a clear and unbiased comparison of hit distributions. The maximum value is typically smaller for the optimized configuration, due to reduced number of hits in high statistics grid points. When increasing the maximum value some details such as the clustering of hits in certain regions of the detector become less visible.

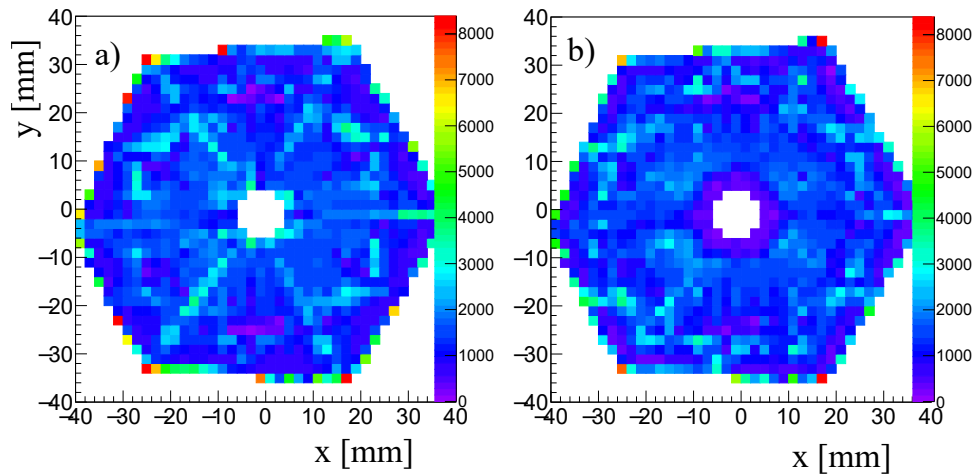


Figure 104: The distribution of hits is shown for $z = 40–42$ mm of crystal A001 using the a) standard and b) optimized configuration. In contrast to Fig. 103 (which depicts the same detector depth) the color scale of the distribution obtained with the standard configuration in a) was adjusted such that the red color corresponds to the maximum value of 8390 of the distribution in b). This means in a) grid points with a red color have 8390 or more counts. This "cut off" highlights changes to the distribution, which are not visible in Fig. 103.

The color code was also adjusted to match the maximum value of the optimized distribution instead, so that these details can be compared for both configurations, which is shown exemplarily for $z = 40–42$ mm in Fig. 104. In this depiction it becomes visible that the clustering of hits in the middle of the segments is no longer present.

A logarithmic depiction in Fig. 105 also reveals changes to the clustering of hits.

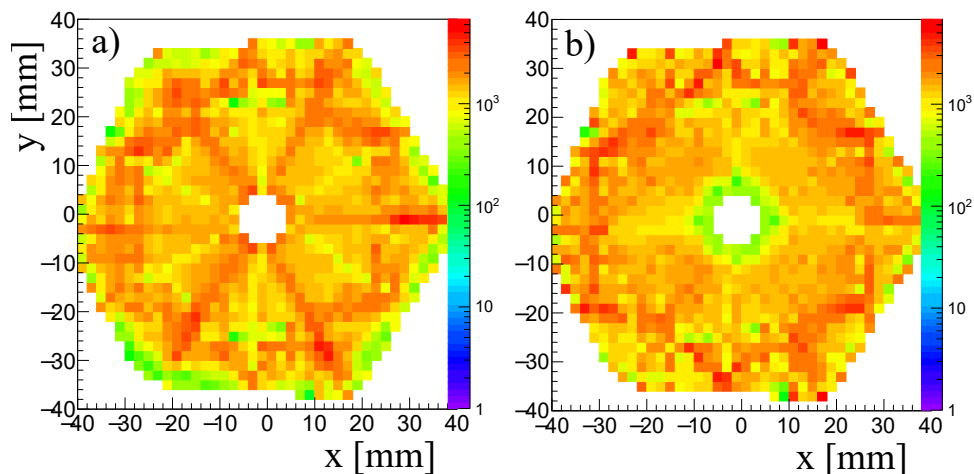


Figure 105: The distribution of hits is shown for $z = 52–54$ mm of crystal A001 using the a) standard and b) optimized configuration. In b) the same color code as in a) was chosen. A logarithmic scale is used. A reduced reduced clustering of hits in the middle of the segments is observed for the PSA results obtained with the optimized configuration.

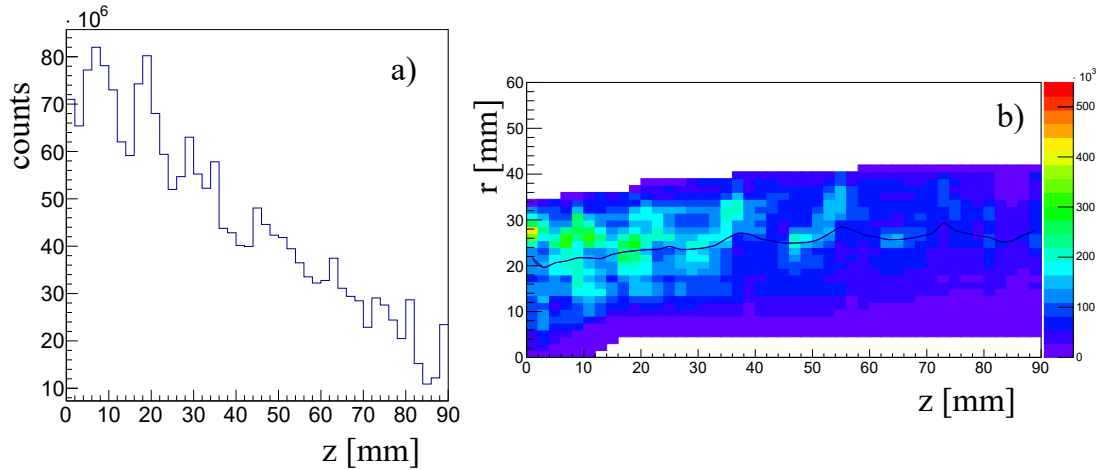


Figure 106: The number of hits in dependence of the detector depth z is plotted in a) for the optimized configuration. In an ideal scenario an exponential decrease and a $1/z^2$ dependence is expected. Significant deviations from this expectation are observed. In comparison to the distribution obtained with the standard configuration, which is depicted in Fig. 13 a), the surplus and the lack of hits at certain detector depths z is reduced. In b) the correlation of radius and z is shown.

The number of hits in dependence of the detector depth z and the correlation of radius and z are plotted in Fig. 106 for the optimized configuration. The corresponding distributions for the standard configuration are shown in Fig. 13 in section 2.3.1. In a first approximation an exponential decrease of the intensity due to absorption and a drop of the intensity proportional to $1/z^2$ due to solid angle coverage is expected. The statistical fluctuation can be estimated using the Poisson error. The observed deviation from this expectation at certain detector depths z is caused by a wrong allocation of hits by the PSA. Using the optimized configuration a reduced deviation from this expectation is observed, especially in the front part of the detectors. In Fig. 106 b) a reduced clustering of hits for certain radius/ z combinations is observed in comparison to the results using the standard configuration in Fig. 13. In addition, the unexpected sudden change of the mean radius (black line) at certain detector depths z is reduced, especially at $z = 0 - 2$ mm.

The difference of measured and simulated signals during charge collection, which was described in section 3.3, is compared for the standard and for the optimized configuration in Fig. 107 and 108. Similar results are obtained for both configurations. The observed deviations of simulation and measurement, which occur at specific times during charge collection for a given radius (correlated with the completed charge collection of either holes or electrons, for more details see section 3.3), are not caused by the drift velocities used by the simulations.

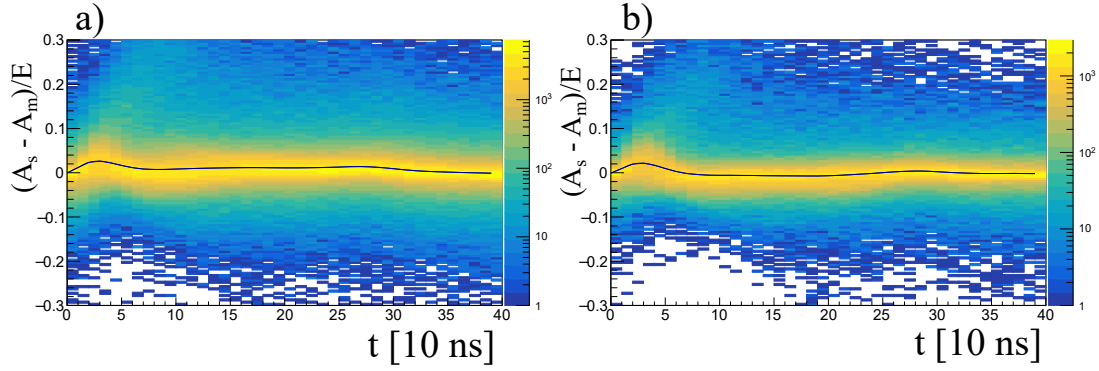


Figure 107: The time dependence of the difference of simulated A_s and measured A_m signals of the hit segment are shown for a determined radius of $r = 35 - 40$ mm for the a) standard and b) optimized configuration. Only interactions in ring three were considered. The average difference of simulation and measurement for a given time t is marked by a black line. A very similar result is obtained in both cases.

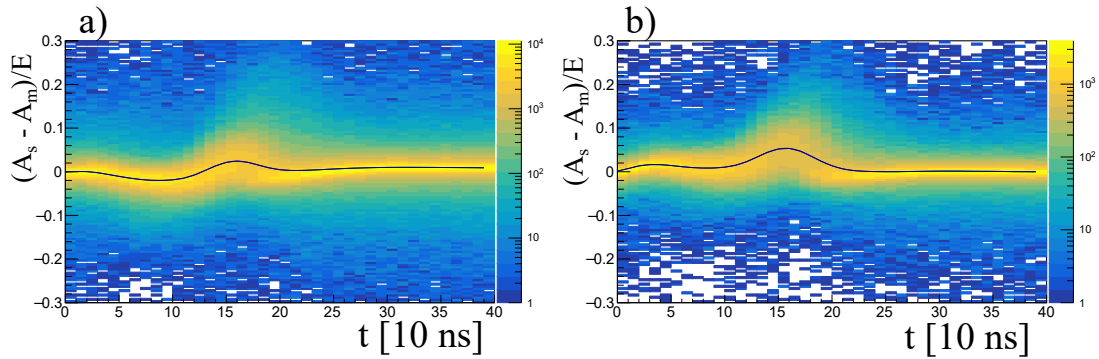


Figure 108: The time dependence of the difference of simulated A_s and measured A_m signals of the core are shown for a determined radius of $r = 20 - 25$ mm for the a) standard and b) optimized configuration. An overestimation of the measurement by the simulation at $t \approx 150$ ns is observed in both cases.

4.4.3 Comparison of homogeneity criteria

The homogeneity criteria, which were introduced in section 4.2, were compared for the standard and for the optimized configuration. These criteria describe the clustering of hits via the correlation factor C , the deviation from the expectation and the ratio of hits in high statistics grid points (see sections 4.2.1, 4.2.2 and 4.2.3, respectively). The observed inhomogeneous hit distributions indicate falsely allocated interaction positions. A more homogeneous distribution therefore corresponds most likely to a better PSA performance. The obtained values for the homogeneity criteria are summarized and compared for both configurations in table 4.13. The values for all criteria are reduced, which corresponds to more homogeneous hit distributions. For example, the number of hits in high statistics grid points (positions in the crystal to which more interactions were assigned by the PSA than can be expected from statistical fluctuation) is reduced by about 23%. These results agree with the observation from the previous section 4.4.2 where a reduced clustering and a reduced surplus of hits in single grid points was shown qualitatively.

Table 4.13: The obtained values for the correlation factor C (eq. 4.6), the deviation from the expectation (eq. 4.8) and the ratio of hits in high statistics grid points (eq. 4.9) are compared for the standard and optimized configurations. All 29 crystals were used. Grid points were only considered to have "high statistics" and contribute to the ratio if the number of hits was 4 times larger than the expectation. Note that the absolute value of the correlation factor C and the deviation is arbitrary, the relative change contains the meaningful information.

	C	deviation	ratio
standard	$1.31 \cdot 10^{12}$	$2.68 \cdot 10^{12}$	4.03%
optimized	$1.08 \cdot 10^{12}$	$2.19 \cdot 10^{12}$	3.09%
rel. change	-17.6%	-18.3%	-23.3%

4.4.4 Summary of results before and after optimization

Summarizing the results from the previous sections, an improved PSA performance is observed when comparing the PSA results obtained with the standard and with the optimized configuration. This becomes evident in the analysis of the ^{22}Na data, as well as in the investigation of the hit distributions from the ^{60}Co source measurement. The connecting lines of the 180° coincidences agree better with the source position. The mean distance of these lines to the source positions was reduced from 2.73 mm to 2.54 mm in the case of two 511 keV interactions. It has to be taken into account that this value does not become 0 mm, even in the case of a perfect position resolution, due to the finite range of the positron, the spreading of the radioactive material and the uncertainty in the knowledge of the source position.

The ^{22}Na data was utilized to estimate the position resolution with both configurations. For this, the most likely interaction positions (x,y,z) were compared to the PSA results (x',y',z') . An improved position resolution was obtained with the optimized configuration. For example, the standard deviation of the difference of most likely interaction position and PSA result in y direction $y - y'$ is reduced from 2.78 mm to 2.58 mm.

It was shown qualitatively and quantitatively that the obtained hit distributions are more homogeneous and agree better with the expected distributions. The introduced homogeneity criteria are reduced by about 20%. Especially the allocation of too many hits in single grid points could be reduced significantly.

When comparing the results of the standard and optimized configurations it should be taken into account that the standard configuration is based on an extensive research and development period. In this phase elaborate investigations were performed to improve the understanding of crucial detector properties and to incorporate them in the simulations. The AGATA PSA in its current state is well established and successfully used for experiments. Therefore, it was not expected that major improvements are achieved easily.

This work constitutes a step towards the physical limit of the PSA position resolution. An improved position resolution of the well established AGATA PSA was achieved.

5 Summary and Outlook

5.1 Summary

In this thesis a detailed study of the AGATA PSA was performed and an increased position resolution was obtained by enhancing the grid-search algorithm as well as improving the simulated reference signals. To achieve this, an in-depth analysis of measured and simulated signals and of the PSA results was performed. The fidelity of the reference signals was increased by considering all parameters which have a major impact on the pulse shape. The performance of the grid search algorithm was improved by investigating and optimizing the way in which simulated and measured signals are compared. In the following, the individual steps of the analysis and of the optimization are summarized.

A ^{60}Co measurement was performed at GANIL employing 29 HPGe AGATA detectors. The obtained interaction positions were analyzed and compared to the expectation. A significant deviation from the determined and expected distribution of hits was ascertained. In particular a clustering of hits in certain regions of the detectors and the assignment of a significant surplus of hits to single interaction positions was observed.

An extensive investigation and comparison of measured and best fitting simulated signals was conducted. In this context several C/C++ programs were written to analyze the trace data. In the AGATA data flow it is not foreseen to save the traces after the PSA (see Fig. 4). Therefore, it was necessary to extend the AGATA software. With the created programs a detailed analysis of the PSA results and of the simulated and measured signals was possible.

The figure of merit for different interaction positions for single events was investigated (section 3.2). The results showed sharp minima along the radial axis and less pronounced minima along the z and ϕ axes (see Fig. 2 regarding the r , ϕ and z coordinates). This finding indicates an increased accuracy in the radius determination and a more challenging determination of z and ϕ coordinates. Since different ϕ and z values predominantly change the shape of the transient signals (and only to a lesser extend the shape of the hit segment and core signals), this motivated the introduction of a weighting coefficient for the transient signals in the figure of merit.

The difference of measured and simulated signals in dependence of time was examined, taking the time interval from interaction to completed charge collection into account (section 3.3). The investigations revealed that the differences of measurement and simulation are not time independent. Systematic deviations of measurement and simulation were observed at specific times during charge collection, depending on the interaction position. These deviations are related to the completed charge collection of either the holes or the electrons. These findings motivated the inspection of the

drift velocity of electrons and holes, especially of their respective mobility.

The $T_{10\%-90\%}$ rise times were determined for different interaction positions (section 3.4). A good agreement of measured and simulated rise times was observed. A slight systematic deviation of measured and simulated rise times was observed in certain regions of the detector and for certain segments, which emphasizes the need for a segment specific transfer function. However, the observed rise time differences are small. The difference of measured and simulated rise times $T_{10\%-90\%,m} - T_{10\%-90\%,s}$ has a standard deviation of $\sigma = 26$ ns which is in the order of the length of a tick of 10 ns (see Fig. 31).

The starting times T_0 of the pulses were investigated and compared to the starting times provided by the digital CFD, revealing the need for a position independent T_0 determination. This is achieved by adding the segment and core signals and fitting them with a first order polynomial. The such determined T_0 values were compared to the T_0 values which are provided by the AGATA software (which uses a very similar approach). The observed differences demonstrate the difficulty and ambiguity of determining the starting time T_0 , especially for low energies.

In the second part of this thesis the PSA performance was determined, employing a ^{22}Na and a ^{60}Co measurement.

A ^{22}Na measurement was performed at GANIL utilizing the measured energies and interaction positions of 29 detectors (see section 4.1). The annihilation radiation of the emitted positron of the β^+ decay of ^{22}Na was measured in coincidence with the AGATA spectrometer. A C/C++ analysis code was written to select the coincidences from the annihilation radiation and extract the necessary information: The coincidences were reconstructed by applying gates to the measured energies, angles and to the multiplicity. The source position was determined in a self consistent variation procedure by maximizing the agreement of the measured coincidences with the expected 180° correlation (see section 4.1.3).

Two different kind of coincidences were considered: i) two segments with 511 keV energy deposition and ii) one segment with 511 keV energy deposition and two segments with a combined energy deposition of 511 keV (corresponding to a single Compton scattering of the 511 keV γ ray). In the following, these are labeled as type i) or type ii) coincidences. The source position is expected to lie on the connecting line of the determined coincidences. The distance of the connecting lines to the source position was used as a measure for the PSA performance. A mean distance of $d = 2.73$ mm for type i) coincidences was determined.

A combination of interaction positions, where one interaction is very near to and one is very far from the source position was utilized to determine most likely interaction positions. The comparison of these most likely interaction positions with the PSA results enabled an estimation of the position resolution (see section 4.1.5). A mean distance of most likely interaction position and PSA result of 4.0 mm was determined.

The distributions of hits from a ^{60}Co measurement were analyzed and compared with the expected results. The agreement with the expectation was described in a quantitative way, utilizing the homogeneity of the hit distributions and the correlation of neighboring grid points (see section 4.2).

The obtained results support the qualitative findings of unexpectedly clustered and inhomogeneous hit distributions in a quantitative way.

In the third part of the thesis the ^{22}Na -coincidence method was utilized to assess the PSA performance and improve the position resolution by employing a variation procedure, in which the mean distance d was minimized.

A weighting coefficient was introduced to increase the impact of the transient signals in the figure of merit calculation. The adjusted figure of merit is given by (see section 4.3.1 and eq. 4.10):

$$\text{Figure of Merit} = \sum_i w_i \sum_{t_j} |A_{i,s}(t_j) - A_{i,m}(t_j)|^p \quad (5.1)$$

The best PSA performance was achieved with a weighting coefficient of $w_i = 2.75$ for type i) coincidences and $w_i = 2$ for type ii) coincidences. The PSA yields better results if a transient weighting is employed. The differing results for the different types of coincidences indicate that the optimal weighting coefficient depends on the energy of the interaction and on the number of hit segments.

The distance metric, which is used for the figure of merit calculation, was investigated (see section 4.3.2). The absolute value of the difference of measured and simulated signals is taken to the power of an exponent p , which defines the used metric. An optimal value of $p = 0.4$ was obtained by employing a variation procedure, minimizing the mean distance d .

The figure of merit was further adjusted by splitting the parts which include the transient signals and the part which include the signals of hit segment and core. It is given by (see also eq. 4.12):

$$\text{FOM} = \underbrace{\sum_{i,t_j} |A_{i,m}(t_j) - A_{i,s}(t_j)|^p}_{\text{hit segment and core}} + \underbrace{\sum_{k,t_j} |A_{k,m}(t_j) - A_{k,s}(t_j)|^q}_{\text{neighboring segments}} \quad (5.2)$$

Individual optimal values for the exponents p and q were determined in an iterative variation. The mean distance d was minimized by $p = 0.4$ (hit segment and core) and $q = 0.7$ (transient signals). An increased performance is observed for $q > p$ which corresponds to a stronger weighting of the transient signals.

The fluctuation of the baseline was estimated for all 1044 channels (29 detectors times 36 segments). An average fluctuation of $\sigma = 3.06$ keV was observed (see section 4.3.3). A linear weighting based on the determined baseline fluctuations was introduced. It increases the impact which a segment with small baseline fluctuations has towards the final figure of merit and decreases the impact of segments with large baseline fluctuations. The weighting based on the baseline fluctuations did not yield an improved PSA performance.

The random allocation of hits within the $2 \text{ mm} \times 2 \text{ mm} \times 2 \text{ mm}$ volume of a grid point was compared to assigning the hit to the center of the grid point (see section 4.3.4). It was determined that the smearing of interaction positions within the volume of a grid point is not favorable.

The electronic response of the preamplifiers was examined (see section 4.3.5). The response was

measured utilizing a Heaviside step function from a fast pulser. It was compared to the used approximation of an exponential response which is described by a single parameter τ . Deviations compared to the measured response were observed. However, the approximation of an exponential response was determined to be still valid. An optimal value for the time constant $\tau = 45$ ns was determined via variation, minimizing the mean distance d .

An optimal τ value was also determined considering the homogeneity criteria introduced in section 4.2. Consistent results were obtained with an optimal τ value of ~ 45 ns (see section 4.3.5.1). The criteria were also used to determine optimal values for single detectors and single segments. However, the application of these detector and segment specific τ values did not improve the ^{22}Na results.

The hole mobility μ_h , which is used for the simulation of the reference signals, was investigated (see section 4.3.6). It is needed to calculate the drift velocity of the holes which is a crucial parameter for the simulation of the pulse shapes. Employing the ^{22}Na -variation procedure an optimal value for the mobility of $\mu_h = 55 \frac{\text{cm}^2}{\text{mVs}}$ was determined, which is about 10% smaller than the previously used ADL value. Since an adjusted mobility μ_h and an adjusted decay constant τ have a similar impact on the pulse shape, these two parameters were evaluated simultaneously. Optimal values of $\mu_h = 55 \frac{\text{cm}^2}{\text{mVs}}$ and $\tau = 40$ ns were obtained.

The mobility of the electrons μ_e was investigated and an optimal value of $\mu_e = 38 \frac{\text{cm}^2}{\text{mVs}}$ was determined, which coincides in good approximation with the ADL value of $\mu_e = 37.165 \frac{\text{cm}^2}{\text{mVs}}$.

The results which are obtained when including all previously mentioned optimizations were compared to the results using the standard AGATA configuration in section 4.4 in a detailed analysis. Both configuration sets were applied to the ^{22}Na data. The respective interaction positions were extracted and compared with the ^{22}Na -coincidence analysis. As a measure to describe the PSA performance the mean distance d was determined for both cases. For type i) coincidences it is given by $d = 2.73$ mm for the standard configuration and $d = 2.54$ mm for the optimized configuration. For type ii) coincidences a mean distance $d = 2.76$ mm and $d = 2.60$ mm was determined for the standard and for the optimized configuration, respectively. The ^{22}Na data was also employed to estimate the position resolution for both configurations. The results are summarized in table 4.11 and an improvement of the position resolution is observed.

The standard and the optimized configuration were applied to the ^{60}Co data and the resulting hit distributions were compared qualitatively and quantitatively (see sections 4.4.2 and 4.4.3). A reduced clustering of hits and a reduced surplus of hits in "high statistics grid points" is observed. This is also reflected in the homogeneity criteria, which are summarized in table 4.13. They are reduced by about 20%, which corresponds to a more homogeneous distribution and an increased agreement of measured and expected hit distributions.

In this thesis the pulse shapes simulated with ADL, the properties of the adaptive grid-search algorithm and the results of the PSA were investigated in detail. A systematic study of all major PSA-input parameters was performed. Their impact on the PSA results was evaluated and optimized values were determined, resulting in an improved PSA performance. The distributions of hits which are obtained with the optimized PSA configuration are more homogeneous, but still deviate from the expectation. The systematic study of the PSA input parameters did not reveal any major discrepancy

between determined optimal values and the ones from the standard configuration. The performed systematic investigation indicates that all detector properties, which have a significant impact on the PSA performance, are described well by the simulations.

The best PSA performance is achieved in a tedious analysis and optimization of all relevant input parameters which affect the results of the PSA. This procedure is especially challenging due to the entanglement of the input parameters, which are not independent of each other. In principle, the problem is described by an N -dimensional optimization, with N being the number of input parameters. This optimization problem is quite difficult to solve, since N is very large and a brute-force approach is not viable due to time constraints. In this work a thorough analysis of all major input parameters was performed, providing a PSA configuration close to the global optimum and thereby paving the way towards a maximized position resolution in high-purity germanium detectors.

However, further efforts are needed to achieve this goal. There are ongoing efforts within the AGATA collaboration and within other groups dedicated to improve the position resolution in highly segmented HPGe detectors. In the next section possible refinements of the results obtained in this thesis and future advancements of the PSA are discussed.

5.2 Outlook

A continued effort is made by the AGATA collaboration to improve the performance of the system and to increase the number of detectors which are operated. Currently, up to 45 crystals are mounted and take data simultaneously, leading to a solid angle coverage of about 1π [67]. Together with the growing number of detectors, the corresponding infrastructure needs to be expanded as well. Among others, this comprises the holding structure, the liquid nitrogen filling, high- and low-voltage power-supply and the read-out electronics.

For example, an advancement of the existing digitizer modules was developed [68]. A set of these digitizers has recently been put into operation in Cologne [69] and it is used to operate the symmetric triple cryostat [70] or any other AGATA detector. In the future, data taking and the PSA can be tested locally under realistic conditions.

The comparison of simulated and measured signals at given interaction positions, which was presented in chapter 3, depends on the results of the PSA to fix the interaction position. A bias is introduced, because it is not clear whether deviations of measurement and simulation originate from the simulated pulse shapes or from the deviation of PSA result and interaction position. The performed analysis should be refined by employing for example scanning-table data to fix the interaction positions.

In this thesis the ^{22}Na data was utilized to estimate the position resolution. In the future, these results should be confirmed with GEANT 4 simulations, which reproduce the results of the ^{22}Na -coincidence analysis and provide a connection between observed mean distance d and the position resolution of the PSA.

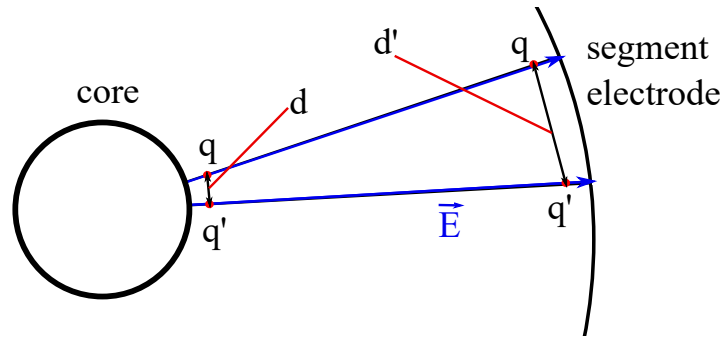


Figure 109: A simple sketch of a cylindrical detector is shown. The field lines (blue) go in radial direction. Two charges q and q' in close vicinity at distance d move along these field lines. During the process of charge collection the distance of the charges increases to d' because of the radial field lines. This effect is only relevant for interactions very close to the core.

5.2.1 Further developments and improvements with ADL

ADL is successfully used to simulate pulse shapes and perform PSA for AGATA experiments. In addition, it is utilized to simulate the pulse shapes for other HPGe detectors. For example, ADL is used for pulse-shape discrimination at the GERDA experiment [71] [72]. Despite the very successful application of ADL, the software could be further improved. For example, the impact of the following applied approximations on the final results could be the subject of future investigations.

5.2.1.1 Point-like charges

When a γ ray interacts in the crystal, for example via photo effect or Compton scattering, energy is transferred to an electron. The electron is stopped in the material, creating electron-hole pairs on its way. A charge cloud is created and its size depends on the energy deposited by the γ ray. During the process of charge collection, the size of the charge cloud increases due to Coulomb repulsion, diffusion and due to the shape of the electrical field.

The assumption of point-like charges, which is made by ADL, is not expected to impact the final results significantly [17]. An exception might be interactions close to the central contact. In a simple approximation the electrical field is radial. Close to the core the initial cloud size of holes becomes relevant, because the holes drift along the field lines such that charge-cloud size grows during charge collection. This effect is illustrated in a simplified sketch in Fig. 109. In addition, close to segmentation borders the finite size of the charge clouds becomes relevant due to charge sharing. The inclusion of non-point like charges in the simulation and the investigation of its impact on the final results could be examined.

5.2.1.2 Hole mobility

The hole mobility and therefore the drift velocity are temperature dependent. As discussed in section 4.3.6, the temperature of the crystal depends on its relative position with respect to the dewar, which holds the liquid nitrogen. The temperature dependence of the hole mobility should be taken into account, resulting in individual mobility values for each crystal.

As discussed in section 4.3.6, the measurement of the hole mobility via rise time measurements is challenging in an n-type HPGe-detector, because interactions close to the central electrode are required (see for example ref. [38]). This is not the case for p-type detectors, because typically the electrodes are interchanged, i.e. holes drift towards the central contact. Interactions close to the segment electrodes can easily be achieved with a low-energy γ -ray source, e.g. ^{241}Am . The experimental error on the hole mobility could be reduced by utilizing a p-type detector.

5.2.1.3 Geometry of the crystals and dead layers

The geometry of the crystals plays a vital role when calculating the weighting potentials and electrical fields with ADL. Identical geometries are assumed by the simulations for each respective A-, B- and C-type crystal. In the crystal growing process and the subsequent cutting of the crystal an uncertainty is introduced. For example the length L of the crystal is given by the manufacturer as $L = 90_{-1.4}^{+0.6}$ mm and the diameter D of the central drilling for core is given by manufacturer as $D = 10_{-0}^{+0.5}$ mm [73] [74]. In addition, some crystals were reprocessed and cut for repairs. It could be tested whether adapted geometries have a significant impact on the simulated pulse shapes and on the PSA results.

Dead layers are present in the germanium crystals, for example at the back of the crystal. The SiO_2 passivation at the back of the crystal is needed to prevent surface leakage currents. The dead layer was measured to up to 7 mm close to the core contact for a cylindrical HPGe detector [75]. In addition, a dead layer of about 0.5 mm exists close to the core contact. The presence of the dead layers change the shape of the electrical field. Future works could concentrate on analyzing the dead layers and their influence on the pulse shapes and incorporate the results into the simulations.

5.2.2 Future developments of the search algorithm

5.2.2.1 Improvements to the weighting of transient signals

In this thesis it was shown that in increased weighting of transient signals in the figure of merit calculation improves the PSA performance. In the future, an energy dependent weighting coefficient should be considered. For low-energy interactions the signal-to-noise ratio is poor, especially for the small transient signals. Depending on the interaction energy, the noise is in the same range as the induced signals. While a correct position determination is very challenging for small energy depositions in any case, a stronger weighting of the transient signals might not be favorable here due to the signal-to-noise ratio. This is also indicated by the different results which are obtained for

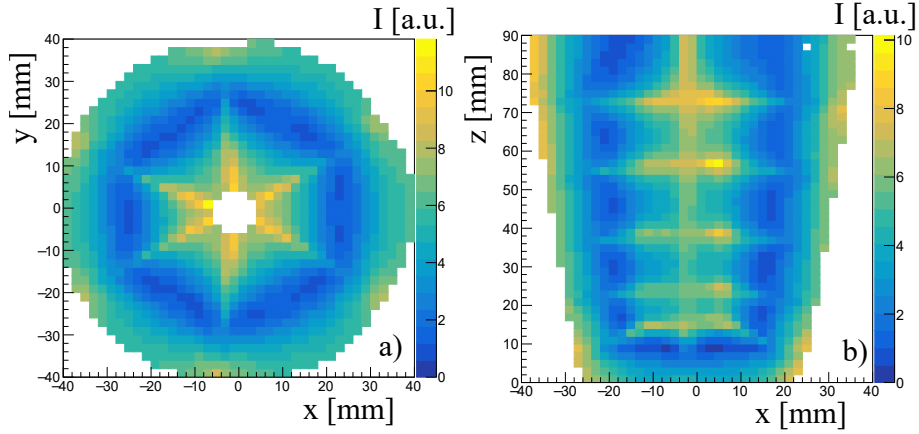


Figure 110: The integrated transient signals I of the nearest neighbors are shown for different interaction positions: a) for a fixed z of 80-82 mm and b) for a fixed y of 14-16 mm. The simulated signals of crystal A001 were used. A decrease for intermediate radii as well as for z values in the middle of the segment is observed.

type i) ("photo") and type ii) ("Compton") coincidences in the variation of the weighting coefficient (see section 4.3.1). The optimal weighting coefficient for type ii) coincidences (less than 340 keV deposited) is smaller than for type i) coincidences (511 keV energy deposition). An energy dependent weighting coefficient could have the following form:

$$w_i(E) = w_0 + w_{\max}(1 - \exp(-\lambda E)) \quad (5.3)$$

With w_0 , w_{\max} , λ as parameters. Reasonable values could be $w_0 = 1$ and $w_{\max} = 1.75$. A starting value for the exponential parameter λ could be derived from the parameter a_2 from eq. 3.3 in section 3.2. The parameter describes the saturating increase of the PSA performance for higher energies.

Additionally, the position dependent amplitude of the transient signals should be taken into account. Especially for intermediate radii, when the sign of the transient signals changes, the signals tend to vanish (see for example Fig. 68). This holds also partly true for intermediate angles and z values. The weighting coefficient should be proportional to the integral I of the absolute values of all transient signals:

$$I = \sum_i \sum_{t=0}^{40} \frac{|A_i(t)|}{E} \quad (5.4)$$

With $A_i(t)/E$ being the normalized pulse height at time t of segment i , which is adjacent to the hit segment. A distribution of the position dependent integral value I is shown for simulated signals in Fig. 110.

In a more refined grid search, the weighting coefficient should be proportional to the integrated transient signal of each individual neighboring segment I_i :

$$I_i = \sum_{t=0}^{40} \frac{|A_i(t)|}{E} \quad (5.5)$$

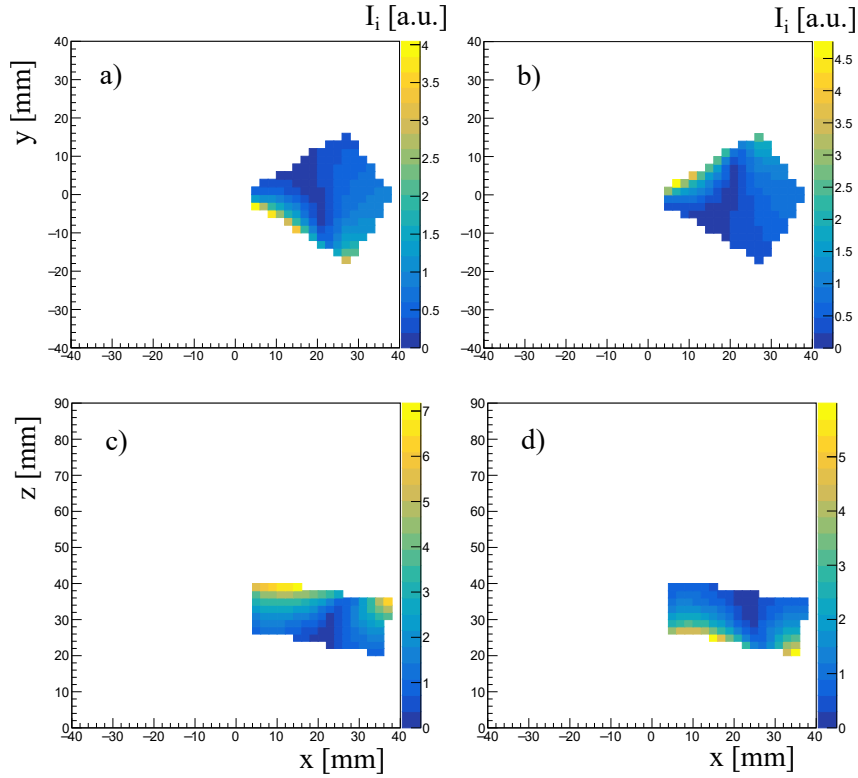


Figure 111: The simulated integrated transient signals I_i are shown for the a) left b) right c) upper and d) lower neighbor of segment A3 of crystal A001. The transient signals are smaller for intermediate radii and for interaction positions that are far away from the considered neighboring segment.

The integrated transient signals for the upper, lower, left and right neighbor are shown for a single segment in Fig. 111. In future investigations, these expected pulse shapes should be taken into account and a dynamic weighting should be used. A dynamic weighting coefficient could have the following form:

$$w_i = w_0 + c \cdot (I_i - I_0) \quad (5.6)$$

With w_0 and c being to be determined parameters and I_0 the expected value for summing up noise in the 400 ns time window.

5.2.2.2 Two hits within a single segment

The adaptive grid search only considers single interactions per segment. For typical γ -ray energies of a few hundred keV to a few MeV there is non negligible probability that the γ ray interacts twice within a segment. The mean free path of a γ ray in germanium for different energies is depicted in Fig. 112.

Two interaction positions in a single segment are difficult to resolve, since the number of possible solutions grows exponentially with the degrees of freedom. For example, the solution S of the adaptive grid search consists of the interaction position and the determined starting time T_0 , which is included

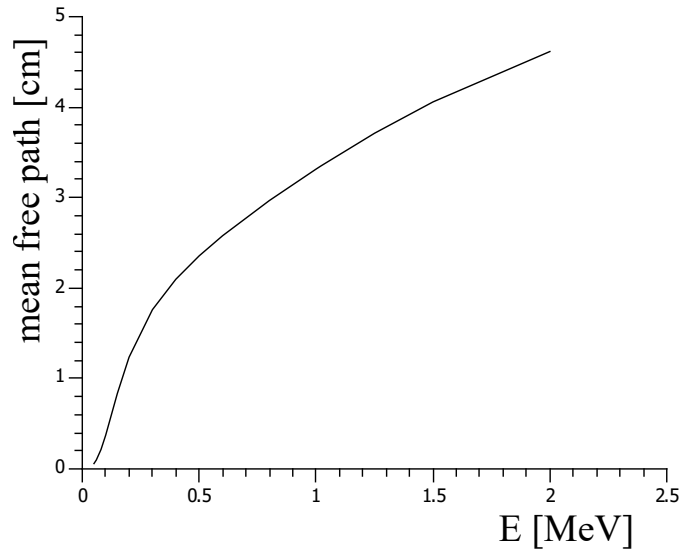


Figure 112: The mean free path of a γ ray in germanium is plotted in dependence of the γ -ray energy. There is a non-negligible chance for multiple interactions within a single segment. Values calculated from [76].

in the grid search: $S = (x, y, z, T_0)$. In case two interactions are considered the dimension of S is much larger: $S = (N_{\text{int}}, x_1, y_1, z_1, T_{0,1}, x_2, y_2, z_2, T_{0,2}, E_1/E_2)$. The solution S consists of the number of interactions $N_{\text{int}} = 1$ or 2, the two interaction positions and their respective starting times T_0 and the unknown energy ratio E_1/E_2 of the two interactions. As discussed in section 2.1.2.1, the problem is mathematically underdetermined, i.e. the number of possible solutions is large compared to the available data.

As a result, the solution with $N_{\text{int}} = 2$ often improves the χ^2 or figure of merit, due to the increased number of degrees of freedom which can be fitted to the measured data. However, the improved χ^2 is not necessarily connected to an improved position resolution. Algorithms which include multiple interactions per segment have to cope with this problem. For example, the GRETINA signal decomposition [77] introduced arbitrary "penalty factors" such that the two-hit result is only used if a certain improvement of the χ^2 is achieved.

In the future two interactions per segment should be included in the adaptive grid search and the impact on the PSA results investigated.

5.2.2.3 New search algorithms

The improvement of the existing adaptive grid search is an ongoing effort within the AGATA collaboration. For example, the sensitivity [42] of the individual interaction positions could be taken into account. At some positions in the crystal, for example at segment borders, the pulse shapes change considerably, when comparing neighboring grid points. At other locations, e.g. in the segment centers, the pulse shapes change only slightly. An irregular grid is utilized by the GRETINA signal decomposition, which has a high density of grid points at locations where signals change rapidly [43].

A similar approach could be utilized for the adaptive grid search.

This approach is also of interest, since the size of the grid points can not be reduced without accepting longer computing times. With the growing number of crystals, the time it takes to calculate the PSA results becomes more and more relevant. Using the current infrastructure at GANIL and employing 45 crystals, the count rates are already limited by the PSA for some high-intensity experiments.

The research of new approaches, which consider new possibilities beyond the well established grid-search algorithms, is of high interest. One possibility is a machine-learning approach employing neural networks. Such a network could be trained to recognize pulse shapes and associate them with interaction positions. An effort has been made to determine interaction positions in HPGe detectors utilizing machine-learning techniques, but the development is in an early stage [78]. The performance of the neural network relies heavily on the training data. In a simple approach the simulated ADL pulse shapes could be used. Other training parameters, like the agreement with simulated hit distributions, the correct reconstruction of ^{22}Na 180° coincidences or the width of a Doppler corrected peak could be utilized as well.

The major advantage of a machine-learning approach is that all details of the simulation and of the grid search, e.g. segment specific transfer functions or optimal weightings, are incorporated automatically. The drawback of this technique is that it works as a "black box", i.e. it is not known how the algorithm obtains its results. The results can not be traced back to physical parameters, like drift velocities.

5.2.3 New developments for position-sensitive HPGe-detectors

New HPGe detector types are under development which are designed to complement the current state-of-the-art tracking arrays AGATA and GREYTA. A promising candidate is the inverted coaxial point-contact (ICPC) detector [79]. In comparison to closed-end coaxial detectors, the core electrode is a point contact at the back of the detector. As a result, the corresponding charge carriers drift through the complete crystal and drift times are considerably increased. As a consequence, multiple interactions per segment are easily disentangled and pulse-shape analysis is significantly simplified. A position resolution below 1 mm is expected [80].

Disadvantages of this technology are the limitation of the counting rate and an increased amount of trapping. The trapping occurs during the long drift times which reduces the energy resolution. Correction algorithms were developed to partially retain the good energy resolution of the HPGe crystal [81]. The low counting rate capability limits the use for in-beam experiments. Applications in low counting-rate experiments, such as GERDA, are more promising [82]. Up to now, the tracking arrays, such as AGATA, are the solution of choice for the γ -ray spectroscopy of exotic nuclei.

Bibliography

- [1] P. Spiller and G. Franchetti. “The FAIR accelerator project at GSI.” *Nuclear Instruments and Methods in Physics Research Section A: Accelerators, Spectrometers, Detectors and Associated Equipment* 561.2 (2006). Proceedings of the Workshop on High Intensity Beam Dynamics, pp. 305–309 (cit. on p. 7).
- [2] M. Lindroos, P. Butler, M. Huysse and K. Riisager. “HIE-ISOLDE.” *Nuclear Instruments and Methods in Physics Research Section B: Beam Interactions with Materials and Atoms* 266.19 (2008). Proceedings of the XVth International Conference on Electromagnetic Isotope Separators and Techniques Related to their Applications, pp. 4687–4691 (cit. on p. 7).
- [3] G. Prete, A. Andrichetto, J. Esposito, P. Mastinu and J. Wyss. “The SPES project: a second generation ISOL facility.” *Physics Procedia* 26 (2012). Proceedings of the first two meetings of the Union of Compact Accelerator-Driven Neutron Sources, pp. 274–283 (cit. on p. 7).
- [4] M. Lewitowicz. “The SPIRAL 2 Project.” *AIP Conference Proceedings* 891.1 (2007), pp. 91–98 (cit. on p. 7).
- [5] I.-Y. Lee. “The GAMMASPHERE.” *Nuclear Physics A* 520 (1990). Nuclear Structure in the Nineties, pp. c641–c655 (cit. on p. 7).
- [6] J. Simpson. “The Euroball Spectrometer.” *Zeitschrift für Physik A Hadrons and Nuclei* 358.2 (Feb. 1997), pp. 139–143 (cit. on p. 7).
- [7] N. Warr et al. “The Miniball spectrometer.” *The European Physical Journal A* 49.3 (Mar. 2013), p. 40 (cit. on p. 7).
- [8] G. de France. “EXO GAM: A γ -ray spectrometer for exotic beams.” *AIP Conference Proceedings* 455.1 (1998), pp. 977–980 (cit. on p. 7).
- [9] I. Lee, R. Clark, M. Cromaz, M. Deleplanque, M. Descovich, R. Diamond, P. Fallon, A. Macchiavelli, F. Stephens and D. Ward. “GRETINA: A gamma ray energy tracking array.” *Nuclear Physics A* 746 (2004). Proceedings of the Sixth International Conference on Radioactive Nuclear Beams (RNB6), pp. 255–259 (cit. on p. 7).
- [10] Akkoyun et al. “AGATA - Advanced GAMMA Tracking Array.” *Nuclear Instruments and Methods in Physics Research Section A: Accelerators, Spectrometers, Detectors and Associated Equipment* 668 (2012), pp. 26–58 (cit. on pp. 7–8, 12, 17, 54).
- [11] B. Bruyneel et al. “Correction for hole trapping in AGATA detectors using pulse shape analysis.” *The European Physical Journal A* 49.5 (May 2013), p. 61 (cit. on p. 8).
- [12] M. Descovich, I. Lee, P. Luke, R. Clark, M. Cromaz, M. Deleplanque, R. Diamond, P. Fallon, A. Macchiavelli, E. Rodriguez-Vieitez, F. Stephens and D. Ward. “Effects of neutron damage on the performance of large volume segmented germanium detectors.” *Nuclear Instruments and Methods in Physics Research Section A: Accelerators, Spectrometers, Detectors and Associated Equipment* 545.1 (2005), pp. 199–209 (cit. on p. 8).

- [13] A. Wiens, H. Hess, B. Birkenbach, B. Bruyneel, J. Eberth, D. Lersch, G. Pascovici, P. Reiter and H.-G. Thomas. “The AGATA triple cluster detector.” *Nuclear Instruments and Methods in Physics Research Section A: Accelerators, Spectrometers, Detectors and Associated Equipment* 618.1 (2010), pp. 223–233 (cit. on p. 8).
- [14] E. Farnea, F. Recchia, D. Bazzacco, T. Kröll, Z. Podolyák, B. Quintana and A. Gadea. “Conceptual design and Monte Carlo simulations of the AGATA array.” *Nuclear Instruments and Methods in Physics Research Section A: Accelerators, Spectrometers, Detectors and Associated Equipment* 621.1 (2010), pp. 331–343 (cit. on p. 8).
- [15] A. Lopez-Martens, K. Hauschild, A. Korichi, J. Roccaz and J.-P. Thibaud. “Gamma-ray tracking algorithms: a comparison.” *Nuclear Instruments and Methods in Physics Research Section A: Accelerators, Spectrometers, Detectors and Associated Equipment* 533.3 (2004), pp. 454–466 (cit. on p. 8).
- [16] D. Bazzacco. “The Advanced Gamma Ray Tracking Array AGATA.” *Nuclear Physics A* 746 (2004). Proceedings of the Sixth International Conference on Radioactive Nuclear Beams (RNB6), pp. 248–254 (cit. on p. 8).
- [17] B. Bruyneel, B. Birkenbach and P. Reiter. “Pulse shape analysis and position determination in segmented HPGe detectors: The AGATA detector library.” *The European Physical Journal A* 52.3 (Mar. 2016), p. 70 (cit. on pp. 9–10, 41, 98, 120).
- [18] R. Venturelli and D. Bazzacco. “Adaptive Grid Search as Pulse Shape Analysis Algorithm for γ -Tracking and Results.” *LNL Annual Report 2004* (2005), p. 220 (cit. on p. 9).
- [19] P. Medina, C. Santos and D. Villaume. “A simple method for the characterization of HPGe detectors.” *Proceedings of the 21st IEEE Instrumentation and Measurement Technology Conference (IEEE Cat. No.04CH37510)*. Vol. 3. May 2004, 1828–1832 Vol.3 (cit. on p. 9).
- [20] M. Schlarb, R. Gernhäuser, S. Klupp and R. Krücken. “Pulse shape analysis for γ -ray tracking (Part I): Pulse shape simulation with JASS.” *The European Physical Journal A* 47.10 (Oct. 2011), p. 132 (cit. on pp. 9, 14).
- [21] fieldgen. <https://radware.phy.ornl.gov/gretina/fieldgen/>. Accessed: 2019-06-11 (cit. on p. 9).
- [22] siggen. <https://radware.phy.ornl.gov/gretina/siggen/>. Accessed: 2019-06-11 (cit. on p. 9).
- [23] A. Boston, H. Boston, J. Cresswell, M. Dimmock, L. Nelson, P. Nolan, S. Rigby, I. Lazarus, J. Simpson, P. Medina, C. Santos and C. Parisel. “Gamma-ray tracking: Characterisation of the AGATA symmetric prototype detectors.” *Nuclear Instruments and Methods in Physics Research Section B: Beam Interactions with Materials and Atoms* 261.1 (2007). The Application of Accelerators in Research and Industry, pp. 1098–1102 (cit. on p. 9).
- [24] T. Ha, A. Korichi, F. L. Blanc, P. Désesquelles, N. Dosme, X. Grave, N. Karkour, S. Leboutelier, E. Legay, D. Linget, B. Travers and P. Pariset. “New setup for the characterisation of the AGATA detectors.” *Nuclear Instruments and Methods in Physics Research Section A: Accelerators, Spectrometers, Detectors and Associated Equipment* 697 (2013), pp. 123–132 (cit. on p. 9).
- [25] A. Hernández-Prieto and B. Quintana. “Towards a deep characterization of a 64-fold-pixelated position sensitive detector for a new γ -scanning system of HPGe segmented detectors.” *2011 2nd International Conference on Advancements in Nuclear Instrumentation, Measurement Methods and their Applications*. June 2011, pp. 1–5 (cit. on p. 10).

- [26] M. Ginz. “Characterization of high-purity, multi-segmented germanium detectors.” PhD thesis. IPHC Strasbourg, 2015 (cit. on p. 10).
- [27] P. Désesquelles, A. Boston, H. Boston, J. Cresswell, M. Dimmock, I. Lazarus, J. Ljungvall, L. Nelson, D.-T. Nga, P. Nolan, S. Rigby, J. Simpson and N.-T. Van-Oanh. “Direct determination of the hit locations from experimental HPGe pulses.” *Nuclear Instruments and Methods in Physics Research Section A: Accelerators, Spectrometers, Detectors and Associated Equipment* 729 (2013), pp. 198–206 (cit. on p. 10).
- [28] H. J. Li, J. Ljungvall, C. Michelagnoli, E. Clément, J. Dudouet, P. Désesquelles, A. Lopez-Martens and G. de France. “Experimental determination of reference pulses for highly segmented HPGe detectors and application to Pulse Shape Analysis used in γ -ray tracking arrays.” *The European Physical Journal A* 54.11 (Nov. 2018), p. 198 (cit. on pp. 10, 15).
- [29] B. Birkenbach, B. Bruyneel, G. Pascovici, J. Eberth, H. Hess, D. Lersch, P. Reiter and A. Wiens. “Determination of space charge distributions in highly segmented large volume HPGe detectors from capacitance–voltage measurements.” *Nuclear Instruments and Methods in Physics Research Section A: Accelerators, Spectrometers, Detectors and Associated Equipment* 640.1 (2011), pp. 176–184 (cit. on p. 11).
- [30] B. Bruyneel, B. Birkenbach and P. Reiter. “Space charge reconstruction in highly segmented HPGe detectors through capacitance-voltage measurements.” *Nuclear Instruments and Methods in Physics Research Section A: Accelerators, Spectrometers, Detectors and Associated Equipment* 641.1 (2011), pp. 92–100 (cit. on p. 11).
- [31] G. F. Knoll. “Radiation Detection and Measurement.” *Fourth edition*. 2010 (cit. on p. 12).
- [32] M. J. Berger, J. S. Coursey, M. Zucker and J. Chang. ESTAR, PSTAR, and ASTAR: Computer Programs for Calculating Stopping-Power and Range Tables for Electrons, Protons, and Helium Ions (version 1.2.3). [Online] Available: <http://physics.nist.gov/Star>. National Institute of Standards and Technology. June 2019 (cit. on p. 13).
- [33] E. Gatti, G. Padovini and V. Radeka. “Signal evaluation in multielectrode radiation detectors by means of a time dependent weighting vector.” *Nuclear Instruments and Methods in Physics Research Section A: Accelerators, Spectrometers, Detectors and Associated Equipment* (1982) (cit. on p. 13).
- [34] B. Bruyneel, P. Reiter, A. Wiens, J. Eberth, H. Hess, G. Pascovici, N. Warr and D. Weisshaar. “Crosstalk properties of 36-fold segmented symmetric hexagonal HPGe detectors.” *Nuclear Instruments and Methods in Physics Research Section A: Accelerators, Spectrometers, Detectors and Associated Equipment* 599.2 (2009), pp. 196–208 (cit. on p. 14).
- [35] B. Bruyneel, P. Reiter, A. Wiens, J. Eberth, H. Hess, G. Pascovici, N. Warr, S. Aydin, D. Bazzacco and F. Recchia. “Crosstalk corrections for improved energy resolution with highly segmented HPGe-detectors.” *Nuclear Instruments and Methods in Physics Research Section A: Accelerators, Spectrometers, Detectors and Associated Equipment* 608.1 (2009), pp. 99–106 (cit. on p. 14).
- [36] B. Bruyneel. On the origin of differential crosstalk in segmented detectors. 2008. URL: https://www.ikp.uni-koeln.de/research/agata/talks/AGATA_Bruyneel_1_2008.ppt (cit. on p. 14).
- [37] B. Bruyneel. Pulse Shape Analysis with the AGATA Demonstrator. 2010. URL: <https://www.ikp.uni-koeln.de/research/agata/talks/Berkeley-Bruyneel-2010.pdf> (cit. on p. 14).

- [38] B. Bruyneel, P. Reiter and G. Pascovici. “Characterization of large volume HPGe detectors. Part II: Experimental results.” *Nuclear Instruments and Methods in Physics Research Section A: Accelerators, Spectrometers, Detectors and Associated Equipment* 569.3 (2006), pp. 774–789 (cit. on pp. 14, 98–99, 102, 121).
- [39] M. Schlarb. “Simulation and Real-Time Analysis of Pulse Shapes from segmented HPGe-Detectors.” PhD thesis. Technische Universität München, 2009 (cit. on p. 14).
- [40] M. Schlarb, R. Gernhäuser, S. Klupp and R. Krücken. “Pulse shape analysis for γ -ray tracking (Part II): Fully informed particle swarm algorithm applied to AGATA.” *The European Physical Journal A* 47.10 (Oct. 2011), p. 131 (cit. on pp. 14–15).
- [41] J. Eberth, G. Pascovici, H. Thomas, N. Warr, D. Weisshaar, D. Habs, P. Reiter, P. Thierolf, D. Schwalm, C. Gund, H. Scheit, M. Lauer, P. V. Duppen, S. Franchoo, M. Huysse, R. Lieder, W. Gast, J. Gerl and K. Lieb. “MINIBALL A Ge detector array for radioactive ion beam facilities.” *Progress in Particle and Nuclear Physics* 46.1 (2001), pp. 389–398 (cit. on p. 15).
- [42] K. Vetter, A. Kuhn, M. Deleplanque, I. Lee, F. Stephens, G. Schmid, D. Bechedahl, J. Blair, R. Clark, M. Cromaz, R. Diamond, P. Fallon, G. Lane, J. Kammeraad, A. Macchiavelli and C. Svensson. “Three-dimensional position sensitivity in two-dimensionally segmented HP-Ge detectors.” *Nuclear Instruments and Methods in Physics Research Section A: Accelerators, Spectrometers, Detectors and Associated Equipment* 452.1 (2000), pp. 223–238 (cit. on pp. 15, 124).
- [43] D. Radford. The GRETINA Signal Decomposition Algorithm. 2016. URL: <https://indico.in2p3.fr/event/13409/contributions/14197/> (cit. on pp. 15, 124).
- [44] R. Venturelli. PSA: The adaptive grid search. Tech. rep. INFN Padova, 2006 (cit. on p. 17).
- [45] A. Pullia, G. Pascovici, B. Cahan, D. E. Weisshaar, C. Boiano, R. Bassini, M. Petcu and F. Zocca. “The AGATA charge-sensitive preamplifiers with built-in active-reset device and pulser.” *IEEE Symposium Conference Record Nuclear Science 2004*. 3 (2004), 1411–1414 Vol. 3 (cit. on pp. 17, 90).
- [46] G. Pascovici, A. Pullia, F. Zocca, B. Bruyneel and D. Bazzacco. “Low Noise, Dual Gain Preamplifier with Built in Spectroscopic Pulser for Highly Segmented High-purity Germanium Detectors.” *WSEAS Trans. Cir. and Sys.* 7.6 (June 2008), pp. 470–481 (cit. on pp. 17, 90).
- [47] L. Arnold, R. Baumann, E. Chambit, M. Filliger, C. Fuchs, C. Kieber, D. Klein, P. Medina, C. Parisel, M. Richer, C. Santos and C. Weber. “TNT digital pulse processor.” *Nuclear Science, IEEE Transactions on* 53 (July 2006), pp. 723–728 (cit. on p. 17).
- [48] A. Georgiev and W. Gast. “Digital pulse processing in high resolution, high throughput, gamma-ray spectroscopy.” *IEEE Transactions on Nuclear Science* 40.4 (Aug. 1993), pp. 770–779 (cit. on p. 17).
- [49] F. Recchia, D. Bazzacco, E. Farnea, A. Gadea, R. Venturelli, T. Beck, P. Bednarczyk, A. Buerger, A. Dewald, M. Dimmock, G. Duchêne, J. Eberth, T. Faul, J. Gerl, R. Gernhäuser, K. Hauschild, A. Holler, P. Jones, W. Korten, T. Kröll, R. Krücken, N. Kurz, J. Ljungvall, S. Lunardi, P. Maierbeck, D. Mengoni, J. Nyberg, L. Nelson, G. Pascovici, P. Reiter, H. Schaffner, M. Schlarb, T. Steinhardt, O. Thelen, C. Ur, J. V. Dobon and D. Weißhaar. “Position resolution of the prototype AGATA triple-cluster detector from an in-beam experiment.” *Nuclear Instruments and Methods in Physics Research Section A: Accelerators, Spectrometers, Detectors and Associated Equipment* 604.3 (2009), pp. 555–562 (cit. on p. 27).

- [50] P-A. Söderström, F Recchia, J. Nyberg, A. Al-Adili, A. Ataç, S. Aydin, D. Bazzacco, P Bednarczyk, B. Birkenbach, D. Bortolato, A. Boston, H. Boston, B. Bruyneel, D. Bucurescu, E. Calore, S. Colosimo, F. Crespi, N. Dosme, J. Eberth, E. Farnea, F. Filmer, A. Gadea, A. Gottardo, X. Grave, J. Grebosz, R. Griffiths, M. Gulmini, T. Habermann, H. Hess, G. Jaworski, P. Jones, P. Joshi, D. Judson, R. Kempley, A. Khaplanov, E. Legay, D. Lersch, J. Ljungvall, A. Lopez-Martens, W. Meczynski, D. Mengoni, C. Michelagnoli, P. Molini, D. Napoli, R. Orlandi, G. Pascovici, A. Pullia, P. Reiter, E. Sahin, J. Smith, J. Strachan, D. Tonev, C. Unsworth, C. Ur, J. Valiente-Dobón, C. Veysiére and A. Wiens. “Interaction position resolution simulations and in-beam measurements of the AGATA HPGe detectors.” *Nuclear Instruments and Methods in Physics Research Section A: Accelerators, Spectrometers, Detectors and Associated Equipment* 638.1 (2011), pp. 96–109 (cit. on pp. 27, 31).
- [51] S. Klupp. “A Calibration Experiment for the AGATA Pulse Shape Analysis.” MA thesis. TU München, 2011 (cit. on p. 27).
- [52] F. Recchia. “In-beam test and imaging capabilities of the AGATA prototype detector.” PhD thesis. Università degli Studi di Padova, 2008, pp. 108–109 (cit. on p. 29).
- [53] L. Lewandowski. “Optimization of the Pulse Shape Analysis for the Position-Sensitive γ -Ray Spectrometer AGATA.” MA thesis. 2014 (cit. on pp. 29, 35–36, 72).
- [54] R. Brun and F. Rademakers. “Proceedings AIHENP’96 Workshop.” *Nucl. Inst. and Meth. in Phys. Res. A* (1996) (cit. on p. 50).
- [55] J. Dryzek. “Detection of Positron Implantation Profile in different Materials.” *Proceedings of the 35th Polish Seminar on Positron Annihilation* (cit. on p. 59).
- [56] L. Lewandowski, P. Reiter, B. Birkenbach, B. Bruyneel, E. Clement, J. Eberth, H. Hess, C. Michelagnoli, H. Li, R. M. Perez-Vidal and M. Zielinska. “Pulse-Shape Analysis and position resolution in highly segmented HPGe AGATA detectors.” *The European Physical Journal A* 55.5 (May 2019), p. 81 (cit. on p. 77).
- [57] M. Descovich, I. Lee, P. Fallon, M. Cromaz, A. Macchiavelli, D. Radford, K. Vetter, R. Clark, M. Deleplanque, F. Stephens and D. Ward. “In-beam measurement of the position resolution of a highly segmented coaxial germanium detector.” *Nuclear Instruments and Methods in Physics Research Section A: Accelerators, Spectrometers, Detectors and Associated Equipment* 553.3 (2005), pp. 535–542 (cit. on p. 89).
- [58] A. Pullia, D. Barrientos, D. Bazzacco, M. Bellato, D. Bortolato and R. Isocrate. “A 12-channel 14/16-bit 100/125-MS/s digitizer with 24-Gb/s optical output for AGATA/GALILEO.” *2012 IEEE Nuclear Science Symposium and Medical Imaging Conference Record (NSS/MIC)*. Oct. 2012, pp. 819–823 (cit. on p. 91).
- [59] C. Mittermayer and A. Steininger. “On the determination of dynamic errors for rise time measurement with an oscilloscope.” *IEEE Transactions on Instrumentation and Measurement* 48.6 (Dec. 1999), pp. 1103–1107 (cit. on p. 91).
- [60] B. Bruyneel, P. Reiter and G. Pascovici. “Characterization of large volume HPGe detectors. Part I: Electron and hole mobility parameterization.” *Nuclear Instruments and Methods in Physics Research Section A: Accelerators, Spectrometers, Detectors and Associated Equipment* 569.3 (2006), pp. 764–773 (cit. on pp. 98, 102).
- [61] B. Bruyneel, B. Birkenbach, G. Pascovici, J. Eberth, H. Hess, D. Lersch, P. Reiter, A. Wiens, D. Bazzacco, E. Farnea and F. Recchia. “Determination of the Crystal Orientation of the AGATA Detectors.” *LNL Annual Report*. 2010 (cit. on p. 98).

- [62] L. Reggiani, C. Canali, F. Nava and G. Ottaviani. “Hole drift velocity in germanium.” *Phys. Rev. B* 16 (6 Sept. 1977), pp. 2781–2791 (cit. on pp. 99–100).
- [63] L. Mihailescu, W. Gast, R. Lieder, H. Brands and H. Jäger. “The influence of anisotropic electron drift velocity on the signal shapes of closed-end HPGe detectors.” *Nuclear Instruments and Methods in Physics Research Section A: Accelerators, Spectrometers, Detectors and Associated Equipment* 447.3 (2000), pp. 350–360 (cit. on pp. 99, 102).
- [64] V. Prasher, M. Cromaz, E. Merchan, P. Chowdhury, H. Crawford, C. Lister, C. Campbell, I. Lee, A. Macchiavelli, D. Radford and A. Wiens. “Sensitivity of GRETINA position resolution to hole mobility.” *Nuclear Instruments and Methods in Physics Research Section A: Accelerators, Spectrometers, Detectors and Associated Equipment* 846 (2017), pp. 50–55 (cit. on p. 99).
- [65] F. J. Morin. “Lattice-Scattering Mobility in Germanium.” *Phys. Rev.* 93 (1 Jan. 1954), pp. 62–63 (cit. on p. 100).
- [66] M. A. Omar and L. Reggiani. “Drift velocity and diffusivity of hot carriers in germanium: Model calculations.” *Solid-State Electronics* 30.12 (1987), pp. 1351–1354 (cit. on p. 100).
- [67] E. Clément, C. Michelagnoli, G. de France, H. Li, A. Lemasson, C. B. Dejean, M. Beuzard, P. Bougault, J. Cacitti, J.-L. Foucher, G. Fremont, P. Gangnant, J. Goupil, C. Houarner, M. Jean, A. Lefevre, L. Legeard, F. Legruel, C. Maugeais, L. Ménager, N. Ménard, H. Munoz, M. Ozille, B. Raine, J. Ropert, F. Saillant, C. Spitaels, M. Tripon, P. Vallerand, G. Voltolini, W. Korten, M.-D. Salsac, C. Theisen, M. Zielińska, T. Joannem, M. Karolak, M. Kebbiri, A. Lotode, R. Touzery, C. Walter, A. Korichi, J. Ljungvall, A. Lopez-Martens, D. Ralet, N. Dosme, X. Grave, N. Karkour, X. Lafay, E. Legay, I. Kojouharov, C. Domingo-Pardo, A. Gadea, R. Pérez-Vidal, J. Civera, B. Birkenbach, J. Eberth, H. Hess, L. Lewandowski, P. Reiter, A. Nannini, G. D. Angelis, G. Jaworski, P. John, D. Napoli, J. Valiente-Dobón, D. Barrientos, D. Bortolato, G. Benzoni, A. Bracco, S. Brambilla, F. Camera, F. Crespi, S. Leoni, B. Million, A. Pullia, O. Wieland, D. Bazzacco, S. Lenzi, S. Lunardi, R. Menegazzo, D. Mengoni, F. Recchia, M. Bellato, R. Isocrate, F. E. Canet, F. Didierjean, G. Duchêne, R. Baumann, M. Brucker, E. Dangelser, M. Filliger, H. Friedmann, G. Gaudiot, J.-N. Grapton, H. Kocher, C. Mathieu, M.-H. Sigward, D. Thomas, S. Veeramootoo, J. Dudouet, O. Stézowski, C. Aufranc, Y. Aubert, M. Labiche, J. Simpson, I. Burrows, P. Coleman-Smith, A. Grant, I. Lazarus, P. Morrall, V. Pucknell, A. Boston, D. Judson, N. Lalović, J. Nyberg, J. Collado, V. González, I. Kuti, B. Nyakó, A. Maj and M. Rudigier. “Conceptual design of the AGATA 1π array at GANIL.” *Nuclear Instruments and Methods in Physics Research Section A: Accelerators, Spectrometers, Detectors and Associated Equipment* 855 (2017), pp. 1–12 (cit. on p. 119).
- [68] D. Barrientos, M. Bellato, D. Bazzacco, D. Bortolato, P. Cocconi, A. Gadea, V. González, M. Gulmini, R. Isocrate, D. Mengoni, A. Pullia, F. Recchia, D. Rosso, E. Sanchis, N. Toniolo, C. A. Ur and J. J. Valiente-Dobón. “Performance of the Fully Digital FPGA-Based Front-End Electronics for the GALILEO Array.” *IEEE Transactions on Nuclear Science* 62.6 (Dec. 2015), pp. 3134–3139 (cit. on p. 119).
- [69] R. Hetzenegger. “platzhalter.” MA thesis. Universität zu Köln, 2019 (cit. on p. 119).
- [70] A. Boston, H. Boston, J. Cresswell, M. Dimmock, L. Nelson, P. Nolan, S. Rigby, I. Lazarus, J. Simpson, P. Medina, C. Santos and C. Parisel. “Gamma-ray tracking: Characterisation of the AGATA symmetric prototype detectors.” *Nuclear Instruments and Methods in Physics Research Section B: Beam Interactions with Materials and Atoms* 261.1 (2007). The Application of Accelerators in Research and Industry, pp. 1098–1102 (cit. on p. 119).

- [71] B. Lehnert. “Background rejection of n^+ surface events in GERDA Phase II.” *Journal of Physics: Conference Series* 718 (May 2016), p. 062035 (cit. on p. 120).
- [72] A. Domula, M. Hult, Y. Kermaidic, G. Marissens, B. Schwingenheuer, T. Wester and K. Zuber. “Pulse shape discrimination performance of inverted coaxial Ge detectors.” *Nuclear Instruments and Methods in Physics Research Section A: Accelerators, Spectrometers, Detectors and Associated Equipment* 891 (2018), pp. 106–110 (cit. on p. 120).
- [73] M. Allali. Irregular AGATA Canister N°C 001, manual. 2005 (cit. on p. 121).
- [74] M. Allali. AGATA Canister C014, manual. 2015 (cit. on p. 121).
- [75] J. Eberth and J. Simpson. “From Ge(Li) detectors to gamma-ray tracking arrays—50 years of gamma spectroscopy with germanium detectors.” *Progress in Particle and Nuclear Physics* 60.2 (2008), pp. 283–337 (cit. on p. 121).
- [76] M. Berger, J. Hubbell, S. Seltzer, J. Chang, J. Coursey, R. Sukumar, D. Zucker and K. Olsen. XCOM: Photon Cross Sections Database. NIST Standard Reference Database 8 (XGAM). 2010. URL: <https://dx.doi.org/10.18434/T48G6X> (cit. on p. 124).
- [77] S. Paschalis, I. Lee, A. Macchiavelli, C. Campbell, M. Cromaz, S. Gros, J. Pavan, J. Qian, R. Clark, H. Crawford, D. Doering, P. Fallon, C. Lionberger, T. Loew, M. Petri, T. Stezelberger, S. Zimmermann, D. Radford, K. Lagergren, D. Weisshaar, R. Winkler, T. Glasmacher, J. Anderson and C. Beausang. “The performance of the Gamma-Ray Energy Tracking In-beam Nuclear Array GRETINA.” *Nuclear Instruments and Methods in Physics Research Section A: Accelerators, Spectrometers, Detectors and Associated Equipment* 709 (2013), pp. 44–55 (cit. on p. 124).
- [78] F. Holloway. Development of Novel PSA Algorithms for AGATA. 2018. URL: https://indico.in2p3.fr/event/17160/contributions/64834/attachments/49892/63569/AG5-4_Holloway_AGATA_Week_Presentation.pptx (cit. on p. 125).
- [79] R. Cooper, D. Radford, P. Hausladen and K. Lagergren. “A novel HPGe detector for gamma-ray tracking and imaging.” *Nuclear Instruments and Methods in Physics Research Section A: Accelerators, Spectrometers, Detectors and Associated Equipment* 665 (2011), pp. 25–32 (cit. on p. 125).
- [80] J. Wright, L. Harkness-Brennan, A. Boston, D. Judson, M. Labiche, P. Nolan, R. Page, F. Pearce, D. Radford, J. Simpson and C. Unsworth. “Position resolution simulations for the inverted-coaxial germanium detector, SIGMA.” *Nuclear Instruments and Methods in Physics Research Section A: Accelerators, Spectrometers, Detectors and Associated Equipment* 892 (2018), pp. 84–92 (cit. on p. 125).
- [81] M. Salathe, R. Cooper, H. Crawford, D. Radford, J. Allmond, C. Campbell, R. Clark, M. Cromaz, P. Fallon, P. Hausladen, M. Jones, A. Macchiavelli and J. Wright. “Energy reconstruction of an n-type segmented inverted coaxial point-contact HPGe detector.” *Nuclear Instruments and Methods in Physics Research Section A: Accelerators, Spectrometers, Detectors and Associated Equipment* 868 (2017), pp. 19–26 (cit. on p. 125).
- [82] A. Domula, M. Hult, Y. Kermaidic, G. Marissens, B. Schwingenheuer, T. Wester and K. Zuber. “Pulse shape discrimination performance of inverted coaxial Ge detectors.” *Nuclear Instruments and Methods in Physics Research Section A: Accelerators, Spectrometers, Detectors and Associated Equipment* 891 (2018), pp. 106–110 (cit. on p. 125).

List of figures

1	Segmentation of A001 in xy and xz depiction.	11
2	Depiction of used coordinate system to describe positions in the crystal with either Cartesian or cylindrical coordinates.	12
3	Weighting potential of an A-type crystal calculated with ADL.	13
4	Flow chart for the AGATA data acquisition and subsequent analysis.	18
5	Sketch of an AGATA crystal which indicates positions with identical expected number of hits.	19
6	Interaction positions in the lab system in xy and xz depiction.	20
7	Distribution of hits in crystal coordinate system for A001, gated on $z = 2 - 4$ mm and $z = 14 - 16$ mm.	20
8	Distribution of hits for $z = 46 - 48$ mm and $z = 86 - 88$ mm.	21
9	Distribution of hits for $z = 46 - 48$ mm gated on one triggered segment, $E > 400$ keV and $E < 100$ keV.	22
10	Surface plot depicting the hit distribution for $z = 26 - 28$ mm.	22
11	Overview of hit distribution for crystals 1-15 at $z = 20 - 22$ mm.	23
12	Overview of hit distribution for crystals 16-29 at $z = 20 - 22$ mm.	24
13	Number of hits in dependence of detector depth z and correlation of z and radius.	25
14	Illustration how different color codes change the perceived distribution of hits.	26
15	Illustration how different maximum values for the color codes change the perceived distribution of hits.	26
16	Exemplary super trace, best fitting simulation and residuals.	30
17	Super trace for a low-energy interaction.	31
18	Figure of merit landscape for one exemplary event.	32
19	Figure of merit landscape including transient weighting.	33
20	Figure of merit along r and z axes for one event.	34
21	Figure of merit along r and z axes for one event, including transient weighting.	34
22	Ratio of minimal and maximal figure of merit along r and z axes for multiple events.	35
23	Dependence of ratio of minimal and maximal figure of merit on energy.	36
24	Figure of merit of best fitting simulated signals in dependence of energy.	36
25	Difference of measurement and simulation during charge collection for different radii for the core signals.	38

26	Difference of measurement and simulation during charge collection for different radii for the segment signals.	39
27	Difference of measurement and simulation during charge collection for different radii for the transient signals.	40
28	Correlation of time shift and difference of measurement and simulation of first five ticks.	41
29	Mean and standard deviation of difference of measurement and simulation in dependence of radius.	42
30	Difference of measurement and simulation, gated on $E > 300$ keV, of the core signals at $r = 30 - 35$ mm.	43
31	Rise times for all interaction positions of crystal A001.	44
32	Dependence of rise times on radius and energy.	45
33	Rise times in xz depiction and comparison with simulation.	46
34	Rise times in xy depiction and comparison with simulation.	47
35	Rise times in xz depiction and comparison with simulation with adjusted preamplifier rise time.	48
36	Added trace of hit segment and core, fitted with straight line for T_0 determination.	49
37	Determined T_0 with respect to CFD timing.	49
38	Determined T_0 with respect to CFD timing for different interaction positions.	50
39	Comparison of determined T_0 values with values provided by the AGATA software.	51
40	Photo of source positions for two different ^{22}Na measurements.	54
41	Hit segments and hit detectors with coincident 511 keV events for source positioned closer to center of AGATA.	54
42	Hit segments and hit detectors with coincident 511 keV events for source positioned away from center of AGATA.	55
43	Energy spectrum of ^{22}Na measurement.	55
44	Measured angles for reconstructed coincidences.	56
45	Difference of time stamps with and without gating conditions	57
46	Visualization of reconstructed coincidences.	58
47	Schematic sketch of reconstructed coincidences.	58
48	Distribution of distances from the lines connecting the coincidences to the source position.	59
49	Density of coincidence lines in dependence of distance to source.	59
50	Variation of source position and corresponding determined mean distance d	61
51	Schematic sketch of reconstruction of 180° coincidences, including a Compton scattering.	62
52	Difference of measured scattering angle and scattering angle derived from the Compton formula.	63
53	Deposited energies from Compton scattering and photo effect.	64

54	Scattering angles in dependence of ratio of energies deposited by the Compton scattering and the photo effect.	64
55	Angles between 511 keV interaction and Compton scattering and angle between 511 keV interaction and photo effect.	65
56	Visualization of coincidences including a Compton scattering.	65
57	Distances of coincidence lines to source position for different gates on the deviation of measured scattering angle and scattering angle from Compton formula.	66
58	Sketch of method to estimate the PSA position resolution.	68
59	Distances of source position to interaction positions of reconstructed coincidences.	68
60	Depiction of all events which fulfill the conditions for the estimation of the position resolution. Visualization of most likely interaction position and PSA result.	69
61	Difference of most likely interaction positions and PSA results.	70
62	Depiction of used Cartesian and spherical coordinate systems.	70
63	Difference of most likely interaction positions and PSA results in spherical coordinates.	71
64	Correlation of number of hits in neighboring grid points.	73
65	Comparison of measured hit distribution with a random distribution.	74
66	Number of hits per grid point for the measured and random distribution.	75
67	Average standard deviation in dependence of number of events.	76
68	Simulated pulse shapes for different radii.	79
69	Simulated pulse shapes for different angles.	80
70	Variation of weighting coefficient with respect to mean distance d	81
71	Variation of weighting coefficient with respect to standard deviation and mean angle	81
72	Difference of simulated and measured signals, normalized to energy of the interaction.	82
73	Difference of simulated and measured signals	83
74	Energy dependence of difference of measurement and simulation.	84
75	Energy dependence of difference of measurement and simulation, zoomed on $E < 100$ keV.	84
76	Variation of distance metric parameter p with respect to mean distance d	85
77	Variation of distance metric parameter p with respect to standard deviation and angle	85
78	Variation of the distance metric parameters p for hit segment and core and q for the transient signals.	86
79	Super trace for interaction in segment C4 and trace of segment A1, consisting mainly of baseline fluctuation.	87
80	Measured amplitude for segment without signal, as approximation for baseline fluctuation.	88
81	Average baseline and average baseline fluctuation for all segments in crystal A001.	88
82	Average baseline and average baseline fluctuation for all segment channels of all crystals.	89
83	Calculated weighting coefficients based on baseline fluctuation for scaling factor $S = 1$ and variation of scaling factor.	90

84	Measured preamplifier response and comparison with exponential response.	91
85	Comparison of simulated traces with and without exponential response.	92
86	Variation of preamplifier time constant τ	93
87	Variation of preamplifier time constant τ on a global level with respect to homogeneity criteria.	94
88	Optimal preamplifier time constant τ for single detectors minimizing the homogeneity criteria.	95
89	Difference of obtained optimal τ values for single detectors using the different homogeneity criteria.	96
90	Optimal preamplifier time constant τ for single segments minimizing the homogeneity criteria.	97
91	Variation of preamplifier time constant τ for segments B3 and B4	97
92	Hole drift velocity in dependence of the electrical field.	99
93	Variation of the hole mobility with respect to the mean distance d	100
94	Iterative variation of preamplifier time constant τ and hole mobility.	101
95	Simulated pulse shapes for different radii and different hole mobility.	101
96	Variation of the electron mobility.	103
97	Comparison of simulated pulse shapes for different radii and different electron mobility.	103
98	Distribution of distances of coincidence lines to the source position for the standard and optimized configurations.	105
99	Difference of most likely interaction position and PSA result for the standard and optimized configurations.	106
100	Difference of most likely interaction position and PSA result for the standard and optimized configurations for the y_{lab} coordinate.	107
101	Distribution of distances of most likely interaction position and PSA result.	107
102	Distribution of hits for $z = 2 - 4$ mm and $z = 14 - 16$ mm of crystal A001 for the optimized configuration.	109
103	Distribution of hits for $z = 40 - 42$ mm of crystal A001 for the standard and optimized configurations.	109
104	Distribution of hits for $z = 40 - 42$ mm of crystal A001 for the standard and optimized configurations, using a different color code.	110
105	Distribution of hits for $z = 52 - 64$ mm of crystal A001 for the standard and optimized configurations using a logarithmic scale.	110
106	Number of hits in dependence of the detector depth z and correlation of radius and z for the optimized configuration.	111
107	Comparison of time dependence of difference of measurement and simulation for standard and optimized configurations for the hit segment.	112
108	Comparison of time dependence of difference of measurement and simulation for standard and optimized configurations for the core.	112

109	Sketch which explains the growth of the charge cloud due to the radial electrical field for interactions close to the core.	120
110	Depiction of integral of transient signals of all neighboring segments for different interaction positions.	122
111	Depiction of integral of transient signals of specific segments for different interaction positions.	123
112	Mean free path of a γ ray in germanium in dependence of energy.	124

List of Tables

4.1	Determined source positions for the two setups.	62
4.2	Standard deviations and mean values of distributions in Fig. 57.	64
4.3	Mean value, FWHM, FWTM and standard deviation for most difference of most likely interaction position and PSA result.	72
4.4	Mean, standard deviation, FWHM and FWTM of the difference of measurement and simulation depicted in Fig. 72 and 73	83
4.5	Mean distance d with and without smearing of interaction positions.	90
4.6	Mean distances d for different τ values: Global, detector specific or segment specific.	95
4.7	Drift velocity parameterization for the holes.	98
4.8	Electron drift velocity parameterization.	102
4.9	Summary of the results of the optimized configuration in comparison with the standard configuration.	104
4.10	Mean distance d and standard deviation for standard and optimized configurations.	104
4.11	Mean, standard deviation σ , FWHM and FWTM for the difference of most likely interaction position and PSA result for the optimized configuration and comparison with standard configuration.	108
4.12	Mean, standard deviation and maximum of the distribution of distances of most likely interaction position and PSA result.	108
4.13	Comparison of correlation factor C , deviation from the expectation and ratio of hits in high statistics grid points for the standard and optimized configurations.	113

Acknowledgments

I would like to thank Prof. Reiter for the opportunity to become a member in his working group and to participate in various research activities. I was given the chance to present my research in multiple national and international conferences and to discuss the results with fellow scientists, as well as broaden my knowledge in a wider perspective during two summer schools. I would also like to thank him for his support and valuable comments during the writing of my publication and of my thesis.

Prof. Jolie for being second reviewer of my thesis.

My working group for fruitful discussions in- and outside of the scientific context. Especially I would like to thank Rouven Hirsch for his valuable help in solving programming issues and helpful discussions regarding any detector physics problem.

I would also like to give credit to the AGATA collaboration, which operates, extends and constantly improves the system through hard work. Only with the combined effort of all members of the collaboration a measurement with a complex system such as AGATA is possible.

Curriculum vitae

Persönliche Daten

Name: Lars Lewandowski
Anschrift: Höninger Weg 376, 50969 Köln
Geburtsdatum: 10. März 1989
Geburtsort: Langenfeld
Nationalität: deutsch
Konfession: evangelisch
Eltern: Wolfgang Lewandowski
Dagmar Lewandowski, geb. Kampermann

Hochschulstudium und Promotion

seit 2014 Promotion an der Universität zu Köln
im Fach Experimentalphysik
2012-2014 Studium der Physik an der Universität zu Köln
(M.Sc. Physik)
2009-2012 Studium der Physik an der Universität zu Köln
(B.Sc. Physik)

Arbeitsverhältnisse

seit 2014 Wissenschaftlicher Mitarbeiter am Institut für Kernphysik
der Universität zu Köln
2011-2014 Studentische Hilfskraft am Institut für Kernphysik
der Universität zu Köln

Zivildienst

2008-2009 Zivildienst in CBT Wohnheim St. Franziskus Langenfeld

Schulbildung

1999-2008 Konrad Adenauer Gymnasium, Langenfeld
1995-1999 Don Bosco Grundschule, Langenfeld

Erklärung zur Dissertation

Ich versichere, dass ich die von mir vorgelegte Dissertation selbständig angefertigt, die benutzten Quellen und Hilfsmittel vollständig angegeben und die Stellen der Arbeit – einschließlich Tabellen, Karten und Abbildungen –, die anderen Werken im Wortlaut oder dem Sinn nach entnommen sind, in jedem Einzelfall als Entlehnung kenntlich gemacht habe; dass diese Dissertation noch keiner anderen Fakultät oder Universität zur Prüfung vorgelegen hat; dass sie – abgesehen von unten angegebenen Teilpublikationen – noch nicht veröffentlicht worden ist, sowie, dass ich eine solche Veröffentlichung vor Abschluss des Promotionsverfahrens nicht vornehmen werde. Die Bestimmungen der Promotionsordnung sind mir bekannt. Die von mir vorgelegte Dissertation ist von Prof. Dr. Peter Reiter betreut worden.

Teilpublikationen

- L. Lewandowski et al. “Pulse-Shape Analysis and position resolution in highly segmented HPGe AGATA detectors”. *Eur. Phys. J. A* 55: 81 (2019)

Köln, der

(Lars Lewandowski)